# AN EXPERIMENTAL STUDY OF TUNGSTEN WIRE-ARRAY Z-PINCH PLASMAS USING TIME-GATED POINT-PROJECTION X-RAY IMAGING

A Dissertation

Presented to the Faculty of the Graduate School

of Cornell University

in Partial Fulfillment of the Requirements of the Degree of

Doctor of Philosophy

by

Jonathan Daniel Douglass

August 2008

AN EXPERIMENTAL STUDY OF TUNGSTEN WIRE-ARRAY Z-PINCH PLASMAS USING TIME-GATED POINT-PROJECTION X-RAY IMAGING

Jonathan Daniel Douglass, Ph.D.

Cornell University 2008

Cylindrical, wire-array Z-pinch experiments have been performed in which ten tungsten wires are imploded using the COBRA pulsed power accelerator. This generator produces a 1.2MA (peak) current pulse with a zero-to-peak rise-time of approximately 100ns. The tungsten (W) wires used in these experiments had initial diameters ranging from 5.1 to 25$\mu m$. For most experiments the array diameter was 8mm or 12mm and the array height was 8mm.

Wire-array Z-pinch plasmas are initiated by the current-driven explosion of the individual wires in these arrays, leading to the formation of coronal plasmas around dense wire-cores. The coronal plasmas carry virtually all of the current once they form. As current-carrying coronal plasma with current density, $\mathbf{J}$, is ablated from the dense cores, the magnetic field, $\mathbf{B}$, of the entire system causes the plasma to be swept toward the axis of the array by the $\mathbf{J} \times \mathbf{B}$ force, although it is believed that the current and magnetic field remain in the plasmas around the wire cores. This continuous ablation and injection of plasma leads to an accumulation of plasma on the pinch axis known as the "precursor" plasma. Eventually, the main implosion phase begins, evidently correlated with the time that gaps form in the wire-core/corona structures. In this phase an amount of mass much greater than that in the precursor implodes onto the array axis causing the primary x-ray pulse.

In order to predict the x-ray yield of experiments on future pulsed power machines a good understanding of wire-array Z-pinch physics, including the ablation process,

is critical. In order to help achieve this understanding, X-pinches placed in the generator's return current circuit adjacent to the wire-array Z-pinch were used as sources of time-gated (<100ps gating) x-rays for point-projection, soft x-ray (3-5keV) radiography. Areal density measurements of tungsten ablation plasmas are obtained from images captured on x-ray film. This is accomplished by comparison of x-ray film exposure by x-rays that passed through the experimental plasma to exposure levels behind tungsten samples of known thicknesses. Using Abel inversion and reasonable assumptions about the spatial variation of these plasmas, areal density measurements are converted into volume densities.

The novel results of this study are the accurate, time dependent ion density measurements in the three primary structures in the ablation process, dense wire-cores, coronal plasmas, and injected plasma streams. The dense core material and coronal plasma density varied slowly with time during the interval 70-165ns and were primarily influenced by initial wire diameter. Dense core material expanded to a final diameter that was proportional to initial wire diameter and then remained static. It was determined that coronal plasma density scales as $1/r^2$ outside of the dense core. The areal density of injected plasma increases linearly with time and scales as $1/r$ as one moves from the dense core toward the array axis. This scaling implies that a significant amount of current flows in the injected plasma stream near the dense core. Measured tungsten densities are in the range $\sim 10^{17}$ to $\sim 10^{20}/\mathrm{cm}^3$.

## BIOGRAPHICAL SKETCH

Jonathan (Jon) Daniel Douglass was born in Columbia, Missouri in August 1980. He attended David H. Hickman High School where he graduated from in 1998. Jon then began undergraduate instruction at the University of Missouri where he initially studied Mechanical Engineering. After switching engineering fields several times he graduated with his B. S. in Electrical Engineering in the spring of 2003.

This work is dedicated to all of the sources of inspiration and encouragement that I have received throughout my life. In particular, this document is dedicated to the memory of my grandfather, Donald Douglass.

## ACKNOWLEDGEMENTS

The successful completion of this research and dissertation would not have been possible without the support of many individuals. Had it not been for Professor David Hammer I would never been a graduate student at Cornell University. His expert knowledge and advise were instrumental in all of my successes.

Thanks to the fall of the Soviet Union I was able to work directly with two of the most talented experimentalists that I've had the pleasure to meet: Sergei Pikuz and Tanya Shelkovenko. They taught me everything I know about x-ray imaging and spectroscopy. This work is largely an extension of techniques that they pioneered.

I would like to thank my committee members, David A. Hammer, S. Leigh Phoenix, and Charles E. Seyler, for helping me along my way despite my frequent resistance.

Few things are accomplished at LPS without the help of our talented staff. J. Todd Blanchard, Joyce Oliver, and Harry Wilhelm deserve credit as the workhorses of the laboratory. God help us all if anything should happen to them.

The measurements presented in the following chapters would not have been possible without the superb calibration steps made by Kate Bell. Her long hours at the Cornell Nanofabrication Facility are greatly appreciated.

During my stay in upstate New York I had the pleasure of spending several Thanksgivings with Trip and Jenny Radcliffe in Uniontown, Pennsylvania. On each of these occasions the Radcliffe house felt like a second home; I look forward to keeping the tradition alive.

## TABLE OF CONTENTS

## LIST OF TABLES

## LIST OF FIGURES

CHAPTER 1

# INTRODUCTION

## 1.1 The road to wire array Z-pinches

Wire-array Z-pinches belong to a class of objects known as Plasma Radiation Sources (PRS) that are typically driven by $10^{10}$ - $10^{13}$W pulsed power machines. These machines are also used to produce electron and ion beams, intense magnetic fields, etc. These technologies are used for x-ray radiography, x-ray lithography[1], nuclear weapon effects testing[2] and thermonuclear fusion experiments[3],[4]. The primary application of pulsed power machines was initially x-ray radiography followed by weapon effects simulations; other applications grew from the availability of generators that were built to be used for these original purposes. Some of these after-thought experiments, like the first high wire number wire-array Z-pinch tests[5], have been so successful that they have led to independent fields of study.

The pulsed electrical generators that are used to drive today's Z-pinch experiments have not changed dramatically from those of the 1960's. As previously mentioned, the earliest generators were used for x-ray radiography. The 1940's and 50's witnessed the development of nuclear weapons. Their development demanded an x-ray imaging diagnostic for the measurement of core implosion symmetry and convergence. One can imagine the high levels of source intensity and durability that such an environment would demand. Specifically, generators were required with output performance exceeding 1MV and in extreme cases 1MA (for weapon effects simulation), i.e. power levels exceeding $10^{12}$ Watts. It is difficult to appreciate the significance of $10^{12}$ Watts (1TW) of electrical power. Consider that 1TW is roughly thirty times the average power supplied by the entire U.S. power grid in 1950, and approximately equal to the capacity of

the U.S. grid today. Clearly achieving such power levels is not trivial. The science of "Pulsed Power" is what makes this possible.

The pulsed power devices of the 1960's-70's produced intense x-ray sources by generating a relativistic electron beam (REB) and focusing it onto a high-Z (atomic number) target. The high-voltage electrical generators, with output current of about 10kA, used for radiography were specialized to REB loads. As a result, the output impedance of a generator of this era would typically be greater than 30Ω. A detailed description of the largest machine of this type ever constructed, a >10MV machine, can be found in [2]; its $10^{13}$W output was used to generate high energy x-rays for weapon effects testing. Improvements in pulsed power technology led to the introduction of short-pulse, low-impedance, ~1MV generators in the early 1970's that could exceed 1MA of electrical current. These new machines were still primarily used as REB generators. Experiments that placed a fine metal wire in the place of the electron beam diode on a 400kV, 7Ω pulsed power machine showed interesting levels of soft x-ray production[6]. This motivated further experiments on the Gamble II accelerator at the Naval Research Laboratory (NRL) in which this 1MA generator was discharged directly into a fine metal wire[7]. These and later experiments at NRL[8] and Physics International on the OWL II[9] generator showed that high current single wire explosions produce plasmas with very high temperatures and densities. These discharges were researched extensively and remain a subject of interest today[10, 11, 12].

While single wire explosions were certainly a novel x-ray source in the early 1970's it was clear that they did not couple well to electrical generators intended for high current REB applications. Specifically, the impedance of an exploding wire plasma is far less than that of an electron beam diode. As a result, the exploding wire plasma reflects more energy back into the generator then it dissipates, imposing a pessimistic upper

limit on the maximum radiation yield for a given generator. The problem of impedance mismatch is solved by replacing the single wire load with an imploding cylindrical (Z-pinch) load. The time varying inductance ($\dot{L}$ )of an imploding Z-pinch looks like a real impedance (resistance) to the generator. The impedance associated with the implosion process can be tailored to match the generator impedance, which results in dramatically improved conversion of stored generator energy to x-ray output through the intermediary of implosion kinetic energy. This concept was first implemented in the mid 1970's.

There are three basic Z-pinch configurations that can couple effectively to a low impedance pulsed power generator: foil liners[13], gas puffs[14, 15], and wire-arrays[16, 17]. Each of these configurations is essentially a cylindrical distribution of mass that is driven by a very large, short current pulse. In each case the large electrical current causes the bulk material to break down and form a highly conductive plasma cylinder carrying electrical current along its length that implodes due to the Lorentz force.

Foil liners, gas puffs and wire-arrays have their respective benefits and disadvantages. Foil liners are presumed to demonstrate the simplest implosion physics[18], but tend to be the least practical to construct for presently available pulsed power machines. Gas puff Z-pinches are typically initiated from a low density noble gas; this system radiates efficiently but its mass distribution is difficult to control. Wire-arrays are comparatively simple to construct but demonstrate very complicated physics that is not well understood.

From the late 1970's to the early 1990's gas puffs[19] and wire-array Z-pinches[20] were studied in parallel. A good summary of this work is given by Pereira and Davis[21]. Both methods demonstrated good scaling and as a result research facilities grew in size and cost as ever larger objects were to be tested in high radiation fluxes, i.e. weapon

effects testing. The growth of these machines stagnated in the early 1990's when x-ray power ceased to scale with $I^4$ (I = output current), as had been the case in the previous decade[22]. (This means that the x-ray power began to be limited by machine power and/or available energy instead of something to do with pinch physics.)

To this point in wire-array history a "standard" array consisted of six aluminum or tungsten wires in a cylindrical configuration with a diameter of 2-3cm and a height of about 2cm. Operation with sparse arrays having only six wires was typical since it had been shown that, "...six or more wires are theoretically stable against perturbations that destroy cylindrical symmetry[23]"[21], and that increasing the number of wires to as many as 24 did not have a significant effect on total x-ray yield[21]. This belief persisted throughout the 1980's and early 1990's until a systematic study of the effect of wire number on x-ray power and energy led to a major breakthrough. Experiments on the Saturn[24] accelerator at Sandia National Laboratories (SNL), Alubuquerque, showed that increasing the number of wires from 10 to 90, while keeping the total array mass roughly constant, increased the x-ray power by a factor of seven[5].

The increase in x-ray power achieved with high wire number arrays was so significant that it motivated the conversion of the PBFA-II (Particle Beam Fusion Accelerator) light ion fusion accelerator to PBFA-II Z[25] so that it could drive scaled up versions of the wire arrays used on Saturn. Wire-array Z-pinches on PBFA-II Z were so successful that they became the accelerator's primary application; this machine is now simply called "Z". The crowning achievement of wire-array Z-pinches came in 2003 when SNL announced that thermonuclear fusion neutrons had been achieved from a fuel capsule imploded by the x-rays driven by wire-array implosions on the Z-machine[26, 27]. For more detailed descriptions of the historical evolution of wire-array Z-pinches see refs. [28, 29].

While the primary applications of Z-pinches continue to be materials and weapon effects testing, it is hoped that these intense x-ray sources can one day be used to drive high yield nuclear fusion. The main roadblock to the latter application is that significantly higher x-ray power levels are required. There is general agreement that this demands the construction of a larger electrical driver. Thus, the question at hand is how large must the electrical driver be in order to facilitate high yield nuclear fusion? As previously mentioned, our physical understanding of the wire-array Z-pinch is limited; this makes it difficult to predict how large the accelerator must be to achieve this lofty goal. From the mid 1970's to present day, x-ray power scaling has shifted from $I^4$ to $I^2$ to $I^{1.24\pm0.18}$ in the most pessimistic analysis of recent data[30]. This alarming trend calls for an improved understanding of the physics of wire-array Z-pinches, which is the objective of the research presented here.

## 1.2 Large Scale Pulsed Power

The concept of pulsed power is simple. Energy is drawn from a primary power source (usually the wall socket) at a modest power level and stored in an energy reservoir. Once a sufficient amount of energy has been stored in the reservoir some sort of switching mechanism redirects the stored energy to some kind of electrical load in much less time than was needed to fill, or charge, the reservoir. Since power is equivalent to energy divided by time, and the amount of energy in the system is assumed to be constant, this ideal system achieves a power gain proportional to the time to build up the stored energy, divided by the discharge time. Hence, an ideal system that charges in one second and discharges in $1/1000^{th}$ of a second accomplishes a power gain of 1000. A logical extension of this simple example is cascaded systems; this is how awesome electrical power levels are generated.

The pulsed power generators, or accelerators, that drive REBs and the various types of Z-pinches all use the same basic energy storage, switching, compression and transmission components. Electrical energy is stored in large capacitor banks, switching is done with "spark-gap" switches, and the energy is compressed in time and volume and then delivered to the load via parallel plate or coaxial transmission lines. The pulsed power systems discussed here tend to operate in the $10^6$ Volt (1MV), $10^6$ Ampere (1MA), regime with pulse durations ranging from 50 to 500ns (1ns = $10^{-9}$ seconds, i.e. one-billionth of a second).

The capacitor bank is the heart of any large scale pulsed power system. The generators discussed here use a capacitor bank topology known as a "Marx generator". The Marx generator has many benefits and is used extensively with slight variations from one application to another. The basic principle of the Marx generator is to charge capacitors in parallel and then rearrange the circuit so that capacitors are in series connection when discharged into some load. This strategy can accomplish a voltage multiplication approximately equal to the number of capacitors in the bank. The Marx topology is beneficial because of the dangers and complexities associated with high voltages. It is very impractical to charge a large capacitor to voltages over 125kV directly from a DC power supply, yet the generators of interest require voltages exceeding 1MV, hence the need for the voltage multiplication of the Marx generator. Large Marx generators can store megajoules (MJ) of energy. Note that 1MJ = $10^6$J, which is equivalent to the explosive energy stored in a half pound of TNT. A high energy Marx generator tends to be bulky since each capacitor fills 2-3 cubic feet of space and weighs about 200lbs. A typical bank for a 1TW accelerator intended to operate near 1MV would have a footprint of 2.5ft by 6ft and a height of about 8ft. In order to operate at such high voltages these systems are immersed in transformer oil, giving them a delightful smell and texture.

The switching devices used in these systems are unique to this application. The time-scales of interest for output pulses from pulsed-power generators are far too short to allow the use of mechanical contact switches. The use of solid-state switches is impractical at mega-Ampere current levels. The switching speed and resistance of silicon based devices are inadequate for this application. The device of choice is the "spark gap" switch. In its simplest form the spark gap switch is comprised of two metal electrodes separated by a gap of about a centimeter. When a critical voltage across the electrodes is exceeded the insulating material filling the gap breaks down and a highly conductive electrical arc quickly bridges the electrodes, thus "closing" the switch. This type of switch can be designed to withstand voltages above 1MV before closing and can conduct currents in the range of 100's of kilo-Amperes (kA) with a switch impedance far less than solid-state devices when the switch is closed. Turn-on time can be as short as 10ns. The main problem with simple spark gaps is a lack of consistent, predictable operation. This problem is referred to as switch "jitter", and results in a level of uncertainty as to when a switch will close. Fortunately, methods exist to induce gap breakdown at a controlled time (triggerable switches) that dramatically decrease the amount of jitter in a pulsed power system.

Electrical pulse compression is the fundamental idea behind large pulsed power systems. Generally, pulse compression is accomplished by transferring energy from one storage element to another with the charging/discharging of these elements becoming progressively faster with each stage. This technique is inefficient and results in most of the initial energy being lost along the way. In actuality the pulse compression and power transmission systems are one in the same. The specific design of this system is dependent upon the desired output pulse shape and load impedance. When dealing with wire-arrays and other Z-pinches it is desirable to make the generator impedance as low as possible, typically less than 1$\Omega$. In order to achieve low impedance and meet other

requirements, large pulsed power systems generally employ either 1m diameter coaxial or parallel plate transmission lines. De-ionized water is the dielectric of choice because of its high dielectric constant, about 80, high breakdown electric field for short pulses, and self-healing nature.

A more detailed description of a typical pulsed power system can be found in ref. [9].

## 1.3 The magnetic pinch effect

The Z-pinch is just one configuration of current-driven plasma pinch. This effect is caused by the Lorentz force, which arises whenever a charged particle encounters a magnetic field that is perpendicular to the direction of the particle's motion. The force on a charged particle due to an electromagnetic field is:

$$\mathbf{F} = q(\mathbf{E} + \mathbf{v} \times \mathbf{B}) \quad \text{(N)} \tag{1.1}$$

where, $q$ is the charge of the particle, $\mathbf{v}$ is the particle's velocity, and $\mathbf{E}$ and $\mathbf{B}$ are the electric and magnetic fields, respectively. Generally, a plasma can be composed of many species of particles having various values of charge, mass, number density, temperature, and velocity. The use of a fluid treatment is often convenient, especially when the number of species is low. For simplicity, let us consider a two species collisionless plasma, made up of ions ($i$) and electrons ($e$) with parameters, $X_{i,e}$, using such a treatment, where $X_{i,e}$ might be number density, a velocity component, etc. The equations of motion for the two species are then:[31]

$$m_i n_i \dot{\mathbf{v}}_i = q_i n_i \{\mathbf{E} + \mathbf{v}_i \times \mathbf{B}\} + \nabla p_i \tag{1.2}$$

$$m_e n_e \dot{\mathbf{v}}_e = q_e n_e \{\mathbf{E} + \mathbf{v}_e \times \mathbf{B}\} + \nabla p_e \tag{1.3}$$

where $\nabla p_{i,e}$ is the force exerted by thermal pressure. The ions are taken to be ionized $Z$ times, i.e. $n_i = n_e/Z$ and $q_i = -Zq_e$. Summing the two equations of motion and eliminating $n_i$ and $q_i$ in favor of $n_e$ and $q_e$ then gives:

$$n_e\left(\frac{m_i}{Z}\dot{\mathbf{v}}_i + m_e\dot{\mathbf{v}}_e\right) = q_e n_e(\mathbf{v}_e - \mathbf{v}_i)\times\mathbf{B} - \nabla(p_i + p_e) \tag{1.4}$$

If it is assumed that the system is in equilibrium then the left hand side of eqn. 1.2 is approximately zero. The factor $q_e n_e(\mathbf{v}_e - \mathbf{v}_i)$ is the current density, $\mathbf{J}$. Replacing $p_i + p_e$ with $p$, we have

$$\nabla p = \mathbf{J}\times\mathbf{B}\ . \tag{1.5}$$

The current density, $\mathbf{J}$, can be eliminated using Maxwell's equation (neglecting displacement current) $\nabla\times\mathbf{B} = \mu_0\mathbf{J}$, giving

$$\begin{aligned}\nabla p &= \frac{1}{\mu_0}(\nabla\times\mathbf{B})\times\mathbf{B} \\ &= \frac{1}{2\mu_0}\left\{2(\mathbf{B}\cdot\nabla)\mathbf{B} - \nabla(\mathbf{B}\cdot\mathbf{B})\right\}\ .\end{aligned} \tag{1.6}$$

Collecting terms and substituting $B^2$ for $\mathbf{B}\cdot\mathbf{B}$, we find

$$\nabla\left(p + \frac{B^2}{2\mu_0}\right) = \frac{(\mathbf{B}\cdot\nabla)\mathbf{B}}{\mu_0}\ . \tag{1.7}$$

Assuming $\mathbf{B} = B_z(r)\hat{e}_z + B_\theta(r)\hat{e}_\theta$ and $p = p(r)$, for $B_\theta = 0$, the right hand side of 1.7 is zero, in which case the quantity inside the gradient operator in 1.7 is constant. However, for a current carrying plasma column, like a Z-pinch, the right hand side of 1.7 is $\frac{-B_\theta^2}{\mu_0 r}\hat{e}_r$. Multiplying the left hand side of eqn. 1.7 by $r^2$ and integrating by parts over the column radius gives

$$\begin{aligned}\int_0^a r^2\frac{\partial}{\partial r}\left(p + \frac{{B_\theta}^2}{2\mu_0}\right)dr &= a^2\left(p(a) + \frac{{B_\theta}^2(a)}{2\mu_0}\right) - 2\int_0^a\left(p + \frac{{B_\theta}^2}{2\mu_0}\right)rdr \\ &= a^2\frac{{B_\theta}^2(a)}{2\mu_0} - 2\int_0^a\left(p + \frac{{B_\theta}^2}{2\mu_0}\right)rdr\ ,\end{aligned} \tag{1.8}$$

where $a$ is the radius at which the plasma pressure goes to zero.

Multiplying the right hand side of eqn. 1.7 by $r^2$ and integrating over the column radius gives

$$\int_0^a r^2 \frac{(\mathbf{B}\cdot\nabla)\mathbf{B}}{\mu_0} dr = -\int_0^a \frac{{B_\theta}^2}{\mu_0} r dr \ . \tag{1.9}$$

Equating eqns. 1.8 and 1.9 then yields:

$$\begin{aligned} a^2 \frac{{B_\theta}^2(a)}{2\mu_0} &= 2\int_0^a p r dr \\ &= \frac{2\langle p\rangle \pi a^2}{2\pi} \\ \langle p\rangle \equiv \frac{\int_0^a p 2\pi r dr}{\pi a^2} &= \frac{{B_\theta}^2}{2\mu_0} \ . \end{aligned} \tag{1.10}$$

Hence, at the edge of a pinch in equilibrium, where $p$ is zero, the magnetic pressure is $B^2/2\mu_0$, and this pressure balances the area-averaged particle kinetic pressure. This equilibrium was first derived by Bennett[32] in 1934. Bennett showed that in the simple case of electrons and positives flowing in opposite directions with velocities $u$ and $v$ and transverse temperatures $T_1$ and $T_2$, respectively, that a specific current is required in order for an equilibrium to be established. Equation 12 in Bennett's 1934 paper gives the number of electrons and positives per unit length (i.e. $n_0 = n_i = n_e$), $\lambda_0$, and equilibrium current $i_0$ (in c.g.s. units) as:

$$\lambda_0 = \frac{c^2 \cdot 2K(T_1 + T_2)}{e^2(u+v)^2} \ \ (/cm) \tag{1.11}$$

$$i_0 = \frac{c^2 \cdot 2K(T_1 + T_2)}{e(u+v)} \ \ (statamperes) \ . \tag{1.12}$$

Substituting $e(u+v) = i_0/N$ into 1.12, where $N$ is the number of electrons and positives per centimeter gives $i_0$ in its usual form

$$i_0^2 = c^2 \cdot 2NK(T_1 + T_2) \ \ (dyne \cdot \frac{cm^2}{s^2}) \ . \tag{1.13}$$

The S.I. (Standard International) unit form of this expression (in Newtons), as found in [33], is:

$$\frac{\mu_0 I^2}{4\pi} = 2N_e(1 + 1/Z)kT \ \ (N) \ . \tag{1.14}$$

In equation 1.14, the plasma is assumed to consist of $N_e$ electrons and $N_e/Z$ ions (positives) per unit length with uniform temperature, $T$, and total current $I$. Equation 1.14 is the integral form of the differential relationship described by equation 1.7. Bennett published a generalized version of his equilibrium in 1955[34] that allows for any number of particle species with any number of velocities.

A simple expression for energy balance between resistive (Joule) heating and energy lost to bremsstrahlung radiation in a Bennett equilibrium is described by the Pease-Braginskiĭ current, $I_{PB}$. Hence, in a Bennett equilibrium with a current of $I_{PB}$, energy in equals energy out. The value of $I_{PB}$ is a constant for any material at a particular $Z$ (or $\bar{Z}$, the average value of $Z$ if there are several ionization states present). A simple derivation of the Pease-Braginskiĭ current is presented in Ref. [33], the result of which is given by

$$\frac{I_{PB}}{I_A} = \left(\frac{8\ln\Lambda}{\alpha F_b}\right)^{1/2} 2\left(1+\frac{1}{Z}\right) , \tag{1.15}$$

where $I_A$ is the Alfvén-Lawson current, defined by

$$I_A = \frac{ec}{r_e} \tag{1.16}$$

$$r_e = \frac{e^2}{mc^2}\frac{1}{4\pi\epsilon_0} . \tag{1.17}$$

$\ln\Lambda$ is the Coulomb logarithm, $\epsilon_0$ is the permittivity of free space, $e$, $m$, and $c$ are the electron charge and mass, and the speed of light, respectively, $r_e$ is called the classical electron radius at which $e^2/4\pi\epsilon_o r_e = m_e c^2$, and $\alpha$ is the fine structure constant defined as

$$\alpha = \frac{e^2}{c\hbar}\frac{1}{4\pi\epsilon_0} , \tag{1.18}$$

where $\hbar$ is Planck's constant divided by $2\pi$. The factor $F_b$ is taken to be $\sqrt{2\pi/27}$.

While the possible equilibria described by the Bennett relation and Pease-Braginskiĭ current are of fundamental interest, an understanding of the dynamics of these systems is potentially very useful. In terms of dynamics, the simplest type of Z-pinch is that of

a thin annular shell. In this case the inward radial force per unit length exerted on the shell is taken to be the magnetic pressure multiplied by the circumference of the shell:

$$F_r = \hat{m}\ddot{r} = \frac{B^2}{2\mu_0} \times 2\pi r \tag{1.19}$$

Where $B = B(r,t)$, $r = r(t)$ and $\hat{m}$ is the mass of the thin shell per unit length. In this simple case $B$ is given by:

$$B(r,t) = \frac{\mu_0 I(t)}{2\pi r} \tag{1.20}$$

Thus, the radial acceleration of the thin shell is given by:

$$\ddot{r} = -\frac{\mu_0 I^2}{4\pi \hat{m} r} \tag{1.21}$$

A convenient formula for the kinetic energy of the pinch[35], is found by multiplying equ. 1.21 by $\dot{r}$:

$$\begin{aligned} \dot{r}\ddot{r} &= -\frac{\mu_0 I^2}{4\pi\hat{m}}\frac{\dot{r}}{r} \\ \frac{1}{2}\frac{d(\dot{r}^2)}{dt} &= -\frac{\mu_0 I^2}{4\pi\hat{m}}\frac{d}{dt}\ln(r) \qquad (1.22) \\ W(t=t^*) \equiv \frac{\hat{m}\dot{r}^2(t^*)}{2} &= -\frac{\mu_0}{4\pi}\int_0^{t^*} I^2 \frac{d}{dt}\ln(r) dt \qquad (1.23) \end{aligned}$$

Integrating by parts:

$$W_{kin}(t=t^*) = -\frac{\mu_0}{4\pi}\left\{ I^2 \ln r\Big|_0^{t^*} - \int_0^{t^*} \frac{d(I^2)}{dt}\ln r \, dt \right\} \tag{1.24}$$

Since $I(t=0) = 0$, with $W^*_{kin} \equiv W(t=t^*)$,

$$\begin{aligned} W^*_{kin} &= -\frac{\mu_0}{4\pi}\left\{ I(t^*)^2 \ln r(t^*) - \int_0^{t^*} \frac{d(I^2)}{dt}\ln r \, dt \right\} \\ &= -\frac{\mu_0}{4\pi}\left\{ \ln r(t^*) \int_0^{t^*} \frac{d(I^2)}{dt} dt - \int_0^{t^*} \frac{d(I^2)}{dt}\ln r \, dt \right\} \\ &= \frac{\mu_0}{4\pi}\int_0^{t^*} \frac{d(I^2)}{dt}\left\{\ln r - \ln r(t^*)\right\} dt \\ &= \frac{\mu_0}{4\pi}\int_0^{t^*} \frac{d(I^2)}{dt}\ln\frac{r}{r(t^*)} dt \, . \qquad (1.25) \end{aligned}$$

The application of equ. 1.25 is largely academic. While this derivation is pleasing in that it makes no approximations, once the calculation is started, it has many shortcomings, foremost of which is the initial assumption of a thin shell, which is completely unrealistic. In any real system mass cannot remain concentrated in a thin shell due to thermal pressure, electromagnetic forces and fluid instabilities. Furthermore, a numerical integration of equ. 1.21 or some knowledge of the implosion trajectory is required a priori even for this simplest of cases.

The amount of complexity associated with the dynamics of realistic Z-pinches is immense. Closed-form analytic expressions are virtually non-existent. Typically, 2-D or, better still, 3-D computer modeling is used to predict/describe the dynamics of these systems. In order to validate the results of these codes, experimental data is necessary. At present, computer modeling fails to predict many features of wire-array Z-pinches. As a result, experimental data that can be used to elucidate wire-array Z-pinch physics and help validate models used in computer simulations is of tremendous value to this field. Experimental measurement of fundamental parameters associated with wire-array dynamics is the goal of this research. Specifically, we present in Chapter 11 of this thesis detailed density profiles of the plasma as a function of time in tungsten wire-array Z-pinches.

CHAPTER 2

# COBRA

## 2.1 General Description

The COrnell Beam Research Accelerator (COBRA) was originally designed and constructed for light ion-beam research[36]. Evolving research interests demanded a machine capable of driving low-impedance inductive loads like cylindrical wire-array Z-pinches. To meet this need COBRA was redesigned by Applied Pulsed Power, Inc. Construction of the redesigned machine began during the summer of 2003. Low-power testing started in February of 2004 and the first full-power shot was done in April, 2004. At present (Fall of 2007) COBRA has had over 1,000 shots. The number of shots per day typically varies from one to four depending on the complexity of the load configuration and diagnostics.

COBRA was redesigned with three performance goals in mind: 1MA peak output current into a wire array load, a minimum zero-to-peak rise-time of 100ns and variable output pulse shape. The machine is driven by two 55 kJ Marx generators. Each generator feeds a parallel-plate water capacitor. The primary purpose of these capacitors is to ease design constraints on the Marx generators, allowing them to have higher internal inductance. Near peak charge voltage each intermediate storage capacitor is switched into two parallel pulse-forming lines (four total) via a self-breaking (not triggered) spark-gap switch. Once fully charged, each pulse-forming line is switched into the vacuum section of the machine via a laser-triggered, spark-gap switch. These final switches can be laser triggered at different times to provide different output pulse shapes. All of the machine's switches are filled with $SF_6$ (sulfur-hexafluoride) gas. For a more detailed description of COBRA see Ref. [37]. Sample waveforms of the current and voltages seen on COBRA

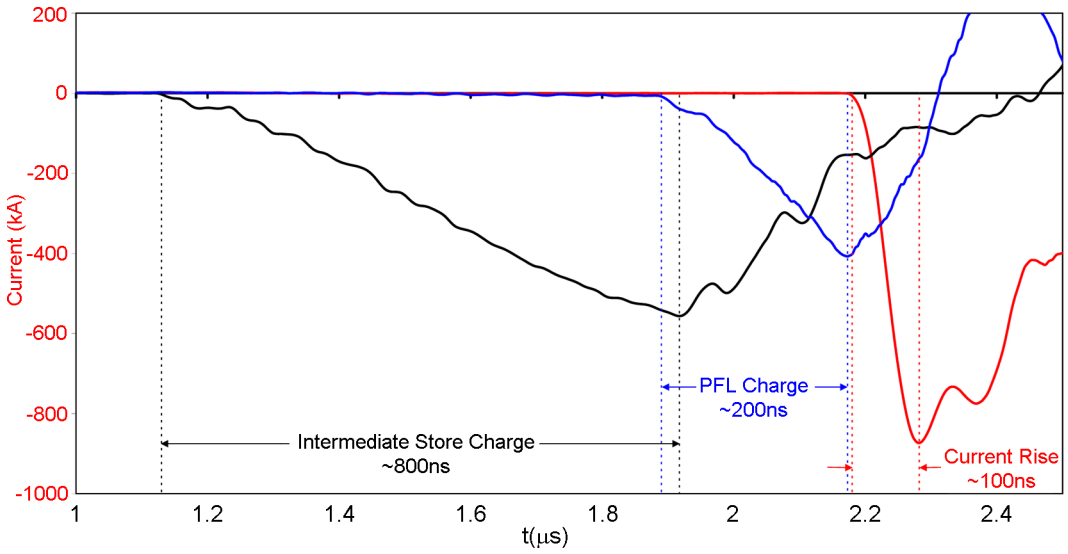


Figure 2.1: Sample current and voltage waveforms from COBRA experiment 132.

are shown in Fig. 2.1. In practice the machine has a minimum rise-time of about 95ns and reaches a peak current as high as 1.2MA into a low inductance wire-array load.

## 2.2 Diagnostics

Wire-array Z-pinches are studied with an extensive suite of x-ray, UV and visible light diagnostics on the CORBA pulsed power generator. These systems contribute to the measurement of basic plasma parameters such as temperature, plasma density, and current density throughout the volume of the wire-array, in addition to experimental parameters like implosion velocity and pinch time. The comprehensive spatial and temporal mapping of these parameters would greatly contribute to the understanding of the largely uncertain physics of wire-array Z-pinches. Such an understanding could improve the performance of these systems and open new frontiers in High Energy Density Physics (HEDP).

Taking direct measurements of basic parameters like temperature and mass density is simple in every day life. This is not the case when dealing with wire-array Z-pinches. In Z-pinch experiments a tremendous amount of data is collected with each shot. The data can be separated into two categories: measurements of pinch parameters (plasma parameters), and properties of the radiation emitted by the pinch (spectral parameters).

An ideal plasma diagnostic, or collection of diagnostics, would measure the current density, $\mathbf{J}$, magnetic field, $\mathbf{B}$, the ion and electron temperatures, $T_i$ and $T_e$, and the ion and electron densities, $n_i$ and $n_e$, at each point within the array volume with nanosecond temporal resolution, i.e. measure $B_r$, $B_\theta$, $B_z$, $J_r$, $J_\theta$, $J_z$, $T_i$, $T_e$, $n_i$, and $n_e$ as functions of space, $\mathbf{x} = (x, y, z) = x\hat{i} + y\hat{j} + z\hat{k}$, and time, $t$. Note that the vector quantities $\mathbf{J}$ and $\mathbf{B}$ each have three components, in general, e.g. $\mathbf{B}(\mathbf{x}, t) = B_r(\mathbf{x}, t)\hat{r} + B_\theta(\mathbf{x}, t)\hat{\theta} + B_z(\mathbf{x}, t)\hat{z}$.

An ideal spectral diagnostic is somewhat simpler in that it need measure only the intensity of radiation emitted from the pinch as a function of wavelength, $\lambda$, $\mathbf{x}$ and $t$, i.e. a five-dimensional record of intensity, $Q(\lambda, \mathbf{x}, t)$. Virtually all forms of radiation detectors can record at best two dimensions. One might record intensity as a function of two spatial variables for a brief instant in time integrated over a range of wavelengths; a black and white photograph obtained with a time-gated camera, for example, is this kind of diagnostic. If more spectral information is desired one can sacrifice a spatial dimension and record intensity as a function of a single spatial direction and wavelength. Similarly, one could record intensity as a function of wavelength and time (emitted from a specific point). The tradeoffs associated with two dimensional records is compensated for by fielding many detectors in parallel and correlating the resulting data set.

The extreme temperatures, radiation intensities, and magnetic fields found in these experiments make the direct measurement of basic plasma parameters exceedingly difficult. As a result, parameters like temperature and density must be inferred from indirect

measurements. Temperature, for example, is commonly inferred from the properties of the radiation emitted by the plasma. Electron density, $n_e$, can be determined by propagating a laser through the plasma and measuring the properties of the beam after it exits the plasma (in addition to spectroscopic methods like those used to infer temperature). Ion density, $n_i$, can be inferred from the x-ray opacity of the plasma. This technique is the crux of this research.

Most of the diagnostics used in wire-array Z-pinch experiments are far less complicated than one might be led to believe by the description of "ideal" devices. Simplifications from an "ideal" device are achieved by lowering the dimensionality of the measurement through integration. For instance, the lens in a camera essentially integrates out one spatial dimension (the depth of field), thereby mapping three-dimensional space onto a two-dimensional film. This method for decreasing dimensionality is not restricted to spatial dimensions and can be applied to temporal and spectral dimensions as well. Most of the diagnostics that are commonly used in these experiments are described in refs. [38, 39].

CHAPTER 3

# WIRE-ARRAY IMPLOSION PROCESS

## 3.1 Implosion Process

The conventional understanding of the implosion process of a wire-array Z-pinch is as follows. Plasma is initiated around each wire in the array by the current-driven explosion of each of these wires (Figure 3.1A). These hot, highly conductive plasmas are referred to as "coronal plasmas". The coronal plasmas carry virtually all of the current once they form. As current-carrying coronal plasma with current density, $\mathbf{J}$, is ablated from the dense cores, the magnetic field, $\mathbf{B}$, of the entire system causes the plasma to be swept toward the axis of the array by the $\mathbf{J} \times \mathbf{B}$ force, although current and magnetic field remain in the plasma around the wire cores (Figure 3.1B). Material that has been swept, or injected, into the interior of the cylindrical array will be referred to as "injected plasma" or "injected mass". The rate at which mass is injected toward the array axis is modulated in the axial direction. The wavelength of the "axial modulation" varies only with wire material. The continuous ablation of the wires and injection of mass toward the array axis leads to the accumulation of plasma on the pinch axis, which will be referred to as "axial plasma". Eventually, the main implosion phase begins (Figure 3.1C), evidently correlated with the time that gaps form along the length of the wire-core/corona structures. Gap formation is a result of the axial modulation. In this phase, 50-70% of the initial array mass, which to this point has remained at rest at the initial wire locations, undergoes tremendous inward radial acceleration. This material stagnates on the array axis due to the collision of counter-flowing mass and the ever present $\mathbf{J} \times \mathbf{B}$ force (Figure 3.1D). An intense x-ray burst occurs at stagnation as a result of the thermalization of kinetic energy, and the current-driven heating and compression

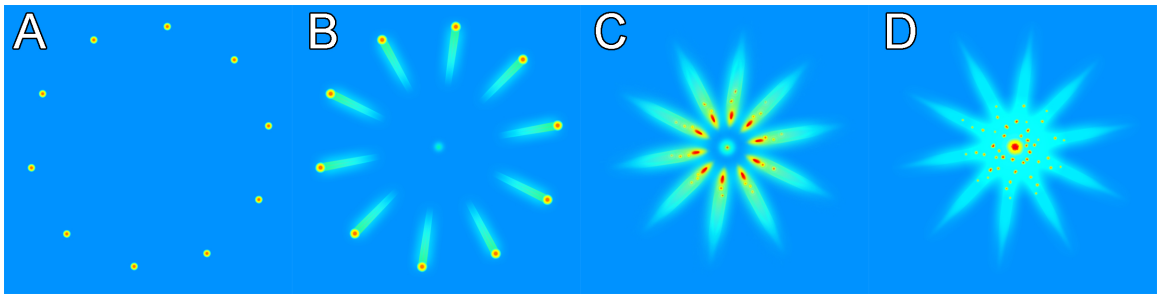


Figure 3.1: End-on view of wire-array implosion process. A - initiation phase, B - ablation phase, C - fast implosion, D - stagnation.

of the axial plasma.

This general description of the wire-array implosion process was formed over a span of years from the late 1990's to the present. As a result, there are many papers that have contributed to our present understanding. The earliest such papers came from work at Maxwell Laboratories on the Blackjack electron beam accelerator, see Refs. [17, 40, 41]. Early work was more concerned with the x-ray power and yield of the implosion than the physics of the processes that led to the implosion. Starting in the mid 1990's, researchers started paying more attention to the events preceding the main implosion (see Refs. [42, 43]), which led to the first descriptions of "coronal" and "ablated" plasma in wire-arrays.

The timing of these phases is often measured using a visible light streak camera. A simplified schematic of such a diagnostic is shown in Figure 3.2. This system records the radial locations of visible light emission, averaged over a small axial distance, as a continuous function of time. A sample streak is shown in Figure 3.3.

The realization that the wires remain at their initial locations for about 80% of the implosion time led to a modification of the "thin-shell" force equation (Eqn. 1.19). To

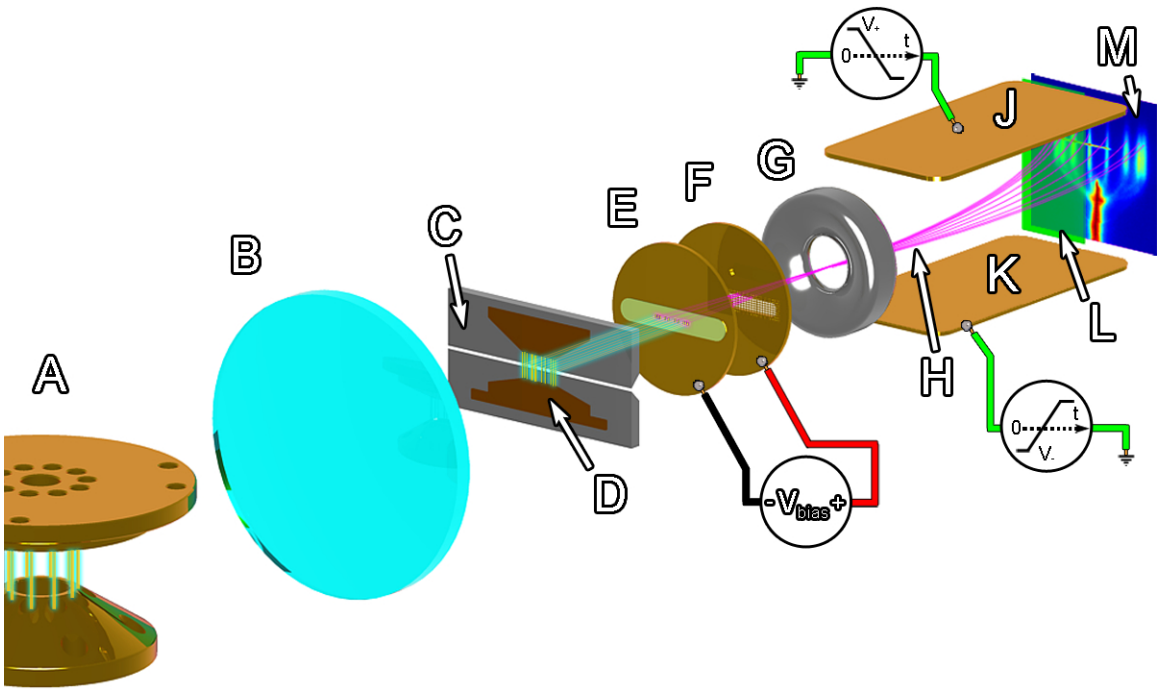


Figure 3.2: Visible light streak camera setup. A - wire-array Z-pinch, B - focusing lens, C - slit (in radial direction), D - real image of wire-array formed by lens, E - electron-emitting photocathode, F - electron accelerating grid, G - electrostatic lens, H - electron trajectories, J - upper sweep plate, K - lower sweep plate, L - scintillation screen, M - detector (film, CCD, etc.).

be more exact, the radial force on a thin shell is the rate of change of radial momentum:

$$F_r = \frac{d\left(\hat{m}\dot{r}\right)}{dt} \tag{3.1}$$

$$= \dot{\hat{m}}\dot{r} + \hat{m}\ddot{r} \ . \tag{3.2}$$

In the case of the classical thin-shell 100% of the initial mass is uniformly accelerated from $t = 0$ to stagnation, hence $\dot{\hat{m}} = 0$. However, in the case of stationary wires with mass being ablated from them, it is assumed that $\dot{\hat{m}}\dot{r} \gg \hat{m}\ddot{r}$. This leads to the Lebedev "Rocket model"[44] of ablation in wire arrays.

In the Rocket model $\dot{r}$ is replaced by "ablation velocity", $v_{abl}$, which is only influenced by the current pulse shape and wire material. The rate of mass ablation per unit

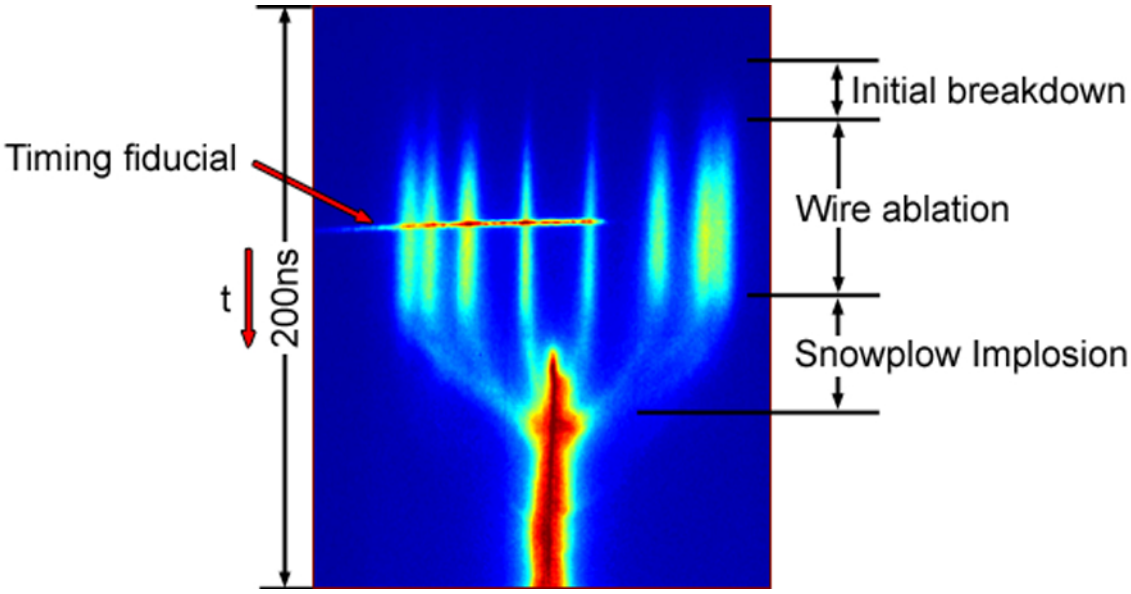


Figure 3.3: Sample visible light streak.

length is then given by:

$$\dot{\hat{m}} = \frac{1}{v_{abl}} F_r \tag{3.3}$$

$$= -\frac{1}{v_{abl}} \frac{\mu_0 I^2}{4\pi R_0} \quad . \tag{3.4}$$

Where $R_0$ is the array radius in meters and $I$ is the generator current.

Integrating Eqn. 3.3 over time and dividing by the initial mass gives the fraction of the original mass that has been ablated as a function of time, $\delta\hat{m}(t)$,:

$$\delta\hat{m}(t) = \frac{1}{m_0 v_{abl}} \frac{\mu_0}{4\pi R_0} \int_0^t I(\tau)^2 d\tau \quad . \tag{3.5}$$

Substituting $N\rho\pi{\phi_0}^2/4$ for $m_0$, the initial mass per unit length:

$$\delta\hat{m}(t) = \frac{\mu_0}{N\rho R_0 v_{abl}\pi^2{\phi_0}^2} \int_0^t I(\tau)^2 d\tau \quad . \tag{3.6}$$

Where $\rho$ is the density of the wire material (kg/m$^3$), $N$ is the number of wires in the array, and $\phi_0$ is the wire diameter in meters.

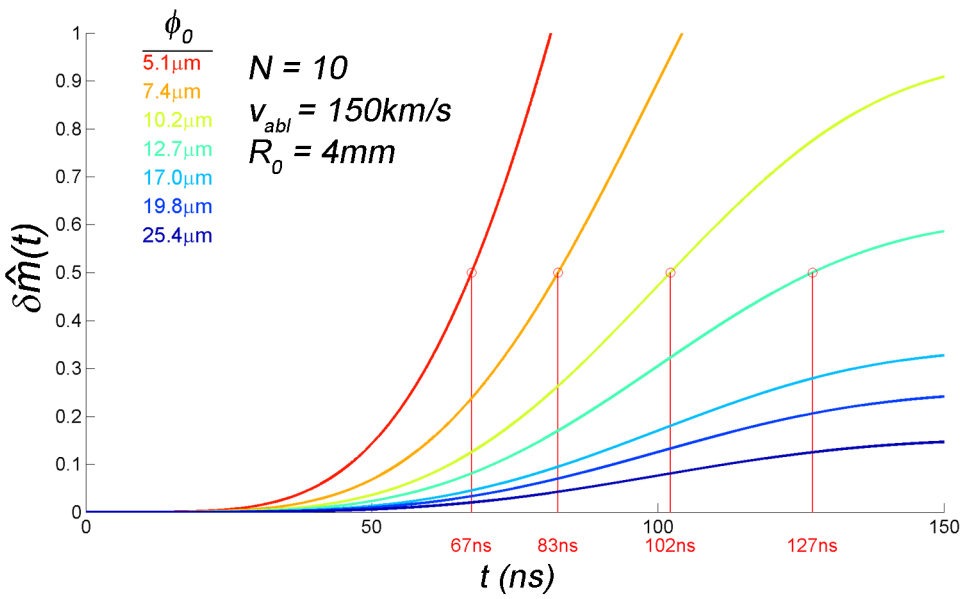


Figure 3.4: Fraction of initial mass ablated versus time as predicted for W wire arrays by Eqn. 3.6 with the parameters $v_{abl}$ = 150km/s, $N$ = 10, $R_0$ = 4mm, and a $\sin^2$ current pulse with $I_{peak}$ of 1.1MA and rise-time of 100ns. The times indicated in red are the times when 50% of the initial mass has been ablated for the various values of $\phi_0$, typically referred to as the time when the fast implosion phase begins, or $t_{imp}$.

If one assumes that the fast implosion phase begins when approximately 50% of the initial mass has been ablated, as is typically done, then one can use Eqn. 3.6 to estimate implosion time, $t_{imp}$. Of course, this assumes that one has a value for $v_{abl}$. This parameter is commonly inferred from radial streak data, like the image shown in Fig. 3.3, or is extrapolated from experimental values for $t_{imp}$ assuming that 50% ablation was achieved.

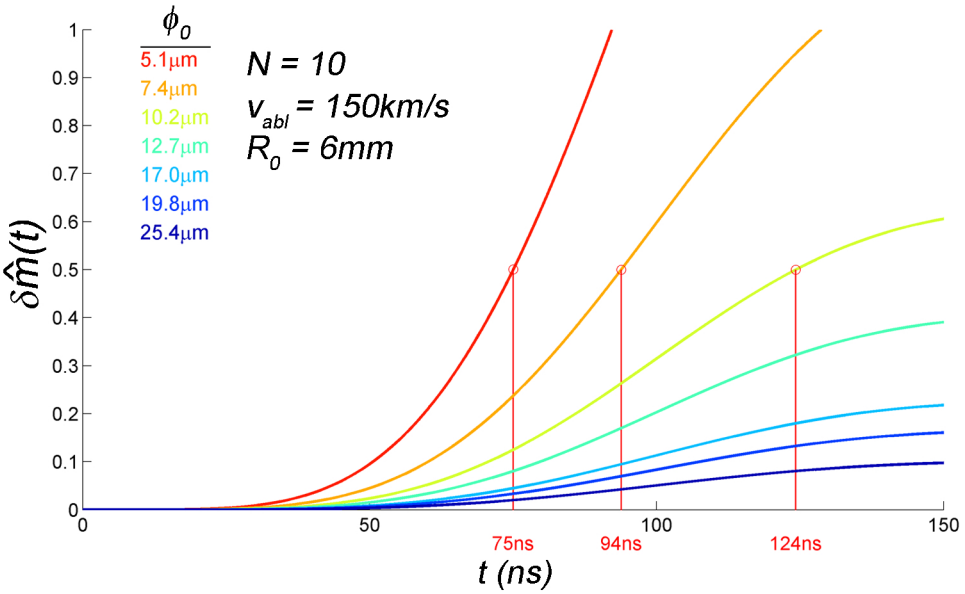


Figure 3.5: Fraction of initial mass ablated versus time as predicted for W wire arrays by Eqn. 3.6 with the parameters $v_{abl}$ = 150km/s, $N$ = 10, $R_0$ = 6mm, and a $\sin^2$ current pulse with $I_{peak}$ of 1.1MA and rise-time of 100ns. The times indicated in red are the times when 50% of the initial mass has been ablated for the various values of $\phi_0$.

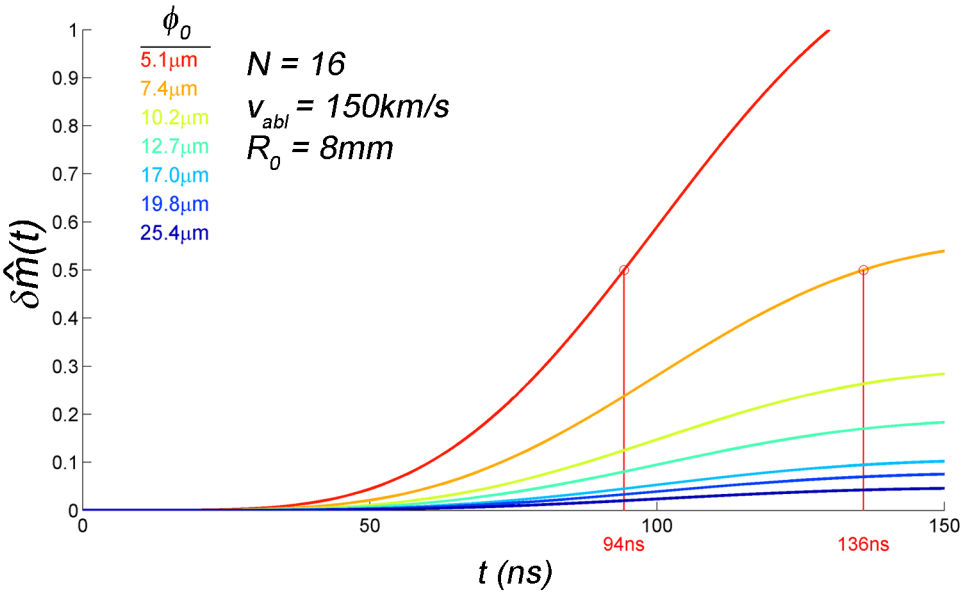


Figure 3.6: Fraction of initial mass ablated versus time as predicted for W wire arrays by Eqn. 3.6 with the parameters $v_{abl}$ = 150km/s, $N$ = 16, $R_0$ = 8mm, and a $\sin^2$ current pulse with $I_{peak}$ of 1.1MA and rise-time of 100ns. The times indicated in red are the times when 50% of the initial mass has been ablated for the various values of $\phi_0$.

On the COBRA pulsed power generator, $v_{abl}$ is usually taken to be approximately 150km/s for W wire arrays. Assuming this value, and approximating the current pulse shape as $I_{peak} \sin^2(\omega t)$, where $\omega = \pi/2\tau$ and $\tau$ is the time of peak current, the fraction of initial mass ablated versus time is plotted in Figs. 3.4, 3.5 and 3.6 for a range of $\phi_0$.

CHAPTER 4

# POINT-PROJECTION X-RAY RADIOGRAPHY

## 4.1 Overview

X-ray imaging, or radiography, allows us to study an object or system that is incompatible or inconvenient with visible light imaging techniques. Most commonly, x-rays are used to image the interior of an object that visible light cannot penetrate, like the bones inside your body and the welds on a submarine bulkhead.

The simplest means of x-ray radiography is point-projection. The primary advantage of this type of system is that no focusing element is required. This is important because focusing elements that are compatible with x-ray wavelengths are generally much more expensive, demonstrate lower spatial resolution, and are far less efficient than equivalent elements used for visible light imaging.

A point-projection radiography system has just two basic components: a point source of x-rays and some sort of detector. The object to be imaged is placed between the source and detector. A shadow of the object is cast onto the detector by the point x-ray source. Ideally, the spatial resolution of the system is roughly equivalent to the size of the source, thus, the smaller the source the better. The temporal resolution of the system is determined by the amount of time that the detector is allowed to collect light, i.e., the speed of a shutter or the duration of a flash bulb.

The comparison of x-ray point-projection to visible light shadowgraphy is an over simplification. In some respects x-ray imaging is simpler since the index of refraction of most materials is very nearly one for x-rays. However, when x-rays pass through matter to form a point-projection image, unique effects arise. The archetypal x-ray image is

that of bones within living tissue. This is an example of an absorption contrast image. Absorption contrast is essentially a 2-D spatial mapping of an object's transparency to x-rays and is the method used for the research presented here.

When an x-ray source is used that exhibits high spatial coherence, and/or spectral coherence, images can be formed that include phase contrast. The X-pinch, to be described in detail in chapter 5, provides such a source. Phase contrast imaging with an X-pinch is particularly useful when imaging the organic compounds in biological objects as shown in [45], but manifests itself as a side effect in this research. Complications arise when the object being imaged is a plasma. The level of ionization and the density gradients found in plasmas influence the local index of refraction within the plasma. Refraction can contribute to edge contrast enhancement and is difficult to predict and correct. Like phase contrast, this effect must be considered when analyzing high resolution details where these effects are likely to appear. For example, image boundaries can appear to be sharper than the diffraction limit.

## 4.2 X-ray Filters

Most detectors that are sensitive to x-rays are also at least somewhat sensitive to visible light. Since most experiments and environments are naturally flooded with visible light a filter that transmits x-rays but not visible light is placed between the object and detector. When x-ray sensitive film is used as the detector, as in our case, this filter also enables the film to be conveniently transported from the experiment to a dark-room for developing. The characteristics of an x-ray filter are determined by the material it is made from. The filter material determines the x-ray wavelengths that it will transmit with reasonable efficiency. The x-ray spectral range of interest in Z-pinch experiments

is typically 100ev-10keV. This dictates that our x-ray filters be made from thin plastic films (1-10$\mu$m) for energies below about 1keV and thin metal foils (4-25$\mu$m) for more energetic radiation. One might conclude that these thin films and foils act like simple high pass filters. While this is certainly the case for energies greater than about 50keV, the spectral response of most materials in the bandwidth of interest is more like a band pass filter. Hence, with the proper choice of filter material(s) one can choose a pass band for a particular soft x-ray source that has reasonable efficiency. As will be seen, this property is of utmost importance to high spatial resolution point-projection imaging using X-pinch x-ray sources.

## 4.3 Time Gating

Simple cameras use mechanical shutters that open and close in a fraction of a second to accomplish time-gating. This technique is very effective when dealing with the time scale of everyday life, down to perhaps 1 millisecond. However, wire-array Z-pinch dynamics happen on a time-scale that is over one million times faster. This ultra-short time scale precludes the use of mechanical shutters as time-gating elements. To circumvent this problem in a point-projection system the point source is simply switched on and off very quickly, which is a natural feature of the X-pinch. While this method is very simple and effective it also leads to the system's greatest weakness: a direct line-of-sight from object to detector exists for the entire duration of the experiment. Hence, any radiation produced by the object that is transmitted by the x-ray filter will be recorded by the detector, degrading the image produced by the time-gated point source. Since the duration of the point source is assumed to be much shorter than the duration of the experiment, low intensity radiation from the object, once integrated over the entire experiment, can easily dominate the image formed by the point source. Consequently, efforts must be

made to insure that the object to be imaged, in the present case, a radiating wire-array Z-pinch, does not emit a significant amount of radiation within the passband of the x-ray filter.

## 4.4 Detectors

X-ray detection systems range from the very exotic to the very simple. Exotic systems utilize solid-state electronics to provide fast turnaround from experiment to analysis, as well as high repeatability. The detection system used in this research, x-ray sensitive photographic film, is far simpler in principle. X-ray film provides a cost-effective, reliable means of detecting radiation with very high sensitivity, spatial resolution, dynamic range and minimal diagnostic complexity. However, film does have several drawbacks: calibration tends to be complicated, developing can be time consuming and inconsistent, and manufacturers are discontinuing film production. The advantages of film make it ideal for university research.

## 4.5 X-Pinch Backlighting in Practice

A detailed description of how X-pinch backlighting is carried out in practice is given in Appendix D. The Physics of Plasmas paper[46] in this appendix describes the results of a two-frame X-pinch backlighting system used on the COBRA pulsed power accelerator.

The experiments presented in Appendix D study the early stages of tungsten wire-array Z-pinch implosions using two-frame point projection x-ray backlighting on the 1 MA COBRA pulsed power generator. X-pinch backlighter images in this study had

subnanosecond temporal resolution and 4 to 10$\mu$m spatial resolution. Instead of imaging the entire wire-array, these experiments produced images of individual W exploding wires in 8-wire arrays. This two-frame system was used to show the evolution of wire-core and coronal plasma structures. The timing of the X-pinch x-ray bursts relative to the Z-pinch initiation time was adjusted over a 50ns time interval by varying the X-pinch mass per unit length.

The results of these experiments were primarily qualitative since no plasma density calibration scheme was fielded. Nevertheless, many interesting features of the wire-core expansion and ablation were seen with high spatial and temporal resolution for the first time. For instance, wire-cores seen in two images separated in view by 120° showed that the expansion is remarkably azimuthally symmetric. Furthermore, a strong correlation was observed between the structure on the dense exploding wire-cores and the structure of the $10^{18}/\text{cm}^3$ ablation (or injected) plasma being drawn from radial prominences. The wire-core expansion rate was found to be approximately constant with time over the interval 50 to 100ns after the start of the current pulse. Finally, micron-scale axial gaps, seen as early as 70ns into the current pulse and persisting from that time, were observed along the wire-core.

The results presented in the following chapters were obtained using techniques that are largely an extension of those presented in Appendix D.

CHAPTER 5

# THE X-PINCH X-RAY SOURCE

## 5.1 Overview

The X-pinch is a variety of wire-array Z-pinch. An X-pinch consists of two or more fine metal wires that cross onto each other at a single point, thus forming an 'X' configuration. An x-ray image and photograph of an X-pinch are shown in Fig. 5.1. These crossed wires are typically driven by a current pulse with magnitude exceeding 200kA and with a rise-time less than 100ns. At the point where the wires cross a hot dense plasma is formed. This plasma is compressed to a diameter of tens of microns by the intense magnetic field arising from the small current radius at the crossing point. This minute plasma column undergoes intense heating and unstable self-field-driven compression, which leads to a powerful burst of x-ray emission.

In typical single X-pinch experiments, there are several hot spots producing point x-ray sources. The radiation from these hot spots can be divided into two categories: characteristic line radiation of the wire material, and continuum. Sources with strong continuum in the energy range of interest here, >2keV, are usually small, about 1 to 3$\mu$m in diameter for Mo, and brief, lasting less than 150ps. These parameters enable unparalleled spatial and temporal resolution in a point-projection x-ray radiography system. Figure 5.1a is an example of such a radiograph. Unfortunately, the x-ray sources that emit strong line radiation (of which there are usually several) tend to accompany the continuum source and are much larger and longer lasting. The spatial and temporal extents of line radiation sources are dependent upon material but can be as much as 1 to 2mm and 2 to 3ns, respectively. While these sources can be utilized for monochromatic imaging, as discussed in Appendix B, they are clearly detrimental to point-projection

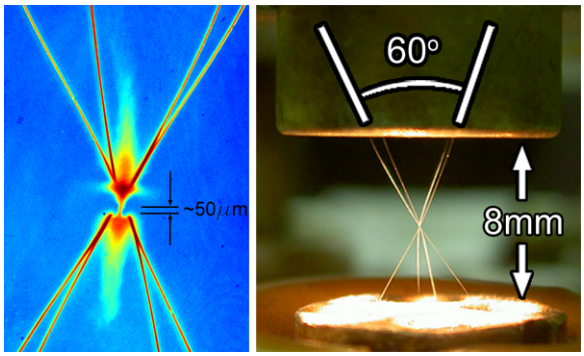


Figure 5.1: Point-projection X-ray image of a 4-wire molybdenum X-pinch obtained with a nearby X-pinch, is shown together with a typical 4-wire X-pinch experimental arrangement.

imaging. The problem of radiation intensity from the relatively large line sources, which would be detrimental to spatial resolution, is overcome by intelligent x-ray filtering.

## 5.2 Spectral Filtering

Most materials are strongly absorbing, or opaque, in the ultraviolet (UV) to extreme ultraviolet portions of the spectrum (EUV and XUV). This is even the case for materials like mylar or polycarbonate that are transparent to visible light. For most materials this absorption persists until photon energies exceed about 100eV, i.e., soft x-rays. Above this threshold, opacity is strongly dependent upon material. As examples, several material opacity curves are shown in Fig. 5.2. Note that the metals in Fig. 5.2, with the exception of beryllium (Be), all have a prominent transmission "window" that precedes the threshold at which the materials act like high pass filters. These transmission windows are extremely useful for X-pinch point-projection imaging. By choosing the proper combination of x-ray source and filter one can potentially filter out low-resolution line radiation sources and transmit radiation from the high-resolution continuum source. Furthermore, one can cut off the more energetic end of the continuum spectrum, which

generally improves image contrast (absorption contrast).

Clearly, to attain the highest possible resolution from X-pinch point-projection imaging one must find an appropriate combination of source spectrum and filter transmission. When used with absorption contrast imaging this means that the filter transmission window must coincide with an energy range over which the opacity of the object to be imaged has an appreciable range. Hence, one generally starts the source/filter selection process by considering the transmission spectrum of the object to be imaged. For example, consider an object consisting of copper (Cu) structures ranging from 0.5 to 50$\mu$m thick, for which the x-ray transmission curves are shown in Fig. 5.3. The difference in transmission between 0.5$\mu$m and 50$\mu$m Cu is maximal near 6keV, which suggests that optimal absorption contrast can be achieved there. Note that near 6keV the thin copper is still not completely transparent and the thick copper is not completely opaque, which is necessary for the full thickness range to be detectable. Of course determining the energy level that gives optimum contrast is far more complicated since saturation effects and the detector's spectral response come into play. In this simple example we take the detector to have a uniform response to all x-ray energies and have ignored saturation. The selection of 6keV suggests the use of an iron (Fe) x-ray filter since the Fe transmission window is about 4 to 7keV, as shown in Fig. 5.2. Note that titanium (Ti) would be inappropriate because energies above 5keV would be cut off, making all copper structures 30$\mu$m and thicker appear as completely opaque. The use of a copper filter, spanning roughly 5 to 9keV, would result in an image with between 0.5 to 3$\mu$m copper structures and would also be avoided. What remains is to find an X-pinch material that radiates intense 4 to 7keV continuum without any line radiation sources in this region. Finding such a material would result in an ideal source/filter combination for imaging the object of interest.

Unfortunately, for several reasons not many ideal source/filter combinations exist. Foremost, the number of materials that can be made into fine wire and/or thin metal foil is very limited. Secondly, very few materials that can be made into an X-pinch emit a spectrum with a strong continuum that is adequately separated from its line radiation for filtration to be effective. Additionally, some materials tend to produce multiple continuum sources, thus degrading spatial and temporal resolution. The most common source/filter combination used for X-pinch point-projection imaging is Mo/Ti and is the combination of choice for this research. The line sources of Mo (neon-like Mo) are found to be most intense from 2.5 to 2.75keV whereas the Ti window is 3 to 5keV, where Mo X-pinches emit strong continuum, making an ideal pair.

## 5.3 Resolution

### 5.3.1 Spatial Resolution

As previously mentioned the spatial resolution of a point-projection imaging system is usually proportional to the size of the source. However, the Mo X-pinch continuum source is so small that this system's spatial resolution is diffraction limited. An imaging systems diffraction limit, $\delta x$, is given by:

$$\delta x = \sqrt{\lambda \alpha} \tag{5.1}$$

Where $\lambda$ is the wavelength of the incident radiation and $\alpha$ is the distance from source to object. If $\lambda$ is in angstroms (Å) and $\alpha$ in centimeters then $\delta x$ is in microns. In the imaging system for this research $\alpha = 6.67$cm and $\lambda_{max} \approx 4.1$Å, which gives a diffraction

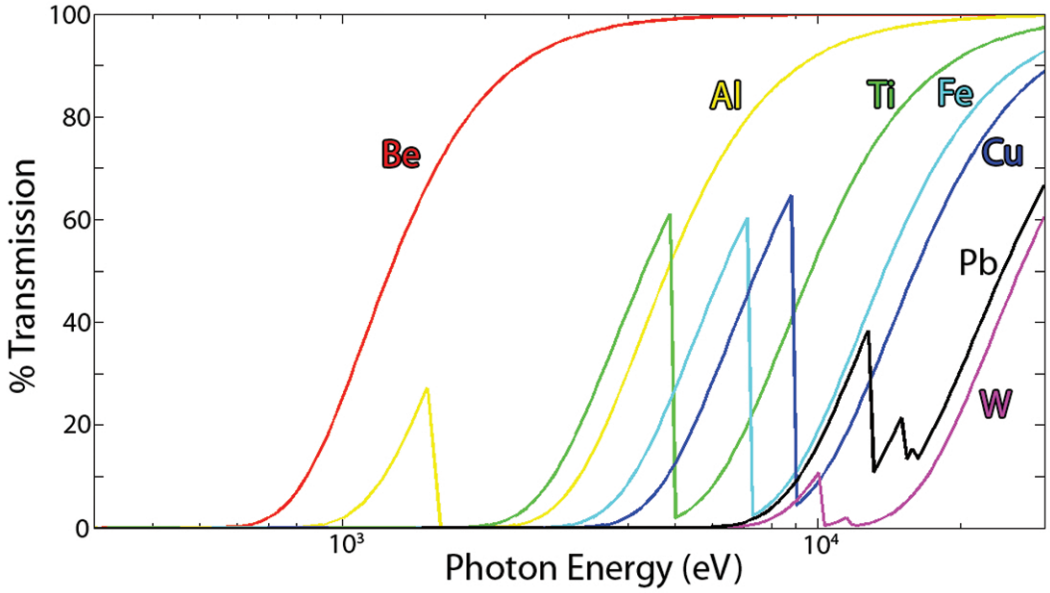


Figure 5.2: X-ray transmission curves for various metals as a function of photon energy. Each curve is for a solid density foil with thickness of 12.5$\mu$m.

limit of 5.2$\mu$m. Note that the diffraction limit is two to three times larger than the estimated source size of the X-pinch.

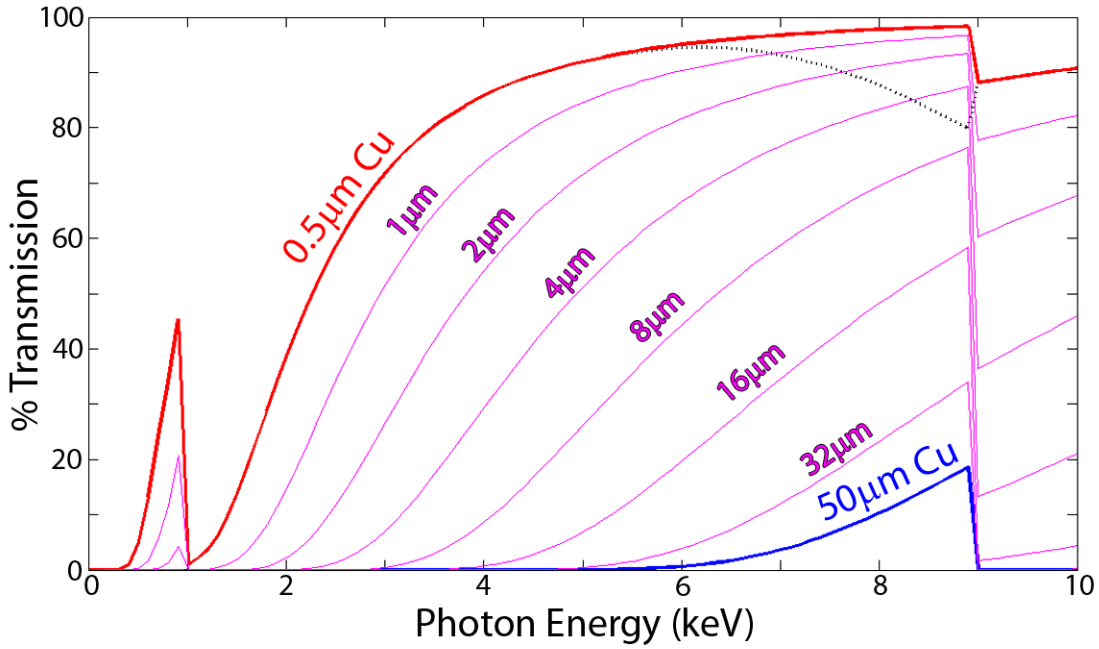


Figure 5.3: X-ray transmission curves for 0.5$\mu$m through 50$\mu$m copper. The dotted black curve is the difference in transmission between 0.5$\mu$m and 50$\mu$m

### 5.3.2 Temporal Resolution

The time scale of these experiments demands diagnostics with extraordinarily good temporal resolution. The duration of most experiments is only 200ns (1ns = $10^{-9}$s). Hence, resolution on the order of nanoseconds or better is essential. Fortunately, the continuum sources found in X-pinches have been observed to last no longer than 150ps (1ps = $10^{-12}$s). However, much like the situation with spatial resolution, the X-pinch parameters are not the limiting factor in temporal resolution. Solid-state detectors are used to determine when the X-pinch's x-ray burst occurs. These devices have a turn-on time of 250ps, making them and the accompanying digitizing oscilloscopes the limit of temporal resolution. For a more thorough description of the temporal parameters of the X-pinch see Ref. [47].

CHAPTER 6

# DENSITY CALIBRATION OF POINT-PROJECTION IMAGES

## 6.1 Overview

While tremendous amounts of qualitative information can be extracted from images alone, quantitative analysis is essential to developing a full understanding of the dynamics of wire-array Z-pinches. To this end, thin films of known thicknesses are deposited onto the Ti x-ray filters that enable the images to be calibrated. From the calibrated images measurements of mass ablation and density distributions can be made as functions of time and space. This technique is also presented in [48].

## 6.2 Film Deposition

An array of thin W films was deposited onto each edge of the Ti x-ray filters used in these experiments. This was done using a magnetron sputtering system. Stainless steel contact masks were used to control the deposition pattern. The thickness of the films was controlled by varying the time of the deposition process. The thickness of the films was measured using a profilometer which is accurate to about 30Å. The thickness of the W films, or steps, ranged from 0.015 to 1.1$\mu$m. Each step array contains thirteen steps of seven different thicknesses. They are symmetric about the middle step, which is the thickest, making a pyramid profile. Step thickness is successively doubled (approximately) from thinnest to thickest, i.e. target thicknesses were 0.015, 0.03, 0.06, 0.12, 0.25, 0.5 and 1.0$\mu$m. The step arrays used in these experiments were manufactured on campus in the Cornell Nanofabrication Facility (CNF) by Kate S. Bell.

## 6.3 Calibration Function

The process of converting film exposure level to areal density is essential to collecting quantitative data from these experiments. The simplest way to generate a calibration function is to fit a curve to the points generated by step thickness versus exposure level on a given film. Complications begin to arise when one considers that there are four sets of calibration steps on each film. The exposure levels behind each set of steps on the same film can vary significantly, especially for the thinnest steps. Hence, the calibrations derived from the different step arrays vary significantly in the low density range of $10^{16}$ to $10^{17}$ (/cm$^2$) (1$\mu$m W at solid density is about $6.3\times10^{18}$/cm$^2$). Obviously, it is desirable to use the calibration function that is most appropriate to the area of the image that is being analyzed. When analyzing the left half of the film the calibration is derived from the exposure levels behind the left step arrays. In order to account for variation in background exposure level along the height of the film, the calibration points are linearly weighted towards the top or bottom step array depending on the location of the film area to be analyzed. An example of this weighting is shown in Fig. 6.1.

Once the weighted exposure levels have been determined a calibration curve is generated. Specifically, a linear fit is made to the first four exposure levels (thinnest steps) and the last three points are fit by a quadratic function that is spliced to the linear fit of step four in first and second order. The linear fit to the first four steps, $f_1(x)$, is generated by a fitting tool such as matlab. The 2nd order splice of the quadratic function, $f_2(x)$, to $f_1$ at step four determines all but one of the coefficients of $f_2$. The last coefficient of $f_2$ is determined by minimizing the deviation from the experimental points given by steps five through seven, as follows:

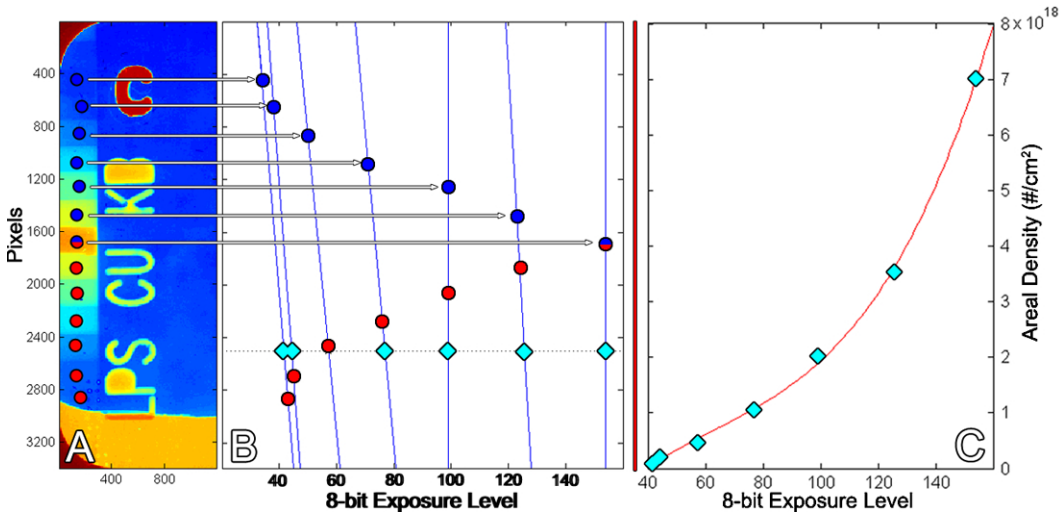


Figure 6.1: Step array weighting and calibration. A - false-color scan of the left step array in film C from experiment 795. B - plot of the vertical position of each step (in pixels) versus the 8-bit exposure level behind each step. The cyan diamonds indicate the weighted exposure values that would be used to analyze portions of film along the vertical position indicated by the dotted black line. C - sample calibration curve for the cyan diamonds from B.

$$
\begin{aligned}
f_1(x) &= mx + b && (6.1)\\
f_2(x) &= a_2(x - x_4)^2 + a_1(x - x_4) + a_0 \\
f_2(x_4) &= f_1(x_4) = a_0 = mx_4 + b \\
f_2'(x_4) &= f_1'(x_4) = a_1 = m \\
f_2 &= a_2(x - x_4)^2 + m(x - x_4) + mx_4 + b \\
f_2 &= a_2(x - x_4)^2 + mx + b && (6.2)
\end{aligned}
$$

Minimizing the deviation between $f_2$ and the experimental data from steps five through seven gives the coefficient $a_2$:

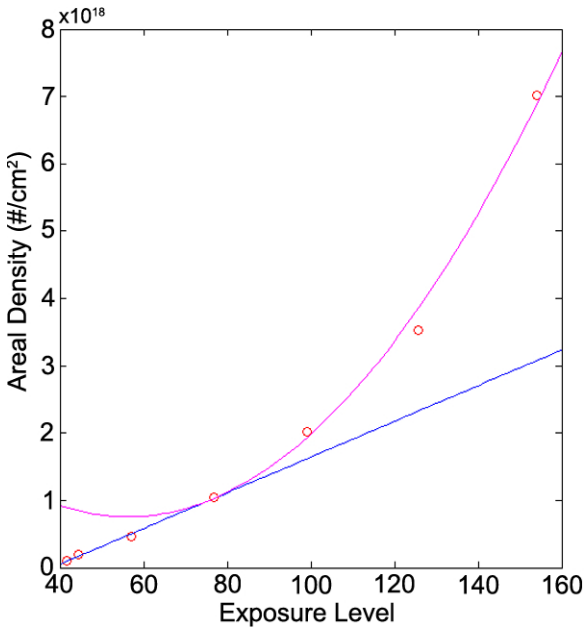


Figure 6.2: Curve fitting process. The data shown here are the same as those in Fig. 6.1. The blue line is a linear fit, $f_1$, to steps one through four. The magenta line is a quadratic function, $f_2$, spliced to $f_1$ at step four in second order. The quadratic coefficient is determined by a least squares fit to steps five through seven, as described by Eqn. 6.3.

$$a_2 = \frac{\sum_{n=5}^{7} (x_n - x_4)^2 (y_n - m x_n - b)}{\sum_{n=5}^{7} (x_n - x_4)^4} \tag{6.3}$$

A sample of this piecewise calibration is shown in Fig. 6.2.

At this point in the calibration process a reasonable fit has been generated that is specific to either the left or right side of the film and has first order compensation for variations along the vertical direction of the film. What remains is to account for background exposure variations from the extreme left and right edges of the film, where the step arrays are located, to the area of the film that is to be analyzed. These variations can be caused by $1/R^2$ effects, non-uniform x-ray illumination, and the film develop-

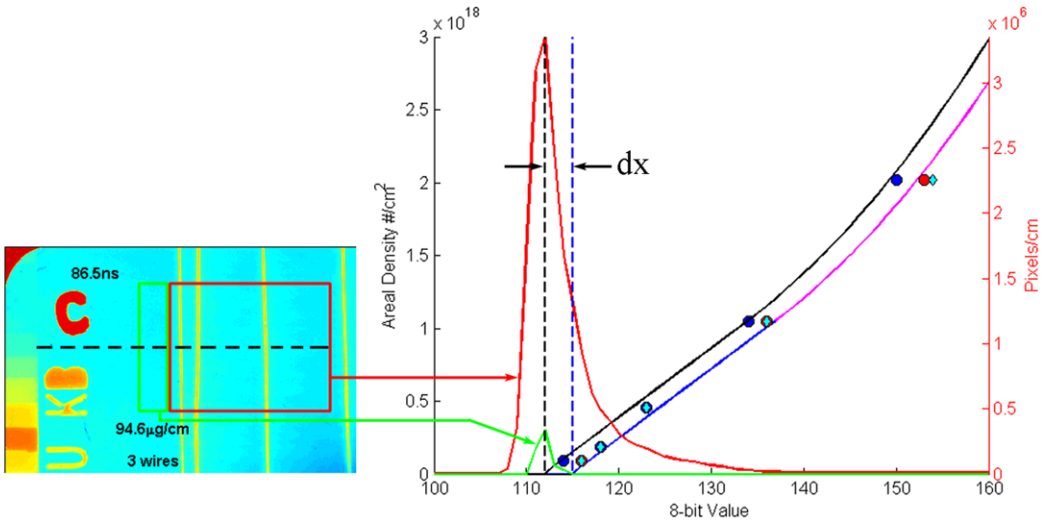


Figure 6.3: Correction of calibration function due to center-edge exposure variation. The blue/magenta curve is the original piece-wise fit to step exposure levels with vertical position weighting. The red and green curves are histograms of the respective areas in the inset to the left. The dashed, vertical, black line is the average exposure level in the area within the green rectangle and represents the "zero-mass" threshold. The dashed blue line indicates the zero-mass level in the original piece-wise calibration function. The solid black curve is the piece-wise function shifted by an amount, $dx$, such that the two zero-mass levels agree.

ment process. The least significant of these effects, $1/R^2$, is the only one that can be predicted and accurately accounted for. Unfortunately, the unpredictable effects tend to dominate, making compensation for $1/R^2$ somewhat pointless.

After examining various methods for dealing with edge-center variations a simple approach was adopted. The calibration curve generated by the preceding procedure is shifted (along the exposure level axis) so that the exposure-intercept (areal density = 0) coincides with the local background exposure of the area to be analyzed, an example is shown in Fig. 6.3. The local background exposure level is generally found by averaging a portion of the film that is immediately outside of the array edge, at the same height as the area to be analyzed. The legitimacy of this shift is certainly questionable. Further-

more, it is difficult, if not impossible, to quantify the amount of error introduced by such an operation. Our only justification is that application of the calibration as discussed, including this zero-point shift, accurately accounts for the initial mass in the wire-arrays at times when the average mass density is within the sensitivity range of the diagnostic.

CHAPTER 7

# CONVERTING AREAL DENSITY TO VOLUME DENSITY

## 7.1 Overview

The accurate measurement of the areal densities in these experiments has considerable value. However, accurate mass and volume density estimates are far more useful. In order to transform an areal density into a volume density assumptions must be made. Generally, one assumes a spatial variation for the volume density in order to invert an areal density. In the quantitative analysis given in chapter 11, three types of inversions are used. Two of these inversions are based on line-out processing and the other uses surface integration.

### 7.1.1 Line-out Processing

A "line-out" is generated by averaging the exposure levels in an image along one of its dimensions. For example, taking a horizontal line-out of an image that is $m \times n$ pixels in the vertical and horizontal directions, respectively, results in a list of exposure level versus horizontal position with $n$ values.

The densities of plasmas in these experiments have variations in the axial and radial directions. In order to preserve the dependence on each direction, line-outs are taken in the radial direction at many locations in the axial direction separated by about $20\mu m$. Each line-out averages about $10\mu m$ in the axial direction. Thus, maximum spatial resolution is maintained in the radial direction, while spatial resolution in the axial direction is decreased by about a factor of five (each pixel corresponds to about $2\mu$m) in order to

ease computation. This is a logical choice since axial density variations have a much longer length scale than the radial density variations.

Once an areal density line-out has been generated it can be transformed into a volume density line-out by assuming a spatial profile for the plasma.

### 7.1.2 Cylindrical Systems

In a system that has cylindrical symmetry, specifically, no theta dependence, the well known Abel transform[49] can be used to invert areal density line-outs or chordal integrals:

$$f(r) = -\frac{1}{\pi}\int_r^a \frac{dF}{dy}\frac{dy}{\sqrt{y^2 - r^2}} \quad , \tag{7.1}$$

where $F(y)$ is the chordal integral of $f(r)$, and $f(r \geq a) = 0$. Specifically, the chordal integral, $F(y)$ is:

$$F(y) = \int_{-\sqrt{a^2-y^2}}^{+\sqrt{a^2-y^2}} f(r)dx \quad . \tag{7.2}$$

The relationship of the variables in Eqns. 7.1 and 7.2 is shown in Fig. 7.1.

In the case of an azimuthally uniform, radially varying density distribution around each wire, as will be assumed for the coronal plasma in chapter 11, an areal density line-out taken in the radial direction gives the chordal integral, $F(y)$. Hence, areal density line-outs of coronal plasma will be analyzed using eqn. 7.1 to generate coronal plasma volume density distributions. A detailed, step-by-step example of this conversion process is given in Appendix A.

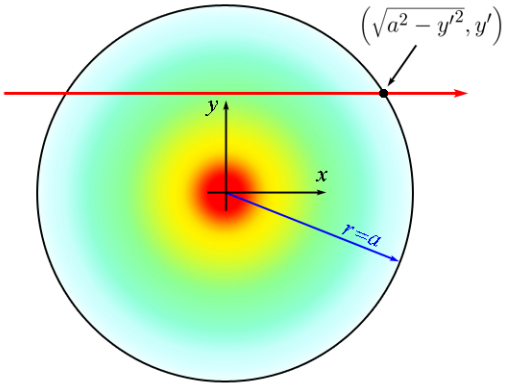


Figure 7.1: Coordinate system of Abel transform (overhead view). The shaded interior represents an azimuthally uniform, radially varying distribution, $f(r)$, that is zero for all $r$ greater than $a$. The red line indicates a chordal integration path to generate $f(r)$ at $y = y'$ from $F(y)$.

### 7.1.3 Uniform Distributions

The simplest method of transforming areal density line-outs to volume densities is by assuming a uniform, or constant, density along the chordal direction (image projection direction). In chapter 11 injection stream density distribution will be assumed to vary in this way. Specifically, it will be assumed that the injection stream density does not vary across its width, $w_s$ in Fig. 7.2. Hence, the injection stream's volume density is determined by simply dividing its areal density by $w_s$.

Note, both methods of line-out processing that have been described require chordal integral functions, $F(y)$, along chords from source to detector that intersect only the density distribution of interest. Specifically, these inversions can be applied only to the portions of an image where the density distributions from different wires do not overlap in side-on view. Consequently, only the plasma density distributions at the extreme right and left edges of an array, when viewed side-on, can be inverted by the previously described methods.

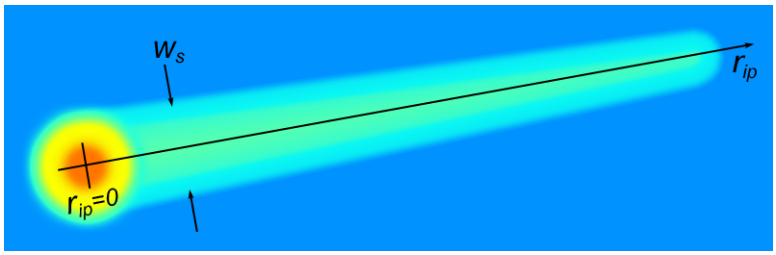


Figure 7.2: Hypothetical injection stream density profile (overhead view). The stream coordinate system has its origin at the center of the dense wire core and the $x-y$ plane is rotated so that the $x$-axis intersects the array axis. The width of the stream is $w_s$. The red arrow indicates the chordal integration direction that will be used to determine the stream's areal and volume density in chapter 11.

## 7.2 Surface Integration

Instead of adding dimensionality by inverting areal density distributions, as described in the previous section, one can perform a surface integration of areal density to determine the amount of mass in a specific area of an image. This process is advantageous in that it makes no assumptions about the spatial distribution of the mass and, as a result, is very accurate. Furthermore, overlapping distributions when viewed side-on are no longer an issue. This type of analysis will be used to determine global quantities such as the amount of mass ablated and the amount of mass in axial plasma structures.

In the case of axial plasma structures, one can estimate the volume of the axial plasma column. The average density of the axial plasma column can then be determined by dividing the amount of axial mass, found from surface integration, by the inferred volume of the column.

CHAPTER 8

# COBRA STAR

## 8.1 Overview

The COBRA Sequential Trans-Axial Radiography (STAR) system is a high resolution, large field-of-view, five-frame, point-projection radiography system. This diagnostic has produced unprecedented data for the ablation and implosion phases of 1MA-scale wire-array Z-pinches.

The STAR system uses return current circuit X-pinches to produce point x-ray sources for radiography of wire-arrays. This method of x-ray imaging wire-arrays has been used for many years[43, 50, 46], and has been very successful due to its low cost and high temporal and spatial resolution. All of the systems preceding the STAR system replaced one or at most two of the generator's return current paths with X-pinches, yielding at most two images per experiment. All previous systems also used a comparatively small field-of-view that covered 10-30% of the array diameter. The STAR system places X-pinches in all five of the generator's return current paths and captures the entire wire-array in the field-of-view.

## 8.2 Experimental Setup

The STAR setup uses most of the standard experimental hardware of the COBRA pulsed power generator, shown in Fig. 8.1. The wire-array cathode electrode is 37.75mm in diameter with a six point, 3-48 bolt pattern of 15mm radius. The array cathode (Fig. 8.1G) is typically 3.18mm (0.125") thick and sits on the cylindrical cathode wedge (Fig.

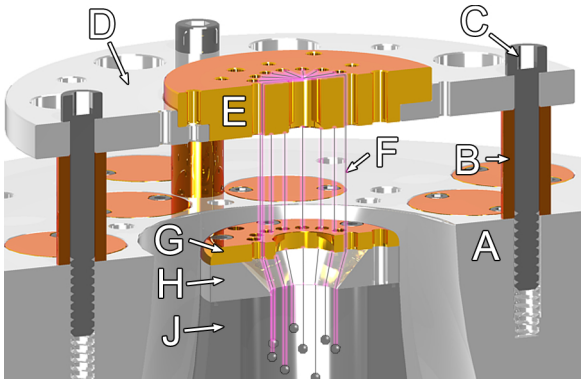


Figure 8.1: Standard COBRA load hardware. A - anode block (machine ground), B - return current post, C - 10-32 socket head cap screw, D - anode plate, E - anode disc, F - wire-array, G - cathode disc, H - cathode wedge, J - machine cathode.

8.1H) which is 6.85mm (0.27") thick, so that the upper surface of the cathode disc (Fig. 8.1G) is coplanar with the upper surface of the anode block (Fig. 8.1A). The array anode, the "anode disc" (Fig. 8.1E), fits into the "anode plate" (Fig. 8.1D) so that array diameter and wire number can easily be set by replacing two simple parts (the anode and cathode discs). Copper return current posts (Fig. 8.1B) support the anode plate and determine the array height. There are several eight point, 10-32 bolt circles where return current posts can be positioned. The inner return current bolt circle has a radius of 34.9mm (1.375") and the outer bolt circle has a radius of 44.5mm (1.75"). The bore through the anode block is 60.3mm (2.375"), so that the radial anode-cathode gap is about 11mm.

In the normal load configuration there are eight inner and six outer locations where return current X-pinches can be placed. The STAR system, shown in Fig. 8.2, uses an adapter plate that has five outer X-pinch locations. The radius of this five point pattern is 66.7mm (2.625"). A five point pattern was chosen because it enables each return current X-pinch to have an unobstructed view of the entire experiment. The use of the adapter plate requires the addition of a 12.7mm (0.5") spacer to increase the height of

the cathode. The return current X-pinch hardware is configured to make use of four-wire X-pinches that are 8mm tall, with height centered in the 20mm gap between the pental anode plate and anode block (see Figs. 8.2C and 8.1A, respectively). The X-pinch wires cross with an included angle of 60°. Since all of the copper return current posts are replaced with X-pinches, some other means of supporting the anode plate had to be fashioned. The STAR anode plate is supported by five aluminum beams that stand off from the machine ground near the chamber wall on plastic legs, as shown in Fig. 8.3. This support system provides both resistive and inductive isolation for the anode plate.

In order for the STAR system to have a field of view that encompasses the entire experiment, the wire-array is shortened to 8mm in height. The center of the shortened array is centered about 12.5mm above the standard cathode height. Conical electrodes are used so that they cast minimal shadows over the point-projection images. For ease of manufacturing, the electrodes both have bores through their centers that are nearly the diameter of the wire-array. These bores and/or the taper of the conical electrodes may have effects on wire ablation near the electrodes.

The current in each of the five return current X-pinches in the STAR system is monitored using a separate Rogowski coil that is embedded in the anode adapter plate. These coils produce signals that suggest that the current is divided very evenly between the five return paths for at least the first 100ns of each experiment, as shown in Fig. 8.4. After roughly 100ns, the X-pinch coils tend to flat-line. It is believed that this is due to current being shunted to other paths such as the lead collimation shields that are close to each X-pinch (see Fig. 8.3J). Coil flat-lining could also be due to the field penetration gap (see Fig. 8.2F) being shorted out.

Since the support system for the anode of the STAR system is located far from the wire-array, near the vacuum chamber wall, care must be taken to insure that the

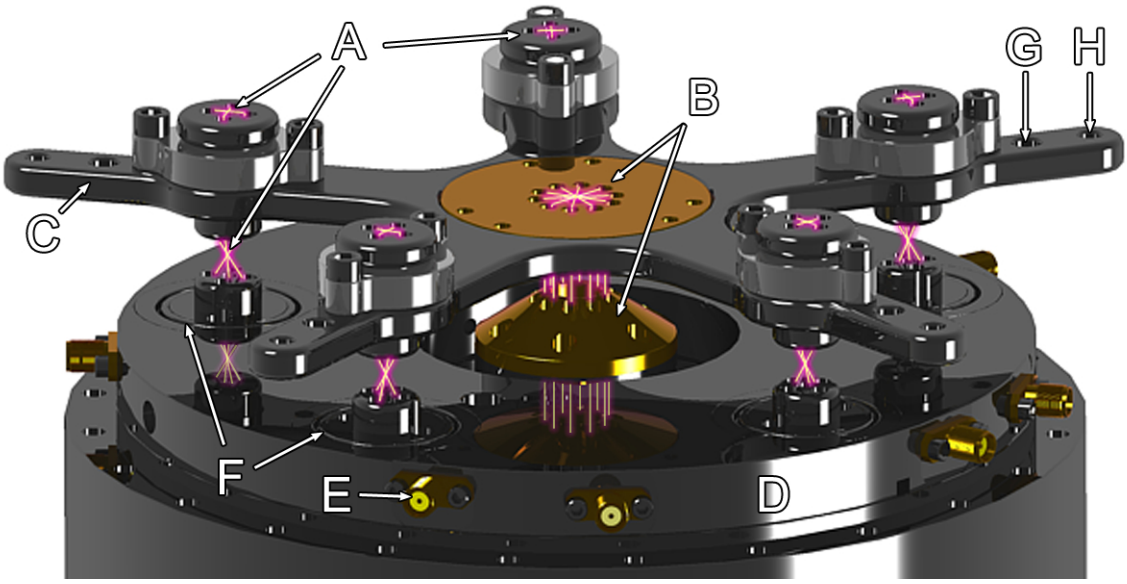


Figure 8.2: COBRA - STAR load hardware. A - return current X-pinch wires, B - wire-array Z-pinch electrodes, C - pental anode plate, D - six-to-five adapter plate, E - X-pinch Rogowski coil output, F - X-pinch Rogowski coil gap, G - alignment pin location, H - support beam mount hole.

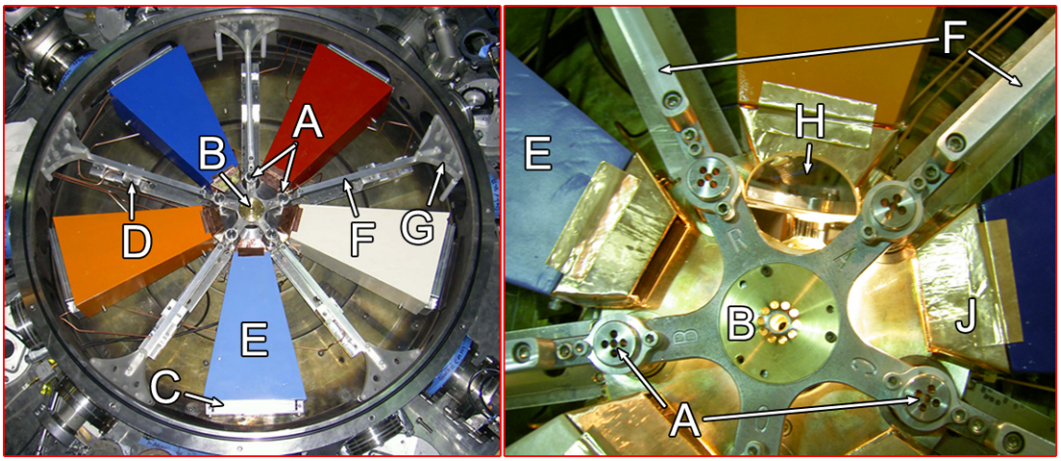


Figure 8.3: COBRA - STAR load hardware. A - return current X-pinch backlighters (five total), B - wire-array Z-pinch, C - film cassette (one of five), D - collimated Si diode (one of five), E - lead image collimation (4mm thick), F - anode support beam (five total), G - one of five plastic anode isolation standoffs (Rexolite and Delrin), H - array inspection mirror, J - lead x-ray "muzzle" (4mm lead covered with copper tape on each camera shield).

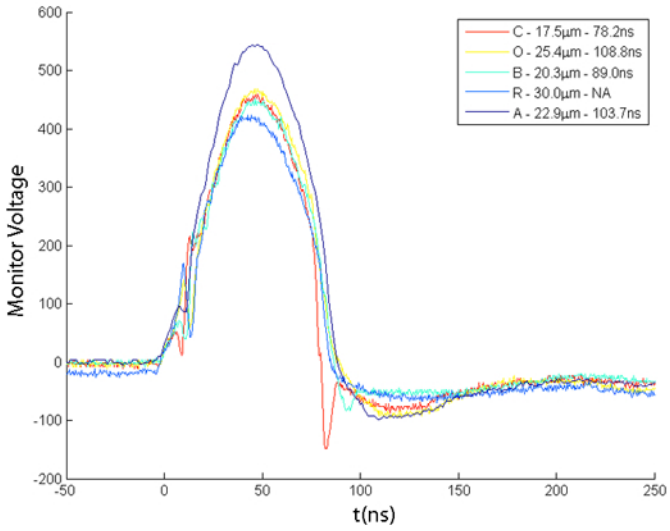


Figure 8.4: Time derivative of current signals from individual X-pinch Rogowski coils from COBRA experiment 795 (uncalibrated, nominally identical coils). The legend indicates the diameter of Mo wire used to make each 4-wire X-pinch and the corresponding time of x-ray bursts.

array anode and cathode remain coaxial. This can be challenging since the experimental assembly is so tightly packed around the wire-array that inspection is difficult. For rough alignment, locating pins (located at 8.2G) are used to center the anode plate (8.2C) over the adapter plate (8.2D). These pins must be removed prior to firing since they are in parallel, electrically, with the return current X-pinches and would prevent them from working. For final alignment a mirror is used to inspect the wire-array. If the array is found to be tilted in one direction or another then the anode plate is adjusted as needed to make the necessary correction.

The timing of the X-pinch backlighters is controlled by varying their mass per unit length (the diameter of Mo wire used). X-pinch timing is fairly linear with $\mu$g/cm, as shown in Fig. 8.5. The actual timing of the X-pinch x-ray bursts shown in 8.5 were measured with sub-nanosecond precision by silicon photoconducting detectors that are sensitive to soft x-rays. The radiation reaching these solid state detectors is filtered

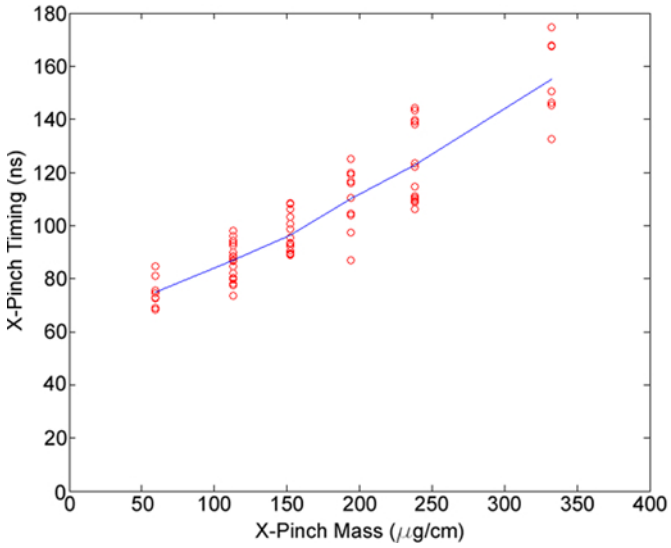


Figure 8.5: Scaling of Mo, X-pinch x-ray burst timing with X-pinch mass per unit length ($\mu$g/cm).

by a 12.5$\mu$m thick Ti foil (the same as the radiation incident on imaging films). Each detector is highly collimated so as to see only one X-pinch and any radiation emitted by the wire-array that falls in the Ti filter's pass-band.

The imaging cassettes containing photographic films, Ti-filters, and W step arrays (or " step-wedges") are located near the vacuum chamber wall for maximum magnification and physical protection from debris and other sources of damage. The precise location varies depending on the desired field of view. For these experiments the film plane was 380mm (15.0") from the wire-array axis, yielding a magnification of about 6.7 (slightly different for each wire, depending on its exact location).

The film used for these experiments was Kodak Industrex DR-50. By happenstance, the combination of this film with 3 to 5keV Mo continuum, and the opacity of the tungsten plasmas in these experiments, conspired to give very high image contrast. This serendipitous combination enabled the observation of many qualitative features of wire-array Z-pinches that had not been seen before these experiments.

CHAPTER 9

# IMAGE FEATURE DEFINITIONS

## 9.1 Overview

The results presented in the following chapters are derived from side-on, point-projection images of wire-array Z-pinches using the STAR system as described in chapter 8. Various features of these images are frequently cited in the following analysis. The most common of these features will be defined in this section.

## 9.2 Orientation and Dimensions

The images produced by these experiments were captured on Kodak Industrex DR-50 x-ray film. The film cassettes used in this radiography system (STAR system) accept films that are 5.5" by 2.5". The edges of the film cassettes generate a border around each film so that the resulting images are approximately $5\frac{1}{8}" \times 2\frac{1}{8}"$. In the following chapters the "vertical" (or "axial") and "horizontal" (or "radial") direction refer to the narrow and long dimensions of the films, respectively. Note that the horizontal and radial directions are truly synonymous only for the outer-most wires ("edge-wires") in each image.

In each image there is an identification tag that indicates orientation. This tag, "LPS CU KB" (Laboratory of Plasma Studies, Cornell University, manufactured by Kate Bell), indicates up-down and front-back. The orientation of the id tag relative to the experiment is shown in Figure 9.1. These marks are generated by a tungsten pattern that is deposited on the titanium x-ray filters (see chapters 5 and 8).

In each image (oriented as shown in Fig. 9.1) the electrodes at the top and bottom

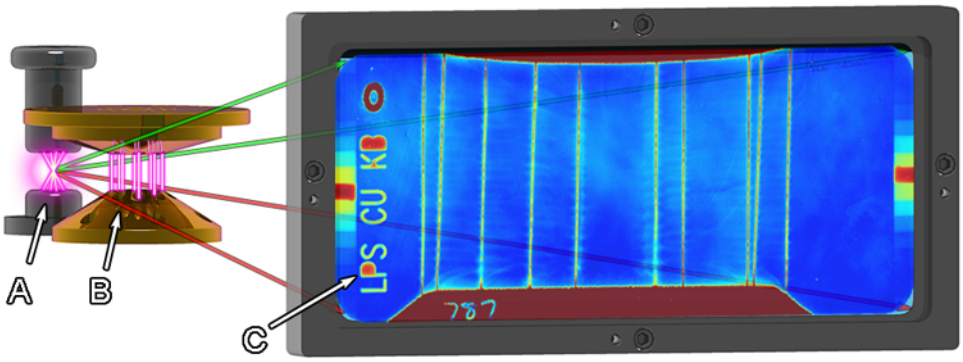


Figure 9.1: Orientation of films relative to the wire-array. A - backlighting X-pinch, B - wire-array Z-pinch, C - identification tag.

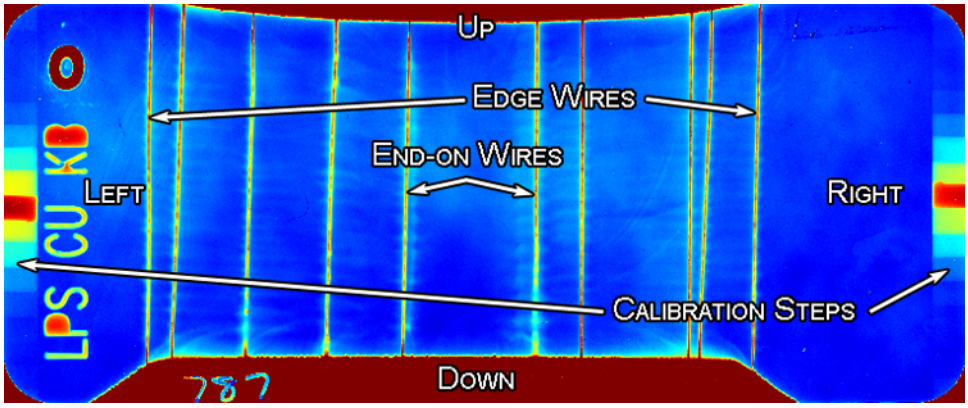


Figure 9.2: Locations of commonly referred to image features.

of the image are the anode and cathode, respectively, as shown in Fig. 9.3. The $r-z$ (horizontal-vertical) coordinate system to be used in the following chapters is also shown in Fig. 9.3.

The wires that appear at the extreme right and left of each image are referred to as "edge-wires", as shown in Fig. 9.2. The two wires closest to the center of each image are referred to as "end-on" wires, since the view of the edge wires is considered to be "side-on".

The wide, opaque structure that appears in images from all experiments with an

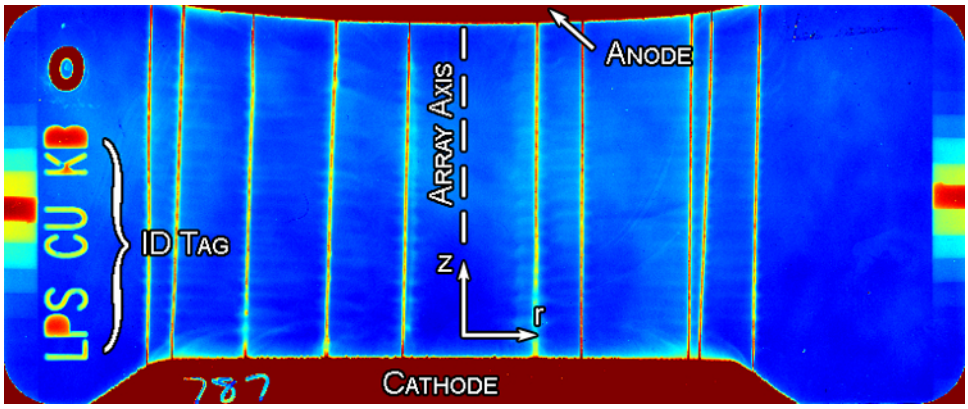


Figure 9.3: Image orientation, coordinate system and electrode locations.

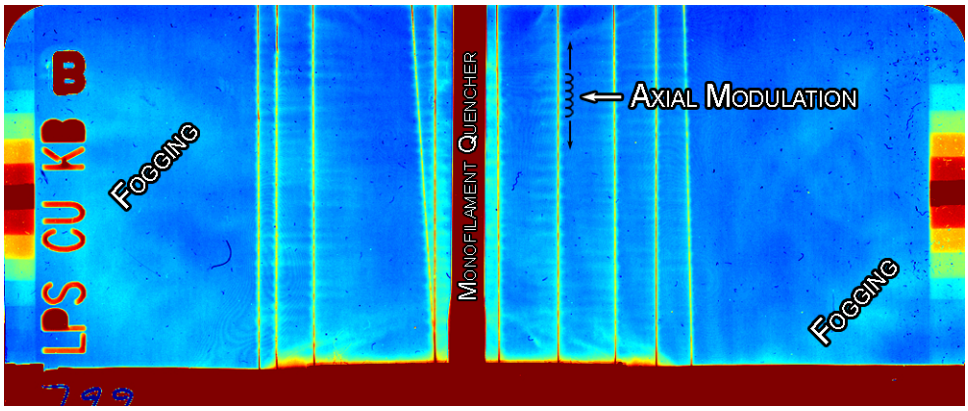


Figure 9.4: Sample image with monofilament quencher and prominent axial modulation of injected plasma streams. This image also contains visible levels of fogging that were introduced during film development.

array radius of 4mm and certain 6mm arrays is the monofilament "quencer." A sample image with this included is shown in Fig. 9.4. The quencher prevents the array from radiating in the 3 to 5keV range at stagnation, which would ruin the point-projection (open-shutter) images.

The ablation of plasma from the wires in a cylindrical wire array is modulated in the axial ($z$) direction. This modulation is frequently noted in subsequent chapters. The image in Fig. 9.4 includes this feature.

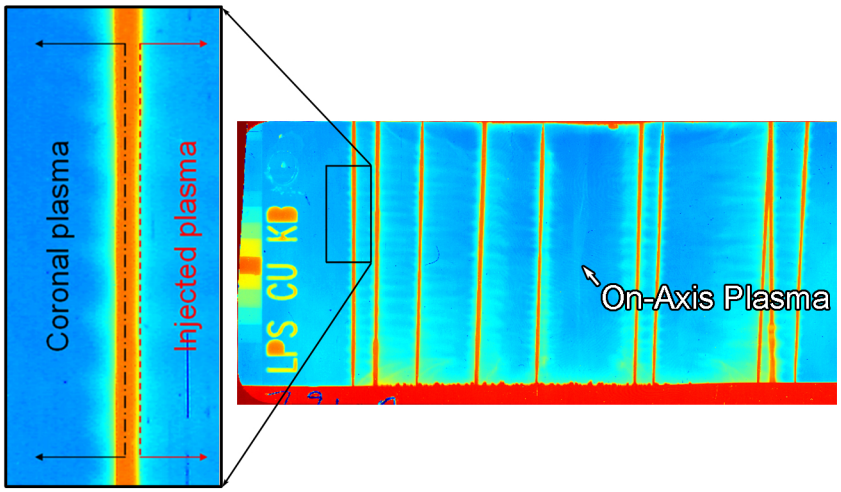


Figure 9.5: Boundaries of coronal and injected plasma structures emanating from the left edge-wire.

The term "coronal plasma" generally implies reference to the plasma around an edge wire in both the qualitative and quantitative results in the next two chapters. The coronal plasmas around other wires overlap injection stream distributions in the images we obtain with the STAR system. Hence, the coordinate system used to describe coronal plasma is typically taken to have its origin at the center of an edge wire, with the radial direction being the same as if the origin were on the array axis, the theta direction encircling the dense core, and the $z$ or axial direction being along the length of the dense core. This coordinate system is shown for an edge wire from the side in 9.5 and, in Fig. 9.6 from the axial (overhead) perspective.

As Figure 9.6 implies, and the caption explains, the coronal plasma is not assumed to be azimuthally uniform around the entire perimeter of the dense wire-core. The details of the transition from coronal plasma to injection plasma stream are difficult to measure. For simplicity, this transition region will not be analyzed. Instead, only the regions where the two structures are distinct will be analyzed. The two structures are assumed to be distinct within the respective bounds of an edge-wire image as shown in Fig. 9.6.

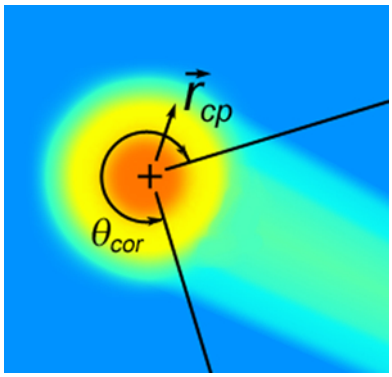


Figure 9.6: Coordinate system used for coronal plasma analysis. The origin of the cylindrical system of the wire-array is shifted to the center of the dense wire-core. The coronal plasma density is assumed to be uniform in the azimuthal direction over the angle $\theta_{cor}$.

The bounds implied in Fig. 9.6 do not tell the entire story of how these structures will be analyzed. In subsequent chapters, when fits are generated to model the coronal and injected plasma density distributions, in both cases, the center of the dense core is chosen for $r = 0$. For instance, injection stream density will be shown to scale as $1/r$, where $r = 0$ is at the center of the dense core and $r$ increases as one moves toward the array axis. The dashed red line in Fig. 9.5 would then be the smallest radius at which the $1/r$ fit would be valid. Exactly where this radius is chosen is somewhat arbitrary. Of greater importance is the lower bound of the range of experimental data that is used to generate the $1/r$ fit. If the lower bound of this range is too low (or high) then a poor fit will be produced. Generally, this lower bound is taken to be the position where the areal density of the injection stream is about $10^{18}/\text{cm}^2$, but this choice varies with initial wire diameter. The coronal plasma will be modeled using a $1/r^2$ fit; the same bounding issues apply. In this case the boundary can be closer to the center of the dense core, where $r = 0$. Specifically, the range of experimental data used to generate a fit to the coronal plasma density distribution generally starts where its areal density is about $10^{19}/\text{cm}^2$.

CHAPTER 10

# QUALITATIVE RESULTS

## 10.1 Introduction

Qualitative observation of wire-array Z-pinches plays an important role in achieving an improved understanding of the physics behind these impressive x-ray sources. This type of data can be used to quickly invalidate, or qualitatively support computer simulations and theoretical models. In the context of these experiments, "qualitative data", is anything inferred from the general appearance of an image, or sequence of images, without quantitative calibration.

## 10.2 Ablation Uniformity

The high spatial resolution and large field-of-view of the STAR system has shown that wire expansion and ablation, even in low wire number arrays, is very uniform, meaning very much the same rather than without spatial variation, from wire to wire. A sample image illustrating this uniformity is shown in Fig. 10.1. The uniformity of the features evident in the image has implications about the physics of wire-array initiation and the radiography system itself.

The fact that wire ablation and expansion are so similar from wire-to-wire despite the very large inter-wire gaps that are present in these experiments suggests that the driving current is evenly distributed among all of the wires. Since this is true at times early ($\sim$ 60ns), and late ($\sim$150ns) in the experiment based on the images that we have obtained, it is reasonable to conclude that the current reaches an even division early in

Table 10.1: Experimental parameters: $R_0$ - array radius, $N$ - wire number, $\phi_0$ - initial wire diameter, $h$ - array height, $\theta_A$ - rotation of the array about its axis from having a wire lie on the $x$-axis, Quencher - presence of monofilament radiation suppressor, Axial Radiation - presence of radiation from wire array implosion.

| Shot | $R_0$ (mm) | $N$ | $\phi_0(\mu\text{m})$ | $h$ (mm) | $\theta_A$ (deg) | Quencher | Axial Radiation |
|---|---|---|---|---|---|---|---|
| 784 | 8 | 16 | 10.16 | 20 | 30 | N | N |
| 785 | 6 | 10 | 12.7 | 8 | 24 | N | N |
| 786 | 6 | 10 | 12.7 | 8 | 24 | N | N |
| 787 | 6 | 10 | 12.7 | 8 | 24 | N | N |
| 788 | 6 | 10 | 10.16 | 8 | 24 | N | Y |
| 789 | 6 | 10 | 12.7 | 8 | 24 | N | Y |
| 790 | 6 | 10 | 17.02 | 8 | 24 | N | Y |
| 791 | 6 | 10 | 19.81 | 8 | 24 | N | N |
| 792 | 6 | 10 | 25.4 | 8 | 24 | N | N |
| 793 | 6 | 10 | 25.4 | 8 | 24 | N | N |
| 794 | 6 | 10 | 10.16 | 8 | 24 | Y | N |
| 795 | 6 | 10 | 7.37 | 8 | 24 | Y | N |
| 796 | 6 | 10 | 5.08 | 8 | 24 | Y | Y |
| 797 | 6 | 10 | 12.7 | 8 | 24 | Y | N |
| 798 | 6 | 10 | 10.16 | 8 | 24 | Y | N |
| 799 | 4 | 10 | 7.37 | 8 | 4 | Y | N |
| 800 | 4 | 10 | 7.37 | 8 | 4 | Y | N |
| 801 | 4 | 10 | 5.08 | 8 | 4 | Y | N |
| 802 | 4 | 10 | 10.16 | 8 | 4 | Y | N |
| 803 | 4 | 10 | 12.7 | 8 | 4 | Y | N |
| 804 | 4 | 10 | 17.02 | 8 | 4 | Y | N |
| 805 | 4 | 10 | 19.81 | 8 | 4 | N | Y |
| 806 | 4 | 10 | 25.4 | 8 | 4 | Y | N |
| 807 | 4 | 10 | 5.08 | 8 | 4 | Y | N |
| 887 | 8 | 16 | 10.16 | 20 | 30 | N | N |
| 888 | 8 | 16 | 10.16 | 20 | 30 | N | N |
| 891 | 8 | 16 | 10.16 | 20 | 30 | N | N |
| 892 | 8 | 16 | 10.16 | 20 | 30 | N | N |

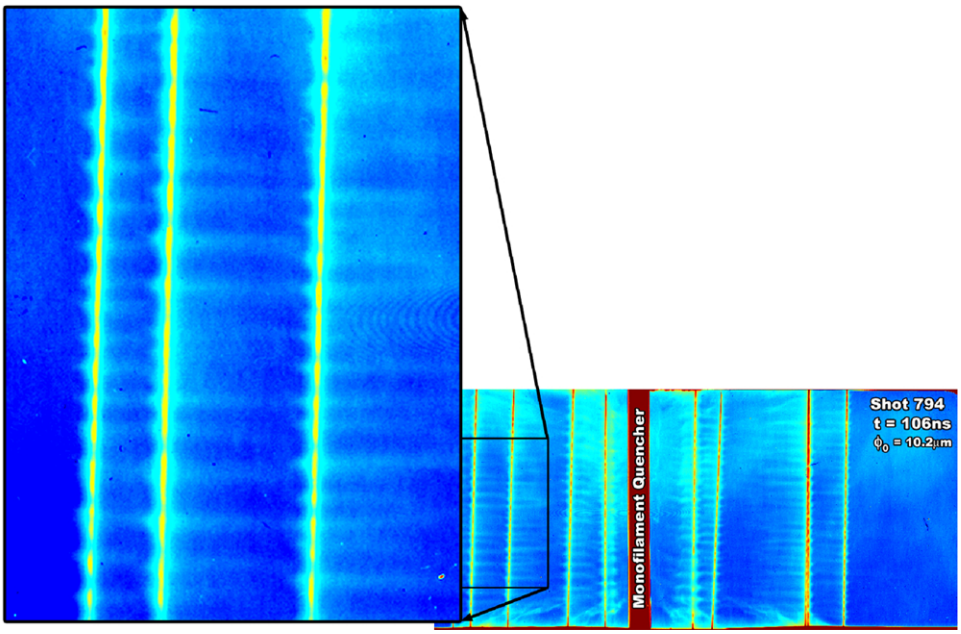


Figure 10.1: Image from COBRA experiment 794. Array parameters: $\phi_0$ = 10.2$\mu m$, $R_0$ = 6mm, $N$ = 10. Image was taken 106ns after start of current pulse.

time and remains that way at least until the fast implosion phase begins. It should be noted that cases were observed where one or two of the ten wires in an array were far more ablated than the others, but the rest were similarly ablated (see Fig. 10.2). The opposite case, where one or two wires were relatively pristine while the others were "normally" ablated, has not been seen. This was true even when the cathode connection of one wire was accidentally made far from the intended array radius. This loading error occurred twice, both of which are shown in Fig. 10.3; in both cases the odd wire appeared to be ablated to the same degree as the normally connected wires.

One of the major concerns regarding this diagnostic is to what degree it influences the experiment. Specifically, do the five return current X-pinches, which are usually not identical, divide the return current evenly? Rogowski coils monitor each leg of the return current (see Fig. 8.2) and suggest that it is divided nearly evenly, as was shown in Fig. 8.4. The uniformity of expansion and ablation seen in the radiographs of array wires

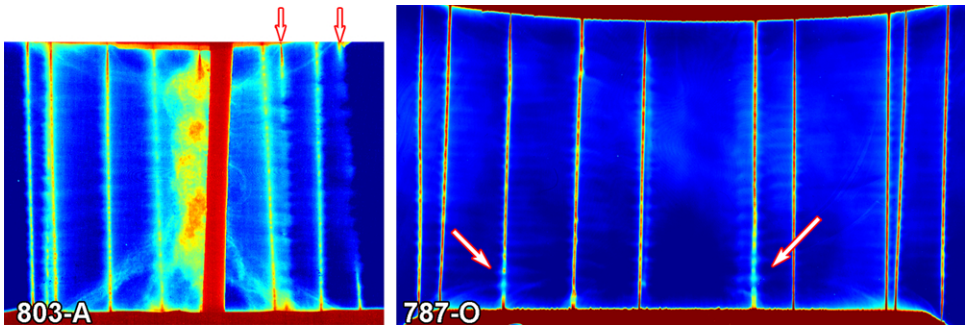


Figure 10.2: Images from COBRA experiments 803 at 150ns and 787 at 109ns. These arrays used 12.7$\mu m$ wire with $R_0$ = 4mm and 6mm, respectively, and $N$ = 10. These are the only two images from the data set in which ablation was significantly different from wire to wire, but only for the two wires marked by the arrows in the two cases.

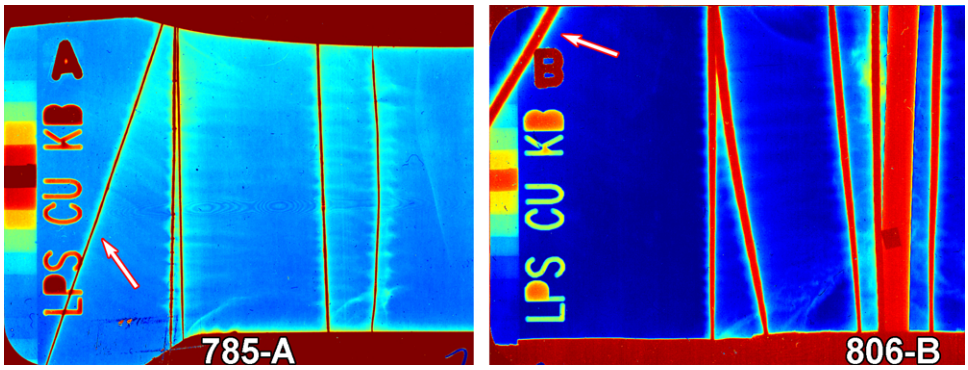


Figure 10.3: Images from COBRA experiments 785 at unknown time and 806 at 140ns. Array parameters: 12.7$\mu m$ wire with $R_0$ = 6mm, and 25.4$\mu m$ wires with $R_0$ = 4mm, respectively, and $N$ = 10. The wires indicated by the arrows were loaded improperly. These wires missed their pilot-holes in the cathode electrode, resulting in the slanted positioning seen here.

further supports the conclusion that current is divided evenly among the five X-pinches in the return current circuit.

## 10.3 Axial Mass Transport

It has been established that wire expansion and ablation are modulated in the axial direction with a characteristic wavelength that varies with, and only with, wire material. This modulation can be seen in Figs. 10.1 and 10.4. For tungsten, the Fundamental Wavelength Modulation (FWM), is about 250$\mu$m. Previous radiography results at Cornell[46], showed that the expansion of a wire-core and the ablation of plasma from it, were perfectly correlated in the axial direction. Specifically, it was found that ablated material streaming toward the array axis (injected material) appeared to come from portions of the wire that had expanded the most. This might lead one to conclude that the portions of the wire core that were expanded the most were also the hottest, resulting in intensified ablation in these locations. If this were the case, one would expect the expanded portions of the wires to become completely ablated first, leaving only the colder, narrow portions of the wires behind. In fact, the opposite situation is observed. The portions of the wires that have expanded the least, from where injection streams do not emanate, become completely ablated first. See Fig. 10.1, for example. This implies that some mechanism(s) exists that enables mass to be transported in the axial direction from the local minima of wire expansion to the local maxima before it starts to move radially inward as part of the injected plasma streams. The same effect was observed in experiments with aluminum wire arrays at Imperial College[44].

## 10.4 Axially Correlated Structures

Previous experiments have shown that the fast snowplow phase of a wire-array implosion is preceded by the formation of gaps along the length of the dense wire-cores[51, 52, 46]. The physics that leads to the formation of these structures is of the

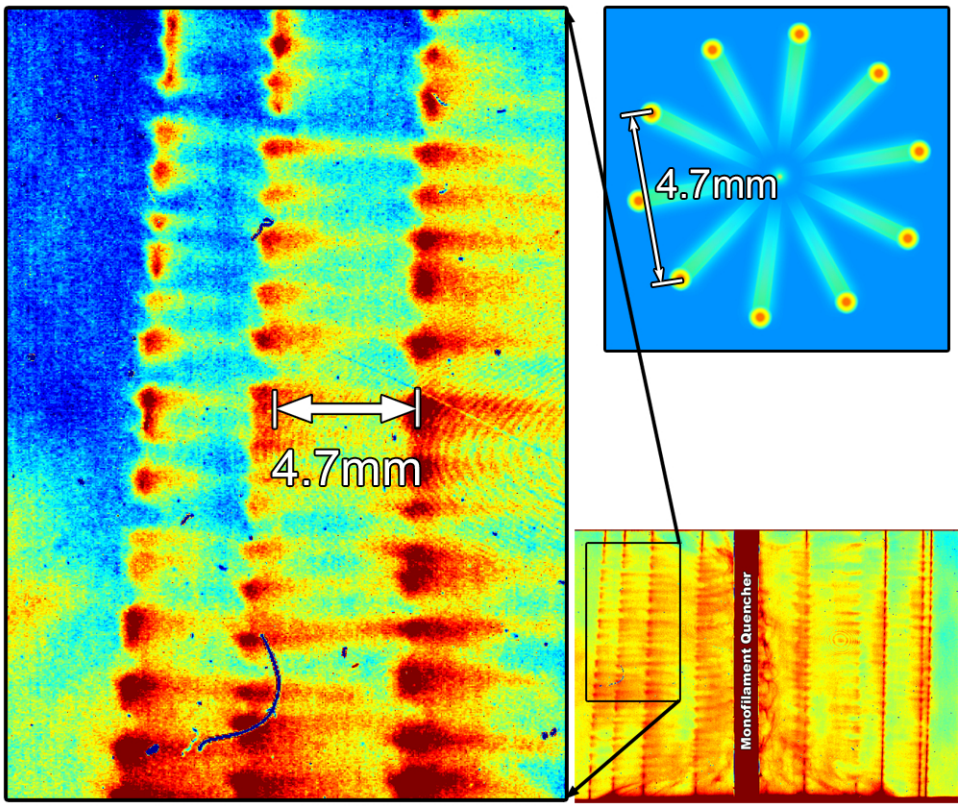


Figure 10.4: Image from COBRA experiment 800. Array parameters: $\phi_0$ = 7.4$\mu m$, $R_0$ = 4mm, $N$ = 10. Image was taken 99ns after start of current pulse.

utmost interest to the field. It is clear that the axial distribution of these structures is coupled with the FWM, as described in the previous section. What drives the FWM is still unknown, but these results offer a few clues.

Radiographs of wire-arrays when significant gap formation is observable show that these structures are strongly correlated in the axial direction from wire-to-wire. This is especially striking since the inter-wire gap in these experiments is relatively large, 4.7mm in the case of the 4mm radius array shown in Fig. 10.4. Wires that are separated by a distance greater than the array radius still demonstrate nearly perfect axial correlation. The only reasonable means of communication from one wire to another on such a length scale is the global magnetic field. While recent measurements by Patrick

F. Knapp imply that the global magnetic field does not initialize the FWM, these data indicate that it very strongly influences the axial nonuniformity correlation at the time when the fast snowplow phase begins.

## 10.5 Electrode Effects

One of the motivations for designing a diagnostic with a full view of the wire-array region was to investigate electrode effects, which had not been done previously using x-ray radiography. Single-wire experiments have shown that wire contacts can have significant effects on initial energy deposition and lead to non-uniform wire expansion[53]. It is not well understood to what degree wire-contacts and electrode shape are important to wire-array dynamics. This is particularly troubling since the load hardware used at wire-array research facilities throughout the world varies significantly, making comparison of results between facilities difficult.

The brass electrodes used in these experiments were similar to the standard COBRA hardware in that they were of the top-loaded, inward-radial-force, doubled-wire configuration. A sectioned view of the hardware is shown in Fig. 10.5. To minimize the shadows cast by the electrodes on to the images, they were conical. In the case of 12mm diameter arrays, the taper angle on the anode and cathode cones (shown in Fig. 10.5) is 15° and 32°, respectively. For ease of manufacturing, the anode and cathode both had a through hole on-axis. The through hole diameter was close to the array diameter in the case of both 8mm and 12mm array electrodes.

Radiographs of tungsten wire-arrays in these experiments indicate that material is preferentially ablated near the electrodes. The left image shown in Fig. 10.3 is an extreme example of this behavior. While it is unclear whether this material is ablated from

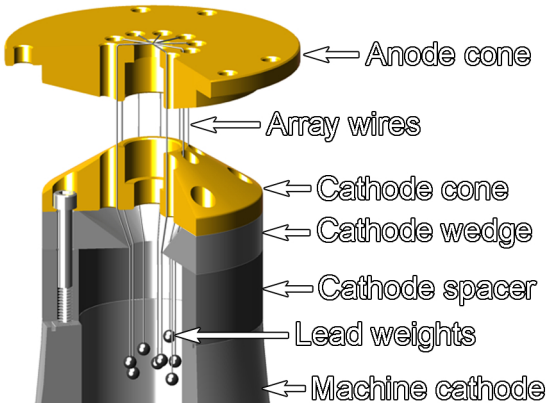


Figure 10.5: Section view of the STAR 12mm load hardware.

the wires or from the electrodes themselves, it is very clear that the injection streams emanating from near the electrode-wire contact points do not move purely in the inward radial direction; they appear to have axial motion as well. Plasma streaming toward the array axis from the cathode is inclined toward the anode, and vice versa. The trajectories of anode streams (top of the array in images) appear to have a distinct curvature, implying that the interior of the wire-array is not force-free in this region. This effect is the most pronounced in over-massed arrays where the mass ablation rate is higher. The trajectory of cathode streams do not have significant curvature.

The presence of enhanced ablation near the anode has not been observed in any other experiments. The unique features of these experiments include: the use of the STAR diagnostic system, conical electrodes, small array diameter with low wire number, and the array height of 8mm.

In most experiments, wire material is left behind by the main implosion front and this is certainly true at the anode electrode (see Fig. 10.6). In fact, portions of dense wire, on the order of 1mm long, are left at the anode contact point in quasi-ideally massed arrays. The amount of wire "stem" that is left behind the implosion front appears to be very similar from wire to wire. Thus, if this effect is related to the quality of initial

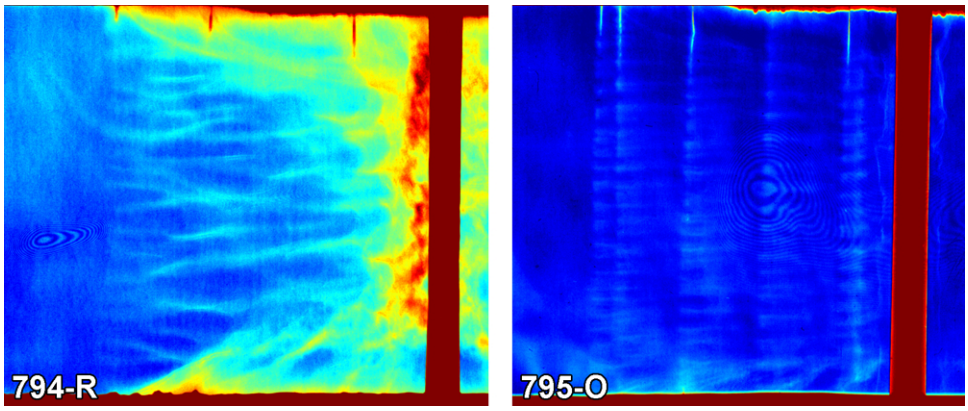


Figure 10.6: Images from COBRA experiments 794 (167ns) and 795 (109ns). Array parameters: $\phi_0 = 10.2\mu m$ and $\phi_0 = 7.4\mu m$, respectively, with $R_0 = 6$mm, and $N = 10$.

electrical contact then the initial contact must be very similar from wire-to-wire. Since no material appears to be left behind at the cathode there are clearly polarity effects involved.

## 10.6 On-Axis Plasmas

The formation of plasma structures on the axis of the wire-arrays in these experiments is observable in the later images of most experiments. This is true whether a monofilament quencher is used or not. When the quencher is present it is difficult to discern how the on-axis plasma interacts with it. Sometimes, the quencher was not well centered in the array and a plasma column formed adjacent to it. In such cases, on-axis plasma structures appear to be similar to the structures observed when no quencher is used (see image 797-A in Appendix G, for example).

On-axis plasma structures are generally nonuniform. The simplest explanation for this is that injected plasma streams converge on axis at different moments and are axi-

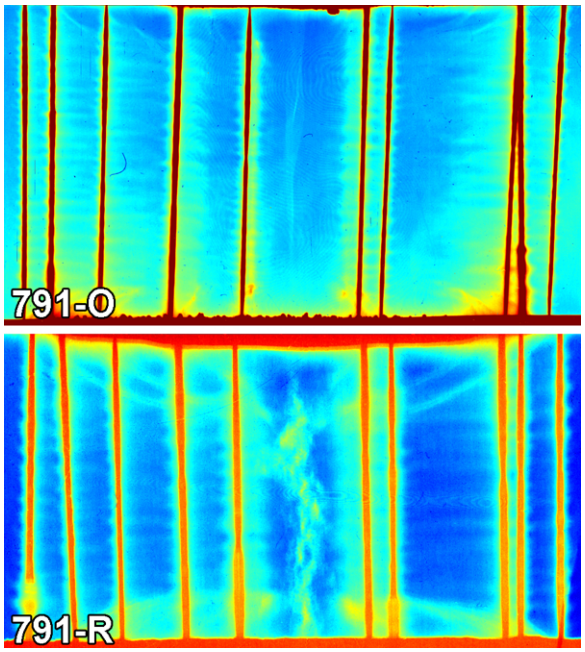


Figure 10.7: Images from COBRA experiment 791 (122ns and 168ns). Array parameters: $\phi_0 = 19.8\mu m$, $R_0 = 6$mm, $N = 10$. Illustration of on-axis plasma features. Note the transition from a smooth axial profile with sharp boundaries in the first image to the turbulent structure seen in the second image.

ally non-uniform. However, examples exist where on-axis plasmas are seen to exhibit smooth, uniform structure with sharp boundaries. Both types of on-axis plasma were seen in COBRA experiment 791, shown in Fig. 10.7, where a transition from a smooth structure to a highly structured one was observed.

## 10.7 Injection Stream Profiles

When analyzing injected plasma streams, one generally measures how the density of the stream varies with distance from the wire core and with the FWM. In previous work[46], when examining radiographs the majority of attention is given to the edge wires where these variations can be measured with the best accuracy. Little attention was given to the

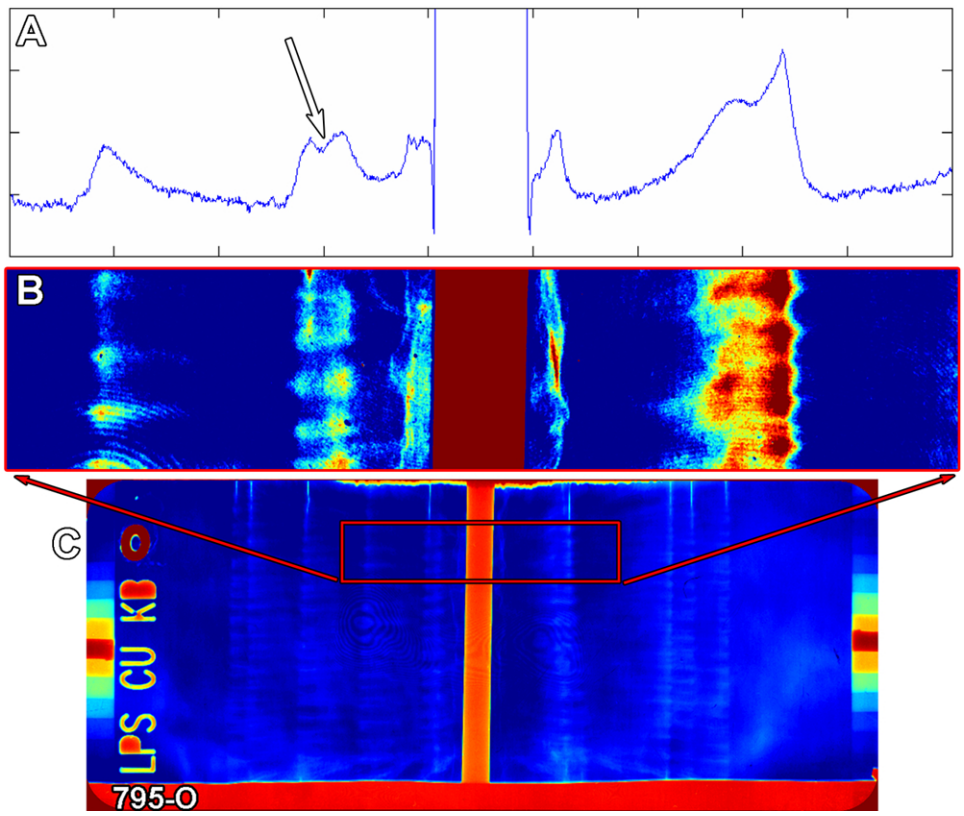


Figure 10.8: Image from COBRA experiment 795 (109ns). Array parameters: $\phi_0 = 7.4\mu m$, $R_0 = 6$mm, $N = 10$. A - line-out of inset shown in B. B - magnified inset of film 795-O. C - False colored scan of image 795-O. Note the local minimum in exposure indicted by the arrow in A.

variation of the injection plasma stream along its width, i.e. the direction perpendicular to its radial flow. The full field-of-view and high spatial resolution afforded by the STAR system allows us to address this issue for the first time. Images of injection streams that flow almost parallel to the system's line-of-sight indicate that the density of these streams is not uniform across their width. The injection streams appear to be more dense near their boundaries, giving a hollowed distribution. An example of this profile is shown in Fig. 10.8, in which the wires are nearly fully ablated yet the center of the stream indicated by the arrow appears to be hollow. The necessary line-of-sight and other circumstances for this observation make it suspect. A common question is

whether the structure indicated by the arrow in Fig. 10.8A is actually two wires that overlap; this is definitely not the case. If one counts the number of wire "stems" near the anode contact point in Fig. 10.8C there are clearly five wires on each side of the monofilament, with only one wire in the structure indicated by the arrow.

CHAPTER 11

# QUANTITATIVE RESULTS

## 11.1 Overview

The major breakthrough of these experiments is the accurate measurement of the plasma ion densities within tungsten wire-array Z-pinches at as many as five different times in a single pulse. Previous techniques made estimates of ion densities using spectroscopy and computer modeling. These efforts were estimated to be accurate to within a factor of two at best. The use of step wedge areal density calibration in these experiments enables accuracy of ±10% from high quality images.

The quantitative analysis of the data from these experiments focused on three measurements: the radius of the dense wire-cores, the volume density of the coronal plasma, and the areal density of injected plasma, all as functions of time. The boundaries of the dense core, coronal plasma, and injected plasma distributions, as defined here and used in the analysis that follows, are shown in Fig. 11.1.

It will be shown in this section that the dense wire-cores stop expanding once they reach a "final" radius, $r_f$, that is a function of the initial wire radius, $r_i$. Specifically, $r_f = 7.0 r_i - 9.6$, where all quantities are in microns. This relationship did not show any variation with array radius, $R_0$, or wire number, $N$. This trend may not hold for initial wire radius $\geq 20\mu$m, as will be shown in the following analysis.

The volume density distribution of the coronal plasma is coupled to the expansion of the dense core. It will be shown that the coronal plasma density, $\mathrm{n}_{cp}$ scales as:

$$\mathrm{n}_{cp}(r_{cp}) = \frac{\beta \cdot \mathrm{n}_W}{\left(\frac{r_{cp}}{r_i} - \frac{r_f}{2r_i}\right)^2} \quad \frac{\#}{\mathrm{cm}^3} \quad \text{for } r_{cp} \geq r_f \quad , \tag{11.1}$$

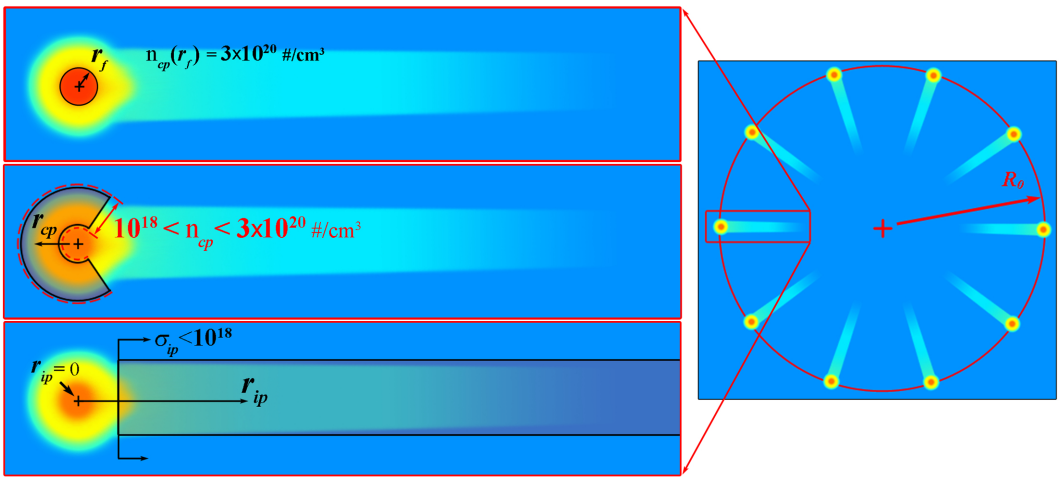


Figure 11.1: Illustration of the boundaries of the dense wire-core, coronal plasma, and injected plasma. The image to the right is an axial view of a 10-wire array. The three images at left, from top to bottom, show the (conceptual) boundaries of the dense wire-core, the coronal plasma, and injected plasma.

where $n_W$ is the number density of solid tungsten ($6.42 \times 10^{22}/\text{cm}^3$), and $\beta$ is a dimensionless constant, empirically determined to be about 0.03. Like the final core radius, $r_f$, the coronal plasma density distribution varies only with initial wire radius, $r_i$, for $r_i \leq 20\mu$m.

The areal density of injected plasma, $\sigma_{ip}$ will be shown in this section to scale as $1/r_{ip}$. Unlike the behavior of the dense cores and the coronal plasma density, $\sigma_{ip}$ increases with time and decreases with wire number. Furthermore, the areal density of injected plasma is far less sensitive to initial wire radius, albeit the amount of possible error is significant.

## 11.2 Aberrations and Error

The most arduous part of analyzing these data was determining the best method of interpreting the step array exposure levels and applying them to the portion of the film to be analyzed. This process was described in chapter 6. Further ambiguity lies in deciding which portions of each film are the most representative of "normal" behavior. Analyzing different portions of a given film produces results that vary to a degree determined by the severity of film aberrations.

The worst aberrations come from issues related to the developing process. An extreme example of this type of problem is shown in Fig. 11.2. The dimensions of the films used in these experiments are much larger than what has been used in the past. As a result, it is difficult to keep a uniform concentration of developer over the entire surface of the film during development. This problem is most serious when a film develops unusually quickly, which is caused by a strong developer and/or a strong x-ray exposure. The unfortunate outcome of nonuniform developing is the appearance of cloud-like features on a film. Since these features are generally randomly distributed it is difficult to compensate for them. Consequently, the portions of a film that have these cloud-like aberrations are not used for quantitative analysis.

The most difficult aspect of this analysis lies in assessing error. Error is generally a function of detector accuracy and sensitivity, round-off, and statistical deviation. There are simply not enough data in this set to make statements based upon statistics. The only measurements taken are those of the step thicknesses and the digitization of the films' exposure profile. The error in step thickness, except for the two thinnest steps, is less than 1%. The round-off error from digitization is also small. Experience dictates that subtle changes in calibration functions, and/or the portion of the film being analyzed,

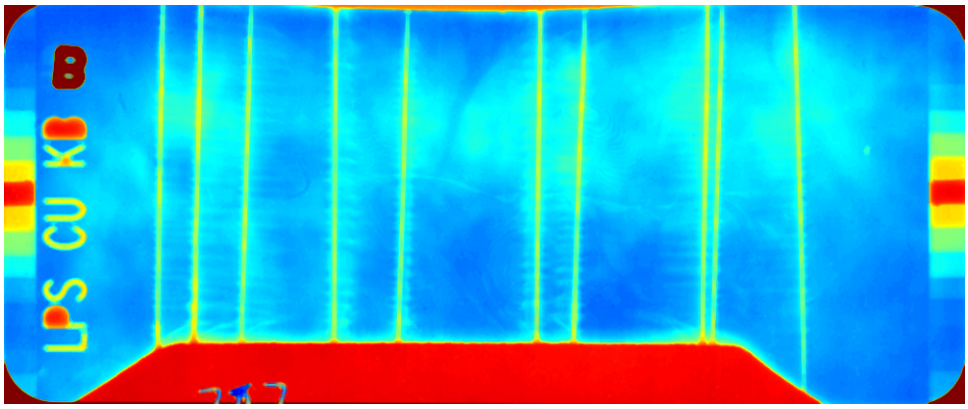


Figure 11.2: Image from COBRA experiment 787 (87ns). Array parameters: $\phi_0$ = 12.7$\mu m$, $R_0$ = 6mm. Note the fogging of the image along the upper half of the array. This film had the worst developing aberrations of the entire data set.

tend to change the results of image analysis on the order of 10%. Thus, the accuracy of areal densities obtained from the images is believed to be as good as ±10% but not worse than ±30%, based on observations during analysis.

## 11.3 Dense Wire-Core Analysis

In this analysis, the "dense wire-core" is defined as the cylindrical volume of material that is coaxial with the initial wire location and has a radial extent that encloses all local material with density greater than $3 \times 10^{20}/\text{cm}^3$.

In side-on, point-projection x-ray images, it is not practical to determine the literal initial wire location. Instead, it is assumed that the cylindrical axis of the initial wire location coincides with the center of the full-width, half-maximum (FWHM) areal density line-out of an exploding wire when viewed side-on.

On the basis of the above considerations, the radial extent of the dense core is defined

as the distance from the center of the areal density FWHM to the point where the volume density falls below $3 \times 10^{20}/\text{cm}^3$. This distance is found by Abel inverting the areal density line-out. The value of the density threshhold that defines the edge of the dense core was chosen for maximum compatibility with the dataset. Consider that the peak volume density at the center of the dense core depends on the specific experimental parameters of an image (time, initial wire size, wire number, etc.). The dense core threshold is chosen so that it is approximately equal to the minimum FWHM density value found in the set of images that clearly contain dense core material and are suitable for analysis. This assures that the boundary of dense core material can be consistently defined over the entire dataset.

For arrays with initial wire diameter less than $20\mu$m, the radial extent of dense core material did not vary with time over the time interval covered by the images, 70 to 170ns. Furthermore, the only variable that affected the radial core extent, $r_f$, was the initial diameter, $\phi_0$ (for $\phi_0 < 20\mu$m). This result is shown in Fig. 11.3.

For experiments with initial wire diameter less than $20\mu$m, dense core radius was found to be:

$$r_f = 7.0 r_i - 9.6 \tag{11.2}$$

where all quantities are in $\mu$m and $r_i$ is the initial wire radius ($\phi_0/2$).

Ideally, one would examine the volume density distribution of the entire dense core region. In most cases, this is not possible due to the maximum detectable areal density of the diagnostic (which corresponds to the minimum level of film exposure that can be attained), i.e. solid W with a thickness of $1\mu$m is indistinguishable from $10\mu$m thick W. The use of a higher energy backlighter could be used to explore this region, but will be left for the eager minds of the future as it is not essential to this research. The primary motivation for defining a dense core boundary is that it is a prerequisite for describing

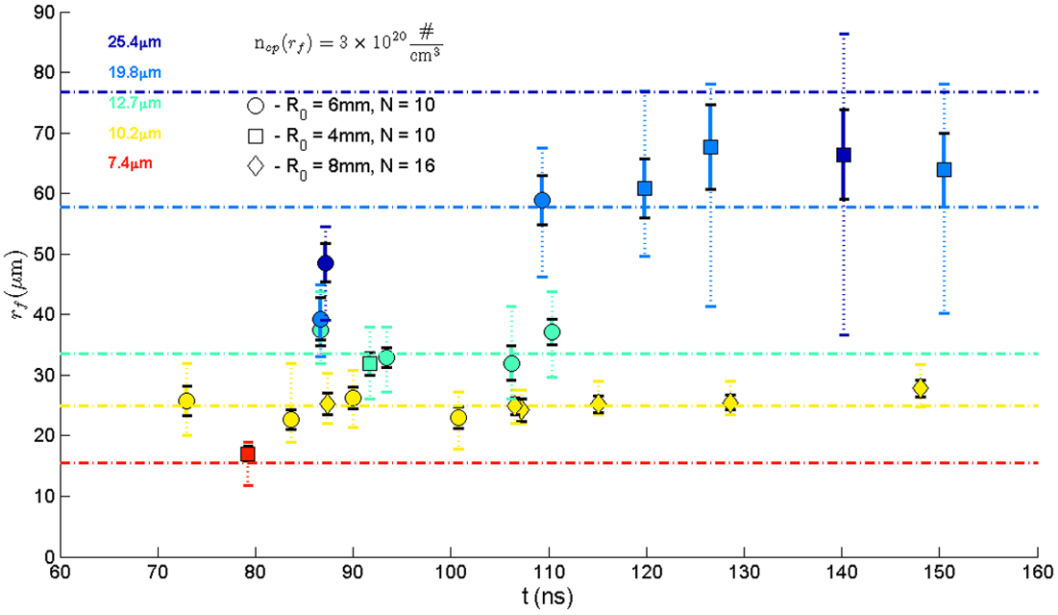


Figure 11.3: Dense core radius versus time. Each data point indicates the average core radius (averaged along the axial direction) of one edge-wire in a specific image, i.e. there is no averaging over the dataset. The color of data points indicates initial wire diameter, $\phi_0$. Marker shape indicates wire number, $N$, and array radius, $R_0$. The dashed vertical lines indicate the maximum and minimum values of core radius for each data point due to axial modulation. The solid vertical lines indicate the RMS variation of core radius due to axial modulation. The horizontal dot-dashed lines indicate the final core radius predicted by Eqn. 11.2.

the surrounding coronal plasma, which is presently of great interest to the field.

## 11.4 Coronal Plasma

Quantitative data describing coronal plasma volume density, $n_{cp}$, was obtained by Abel inverting the areal density line-outs of edge-wires in side-on images, as described in Appendix A. Less than 50% of all images were suitable for coronal plasma analysis, primarily because of multiple source issues. All images that contained multiple images

from multiple sources that were displaced radially by more than 8$\mu$m and/or axially by more than 80$\mu$m at the array (2$\mu$m and 20$\mu$m at the X-pinch), were rejected from this analysis. The maximum displacements of multiple images for each film in the data set are given in table G.2 in Appendix G. Failure to reject these data points, especially with radially displaced secondary sources, results in wildly varying coronal plasma density distributions, making it impossible to generalize coronal plasma dynamics. Proper data exclusion results in a clear trend. Note that rejection of one image from the set, from a particular shot, does not affect the validity of the others for present purposes.

Early on, it was noticed that the coronal plasma and dense core material appeared to be separate structures, divided by a very steep density gradient. This motivated the assumption that the coronal plasma density distribution should be a function $r_{cp} - r_f$, i.e. the coronal plasma distribution does not "start" until one is outside the dense core radius, $r_f$.

It was found that the coronal plasma density, $\mathrm{n}_{cp}$ scales as $1/r^2$, once outside the dense core radius, $r_f$. Specifically:

$$\mathrm{n}_{cp}(r_{cp}) = \frac{\beta \cdot \mathrm{n}_W}{(\frac{r_{cp}}{r_i} - \frac{r_f}{2r_i})^2} \tag{11.3}$$

where $r_{cp}$ is the radial distance from the center of the dense core, $r_f$ is the core radius given in Eqn. 11.2, $\mathrm{n}_W$ is the density of solid tungsten, and $\beta$ is a dimensionless constant found from Fig. 11.4 to be approximately 0.03 in most cases ($r_i$, $r_{cp}$, and $r_f$ must have the same units). The units of Eqn. 11.3 are the same as those used for $\mathrm{n}_W$, either #/cm$^3$, #/m$^3$, g/cm$^3$, etc. The factor of $1/2$ that appears with $r_f$ in the denominator of Eqn. 11.3 was determined empirically. This factor was introduced, and chosen to be less than one, so that $\mathrm{n}_{cp}$ would be bounded at $r_{cp} = r_f$. The value of $1/2$ was observed to produce the best agreement between Eqn. 11.3 and experimental data near $r_{cp} = r_f$. Examples of the agreement between Eqn. 11.3 and experiment are shown in Figs. 11.5 and 11.6. For

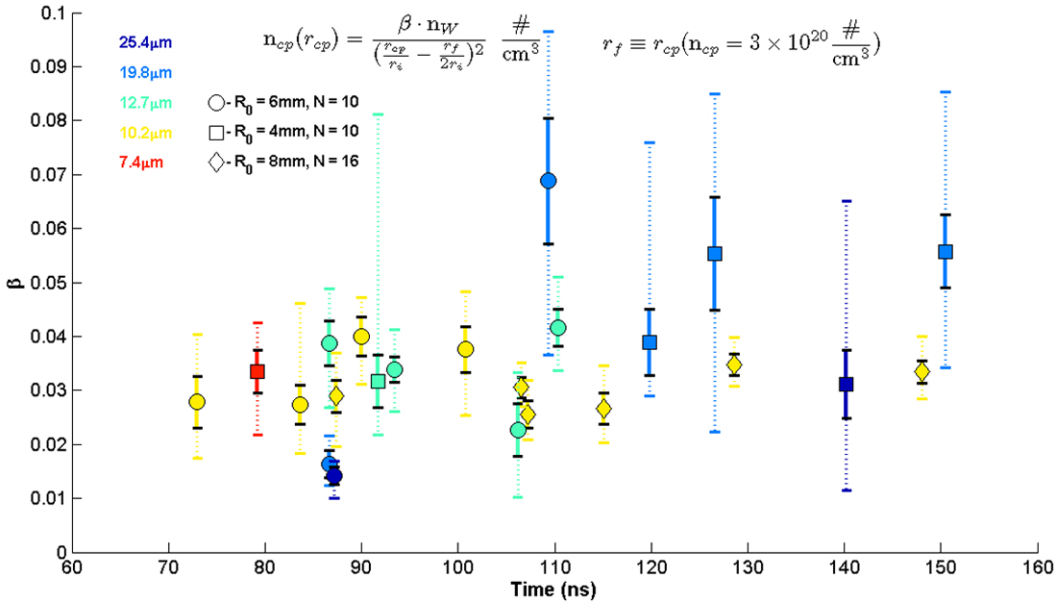


Figure 11.4: Coronal plasma density scaling versus time. Each data point indicates the average value of $\beta$ (averaged along the axial direction) determined by least squares fits of Eqn. 11.3 to 20$\mu$m wide (in the axial direction) radial line-outs of experimental data. Each data point is generated from a single edge wire in a single image, averaged over hundreds of slices (and the corresponding least squares fits) in the axial direction. The color of data points indicates initial wire diameter, $\phi_0$. Marker shape indicates wire number, $N$, and array radius, $R_0$. The dashed vertical lines indicate the maximum and minimum values of core radius for each data point due to axial modulation. The solid vertical lines indicate the RMS variation of core radius due to axial modulation.

example, for the lower-right chart in Fig. 11.5 (797C), $r_i = 6.35\mu$m, hence $r_f \approx 35\mu$m, and

$$n_{cp}(r_{cp}) = \frac{0.03 \cdot n_W}{\frac{r_{cp}}{6.35} - 2.76} \tag{11.4}$$

The agreement is good in this case and the others with small diameter wires, but not for most cases with larger wires.

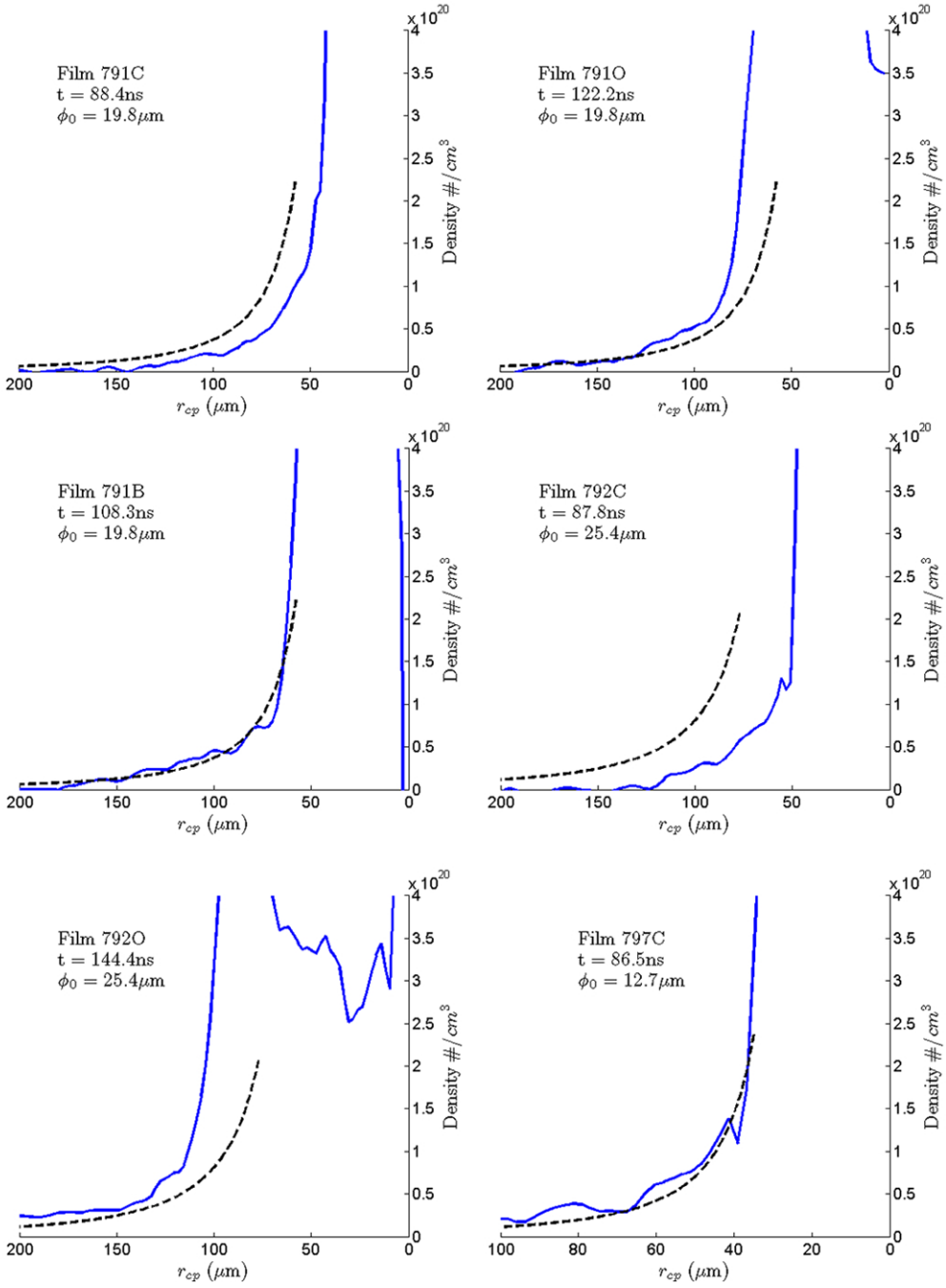


Figure 11.5: The solid blue lines are Abel inversions of the coronal plasma density from the one of the edge wires in the experiments indicated in the respective charts. Each experimental curve is the Abel inversion of one radial line-out averaged over about 20$\mu$m in the axial direction. The dashed black lines are the density profile predicted by Eqn. 11.3 using $\beta = 0.03$.

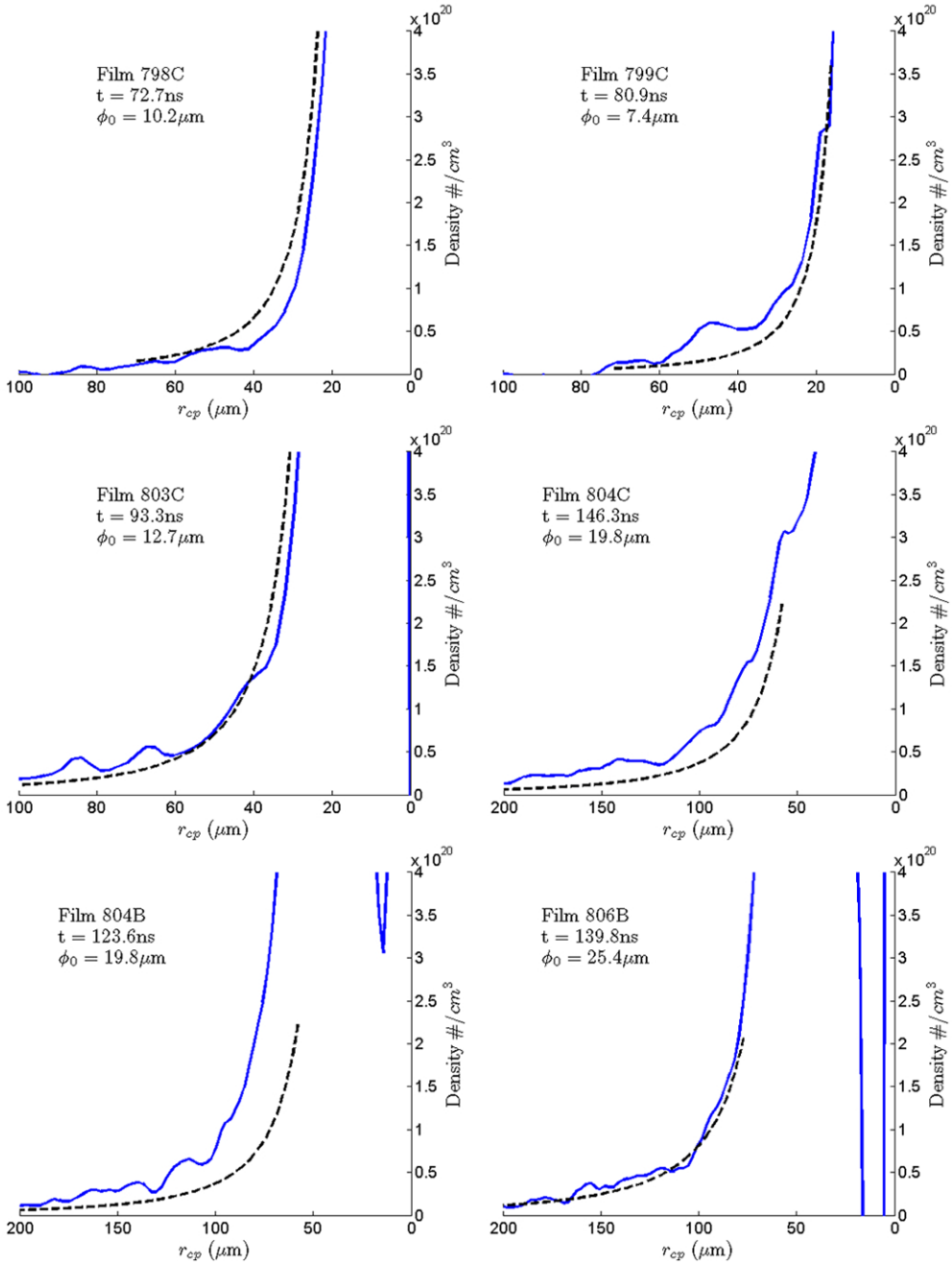


Figure 11.6: The solid blue lines are Abel inversions of the coronal plasma density from the one of the edge wires in the experiments indicated in the respective charts. Each experimental curve is the Abel inversion of one radial line-out averaged over about 20$\mu$m in the axial direction. The dashed black lines are the density profile predicted by Eqn. 11.3 using $\beta = 0.03$.

## 11.5 Injected Plasma

The analysis of injected plasma streams was done with the same data exclusion rules as were used for the coronal plasma. As Fig. 11.1 indicates, the conceptual near-wire-core boundary of the injected plasma is based on its areal density, not volume density, as was the case for the coronal plasma. Specifically, the lower radial boundary of injected plasma was taken to be the position where the injected plasma areal density had fallen to $10^{18}/\mathrm{cm}^2$, as indicated by Fig. 11.1. While this definition may be less meaningful than one based on volume density, it greatly simplifies analysis since it requires no assumptions about the spatial variation of the stream.

In all experiments where injected plasma was detectable, it was found that the areal density of the injected plasma, $\sigma_{ip}$, scales as $1/r_{ip}$. This was found by examining edge-wires in side-on images as described in Appendix A. Unlike the dense cores and coronal plasma, the injected plasma areal density is strongly dependent upon array parameters ($\phi_0$ and $N$) and time, as shown in Fig. 11.7.

The scaling parameter, $\gamma(t, r_i, N)$, shown in Fig. 11.7 is non-dimensional because the areal density is made proportional to $\mathrm{n}_W r_i$, the maximum initial areal density of the wire core, and the radial distance, $r_{ip}$, is divided by $r_f$ (the dense core radius given in Eqn. 11.2). Specifically, stream areal density is given by:

$$\sigma_{ip} = \gamma \frac{\mathrm{n}_W r_i}{r_{ip}/r_f} \quad \frac{\#}{\mathrm{cm}^2} \tag{11.5}$$

where $\mathrm{n}_W$ is the density of solid tungsten in $/\mathrm{cm}^3$, $r_i$ is the initial wire radius in centimeters, $r_f$ is the dense core radius (having the same units as $r_{ip}$), and $r_{ip}$ is the stream radius as explained in Fig. 11.1. The values of the scaling parameter, $\gamma(t)$, that are shown in Fig. 11.7 are derived from least squares fitting of Eqn. 11.5 to experimental data, as explained in the caption.

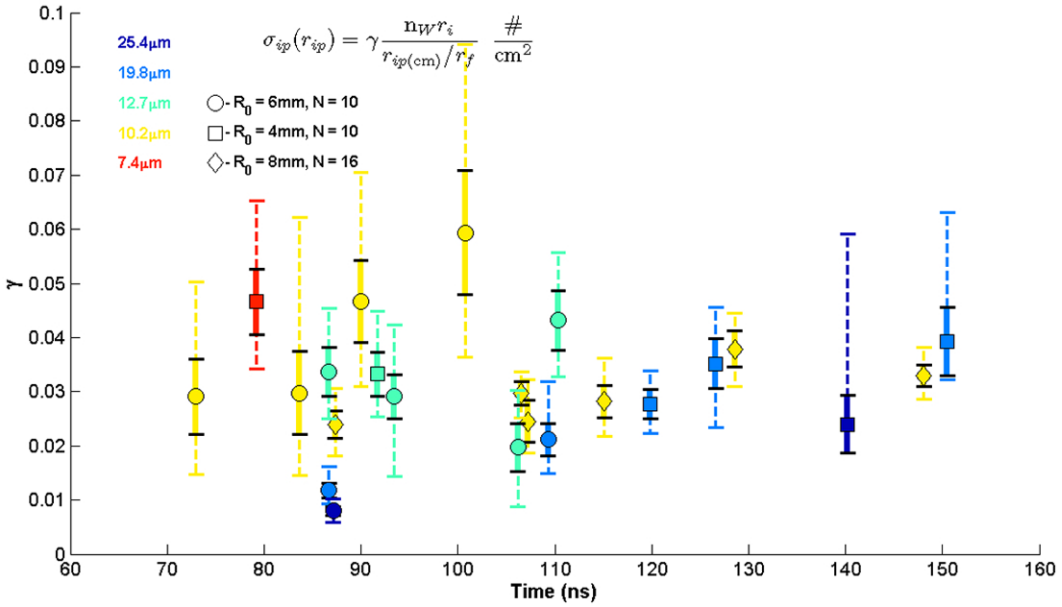


Figure 11.7: Injected plasma areal density scaling, $\gamma$, versus time. Each data point indicates the average value of $\gamma$ (averaged along the axial direction) determined by least squares fits of Eqn. 11.5 to 20$\mu$m wide (in the axial direction) radial line-outs of experimental data. Each data point is generated from a single edge wire in a single image, averaged over hundreds of slices (and the corresponding least squares fits) in the axial direction. The color of data points indicates initial wire diameter, $\phi_0$. Marker shape indicates wire number, $N$, and array radius, $R_0$. The dashed vertical lines indicate the maximum and minimum values of core radius for each data point due to axial modulation. The solid vertical lines indicate the RMS variation of core radius due to axial modulation.

If one assumes that the width of the injected plasma stream is equal to the dense core radius, then the stream's average (over its width) density can be found by dividing Eqn. 11.5 by the stream width, $r_f$. The stream volume density, $n_{ip}(r_{ip})$, is then given by:

$$n_{ip}(r_{ip}) = \frac{\sigma_{ip}}{r_f} = \gamma(t, r_i, N)\frac{n_W}{r_{ip}/r_i} \tag{11.6}$$

where $\gamma(t, r_i, N)$ is estimated from Fig. 11.7, $r_{ip}$ and $r_i$ have the same units, and $n_{ip}$ has the same units as $n_W$ (solid density of tungsten).

One could reasonably argue that the stream width could be 2 to 5 times the dense

core radius, $r_f$. The density distribution given in Eqn. 11.6 would then be decreased by a factor of 2 to 5. It is not the author's intention to estimate an exact value for $n_{ip}$. However, we can estimate that the injected stream volume density is within a factor of at most five of that given in Eqn. 11.6.

By contrast, the amount of mass in the stream per unit axial length, $\hat{m}_{ip}$, can be estimated simply and accurately at the particular instant in time, $t$, of an image by integrating Eqn. 11.5 with respect to $r_{ip}$. It will be assumed that the stream starts at $r_{ip} = r_f$ and terminates at $r_{ip} = R_0$:

$$\begin{aligned} \hat{m}_{ip}(t) &= \int_{r_f}^{R_0} \gamma(t, r_i, N) \frac{n_W r_i}{r_{ip}/r_f} dr_{ip} \\ &= \gamma(t, r_i, N) \cdot r_f \cdot r_i \cdot n_W \ln \frac{R_0}{r_f} \ \frac{\#}{\text{cm}} \end{aligned} \tag{11.7}$$

where all distances are in centimeters. Dividing Eqn. 11.7 by the initial mass per unit length, $\hat{m}_0 = \pi r_i^2 n_W$, gives the fraction of the initial mass contained in the injection stream, $\delta\hat{m}$:

$$\delta\hat{m} = \gamma(t, r_i, N) \frac{1}{\pi} \frac{r_f}{r_i} \ln \frac{R_0}{r_f} \tag{11.8}$$

Substituting Eqn. 11.2 into 11.8 yields:

$$\delta\hat{m} = \gamma(t, r_i, N) \frac{1}{\pi} \left(7 - \frac{9.6}{r_i}\right) \ln \frac{R_0}{7.0 r_i - 9.6} \ , \tag{11.9}$$

where $R_0$ and $r_i$ are now in microns, and $\gamma(t, r_i, N)$ is estimated from Fig. 11.7. This value, $\delta\hat{m}$, makes a very useful comparison to the Rocket model described in chapter 3. The values of $\delta\hat{m}$ predicted by Eqn. 11.8, using the experimental values of $\gamma(t, r_i, N)$ shown in Fig. 11.7, are shown in Fig. 11.8. Specific comparisons of the values of $\delta\hat{m}$ derived from these data and the Rocket model are shown in Figs. 11.9, 11.10, and 11.11.

The agreement between the Rocket model and these experimental data is good in some respects. The temporal behavior of the two is similar in most cases. Furthermore,

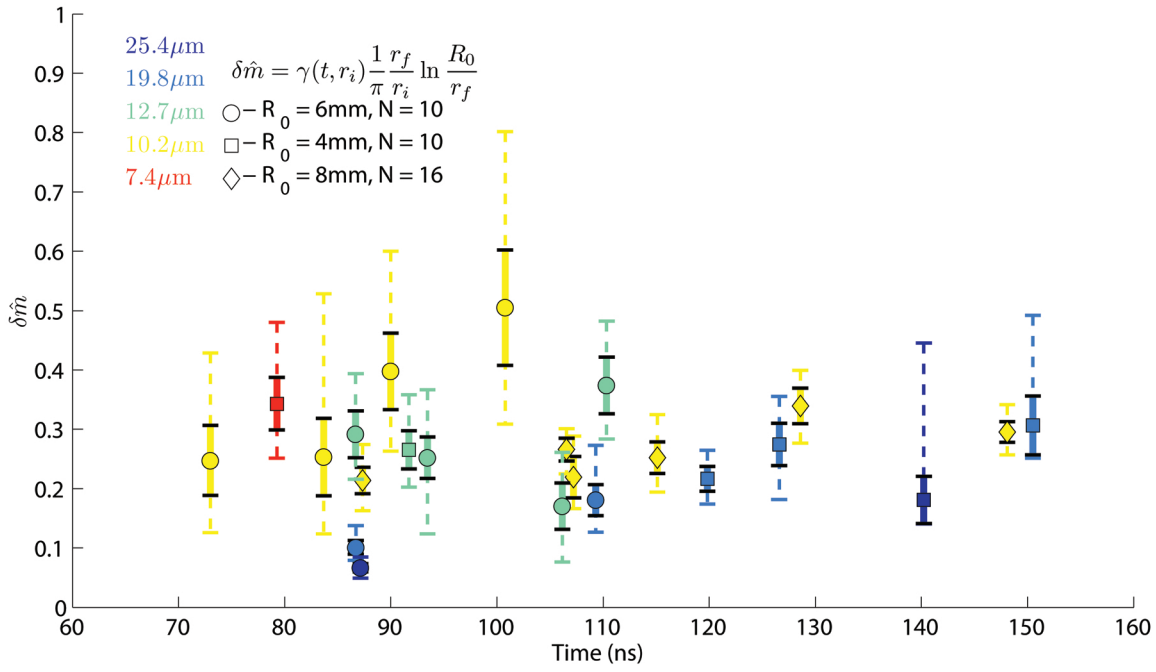


Figure 11.8: Fraction of the initial mass contained in the injected plasma stream. Data points are calculated using Eqn. 11.8 and the values of $\gamma(t, r_i, N)$ shown in Fig. 11.7.

the effect of increasing/decreasing $N$ is in agreement. However, the experimental data suggest that $v_{abl}$ is influenced by array parameters.

The fact that the injected plasma stream density scales as $1/r$, for $r_{ip} \geq r_f$ and up to $r_{ip} \approx 1$mm, has important implications. If one assumes that the momentum flux in the injected plasma stream does not vary along the streams length (along $r_{ip}$), then the product of stream density and velocity must be constant:

$$\mathrm{n}_{ip}(r_{ip}, t) \cdot v_{ip}(r_{ip}, t) = const\ . \tag{11.10}$$

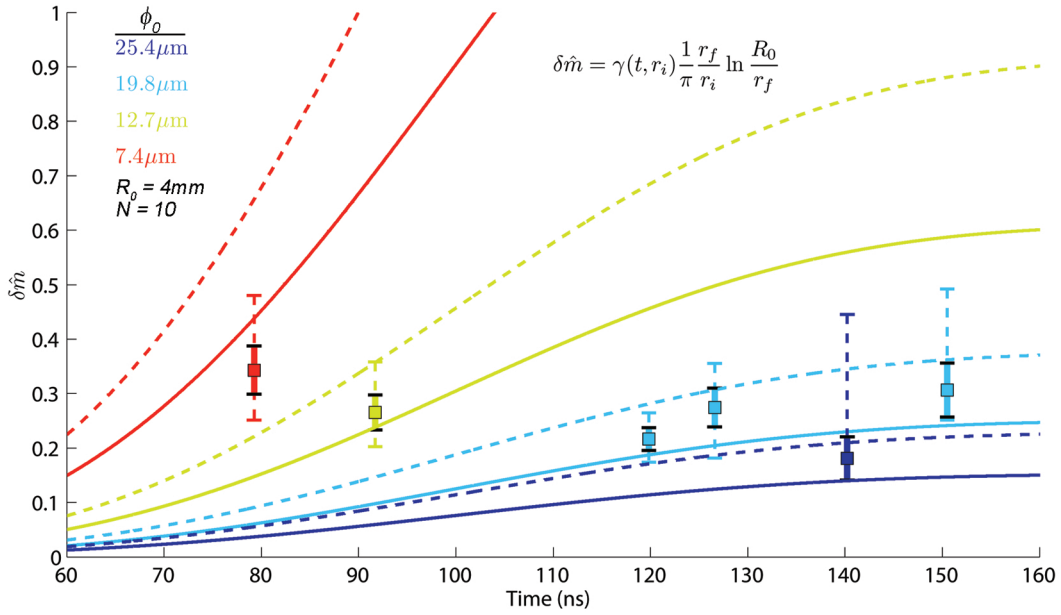


Figure 11.9: Comparison of experimental data with $R_0$ = 4mm to the Rocket model of wire array ablation. The data points are calculated using Eqn. 11.8 with the values of $\gamma(t, r_i, N)$ shown in Fig. 11.7. The dashed and solid curves are the fraction of ablated mass predicted by the Rocket model (Eqn. 3.6) using $v_{abl}$ = 100 and 150km/s, respectively.

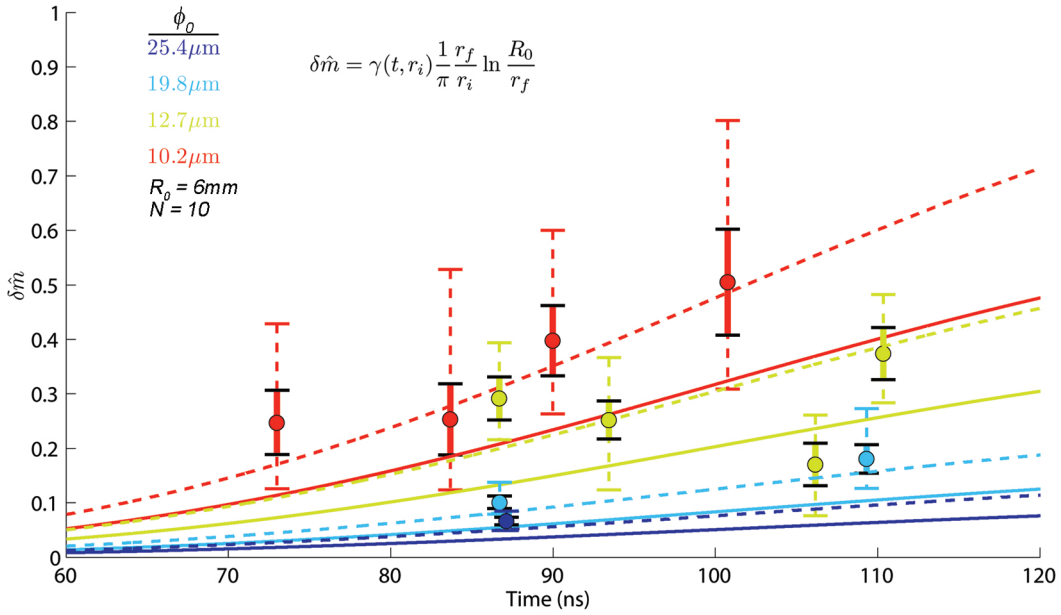


Figure 11.10: Comparison of experimental data with $R_0$ = 6mm to the Rocket model of wire array ablation. The data points are calculated using Eqn. 11.8 with the values of $\gamma(t, r_i, N)$ shown in Fig. 11.7. The dashed and solid curves are the fraction of ablated mass predicted by the Rocket model (Eqn. 3.6) using $v_{abl}$ = 100 and 150km/s, respectively.

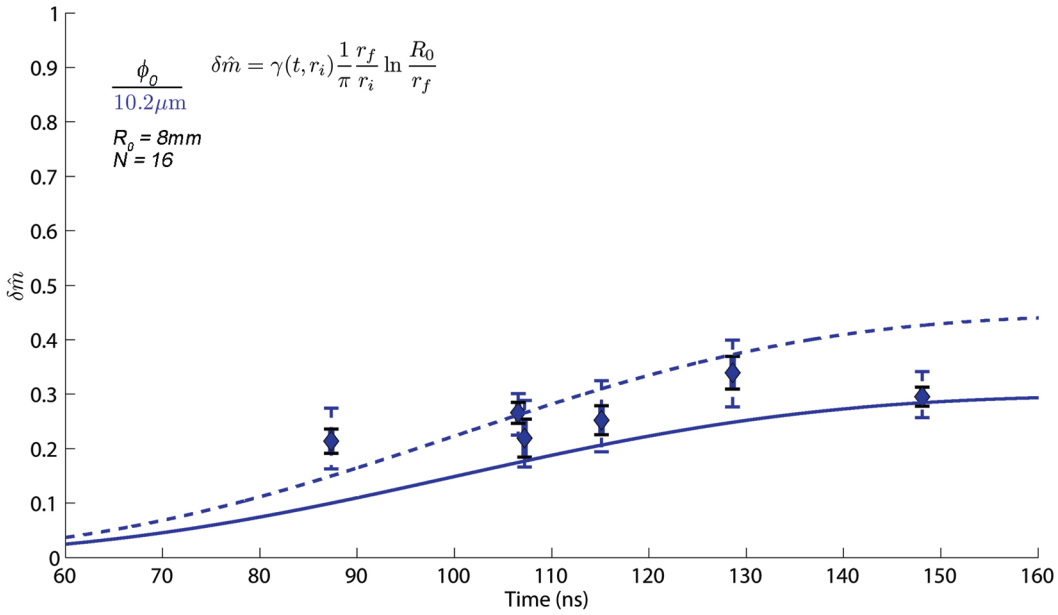


Figure 11.11: Comparison of experimental data with $R_0 = 8$mm to the Rocket model of wire array ablation. The data points are calculated using Eqn. 11.8 with the values of $\gamma(t, r_i, N)$ shown in Fig. 11.7. The dashed and solid curves are the fraction of ablated mass predicted by the Rocket model (Eqn. 3.6) using $v_{abl} = 100$ and 150km/s, respectively.

Therefore, $v_{ip} \propto r_{ip}$. However, if $v_{ip}$ increases along the direction of $r_{ip}$ then the region is not force free and the momentum flux is not constant. The logical conclusion is that the material in the injection stream is being accelerated toward the array axis by current flowing axially in the injection stream within the region of $r_f \leq r_{ip} < 1\text{mm}$. This conclusion assumes that the stream does not fan out significantly (approximately constant width) as it flows toward the array axis, and that the timescale of material flowing along the injection stream is much faster than the timescale over which the drive current changes significantly.

CHAPTER 12

# CONCLUSIONS

## 12.1 Review

The motivation for these experiments was to investigate quantitatively the plasma generation rate as an element of the dynamics of tungsten wire-array Z-pinch ablation and implosions using point-projection x-ray radiography. The data set included 10-wire, 8mm and 12mm diameter, 8mm tall, arrays with mass ranging from 39 to 978$\mu$g/cm (experimental parameters listed in table 10.1). The results from other experiments that used 16-wire, 16mm diameter, 20mm tall, 251$\mu$g/cm W arrays have also been analyzed but are not included in great detail in this thesis as they were taken as part of a different experimental run.

The characterization of mass ablation and injection as a function of time from arrays of wires was accomplished using the STAR system on the COBRA pulsed power generator (described in Chapter 8). The STAR system is a five-frame, point-projection, x-ray radiography diagnostic. The point x-ray sources utilized by this system are Mo X-pinches (Chapter 5) in the return-current circuit. These sources produced images with sub-nanosecond temporal resolution and about 7$\mu m$ spatial resolution. Source radiation was filtered by Ti foils so that only 3-5keV Mo continuum radiation would contribute to film exposure. Thin W films of known thickness were deposited on the Ti filters so that film exposure levels could be converted to W areal density (Chapter 6).

The results from this diagnostic are novel in many respects. Foremost of the accomplishments from this work are accurate mass and density measurements of plasma ablation and injection. Many interesting qualitative features of wire-array dynamics were

also seen for the first time. These measurements and observations were possible only because of the unique features of the STAR diagnostic, namely its high frame-number, large field-of-view, high spatial and temporal resolutions, and direct calibration.

## 12.2 Summary of Qualitative Results

Despite the asymmetric return current configuration that is inherent with this diagnostic system, ablation was found to be uniform from wire to wire in the majority of these experiments. Occasionally, one or two wires (out of ten) were observed to have been far more ablated than the rest, indicating that it is possible for ablation to start early and/or proceed more quickly in one or two wires. The converse, where one or two wires were far less ablated than the rest, was never observed, even when the cathode connection to one wire was accidentally made far outside the array radius.

High resolution radiographs of the dense wire cores, coronal plasmas, and injection plasma streams confirm that mass is being transported in the axial direction along the length of the wires. This was evidenced by the pattern in which gaps formed along the dense cores due to the Fundamental Wavelength Modulation (FWM). The axial locations of gaps in core/corona structures are anti-correlated with the axial locations of injection plasma streams. Hence, mass must be transported in the axial direction from the locations where gaps form to the locations from which injection streams emanate. This is in good agreement with experiments using aluminum wire arrays at Imperial College[44] and recent 3D resistive MHD simulations by J. P. Chittenden et al.[54]. In addition, the timing of gap formation along the core/corona structure is very similar from wire to wire.

Images taken after complete ablation had been reached and the implosion phase had

begun indicate that the injection stream locations are correlated in the axial direction from wire to wire. It is unclear how early in the current pulse that this correlation is established. The only mechanism that could be responsible for this correlation from wire to wire is the global magnetic field.

The full field-of-view of this diagnostic permitted electrode effects at both ends of the array to be radiographed for the first time. The trajectories of injection streams near the electrodes are inclined toward the center of the array, i.e. away from the electrodes. Injection streams emanating from the anode contact have a distinct radius of curvature, indicating that the array interior is not force-free in this region. Injection streams emanating from the cathode have a straight trajectory.

Contact effects were seen at both electrodes. In experiments that reached the implosion phase, over most of the length of the wires, dense wire "stems" about 1mm long were left at the anode electrode. In experiments with over-massed arrays, it was not uncommon for one or two wires to be preferentially expanded at the cathode contact. Each of these effects were exclusive to their respective electrode. These observations indicate that polarity effects do exist but may not influence the dynamics of ablation and injection over most of the length of the wire array, especially in the case of arrays were $t_{imp} \approx t_{peak}$ ($t_{peak}$ being the time when peak current is reached).

The structure of on-axis plasmas was radiographed for the first time in these experiments. In most cases these plasmas were highly nonuniform axially. However, in some experiments material that had accumulated on the array axis was uniformly distributed and had smooth, sharp boundaries. It seems reasonable to conclude that some mechanism exists that drives these structures to be unstable under some circumstances. Current flowing in the on-axis plasma seems to be the most likely mechanism. However, implosion axial non-uniformity is another possibility.

Images of injection streams that flow almost parallel to the image line-of-sight indicate that the density of these streams is not uniform. A plausible explanation of the appearance of these end-on images is that the injection streams are somewhat hollow. This explanation implies that the dense core blocks material that would be injected into the center of the stream.

## 12.3 Summary of Quantitative Results

The quantitative analysis of these experiments focused on three features: the dense wire core radius, the surrounding coronal plasma density, and the density profile of injected plasma.

For arrays with initial wire diameter less than 20$\mu$m, the radial extent of dense core material did not vary with time over the interval of 70-170ns. Furthermore, the only variable that affected the radial core extent, $r_f$, was the initial diameter, $\phi_0$ (for $\phi_0 <$ 20$\mu$m). This result was shown in Fig. 11.3.

It was found that the coronal plasma density, $n_{cp}$ scales as $1/r^2$, once outside the dense core radius, $r_f$. Specifically:

$$n_{cp}(r_{cp}) = \frac{\beta \cdot n_W}{(\frac{r_{cp}}{r_i} - \frac{r_f}{2r_i})^2} \tag{12.1}$$

where $r_{cp}$ is the radial distance from the center of the dense core, $r_f$ is the core radius given in Eqn. 11.2, $n_W$ is the density of solid tungsten, and $\beta$ is a dimensionless constant found to be approximately 0.03 in most cases, as shown in Fig. 11.4 ($r_i$, $r_{cp}$, and $r_f$ must have the same units).

In all images in which injected plasma was detectable, it was found that the areal density of the injected plasma, $\sigma_{ip}$, scales as $1/r_{ip}$. This was found by examining edge-

wires in side-on images as described in Appendix A. Unlike the dense cores and coronal plasma, the injected plasma areal density is strongly dependent upon array parameters and time, as shown in Fig. 11.7.

If one assumes that the width of the injected plasma stream is equal to the dense core radius, then the stream's average (over its width) density can be found by dividing Eqn. 11.5 by the stream width, $r_f$. The stream volume density, $n_{ip}(r_{ip})$, is then given by:

$$n_{ip}(r_{ip}) = \frac{\sigma_{ip}}{r_f} = \gamma \frac{n_W}{r_{ip}/r_i} \tag{12.2}$$

where $\gamma$ is a dimensionless scaling parameter that is a function of $r_i$ and $t$, $r_{ip}$ and $r_i$ have the same units, and $n_{ip}$ has the same units as $n_W$ (solid density of tungsten). The scaling of $\gamma(t, r_i)$ was shown in Fig. 11.7.

The agreement between the Rocket model and these experimental data is good in some respects. The temporal behavior of the two is similar in most cases. Furthermore, the effect of increasing/decreasing $N$ is in agreement. However, the experimental data suggest that $v_{abl}$ is influenced by array parameters.

The fact that the injected plasma stream density scales as $1/r$, for $r_{ip} \geq r_f$ and up to $r_{ip} \approx 1$mm, has important implications. If one assumes that the momentum flux in the injected plasma stream does not vary along the streams length (along $r_{ip}$), then the product of stream density and velocity, $v_{ip}$, must be constant. For this to be the case $v_{ip}$ must increase with $r_{ip}$, which creates a contradiction. Hence, material in the injection stream is being accelerated over a large region from $r_{ip} = r_f$ to at least $r_{ip} = 1$mm. This implies that a significant amount of axial current flows in the injection stream as far as 1mm from the dense wire core.

## 12.4 Concluding Remarks

The data and corresponding analysis presented here mark an improvement in our knowledge of wire-array Z-pinch dynamics in the 1MA, 100ns regime. By no means is our understanding complete. Further studies using the COBRA STAR diagnostic will undoubtedly expand our knowledge of wire-array physics and improve our present understanding.

The findings of these experiments strongly suggest that a substantial portion of the electrical current in sparse wire arrays flows in the interior of the array at times ranging from 70ns to 170ns. The $1/r$ scaling of the injected plasma stream density indicates that the injected plasma is being accelerated over a relatively large distance: from the inner edge of the dense core to as far as 1mm toward the array axis. Furthermore, the nonuniform structure of on-axis plasma could be due to current flowing on the array axis. This result contradicts the well known Rocket model of wire ablation[44], that demands that the drive current remain at the initial array radius, and that material be ablated from the wires with constant velocity, $v_{abl}$. However, quantitative comparison of experimental data to the Rocket model showed reasonable agreement (Figs. 11.9, 11.10 and 11.11). The level of agreement is clearly a function of $v_{abl}$, suggesting that this quantity is dependent upon array parameters other than, and in addition to $R_0$. Despite these issues, the Rocket model can be used to accurately estimate sparse wire array dynamics with a minimum of complexity, as has been done for about a decade.

The value of density measurements using calibrated point-projection x-ray imaging cannot be understated. The numerous results presented here have been derived from only twenty experiments, a two week campaign on the COBRA pulsed power generator. This relatively small number of shots has made a far greater contribution to our knowl-

edge of sparse wire arrays than the hundreds of previous, uncalibrated, but otherwise similar experiments using the same generator. Of secondary importance is the large amount of data per experiment that the frame number and field-of-view of the STAR system allow.

Approximately 50% of the images produced by the STAR system are not suitable for quantitative analysis because of multiple exposures. This is an unfortunate feature of the X-pinch x-ray source. Thanks to the high frame number of this diagnostic large amounts of useful data are still produced by each experiment. It is crucial that anyone analyzing these images be aware of this problem since multiple exposures are not always obvious but tend to cause serious errors.

APPENDIX A

# SAMPLE ANALYSIS PROCESS

## A.1 Coronal Plasma

The coronal plasmas surrounding the dense wire cores in the images analyzed in this thesis are described using the coordinate system shown in Fig. A.1, which is a birds-eye or top view of the wire-array. As indicated in Fig. A.1, the coronal plasma density distribution, $\rho_{cor}$, is assumed to be uniform in $\theta$ over an angle, $\theta_{cor}$, that is assumed to be greater than 180°. Coronal plasma analysis begins by selecting a portion of an edge-wire image to analyze. Typically, this means using one's best judgment as to what is "normal" coronal plasma behavior in the particular image being analyzed, and choosing the axial location to analyze, accordingly, as shown in Fig. A.2. Once the portion of the film to analyze has been determined the next step is to establish a calibration function, i.e. conversion of the 8-bit exposure levels of the film scan to tungsten (W) areal density (/cm$^2$). In order to make the calibration as accurate as possible the location of the area of the film to be analyzed is taken into consideration. This means considering the local "zero-mass" level, as shown in Fig. A.2, and how global (background) exposure varies in the axial direction. The calibration process is described in detail in Chapter 6. A sample calibration function is shown in Fig. A.3. Once a calibration curve has been established, quantitative processing can begin. Coronal plasma density, $n_{cp}$, varies with axial ($z$) position and distance from the center of the dense wire core, $r_{cp}$ (Fig. A.1). The length scales over which $n_{cp}$ varies in the $z$ and $r_{cp}$ directions are about 20$\mu$m (10 pixels) and 2$\mu$m (1 pixel), respectively. Consequently, the radial variation of $n_{cp}$ is analyzed with much higher accuracy than its axial variation. This is implemented by analyzing the radial variation of film exposure, with single-pixel accuracy, at

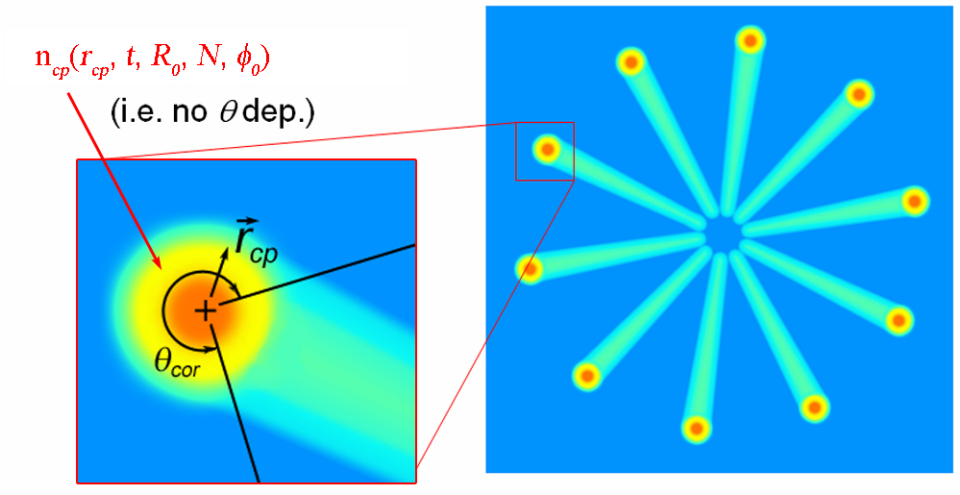


Figure A.1: Axial view of the wire-array and the coordinate system used to describe the coronal plasma.

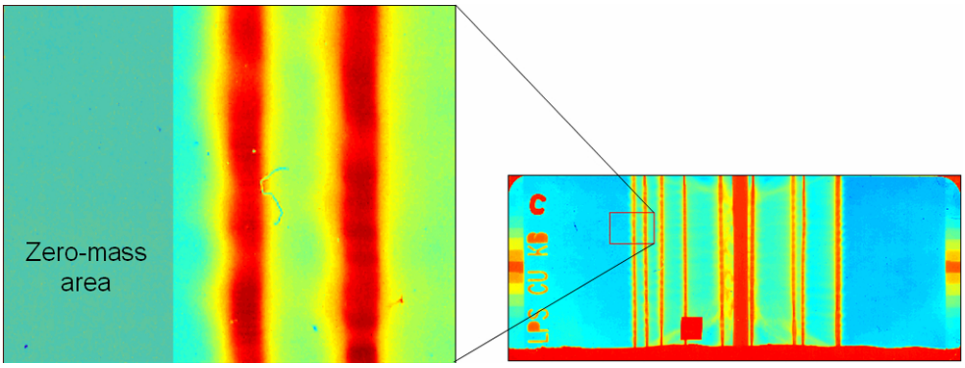


Figure A.2: Sample false-colored film scan with inset of the left edge-wire selection for coronal plasma analysis. The "zero-mass" to the left in the inset is used to establish the level of film exposure that corresponds to empty space or "mass-free" regions on the film.

discrete axial positions ($z_0$ in Fig. A.4) separated in the axial direction by on the order of 20$\mu$m. Typically, some averaging is done in the axial direction ($dz$ in Fig. A.4) in order to compensate for film imperfections from dust, scratches, etc. A raw, 8-bit exposure line-out, like the blue curve in Fig. A.4, is multiplied by its specific calibration curve (Fig. A.3) to produce a calibrated, areal density, radial line-out, as shown in Fig. A.5. When analyzing coronal plasma (or injected plasma) the curve in Fig. A.5 is

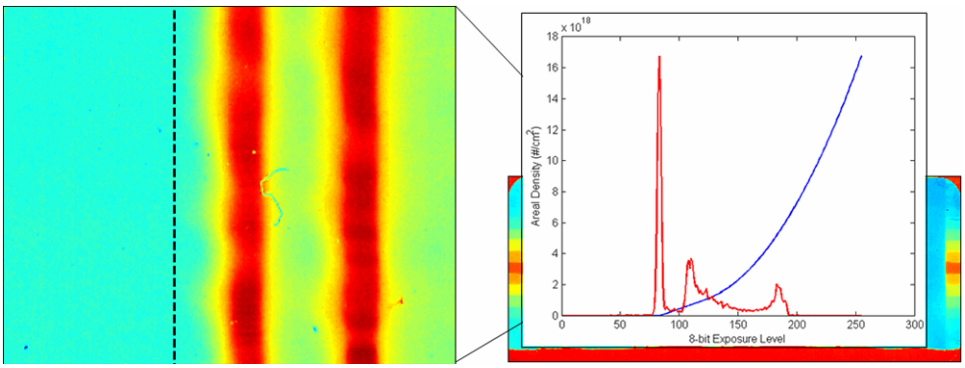


Figure A.3: Sample calibration curve (blue line) for the inset shown in Figures A.2-A.6. The red curve is the corresponding image histogram of the same inset (with arbitrary units). Note that the point where the calibration curve departs from zero coincides with the low density or "mass-free" peak of the image histogram.

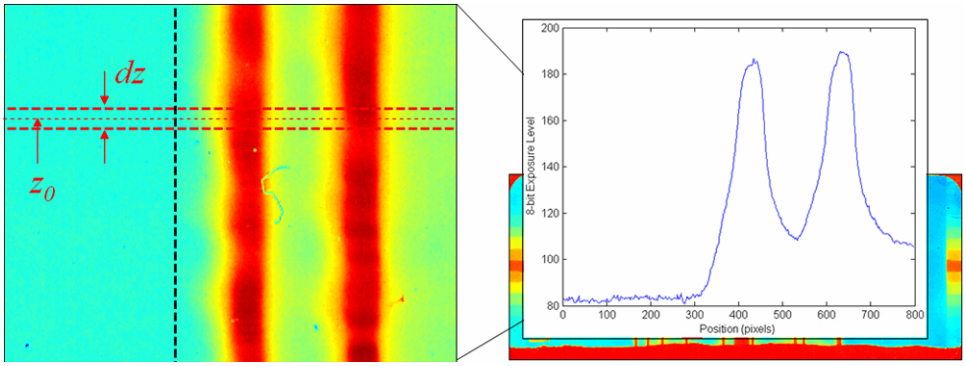


Figure A.4: Example of radial line-out processing. The blue curve at the right shows the average film exposure level (on an 8-bit scale) from $z_0 - \frac{dz}{2}$ to $z_0 + \frac{dz}{2}$ as a function of radial (horizontal) film position.

shifted along the horizontal axis so that the zero of position coincides with the center (as determined by full-width half-maximum) of the dense wire core. The units of the horizontal axis are also converted from pixels to microns, as shown in Fig. A.6. A radial, areal density line-out of coronal plasma that has been prepared for analysis, like the curve to the left of zero in the graph in Fig. A.6, is converted into volume density using cylindrical Abel inversion. For the data presented in Chapter 11, this was done by a MatLAB function, which is given in Appendix F. A sample inversion is shown in Fig.

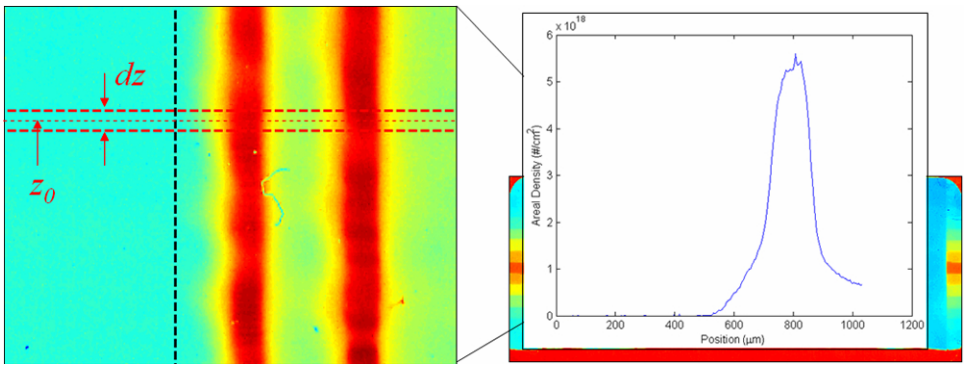


Figure A.5: Calibrated areal density line-out. The blue curve at right was generated by multiplying the raw, 8-bit line-out in A.4 by the calibration curve in A.3. Note that the line-out domain has also been trimmed so that data from wires other than the edge-wire are not included.

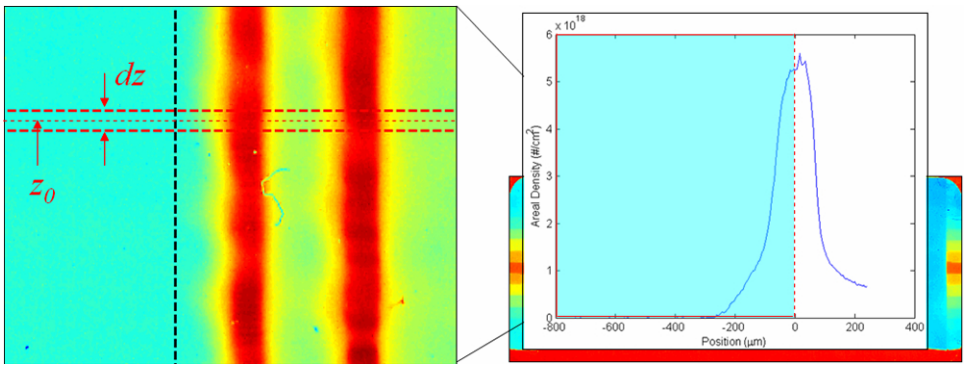


Figure A.6: Example of a radial line-out that is ready for analysis.

A.7 for the curve in Fig. A.6.

Once the coronal plasma areal line-out has been converted into a volume density curve, one would ideally fit a simple function to the experimental data. This could allow one to describe the variation of the density distribution using one or two fit coefficients. If the experimental data allows such a fit to be made, one could then describe how the fit coefficients vary with axial position and/or time. This would allow the temporal and spatial variation of the coronal plasma density to be described in a simple, compact manner. Unfortunately, no simple function exists that fits over the entire domain of the Abel inversion shown in Fig. A.7. Hence, the domain of the experimental data

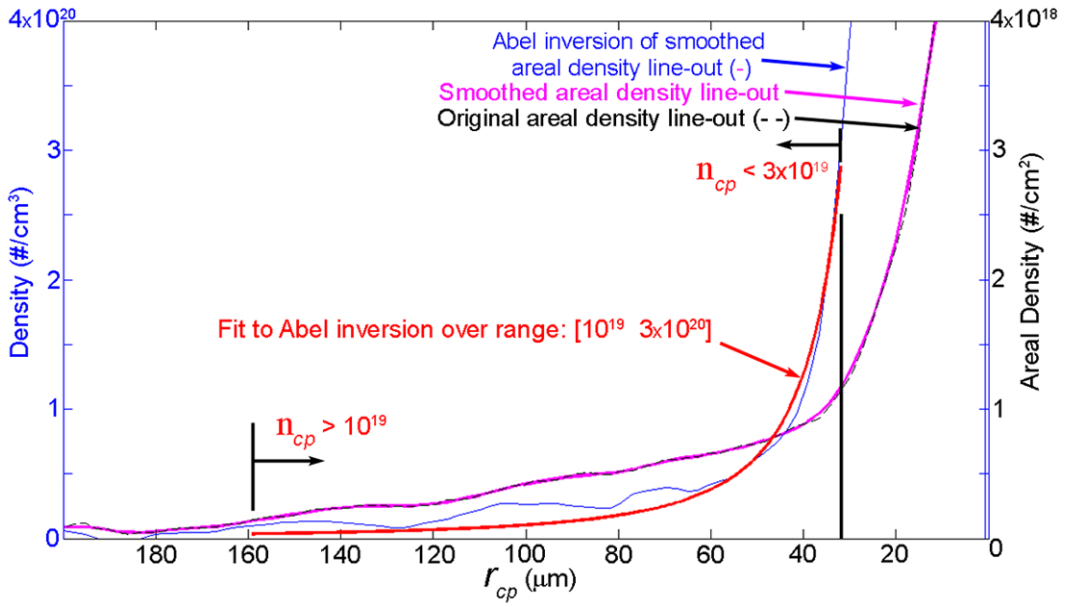


Figure A.7: Sample Abel inversion of coronal plasma areal density line-out. The dashed black curve is the original areal density line-out, similar to the blue curves in Figures A.5 and A.6. The solid magenta curve is a smoothed version of the dashed black curve. The solid blue curve is the Abel inversion of the magenta curve. The red curve is a fit ($1/r^2$) to the Abel inversion over the indicated density range.

that is used for fitting must be restricted if a simple fit function, $1/r^2$ in this case, is to be used. In this analysis, Abel inversion data for curve fitting was bounded by range. Specifically, the data points in an Abel inversion that were within a density range of $10^{19}$ to $3\times10^{20}$/cm$^3$ were used for curve fitting purposes, as indicated by the range of the red curve in Fig. A.7.

## A.2 Injected Plasma

The manner in which images of injected plasma are prepared for analysis is identical to the description of coronal plasma image preparation given in the previous section. The only differences that arise come from the assumed spatial symmetry (cylindrical, in the

case of the coronal plasma), and the bounds used for curve fitting.

The spatial variation of the injected plasma stream does not have an obvious form, unlike the cylindrical system of the coronal plasma. The variation in injected plasma areal density along the stream's radial trajectory, $\sigma_{ip}(r_{ip})$, can be measured with ease. In order to convert this measurement into a volume density ($n_{ip}(r_{ip})$), one must assume a form for the stream's density variation across its width, $w_s$. For instance, if one assumes that the stream density is uniform across its width, then the volume density would be found by dividing the areal density measurement by the stream width (i.e. $n_{ip} = \sigma_{ip}/w_s$). However, even in this simple example, one needs to estimate the stream width, which cannot be done without ambiguity using side-on images like the ones presented here (a bird's-eye view of the injected plasma would give the best measurement of $w_s$). Consequently, the exact value of injection stream volume density is considered to be proportional to (within a factor of 2 to 5) the estimates given here. The amount of mass in the injected plasma streams can be estimated without ambiguity by using the areal density measurements of the injected plasma.

The areal density of injected plasma can be measured with good accuracy within a few millimeters of one of the side-on wires. In all cases, the areal density of injected plasma scales as $1/r_{ip}$, as one moves from the center of the dense core toward the array axis. Clearly, because of the singularity at $r_{ip} = 0$, this scaling is not appropriate for all values of $r_{ip}$. To avoid this singularity, and issues related to the maximum detectable areal density of the diagnostic, the lower bound for curve fitting is set at $\sigma_{ip} = 10^{18}/\text{cm}^2$. A sample fit to experimental data is shown in Fig. A.8.

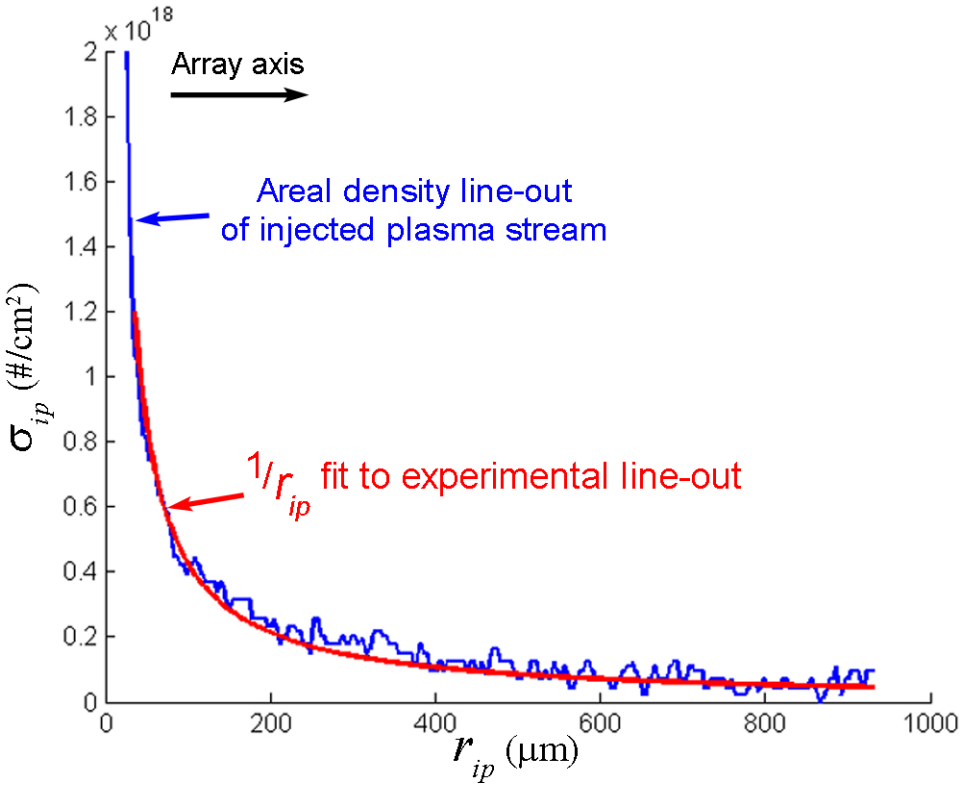


Figure A.8: Sample $1/r_{ip}$ fit to injected plasma stream areal density line-out.

APPENDIX B

# MONOCHROMATIC IMAGING

## B.1 Intorduction

Simple point-projection imaging becomes impractical when a line-of-sight from the source through the object to photo-detector is not usable due to the object's emitting an intense x-ray flux that will pass through the filter or ballistic debris that will destroy the filter and film. These problematic circumstances call for monochromatic x-ray imaging. This system uses a spherically bent crystal is used to reflect (Bragg reflection) and focus a narrow spectral band of x-ray line-radiation (or possibly intense continuum), producing a 2-D shadow image of the target object. This reflection enables an image to be captured while avoiding any line-of-sight from object to detector. The object being imaged must have negligible radiation in the band that will be reflected by the crystal and reach the detector.

An extraordinary monochromatic x-ray imaging system is used on the Z facility at Sandia National Laboratories. This system uses a laser-induced plasma for its x-ray source. Numerous publications can be found that describe this system and the basic principles of monochromatic imaging using spherically bent crystals [55].

While simple in concept this system offers many challenges. First, a suitable characteristic x-ray line source must be found. Next, this line-radiation must be produced at an intensity that is at least comparable to the x-ray intensity emitted by the target object at this wavelength. Additionally, the size of this source should be 0.1-1.0mm. Finally, high quality spherically bent crystals must be manufactured or purchased along with the necessary x-ray filters and detector systems.

In the next section we describe the theoretical requirements for possible monochromatic x-ray sources. Section three describes x-ray optical components such as mirrors and filters. Section four outlines the basic experimental setup. In section five experimental results are presented. Finally, conclusions and discussion are presented.

## B.2 Theoretical Requirements

### B.2.1 Wavelength Considerations

The concept of monochromatic x-ray imaging of wire-array Z-pinches using an X-pinch as the x-ray source was first introduced more than 10 years ago by Pikuz et al. [56]. The system is based on Rowland circle optics. A spherically bent crystal, with radius of curvature $R_c$, is used as an x-ray mirror and focusing element. Schematically, a circle with diameter of $R_c$ (or radius $R_c/2 = R_r$) is drawn such that it tangentially intersects the arc of the spherically bent crystal at the reflection point for x-rays of a specific wavelength, as shown in Fig. B.1; this is referred to as the Rowland circle. A point x-ray source (Fig. B.1A) is placed on the Rowland circle at a position close to normal incidence ($\theta \approx 90^0$) for Bragg reflection of the wavelength of interest. An object to be imaged is placed in the line-of-sight between the mirror and x-ray source such that it lies between the x-ray source and the center of the Rowland circle, i.e. Fig. B.1, item E. Finally, a photographic film (Fig. B.1, item F) is placed in the reflected line of sight (Fig. B.1, item D) at a position, $b$ given by:

$$\frac{1}{a} + \frac{1}{b} = \frac{1}{R_r} \tag{B.1}$$

where $a$ is the distance from the object to crystal and $R_r$ is the radius of the Rowland circle.

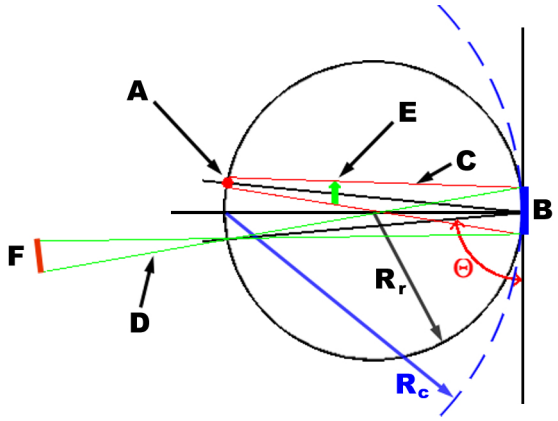


Figure B.1: Rowland circle imaging system. A: x-ray source, B: spherically bent crystal with radius of curvature $R_c$, C: incident rays, D: reflected rays, E: object to be imaged, F: photographic film.

For this system to produce an image focused in two dimensions the angle of incidence, $\theta$, must be close to 90°. More specifically, the angle of incidence should not be less than 70° and for practical reasons should not be greater than 86°, as shown in [56]. The Bragg condition for constructive refraction from a crystal states that:

$$n\lambda = 2d\sin\theta \tag{B.2}$$

where $n$ is the order of reflection ($\geq$1), $\lambda$ is the wavelength of incident radiation, $d$ is the lattice spacing of the crystal and $\theta$ is the angle of incidence. Substitution of the range of acceptable angles-of-incidence ($70-86°$) yields the range of $\lambda$ as a function of $n$ and $d$:

$$\begin{aligned} \frac{2d}{n}\sin 70^\circ \leq \lambda \leq \frac{2d}{n}\sin 86^\circ \\ \frac{2d}{n}\cdot 0.94 \leq \lambda \leq \frac{2d}{n}\cdot 0.998 \end{aligned} \tag{B.3}$$

For this application the crystal of choice is mica. High quality occurs naturally and is relatively abundant and inexpensive. Its simple structure allows the orientation of the crystal planes to be easily determined. Finally, its $2d$ lattice spacing of about 19.94Å is highly compatible with the wavelengths of line radiation that can be obtained from

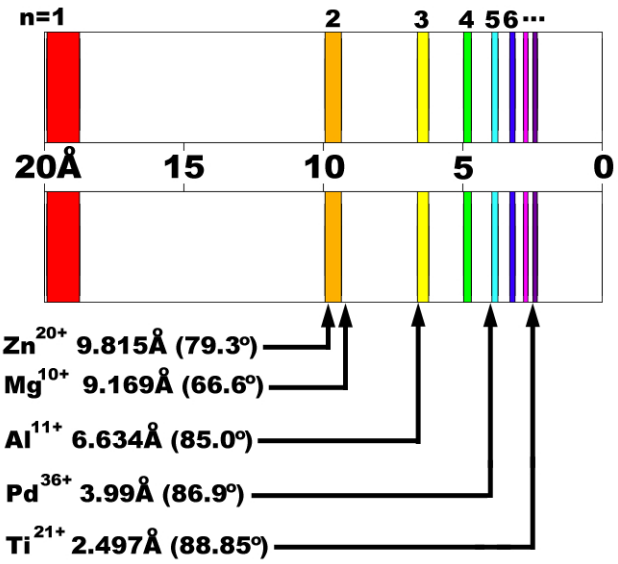


Figure B.2: Spectral bands of possible use for monochromatic imaging using mica crystals. Several characteristic x-ray lines that fall in or around these bands are listed at the bottom of the figure.

X-pinches. Substitution of the mica lattice spacing into Eqn. B.3 yields:

$$\frac{18.74}{n} \leq \lambda \leq \frac{19.90}{n} \tag{B.4}$$

Hence, for each order of reflection, $n$, Eqn. B.4 describes a narrow range of practical wavelengths for monochromatic imaging. These bands are shown graphically in Fig. B.2 along with the characteristic lines of several materials that could be used as x-ray sources.

### B.2.2 Spherically-Bent Crystal Imaging

In many respects monochromatic x-ray imaging using a spherically bent crystal and a quasi-point x-ray source is analogous to a visible light imaging system that uses a spherical mirror or even a simple lens for focusing. However, there are crucial differences that are quite subtle and complex.

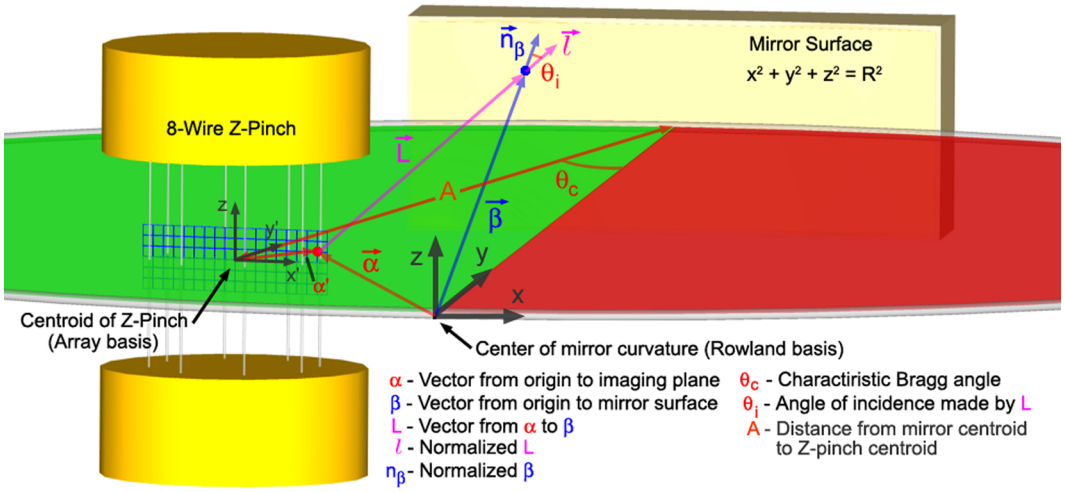


Figure B.3: Vector analysis of Bragg condition.

Consider the system illustrated in Fig. B.3. X-rays emitted from some point in the object to be imaged, $\vec{\alpha}$, will be reflected from the spherically bent crystal only if their angle of incidence satisfies the Bragg condition of Eqn. B.2. (Note that in Fig. B.3 the angle $\theta_i$ is measured from the mirror's normal, hence $n\lambda = 2d\cos\theta$.) Our goal is to determine where on the mirror's surface the Bragg condition is satisfied for a given point in the object to be imaged. More specifically, we will derive the wavelength(s) that satisfy the Bragg condition at point $\beta$ on the mirror surface for a ray emitted from point $\alpha'$ in the object to be imaged. Note that the primed quantities are those referred to the object or array basis, and unprimed quantities are those in the Rowland basis, as illustrated in Fig. B.3. The first step is to refer the object basis to the Rowland basis. This is done with a linear displacement and a rotation about the z-axis. Specifically:

$$\begin{aligned}
\vec{\alpha}' &= a'_x e'_x + a'_y e'_y + a'_z e'_z \\
\vec{\alpha} &= a_x e_x + a_y e_y + a_z e_z \\
a_x &= a'_x \cos\theta_c + (a'_y - A)\sin\theta_c \qquad \text{(B.5)} \\
a_y &= (a'_y - A)\cos\theta_c - a'_x \sin\theta_c + R \qquad \text{(B.6)}
\end{aligned}$$

$$a_z = a'_z \tag{B.7}$$

where $A$ is the distance from the mirror centroid to the origin of the object basis and $R$ is the radius of curvature of the mirror, as shown in Fig. B.3. The point of interest on the mirror surface, $\beta$, is referenced by the vector, $\vec{\beta}$, from the origin of the Rowland basis to the point $\beta$. The $y$ component of $\vec{\beta}$ is eliminated using the equation for the mirror's surface, upon which $\beta$ always lies:

$$\begin{aligned} \vec{\beta} &= b_x e_x + b_y e_y + b_z e_z \\ \left|\vec{\beta}\right|^2 &= R^2 = b_x^2 + b_y^2 + b_z^2 \qquad \text{(B.8)} \\ b_y &= R\sqrt{1 - \frac{b_x^2 + b_z^2}{R^2}} \qquad \text{(B.9)} \end{aligned}$$

The normalization of $\vec{\beta}$ is the mirror's outward normal vector, $\vec{n}_\beta$ in its usual sense:

$$\vec{n}_\beta = \frac{\vec{\beta}}{R} \tag{B.10}$$

Next, we define the incident vector, $\vec{L}$, and its normalization, $\vec{l}$:

$$\begin{aligned} \vec{L} &= \vec{\beta} - \vec{\alpha} \qquad \text{(B.11)} \\ \vec{l} &= \frac{\vec{\beta} - \vec{\alpha}}{\left|\vec{\beta} - \vec{\alpha}\right|} \qquad \text{(B.12)} \end{aligned}$$

Taking the inner product of $\vec{n}_\beta$ and $\vec{l}$ gives:

$$\begin{aligned} \vec{n}_\beta \cdot \vec{l} &= \frac{\vec{\beta}\cdot\left(\vec{\beta} - \vec{\alpha}\right)}{R\left|\vec{\beta} - \vec{\alpha}\right|} = \frac{R^2 - \vec{\beta}\cdot\vec{\alpha}}{R\left|\vec{\beta} - \vec{\alpha}\right|} \qquad \text{(B.13)} \\ &= \left|\vec{n}_\beta\right|\left|\vec{l}\right|\cos\theta_i = \cos\theta_i \qquad \text{(B.14)} \end{aligned}$$

We now substitute the Bragg condition, $\cos\theta_i = \frac{n\lambda_n}{2d}$ into Eqn B.13 to find $\lambda_n$:

$$\lambda_n = \frac{2d}{n}\frac{R^2 - \vec{\beta}\cdot\vec{\alpha}}{R\left|\vec{\beta} - \vec{\alpha}\right|} \tag{B.15}$$

This equation can be used to gain an understanding of the spectral complications associated with monochromatic x-ray imaging. Fig. B.4 is a sample mapping produced by

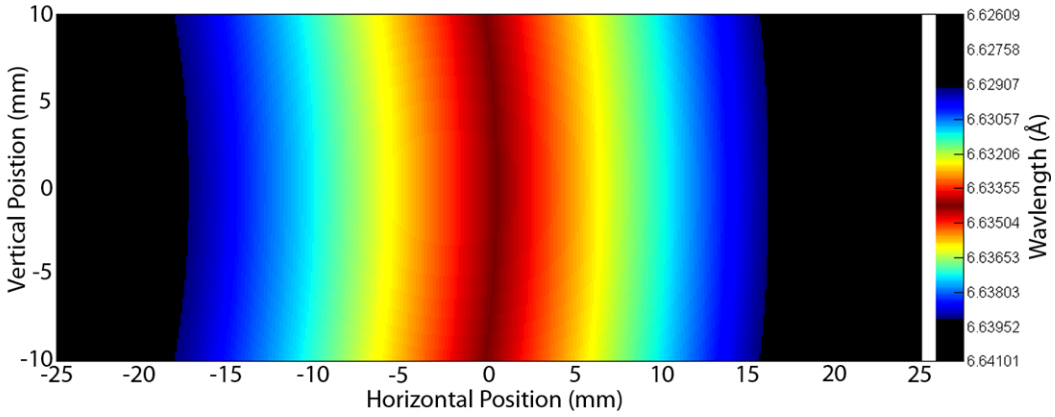


Figure B.4: Sample spectral mapping of a spherically bent crystal (with dimensions of 50mm x 20mm) using B.15. The mapping was generated using the following parameters: $\vec{\alpha}' = (2.5mm, 0, 0)$, $R = 182mm$, $A = 160mm$, $2d = 19.94$Å, $n = 3$, and $\theta_c = 4.37^o$. The color bands are 10mÅ wide and are centered on $\lambda = 6.6343$Å, as shown in the legend to the right of the map.

equation B.15 and illustrates how much of the mirror's surface participates in point-to-point focusing for a given point ($\vec{\alpha}$) in the object to be imaged. By contrast, the entire surface of the mirror would contribute to image formation in a visible light system.

Depending on the spectral width of the line radiation being used with a monochromatic imaging system, the percentage of the spherical mirror contributing to image formation of any given point could be very small. Hence, the average mirror defect size and frequency become very important. Furthermore, the small reflecting area combined with the inherent inefficiency of Bragg reflection emphasize the importance of source intensity.

### B.2.3 X-ray Source Considerations

The spatial resolution of a point-projection imaging system is generally taken to be roughly equivalent to the source size. At first glance, it might seem that this would be

the case in a monochromatic x-ray imaging system that uses a point x-ray source. However, this is not so. A common mistake is to refer to the type of monochromatic x-ray imaging presented here (Rowland circle imaging), as "monochromatic x-ray backlighting". While one could make the argument that the object to be imaged is indeed being backlit, this description is very misleading. For instance, unlike point-projection, in the Rowland system the x-ray source can be placed literally anywhere without affecting the magnification of the system.

The most important difference between Rowland circle imaging and point-projection is that a point-like source will generally result in very poor resolution. In the previous section we saw that the active area of the mirror's surface can be quite small for any given point in the object to be imaged. The situation becomes much more complicated when a finite source size is imposed. The derivation in the previous section allowed radiation to be emitted in any direction from the given point, $\vec{\alpha}$. This is not possible with a finite backlighting source. In the extreme limit of a true point-source, a proportionally point-like area of the mirror contributes to image formation. Hence, if a mirror defect size is on the order of the source size then the resulting image is more of a mapping of mirror defects than an image of the object. For practical geometries with an X-pinch x-ray source, a source size of 1-2mm is acceptable. The upper limit of source size is determined by the properties of the X-pinch. Figure B.5 demonstrates how source size effects combine with spectral limitations. The example in Fig. B.5 illustrates the extreme importance of careful mirror alignment, measurements of incident wavelength, $\lambda$, and measurements of the lattice spacing of the crystal. These mapping were generated by the "crystal_map" function given in Appendix F.2. The projection of the source outline through a field point $\vec{\alpha}$ onto the mirror surface follows a simple relationship. Take the outline of the source to be a set of points described in the array basis of B.3 by the vector set $[\vec{s'}]$. These points are referred to the Rowland basis by the transformation

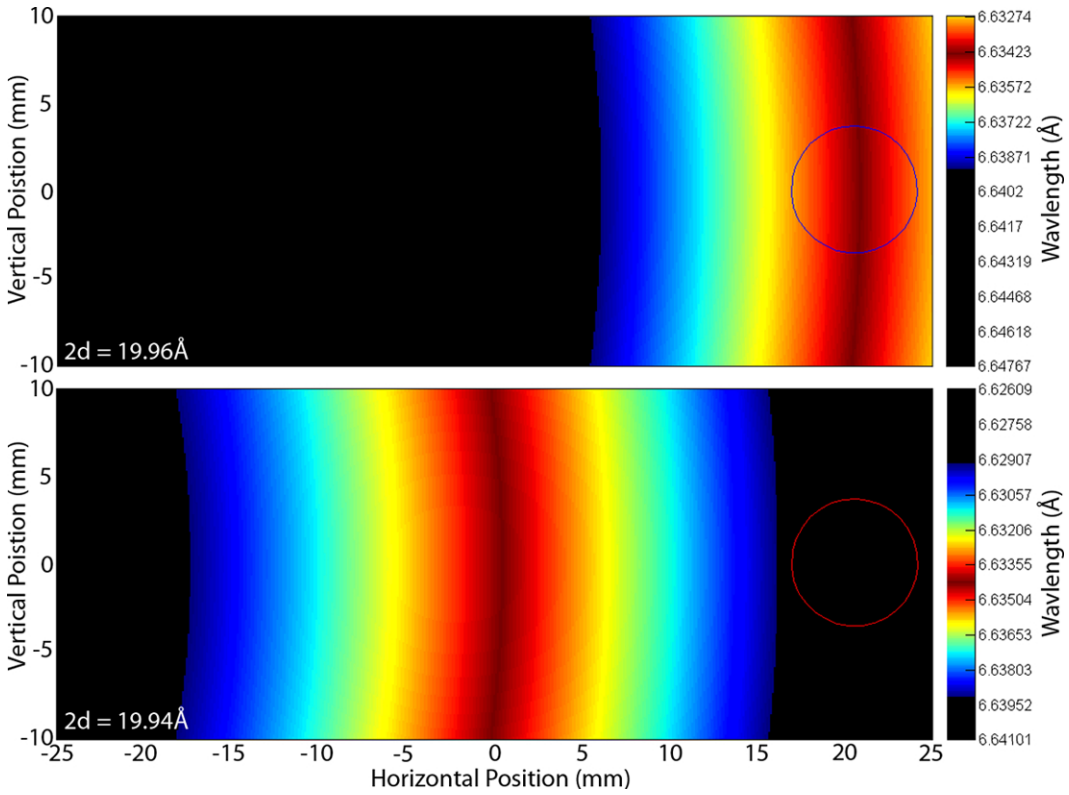


Figure B.5: Sample projections of source size. These mappings are for the same field point, $\vec{\alpha}$, and other parameters, other than $2d$, as used to generate Fig. B.4. The red and blue circles contain the portions of the crystal surface that can be illuminated by a source 1mm in diameter located on the Rowland circle in-line with the center of the object and the center of the mirror. The upper mapping is for $2d = 19.96$Åand the lower is for $2d = 19.94$Å. Note that a small error in lattice spacing can result in complete failure of the imaging system. The Matlab functions used to generate these mappings are given in Appendix F.

given in Eqn. B.5. Let the transformed points be represented by $[\vec{s}]$. The vectors from each point on the source outline, $[\vec{\beta}]$, through $\vec{\alpha}$ are then given by $[\vec{\beta}] = \vec{\alpha} - [\vec{s}]$. The vector sets $[\vec{\beta}]$ and $[\vec{s}]$ are then converted into 3-D cartesian line equations,

$$L_n(t) = \vec{s}_n + t\vec{\beta}_n, \tag{B.16}$$

Where $L_n$ defines all points in 3-D space that lie on the line which passes through source

point $\vec{s_n}$ and the object point $\vec{\alpha}$. The mirror's surface is described by

$$x^2 + y^2 + z^2 = R^2 \tag{B.17}$$

Hence, the line $L_n$ intersects the mirror surface when:

$$\beta_n^2 t^2 + 2\vec{\beta_n} \cdot \vec{s_n} t + s_n^2 - R^2 = 0 \tag{B.18}$$

Solving Eqn. B.18 for $t$ and substituting this value into B.16 gives the point(s) of intersection and maps the projection of the source outline onto the mirror surface.

As previously mentioned, the x-ray source need not lie on the Rowland circle. The source can be moved inward (towards the mirror) to compensate for small source size. However, moving the source closer to the object has the negative effect of decreasing the field-of-view. Similarly, one can move the source outside the Rowland circle for improved field-of-view at the cost of intensity.

## B.3 X-pinch Source Characterization

### B.3.1 Experimental Setup

Experiments were performed on the COBRA pulsed power generator to determine which X-pinch materials would produce a suitable line radiation source for monochromatic x-ray imaging using mica crystals. The load configuration in these experiments consisted of a "standard" 8-wire (12.5$\mu$m diameter wires), 16mm diameter, 20mm tall tungsten wire array, and two return current X-pinches in parallel with two copper return current posts. Each X-pinch was monitored with a silicon photodiode sensitive to soft x-rays, a convex mica spectrograph, and a pinhole camera, as shown in Fig. B.6. The

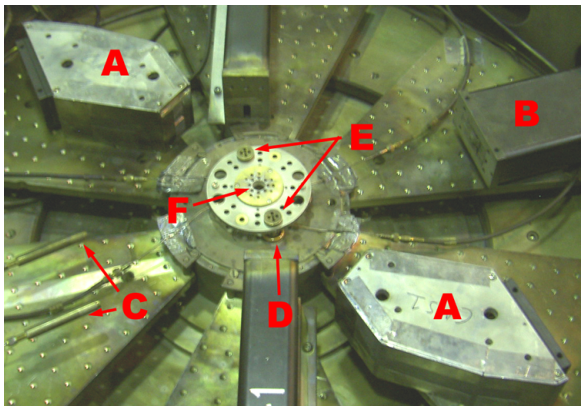


Figure B.6: Experimental setup for X-pinch line source characterization. A - convex mica spectrograph, B - pinhole camera, C - Si photodiodes, D - Rogowski coil, E - return current X-pinches, F - tungsten wire-array.

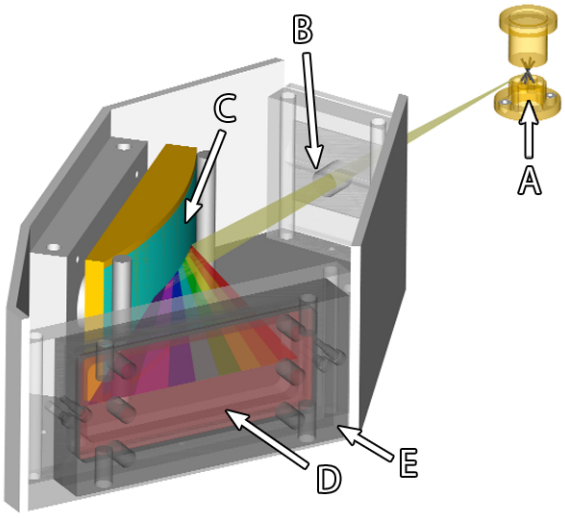


Figure B.7: Convex mica spectrograph for characterization experiments. A - X-pinch, B - 150$\mu$m slit, C - cylindrically bent mica crystal (R = 152mm), D - photographic film, E - film cassette.

details of the convex spectrographs are shown in Fig. B.7. The spectrographs were designed to record a wavelength range of 3-10Å in first order. The radiation reaching the photographic films was filtered with 4$\mu$m polypropylene in most cases. The mica crystal was about 100mm long, 50mm tall, and was spherically bent with a radius of 152mm (6.0in). The materials examined in these experiments were: aluminum (Al), nickel

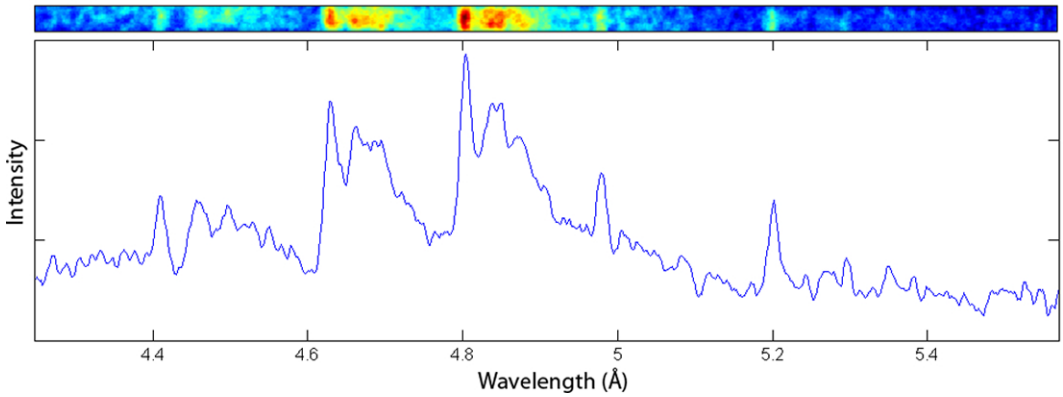


Figure B.8: Sample Mo spectrum from COBRA experiment number 477.

(Ni), zinc (Zn), palladium (Pd), magnesium (Mg) and molybdenum (Mo). The purpose of these experiments was to determine if these materials (in the return current X-pinch configuration) would radiate with significant intensity at wavelengths compatible with monochromatic imaging using mica crystals.

### B.3.2 First Order Spectra

#### Molybdenum

Molybdenum was included in these experiments for control purposes. The characteristics of Mo X-pinches are well known which makes it an ideal baseline reference for other materials. While the Mo X-pinch certainly produces intense line radiation sources it is unsuitable for monochromatic imaging with mica crystals. This is because the wavelengths of Mo line sources do not fall in any of the bands shown in Fig. B.2. A sample spectrum, predominately L-shell lines plus free-bound continuum, from a Mo X-pinch is shown in Fig. B.8.

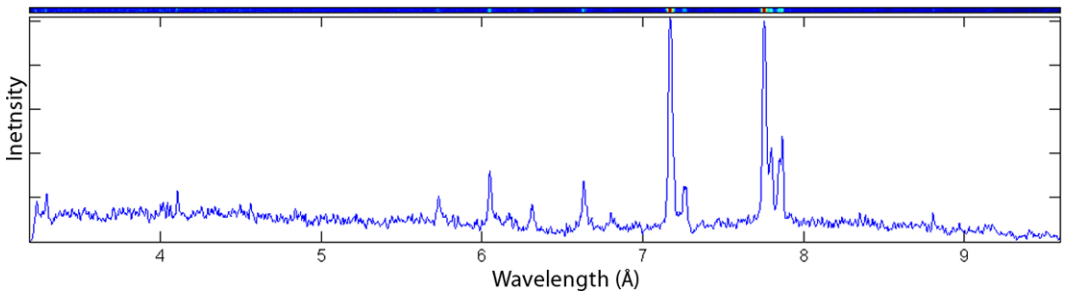


Figure B.9: Sample Al spectrum from COBRA experiment number 484.

**Palladium**

The palladium line of interest to these experiments was the $Pd^{36+}$ 3.99Å (3.11keV) in fifth order reflection. The benefit to this line is that it is much harder than most under examination and hence a harder filter can be used. This could decrease background radiation and ease x-ray filter construction. While these benefits are appealing this material suffers from several negative aspects. First, availability of Pd wire is poor. This severely limits the possible configurations of x-pinches that can be assembled from Pd wire. Specifically, it is difficult to assemble a Pd x-pinch with low enough mass per unit length to produce an intense x-ray burst in the desired wavelength. This was seen repeatedly from Pd backlighters in these experiments and a Pd spectrum was never successfully captured in first order reflection.

**Aluminum**

Perhaps the most promising material for monochromatic imaging using X-pinch sources is Aluminum. This is because it is known to produce intense line radiation and it is widely available. The 6.6343Å (1.87keV) line is a He-like line of Al. Unfortunately, this line is not the most intense one in the Al X-pinch spectrum. A sample Al spectrum recorded is shown in Fig. B.9.

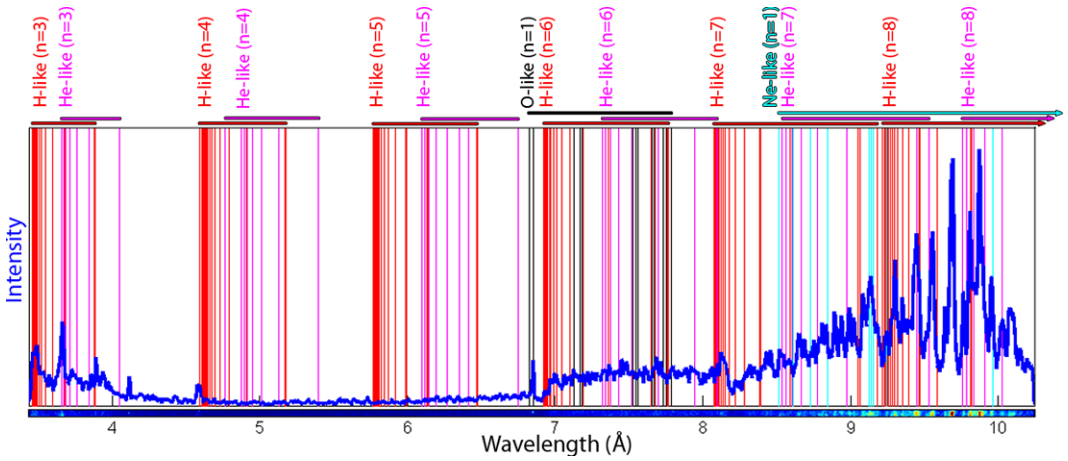


Figure B.10: Sample Ni spectrum from COBRA experiment number 485.

### Nickel

The Ni line of interest is He-like, 1.588Å, and is much shorter than the materials presented thus far. This makes analysis of the convex spectrograph data more complicated since the line appears in many orders of reflection, as shown in Fig. B.10. From the convex spectrograph it is difficult to say with what intensity the 1.588Å will be reflected in the twelfth order as required for monochromatic imaging with mica. More data should be collected that focuses on shorter wavelengths and uses a harder x-ray filter. Further experiments with Ni were not performed in this research due to its poor availability.

### Zinc

The Zn lines of interest are 9.815Å Ne-like and 9.95Å F-like. In experiment, the Zn X-pinch has found to have many lines in the neighborhood of 9.8-10.0Å, as shown in Fig. B.11. This eases the requirements of extremely precise alignment but demands a very soft filter due to the long wavelength. Like most of the materials examined here, fine Zn wire is not available in a wide range of sizes.

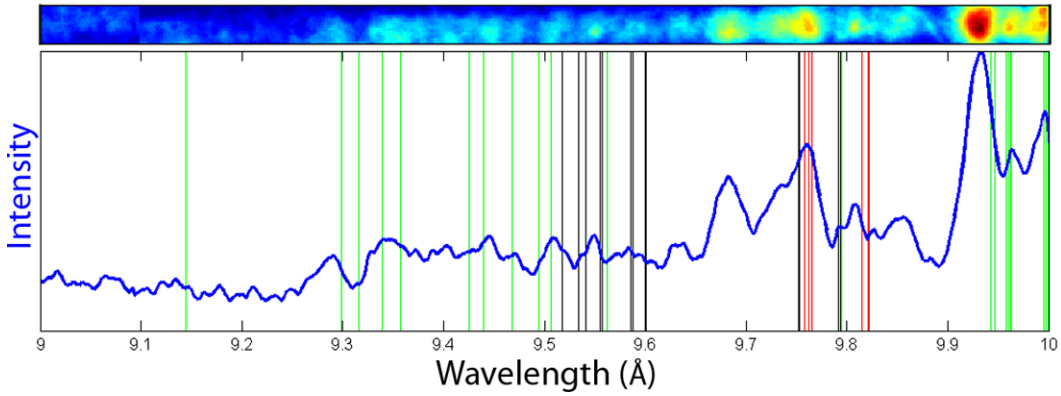


Figure B.11: Sample Zn spectrum from COBRA experiment number 490. Red lines are Ne-like, green are F-like, and black are O-like. All line locations are first order.

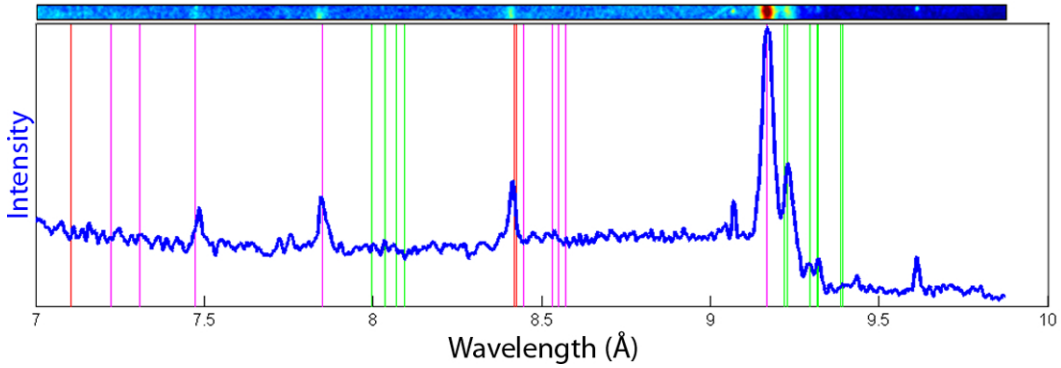


Figure B.12: Sample Mg spectrum from COBRA experiment number 492. Red lines are H-like, magenta are He-like, and green are Li-like. All line locations are first order.

**Magnesium**

Magnesium X-pinches demonstrated the brightest source in the necessary spectral line (9.168Å) for monochromatic imaging. Unfortunately, the angle of incidence associated with this wavelength is quite large and would result in poor 2-D focusing. Furthermore, there is essentially zero availability of fine Mg wire; the material used in this study came from LPS stock that was over a decade old. A sample Mg spectrum is shown in Fig. B.12.

### B.3.3 First Order Results

Most of the materials examined in this study proved unsuitable for various reasons. Foremost, Al and Mo were the only materials examined that are available in a wide range of fine wire sizes. Since the ability to vary the timing of the X-pinch is proportional to one's ability to vary its mass per unit length, this poses a serious limitation. Based on material availability and first order spectra, Al and Zn appear to be the only materials that are worth examining further. The list of potential source materials could expand if it were found that sufficient hard radiation is produced by Ni or Pd X-pinches. It is possible that these short wavelengths would be reflected much more efficiently in high orders. Furthermore, a harder source would allow the use of protective filters and shields in front of detectors and crystals which would be a tremendous advantage over the 1-2keV sources of Al, Zn and Mg.

## B.4 Sample Images

### B.4.1 Static Objects

As a preliminary test, static objects were imaged. These tests allowed us to determine the quality of our homemade bent crystals and to determine how well the source wavelengths of interest would reflect in the order necessary for imaging. These tests used the same load configuration as the first order source characterizing experiments. An image of a copper grid is shown in Fig. B.13. The results from static imaging indicated that crystal quality was not good. Approximately one year was committed to testing new ways to manufacture the spherically bent mica crystals that might yield improved quality. Eventually, a process was developed that produced mirrors with sufficient qual-

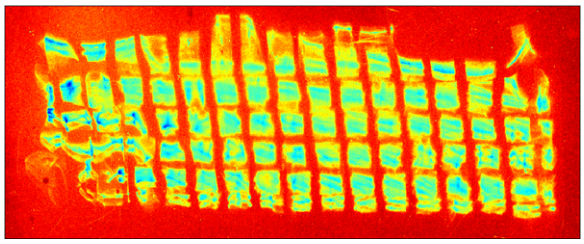

Figure B.13: Sample image of a static object. Shown here is a copper mesh with spacing of about 2mm. This image is from Al X-pinch source.

ity to be used for imaging. This process is described in Appendix C. On the positive side, static images showed that source intensity (from Zn and probably Al) was more than adequate.

### B.4.2 Wire-Array Images

The imaging of wire-arrays proved to be far more difficult than static objects. The increased difficulty stems from alignment issues. When imaging static objects, one is free to manipulate the position of the object, mirror and detector independently of each other relative to the fixed location of the X-pinch source. When imaging a wire-array with an X-pinch source there is no freedom in the positioning of each element if the X-pinch is to lie on the Rowland circle. Collimation and aperaturing also become challenging when one must avoid shorting the anode and cathode of the experiment.

The extreme difficulty of system alignment resulted in very few successful experiments. Of the two materials examined, Al and Zn, only Zn X-pinches were successful. As previously mentioned, the success of Zn over Al is attributed to the density of Zn lines in the neighborhood of 9.8Å, which eases the strict alignment requirements. A sample monochromatic image of a 16-wire W array using a Zn backlighter is shown in Fig. B.14. Note that the image quality shown in Fig. B.14 is still lacking due to mirror

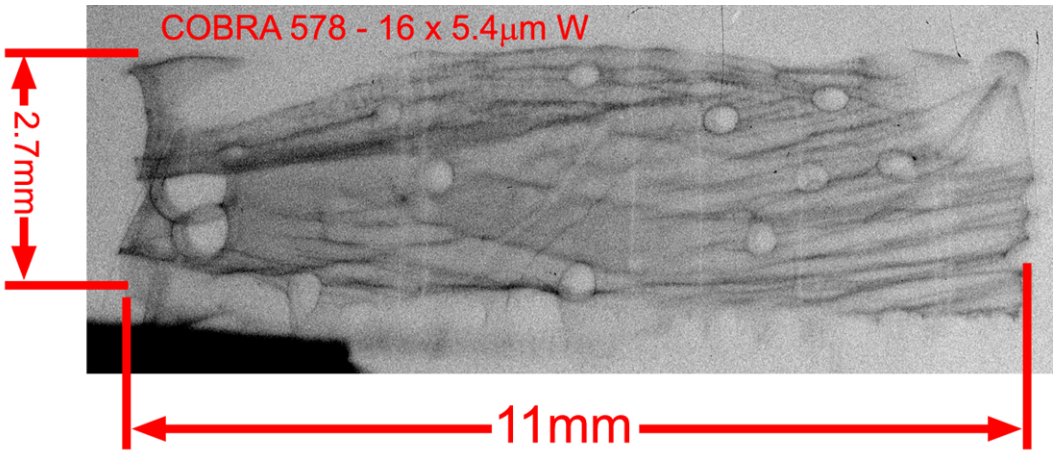


Figure B.14: Monochromatic image of a 16-wire, 16mm diameter W array. The x-ray source for this image was a 4-wire Zn X-pinch.

imperfections, as indicated by the bubbles and streaks. The imperfections on the mirror surface that cause these aberrations do not manifest themselves under visible light, i.e. they are only detected with x-ray imaging. Hence, mirror surface characterization by x-rays is important.

The imaging experiments that were successful were the result of painstaking system alignment that usually took several hours. This rather lengthy procedure could be drastically shortened, and made more accurate, by developing a rigid setup dedicated to this diagnostic. This was not done in these experiments because they were of a preliminary nature. Future efforts would greatly benefit from such an investment.

## B.5 Conclusions

The addition of a high resolution monochromatic x-ray imaging system to the COBRA diagnostic suite would greatly expand our present radiographic capabilities. Such a system would allow the investigation of wire-array ablation and implosion dynamics in

arrays that are intended, and allowed, to radiate over the 100ev-10keV x-ray spectral range. These data would be an excellent addition to the research done thus far with point-projection x-ray imaging.

While the results from initial monochromatic x-ray imaging experiments are largely pessimistic, many improvements can be made from the lessons learned here that could enable a successful system in the future. These lessons are a result of both experimental and analytic examination of monochromatic imaging systems using an X-pinch x-ray source.

First off, one cannot overstate the importance of determining the lattice spacing of the crystal with utmost accuracy. This is particularly true for mica since its spacing has a large natural variance. As shown in Fig. B.5, an error in $2d$ of only a few thousandths of an angstrom can result in complete failure of the imaging system. Lattice spacing can be roughly determined using x-ray spectroscopy with known characteristic wavelengths. The use of a high resolution $\theta$-$\theta$ defractometer is far better. Such an instrument, that can quickly ( 5min) determine lattice spacing to better than a thousandth of an angstrom, is available at the Cornell Center for Materials Research (CCMR).

The spherically bent crystals used in these experiments all had a radius of curvature of 182mm. This radius was dictated by the radius of curvature of off-the-shelf plano convex, f=350mm, BK7 glass lenses, as described in Appendix C. Future efforts would benefit from a larger radius of curvature. A larger radius allows larger magnification and larger separation between wire-array hardware and imaging system components. The added separation could prevent the crystal mirrors from being destroyed in each experiment, representing a tremendous improvement over the 182mm system. Increased separation would also allow one to use rigid, high precision translation stages (that are bulkier than the ones that could be used with the 182mm system) for alignment of the

mirror and aperature, thus improving the accuracy of alignment and probability of success.

Finally, it is strongly suggested that the 6.6343Å (1.8keV) Al line be used despite the success of the Zn sources. It is believed that with the improvements made possible by accurate measurement of the mica lattice spacing and the benefits of a larger radius of curvature, the Al source will be much more successful than Zn. Furthermore, the availability of Al fine wire is far better than that of Zn. The Al line's main advantage is related to filtering. A filter must be used to prevent visible light from exposing the film. It is highly desirable to place a second filter between the wire-array and crystal mirror to decrease the amount of damage the mirror suffers from each experiment. These filters (4-6$\mu$m mylar) significantly attenuate the 1.26keV Zn radiation whereas they are relatively transparent to the Al radiation.

It is hoped that this brief description of monochromatic x-ray imaging using X-pinch sources gives the reader a reasonable foundation to continue the development of such a system. The difficulty of this diagnostic does not become apparent until one tries to implement it, at which point it can be very frustrating. A final recommendation is to combine experimental work with analytic examination. The implementation of a 3-D ray tracing program that emulates the parameters of the experiment will tremendously improve one's predictive ability and general understanding of the system. An example of such a program is given in Appendix E.

APPENDIX C

# SPHERICALLY BENT CRYSTAL MANUFACTURING

## C.1 Overview

The spherically bent crystals used for the monochromatic x-ray imaging experiments presented in Appendix B were manufactured in-house. Generally, one would simply purchase a high quality, spherically bent crystal for about $3,000. This was not practical because these special focusing elements were being destroyed with each experiment. Instead, roughly one year was spent developing a process for constructing spherically bent mica crystals of satisfactory quality, at minimum of cost, and at a production rate of at least four crystals per day. In this process, a thin, rectangular piece of mica, approximately 20mm by 50mm, is glued onto a spherical substrate; the spherical bend is accomplished by pressing the mica onto the concave spherical substrate using a matching convex spherical "pusher".

## C.2 System components

While the process of gluing a piece of mica to a spherical substrate is simple in concept the details of such a system are numerous. The most important components of mirror construction are the spherical substrate and pusher. The quality of these spherical surfaces determines the maximum quality of spherically bent crystal that can be produced.

In this process standard 3 inch diameter, BK7 plano convex lenses were used for the pusher. Thus, the radius of curvature of the spherically bent crystal is determined by the radius of curvature of the particular pusher lens being used. In this system, the pusher

radius was 182mm, however, in retrospect a larger radius would have been better suited for the experimental geometry of the COBRA pulsed power generator.

Typically, commercial crystals are mounted to a glass substrate. The mirrors constructed for the experiments in Appendix B used acrylic substrates. This decision was made because high quality plastic substrates could be made quickly and economically in-house, with any radius of curvature. After rough machining, substrates were polished using the pusher lens and lapping paper with cerium oxide, resulting in a high quality spherical concave surface with radius of curvature slightly larger than the pusher lens'.

Stycast 1266 epoxy was used to bond the mica to the acrylic substrates. It was very important that the glue not be contaminated with particulate material. These contaminates appear to cause tiny bulges in the mirror surface that severely degrade mirror quality. The presence of air bubbles in the glue has a similar effect but can be controlled by de-gassing the glue in a vacuum chamber prior to application.

The use of high quality mica is essential to mirror quality. Mica is graded by a unique scale that ranges from "V-1" to "V-5", with V-1 being the best. Mica graded below V-2 is not suitable for spectroscopy applications. Pre-cut, defect-free mica was purchased from B&M Mica in Flushing, New York. These samples were special ordered to be 21mm wide, 50mm long, and 50$\mu$m to 70$\mu$m thick.

## C.3 Mirror Assembly

The object of mirror assembly is to bond the mica to the spherical substrate and be able to separate the pusher from the finished mirror once the adhesive has set. One method for accomplishing this is to make the mica dimensions larger than the substrate dimensions

so that the adhesive does not spill over the edge of the mica and come in contact with the pusher. Another approach is to coat the pusher with a spray-on mold-release so that the adhesive will not bond to it. The latter method has several advantages and disadvantages. If the mica dimensions are made to be slightly less than the substrate dimensions one can use a smaller piece of mica and a much sturdier mirror is produced because there are no exposed mica edges to snag on things. However, this technique, which allows glue to spill over the edge of the mica, can result in glue spilling in between the pusher and mica, thus degrading mirror quality. To minimize the problem of glue spill, regardless of which method is used, it is important not to use more glue than necessary.

Since the mica crystal resists spherical deformation it is necessary to clamp the pusher, mica, glue and substrate assembly while the glue sets. Clamping the assembly can be difficult since the mica can slip across the substrate, with the glue acting as a lubricant. This problem is best avoided by careful alignment prior to assembly and using a rigid clamping system that does not twist or otherwise deflect.

The most important part of mirror assembly is cleanliness. Assembling mirrors in a clean room is the best option. All components should be cleaned thoroughly and dusted with clean air prior to assembly.

APPENDIX D

# STRUCTURES OF THE DENSE CORES AND ABLATION PLASMAS IN THE INITIATION PHASE OF TUNGSTEN WIRE-ARRAY Z-PINCHES

# Structure of the dense cores and ablation plasmas in the initiation phase of tungsten wire-array Z pinches

J. D. Douglass,[1] S. A. Pikuz,[1,2] T. A. Shelkovenko,[1,2] D. A. Hammer,[1] S. N. Bland,[3] S. C. Bott,[3] and R. D. McBride[1]
[1]*Laboratory of Plasma Studies, 439 Rhodes Hall, Cornell University, Ithaca, New York 14853*
[2]*P. N. Lebedev Physical Institute, Leninsky Prospect 53, Moscow 117924, Russia*
[3]*Blackett Laboratory, Imperial College, London SW7 2BZ, United Kingdom*

(Received 11 October 2006; accepted 14 December 2006; published online 22 January 2007)

The early stages of tungsten (W) wire-array Z-pinch implosions have been studied using two-frame point projection x-ray backlighting on the 1 MA COBRA pulsed power generator [J. D. Douglass, J. B. Greenly, D. A. Hammer, and B. R. Kusse, in *Proceedings of the 15th IEEE International Pulsed Power Conference*, Monterey, 2005 (to be published)]. X-pinch backlighter images with subnanosecond time resolution and 4–10 $\mu$m spatial resolution have been obtained of individual W exploding wires in 8-wire arrays that show evolution of wire-core and coronal plasma structures. The timing of the X-pinch x-ray bursts relative to the Z-pinch initiation time was adjusted over a 50 ns time interval by varying the X-pinch mass per unit length. Wire-cores seen in two images separated in view by 120° show that the expansion is remarkably azimuthally symmetric. A strong correlation is observed between the structure on the dense exploding wire-cores and the structure of the $\geqslant 10^{18}/\mathrm{cm}^3$ ablation plasma being drawn from radial prominences. Plasma ablation velocity was estimated to have a lower bound of 24 km/s. The wire-core expansion rate was found to be approximately constant with time over the interval 50–100 ns after the start of the current pulse. Finally, micron-scale axial gaps, seen as early as 70 ns into the current pulse and persisting from that time, were observed along the wire-core. © *2007 American Institute of Physics*.
[DOI: 10.1063/1.2431633]

## I. INTRODUCTION

Wire array Z pinches driven by the 20 MA Z-machine at Sandia National Laboratories[1] have generated more than 1.8 MJ of soft x-ray energy and peak powers in excess of 200 TW for nearly a decade. These remarkable plasma radiation sources as well as those produced on smaller scale, 1–6 MA pulsed power machines, are of utmost interest to the physics community for their application to inertial confinement fusion (ICF), laboratory astrophysics, validation of numerical methods and high-energy-density physics (HEDP) in general.[2–5]

Wire-array Z-pinch plasmas are initiated by the current-driven explosion of the individual wires in these arrays, leading to the formation of coronal plasmas around dense wire-cores. The coronal plasmas carry virtually all of the current once they form. This earliest stage of the plasma initiation process is very much the same as was reported for single-wire experiments in, for example, Refs. 6–8, in which a few kA/wires were used. In those experiments, the dense wire-cores expanded in the radial direction at an approximately constant rate until at least the time that peak current was reached. Previous experiments with wire arrays have reported that the dense wire-cores expand to 3–8 times their initial diameter and remain at their initial positions until 80% of the implosion time[9] predicted by the standard zero-D implosion model.[10] As current-carrying coronal plasma with current density, **J**, is ablated from the dense cores, the magnetic field, **B**, of the entire wire array causes the plasma to be swept toward the axis of the array by the $\mathbf{J}\times\mathbf{B}$ force,[9] although the current and magnetic field remain in the plasma around the wire-cores.[9] This continuous ablation process leads to an accumulation of plasma on the pinch axis known as the "precursor" plasma.[11] Eventually, the main implosion phase begins, evidently correlated with the time that breaks form in the wire-core/corona structures. In this phase the implosion snowplows mass toward the axis, eventually colliding with the precursor and causing the primary x-ray pulse, as shown in Refs. 9 and 12.

In order to predict the x-ray yield of experiments on future pulsed power machines a good understanding of wire-array Z-pinch physics, including the ablation process, is critical.[13] The ablation plasma from a wire-core in a wire-array Z-pinch and its motion toward the array axis has been studied using laser imaging, x-ray radiography, optical and x-ray streak cameras, various time-gated cameras and various solid-state photo detectors. Such experiments have been performed with low wire number (8-64) arrays on the MAGPIE[14] generator at Imperial College using laser imaging and X-pinch driven x-ray backlighting with spatial resolution of about 15 $\mu$m.[9] Experiments similar to those performed on MAGPIE were also done at the ANGARA-5-1 facility in Russia.[15–18] Studies of wire-cores and ablation plasmas in large wire number arrays, with similar amounts of current per wire, were carried out using monochromatic x-ray backlighting[19] at Sandia National Laboratories[13] with a spatial resolution of 10–20 $\mu$m.

The research presented here focuses on features of the ablation process that have been observed on the 1 MA

 

COBRA[20] accelerator at Cornell University using two-frame point-projection X-pinch backlighting with 4–10 $\mu$m spatial resolution.

Point-projection x-ray backlighting using an X-pinch as the x-ray source has been used routinely at Cornell for more than 10 years to produce high quality x-ray images of exploding wires and other objects with excellent spatial and temporal resolution.[21–26] Specifically, this imaging system is capable of producing images with micron-scale spatial resolution and with sub-ns temporal resolution.

In the experiments reported here, a cylindrical wire-array composed of eight tungsten (W) wires was driven with a 1 MA, 100 ns zero-to-peak risetime current pulse. Two x-ray images of an individual wire in the array were taken from different directions and at relative times varying from simultaneous to as much as 30 ns apart during the current pulse. This dual imaging system has led to the observation of several new ablation features. For instance, when a wire-core is seen in two images separated by 120° in azimuth, it is apparent that the wire-core expansion is remarkably azimuthally symmetric. Wire-cores in 8-wire arrays were seen to have a constant radial expansion velocity of about 250 m/s during the interval 50–100 ns after the start of the current pulse. Additionally, the ability of point-projection imaging to provide a clear differentiation between dense core and coronal plasma has demonstrated a strong correlation between the short scale length (sub-mm) structure on the dense, exploding wire-cores and the structure of the $>10^{18}/\mathrm{cm}^3$ ablation plasma that is leaving the wire-cores. The ablation plasma was found to have a minimum inward radial velocity of about 24 km/s. X-ray backlighting images show that the coronal plasma is ablated preferentially from regions of the wire-core that have undergone the most expansion, as was reported in Ref. 9. Large-scale length (several mm) axial nonuniformities of the wire-cores are also observed in the COBRA experiments. Finally, the development and persistence of micron-scale axial gaps or breaks in the wire-cores is observed as early as 70 ns into the current pulse. All of these features were observed with a spatial resolution of 4–10 $\mu$m or better and subnanosecond temporal resolution.

It should be noted that the term "wire-core" might be used to refer to the dense portion of the coronal plasma around an exploding wire that is imaged using laser backlighting (shadowgraphy or schlieren imaging using optical wavelengths). In the present paper, "wire-core" refers to the dense core of material within the coronal plasma that is imaged by x-ray backlighting. Examples of schlieren images and x-ray point-projection images of exploding wire plasmas showing that these two imaging methods can give very different radii, can be found in Ref. 25. There is an additional ambiguity as to the exact boundary of dense wire-cores in x-ray radiographs due to the resolution limit of different techniques and/or the varying opacity of W for different x-ray wavelengths. When using imaging systems with resolution on the order of the initial wire-core diameter, the experimenter is forced to use coarse measurement techniques, such as a full-width, half-maximum, to determine feature sizes. For instance, the W "wire-cores" in Fig. 1 of Ref. 9 are said to have expanded to ~100 $\mu$m, and have done so preferentially in the radial direction. Furthermore, the authors of Ref. 9 state that this expansion was insensitive to initial wire diameter and wire number (current per wire). These statements agree well with observations of the more dense part of the coronal plasma on COBRA. Therefore, it is assumed here that the observations of W "wire-cores" in Ref. 9 are referring to the more dense coronal plasma.

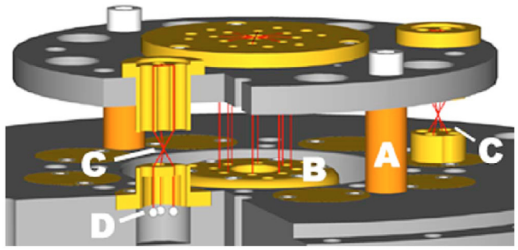


FIG. 1. (Color online) Wire array Z-pinch load assembly with section view of one of two X-pinch backlighters. (A) Return-current post; (B) COBRA pulser cathode; (C) backlighting X pinch; (D) lead weights.

We describe the experimental arrangement and discuss the diagnostics used for the COBRA experiments in Sec. II. Experimental results and discussion are presented in Sec. III. A brief summary and conclusion follows in Sec. IV.

## II. EXPERIMENTAL SYSTEMS AND DIAGNOSTIC INFORMATION

These studies of the structure of individual wire-cores in a cylindrical wire-array Z-pinch and of the coronal plasma in their immediate vicinity were carried out using the COBRA pulsed power generator at Cornell University.[20,23] This generator produces a 1 MA peak current pulse with a zero-to-peak risetime that can be varied between 95 ns and 200 ns or longer by adjusting the timing of the output switches of the generator's four pulse-forming lines. Time-resolved point-projection x-ray images of individual wires in a wire-array z pinch are obtained by placing an X-pinch in the return circuit of the generator's current feed, where the X pinch produces a high-intensity, subnanosecond duration, point x-ray source. Varying the timing of the X-pinch x-ray burst relative to the initiation of the wire-array Z pinch is accomplished by varying the mass per unit length of the X pinch, as will be discussed shortly.

In practice, X-pinch backlighting (XPBL) is implemented on COBRA by placing 4-wire X-pinches in two of the four return current paths around the wire-array Z pinch. Each X pinch has a height of 8 mm and its wires cross with an included angle of about 60°. This setup is illustrated in Fig. 1. In a typical experiment, a 16 mm diameter, 20 mm long wire-array consisting of 8–16 W or Al wires having diameters ranging from 5 to 25 $\mu$m (array masses ranging from 51 to 385 $\mu$g) is imploded, and individual wires are imaged using x rays emitted from the two X-pinch backlighters.

Of particular interest are images obtained from experiments with W wire-array Z pinches. Since W is a high Z (atomic number) material it is possible to observe both the

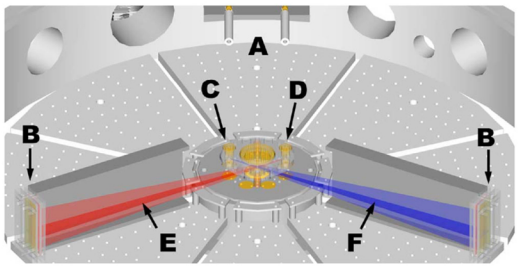


FIG. 2. (Color online) Dual point projection imaging system used on COBRA. (A) Collimated Si diodes; (B) Film cassettes with 12.5 $\mu$m Ti x-ray filters; (C) left XPBL; (D) right XPBL; (E) line-of-sight for right XPBL; (F) line-of-sight for left XPBL.

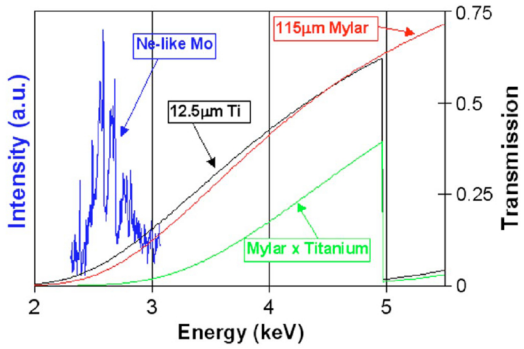


FIG. 3. (Color online) Transmission curves for 12.5 $\mu$m Ti, 115 $\mu$m mylar and their product are shown with a typical Ne-like Mo x-ray spectrum. These illustrate that the Mo line radiation is cut off by these filters, especially by the Ti-mylar combination, leaving only continuum in the bandpass between 3 and 5 keV.

wire-core and coronal plasma moving away from the wire using 3–5 keV radiation from Mo X pinches.[28] For lower Z materials, such as Al, the coronal plasma is not opaque enough to be detected using this imaging technique. As such, all of the wire-core images shown below are of W wires having initial diameters of 12.5 $\mu$m. Approximately 7.5 mm of wire-core length is shown in each image. Each wire-core is one element of an eight-wire cylindrical Z pinch, the other seven wires being identical to the one being imaged. This Z-pinch configuration was chosen because it is too massive to produce an efficient implosion and hence an intense x-ray pulse on the COBRA accelerator. This was desirable for two reasons: the background x-ray flux is significantly decreased, and there is very little ballistic debris produced that tends to destroy x-ray filters.

The backlighting geometry is designed so that two images of the same wire, separated by 120°, can be obtained from each shot. The X pinches are located 45 mm from the Z-pinch axis (47 mm from the wire to be imaged). The two lines of sight are illustrated in Fig. 2. By using two XPBL's having the same (different) mass per unit length, two images of the same wire at nearly the same time (different times) are obtained.

Images were obtained using Kodak BioMAX MS and Technical Pan film. The films are typically placed 420 mm from the X-pinch axis yielding a magnification of about 8.9:1. Imaging cassettes were set up such that x rays passed through a Ti filter (12.5 $\mu$m thick), one piece of Technical Pan film (115 $\mu$m thick), and finally one piece of BioMAX film (185 $\mu$m thick). With this sequence, the Technical Pan film acts as an additional filter for images captured on the BioMAX film, which is more sensitive to hard radiation. The x-ray transmission curves for this system are shown in Fig. 3, using mylar as a surrogate for the Technical Pan film.

The timing of the X-pinch x-ray bursts was monitored using two photosensitive detectors (silicon diodes sensitive to x-ray radiation) that were collimated so as to be able to view only one of the X pinches each (Fig. 2). These detectors (IRD HS01) have a turn-on time of 250 ps. The signals from these detectors were sampled at a rate of 100 ps/pt for most experiments. The radiation incident on these detectors was filtered using 12.5 $\mu$m Ti, the same as the filter used in the XPBL cameras. This filter passes only x-ray radiation between 3–5 keV and above 6 keV, as shown in Fig. 3. Typical Si-diode signals are shown together with the corresponding wire-array current and current derivative signals in Fig. 4. The timing of the x-ray signals relative to the start of the current waveform is accurate to better than ~1 ns.

In order to obtain images of the same wire at different times it was necessary to determine the dependence of XPBL timing on various experimental parameters. Using primarily 4-wire Mo X pinches for backlighters, wire diameter, current pulse shape, and Z-pinch array parameters were varied to this end. It was found that XPBL wire mass per unit length had the strongest influence on x-ray burst timing. No other variables were found to have significant effect on XPBL timing. The effect of XPBL wire mass per unit length is plotted in Fig. 5 as a percentage of the load current zero-to-peak rise-time, $T_{\%}$, which is defined as

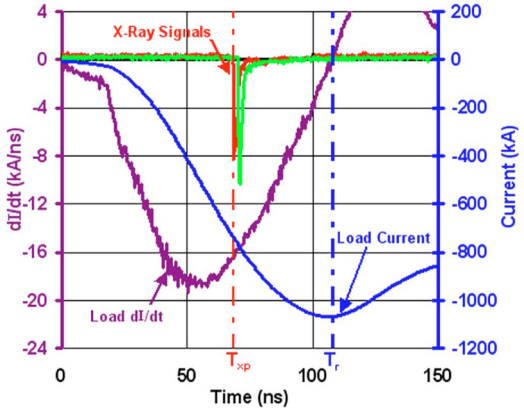


FIG. 4. (Color online) X-ray radiation, $dI/dt$ and current traces from COBRA test 267. The two x-ray signals are from the two collimated Si diodes shown in Fig. 2.

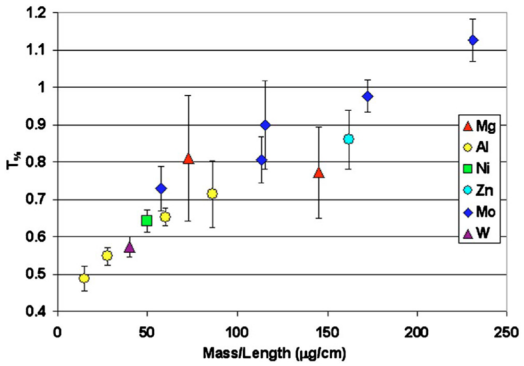


FIG. 5. (Color online) Dependence of $T_{\%}$ on XPBL mass. Different symbols for data points indicate the average $T_{\%}$ value for different XPBL materials. Each data point represents an average of 2–40 shots (with Mo points having the largest data sets and most others having 2–8 shots per data point). Error bars indicate one standard deviation from the average $T_{\%}$ value for a given XPBL material and mass.

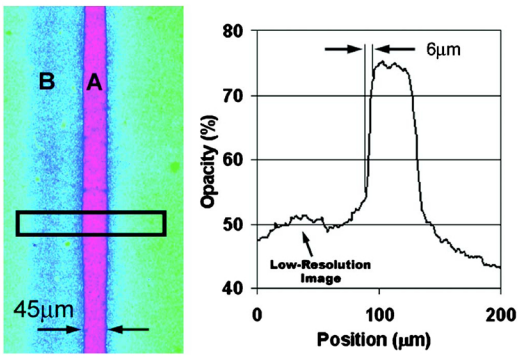


FIG. 6. Demonstration of spatial resolution. (A) High-resolution image of a 12.5 $\mu$m (initial diameter) W wire-core from shot 239; (B) Low-resolution image of the same wire-core produced by a low-intensity secondary XPBL hot spot. The high resolution image was taken at 89 ns into the current pulse.

$$T_{\%} = \frac{T_{xp}}{T_r} \times 100 \tag{1}$$

where $T_{\mathrm{xp}}$ and $T_r$ are the time of the XPBL x-ray burst and the load current zero-to-peak risetime, respectively. These parameters are shown in Fig. 4 for a typical pulse. The error bars in Fig. 5 indicate one standard deviation from the average $T_{\%}$ value for a given XPBL material and mass.

Approximately 75% of XPBL sources with mass less than 200 $\mu$g/cm produced useful images, i.e., with high spatial resolution and adequate contrast. The image in Fig. 6 is an example of one with two images (separated by about 90 $\mu$m) of the same wire-core due to two x-ray bursts separated by about 10 $\mu$m, one with poor contrast and resolution and the other with good contrast and resolution. In this case time-resolved information can still be obtained about the wire-core and coronal plasma. This is because it is known that the first x-ray burst produced by an X pinch is almost always smaller in source size and more intense in the 3–5 keV Ti pass-band. Using the high-resolution (first burst) image shown in Fig. 6 the minimum (worst possible) spatial resolution of this system was inferred from the distance over which film exposure went from background level to nearly completely opaque, about 6 $\mu$m in the case shown.

Such high spatial resolution is possible due to the spectral transmission of the x-ray filters used in these experiments. The combination of Mo XPBLs and 12.5 $\mu$m Ti x-ray filters yields x-ray images that are nearly entirely produced by continuum radiation, which has been shown to originate from an extremely small, ~1 $\mu$m, intense x-ray source.[26] In general, the spatial resolution of a point-projection imaging system should be similar to the diameter of its point source; hence, the spatial resolution reported here (4–10 $\mu$m) seems quite conservative. There are several reasons for this estimate. First, the resolution of this system is diffraction limited. Specifically, the diffraction limit of the system is given by

$$\delta x = \sqrt{\lambda a}, \tag{2}$$

where $\lambda$ is the wavelength of incident radiation in Å, $a$ is the distance from source to object in cm, and $\delta x$ is the resulting diffraction limit in $\mu$m. For this system, with $a$=4.7 cm and $\lambda$=2.5–4.1 Å, the resulting diffraction limit, $\delta x$, is 3.4–4.4 $\mu$m. Furthermore, X pinches tend to produce multiple, secondary, closely spaced (within microns of each other) hot-spots (point sources) that degrade spatial resolution. Additional effects from x-ray diffraction and dispersion through plasmas and solid filters can further compromise spatial resolution. With these considerations in mind it could be said that spatial resolution for this system is about 4 $\mu$m at best and 10 $\mu$m at worst. For a detailed description of the X-pinch source size and the spatial resolution of the resulting images, see Ref. 26.

## III. EXPERIMENTAL RESULTS

The high temporal and spatial resolution of this x-ray imaging technique has led to the observation of several new features of wire-core and coronal plasma dynamics.

First, images of a wire-core that are taken at nearly the same time and separated in view by 120° show that the wire-core structure is highly azimuthally symmetric. This claim is based upon the high degree of symmetry seen about the axis of the wire-core and the similarity between images that are at nearly orthogonal views. This observation implies two important points: first, the forces driving core expansion are locally symmetric, and second, images taken from different angles and at different times can be used to study the time evolution of core structures as if the images were from the same viewing angle. The high degree of symmetry exhibited by the dense wire-cores is most easily observed when the aspect ratio of initial images is greatly biased in the radial direction. For example, an image could be stretched in the radial direction by a factor of 4 and compressed in the axial direction by a factor of 4. This yields an image that has been

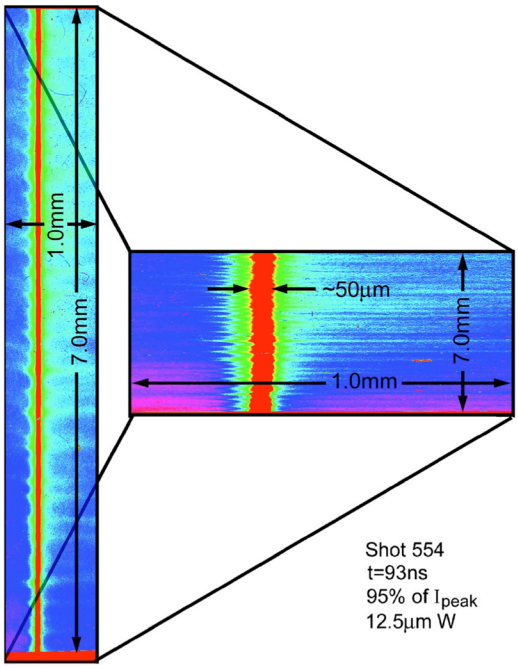


FIG. 7. Before/after example of image distortion. The raw image of this wire-core is compressed by a factor of 4 in the axial direction and stretched by a factor of 4 in the radial direction in order to make details of the core structure more obvious.

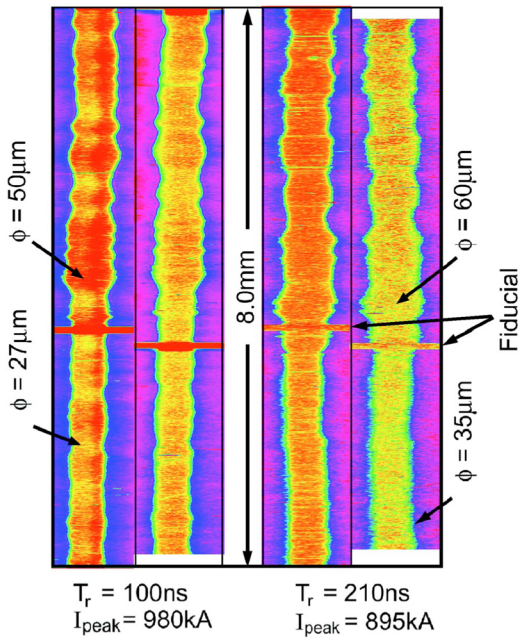


FIG. 8. Illustration of symmetry observed in the structure of W wire-cores. Images on the left were taken at nearly the same instant of the same wire-core in shot 239. Images on the right were taken at nearly the same instant (about 30 ns later than those on the left) of the same wire-core in shot 237. These images imply that core structure is symmetric throughout the time frame examined with this radiography technique.

biased by a factor of 16 in the radial direction while preserving the initial contrast. A before/after example of such a distortion is shown in Fig. 7.

The azimuthal symmetry of dense wire-core structure is seen for both long and short wavelength perturbations through the entire range of the current pulse that we were able to observe (50–120 ns). Additionally, this symmetry was observed regardless of the current pulse shape as indicated in Fig. 8.

It should be noted that the image pairs shown here show mirror symmetry about the radial direction. Hence, the claim of azimuthal symmetry relies on other observations. Large-scale azimuthal symmetry is implied by the similarity in measurement of average core diameter for two wires in the same array that are imaged on the same film from different angles (76° from the radial direction and 60° for a standard image) with different magnifications (8.9:1 and 10.15:1). Accounting for the different magnifications, the average diameter of the two wires typically agrees to ~2%. Furthermore, the wire-core being imaged from a view closer to normal to the radial direction (76°), where one would expect to observe radial elongation, has no tendency to have a larger average diameter than the wire in the standard (60°) view. These observations suggest that large-scale azimuthal symmetry does exist and that any azimuthal asymmetry in wire-core structure is insignificant.

As reported previously,[9,17] the dense W wire-cores exhibited a characteristic mm scale diameter modulation. This modulation was seen throughout the range of observation with a wavelength of 0.25–0.3 mm. It was found that the maximum and minimum wire diameter produced by this modulation increased approximately linearly with time.

While the wire-cores in a Z-pinch array are known to expand by a factor of 3–8 (Refs. 9, 13, and 15–18), it is not clear whether this expansion is linear, exponential, monotonic, etc. Furthermore, the effects of pulse shape, wire number (current per wire) and initial wire diameter on wire-core expansion and ablation are certainly of great importance if 1 MA scale pulser results are to be extrapolated to larger drivers. Data from present experiments indicate that core expansion in nonimploding W arrays is linear with time over the time interval 50–100 ns after the start of the current pulse. It appears that the rate of this linear expansion is not overly sensitive to the zero-to-peak risetime of the current pulse, as shown in Fig. 9. The maximum radial expansion rate of W wire-cores with an initial diameter of 12.5 $\mu$m was 250±10 m/s for pulses with risetimes from 96 to 122 ns and a peak of about 1.1 MA.

In order to compare with results from the Z-machine[13] and Angara-5-1,[15–18] a small number of 16-wire (~68 kA per wire at peak current), imploding W arrays were tested. These experiments on COBRA strongly suggest that linear core expansion does not continue indefinitely. Images of 5.4 $\mu$m and 7.4 $\mu$m W wire-cores in imploding 16-wire ar-

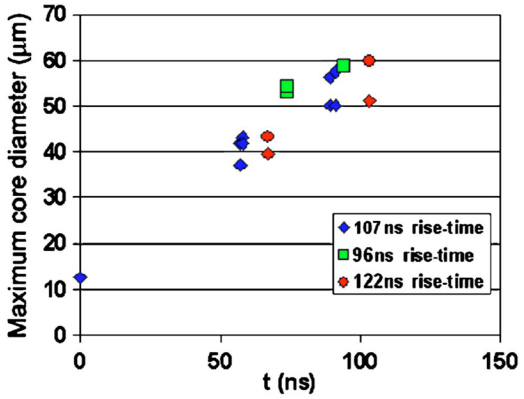


FIG. 9. (Color online) Diameter of the maximally expanded visible parts of the wire-cores in a $8\times12.5$ $\mu$m W wire array versus time. Different markers indicate pulses with different risetimes. Each set implies a linear expansion with radial velocity of about 250 m/s.

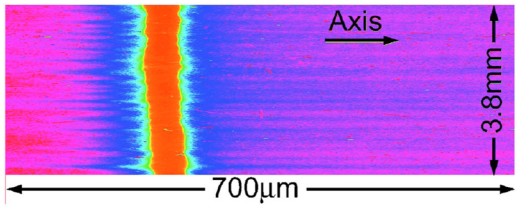


FIG. 10. Illustration of the correlation between wire-core and coronal plasma structures from COBRA shot 554. Image was taken at 93 ns into the current pulse with a risetime of 96 ns. Note that coronal plasma is preferentially ablated from portions of the wire-core that have undergone the most expansion.

rays indicate that these wires stop expanding once they reach diameters of about 16 $\mu$m and 23 $\mu$m, respectively. In Ref. 15 Alexandrov *et al.* report that 5 $\mu$m W wires in 60-wire, 20 mm diameter arrays had expanded to 18–20 $\mu$m when the current had reached ~30 kA per wire (50–60 ns into the current pulse). In Ref. 16 Volkov *et al.* report that 8 $\mu$m W wires in 40-wire, 12 mm diameter arrays had expanded to ~25 $\mu$m when the current reached ~50 kA/wire (70 ns into current pulse). These experiments were performed with a nearly identical backlighting system to that used on COBRA except that only one backlighter was used and a spatial resolution of better than 4 $\mu$m is claimed. The agreement between results from COBRA and Angara is excellent; unfortunately, agreement with Ref. 13 is not as good. In Ref. 13, Sinars *et al.*, state that 11.5 $\mu$m, 7.4 $\mu$m, and 5.0 $\mu$m W wire-cores expanded to 45–50 $\mu$m, 32–37 $\mu$m, and about 26 $\mu$m, respectively. These measurements were taken when the current had reached 19–21 kA per wire. Spatial resolution of ~20 $\mu$m was claimed. In the Z-machine experiments the Z-Beamlet (Ref. 27) laser system was used to produce a 1.865 keV x-ray backlighting source. Given the differences in wire-number, current per wire, pulse shape, array dimensions, spatial resolution and backlighter x-ray energy, perhaps the 50% larger size observed on the Z machine is not unreasonable.

Ablation plasma was not observable throughout the entire time frame of the current pulse that we were able to examine with this radiography technique. We were able to obtain images as early as 49 ns into the pulse and as late as 93 ns (100 ns) for a pulse with a risetime of about 100 ns (122 ns). In most cases the coronal plasma density was not detectable until at least 75 ns or about 75% of the zero-to-peak risetime. Based on previous research involving X-pinch backlighting of W plasmas,[28] an estimate can be made of the minimum density of the corona plasmas seen in the images presented here. It was found in Ref. 28 that the minimum detectable W areal density for this imaging system is ~60 $\mu$g/cm$^2$. Detectable coronal plasmas have a radial extent of ~200 $\mu$m in the direction away from the pinch axis, in reasonable agreement with results from W arrays on Angar-5-1.[17,18] We therefore assume that x rays passing through the coronal plasma near the wire-core have propagated through ~400 $\mu$m of W plasma. This plasma is assumed to be of nearly constant density. Combining this estimate with the minimum detectable areal density yields a minimum coronal plasma mass density of about 1.5 mg/cm$^3$, implying an ion number density of approximately $5\times10^{18}$/cm$^3$. This yields a coronal plasma mass per unit length (per wire) within 200 $\mu$m of the wire-core of 1.8 $\mu$g/cm, which is about one twelfth of the initial mass.

As expected, images taken near the peak current (Fig. 11, for example) showed that the plasma ablating from the W wire-cores was moving inward toward the array axis. The rate of mass ablation per unit length per wire (kg m$^{-1}$ s$^{-1}$) can be related to ablation velocity, $V_{\mathrm{abl}}$, (m s$^{-1}$) using the momentum balance equation[9]

$$V_{\mathrm{abl}}\frac{dm}{dt}=-\frac{\mu_0 I^2}{4\pi R_0}. \tag{3}$$

Integrating both sides of (2) and assuming $V_{\mathrm{abl}}$ to be a constant yields

$$V_{\mathrm{abl}}=\frac{\mu_0}{4\pi R_0 m(t_0)}\int_{t=0}^{t=t_0} I^2(t)dt, \tag{4}$$

where $R_0$ is the initial array radius in meters and $I(t)$ is the current per wire in Amperes.

At about 75 ns, when coronal plasma is clearly observable, the integral of $I^2$ is about $2.3\times10^4$ A$^2$ s. Substitution of this value, and the mass per unit length found previously, into (3) yields an ablation velocity of about 24 km/s. The error associated with this velocity is large but it makes a reasonable lower limit for the actual value. Furthermore, this lower limit shows reasonable agreement with 2D MHD simulations of wire-core ablation velocities found in Ref. 29.

When coronal plasma was observable, a strong correlation between the modulation in the diameter of the dense wire-core and the coronal plasma structure was consistently observed. Figure 10 shows an example of this correlation, which was also observed with laser imaging in Ref. 9.

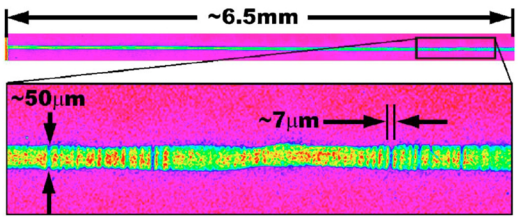


FIG. 11. (Color online) Image of W wire-core from COBRA shot 554 near the peak current (at 93 ns). The upper image is the original film scan. The lower image is a blow-up of one portion of the wire-core where large gaps are clearly visible.

Another common feature of these images is an axial nonuniformity. This can be seen in Fig. 8. In many images taken 80–120 ns into the current pulse (with risetimes varying from 96–210 ns), wire-cores are seen to have distinct regions of short and long wavelength structure. The transition from one type of structure to another appears to happen over a very short distance. (By coincidence the transition region happens to coincide roughly with the position of the fiducial mark in the images shown in Fig. 8.)

Images taken near the peak current, as in Fig. 11, often show that gaps were forming in the wire-core by this time. In our experiments, the formation of ~5 $\mu$m gaps was not observed earlier than 70 ns into the current pulse. Another feature of this micron-scale structure is that it tended to develop preferentially towards the cathode end of the wire-cores, much like the axial nonuniformity mentioned previously. Furthermore, dual images of wire-cores with gaps showed that once a gap opens it tends to widen with time. It is not clear whether these gaps are seeded by defects in the initial wire structure or if they are driven by ablation instabilities.

Another feature of these gaps that is of great interest is that they seem to have little effect on core expansion, as shown in Fig. 12. Clearly, the wire-core in this image has expanded significantly over the 19 ns interval between the two images. This expansion appears to be uniform despite the many gaps that have developed along this portion of the core.

It should be noted that the feature size of these gaps is close to the resolution limit of this diagnostic. As a result, phase contrast effects from x-ray refraction and interference through variations in density along the wire-core could be causing the edges of these gaps to be artificially sharp. While

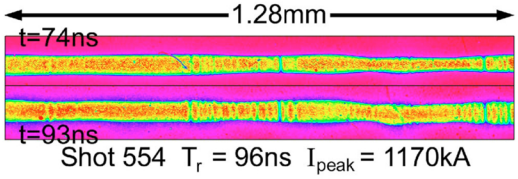


FIG. 12. (Color online) Dynamic behavior of micron-scale structures in dense wire-cores. Images taken ~20 ns apart of the same wire-core show that micron-scale gaps widen with time and become more frequent. These gaps appear to have little influence on core expansion.

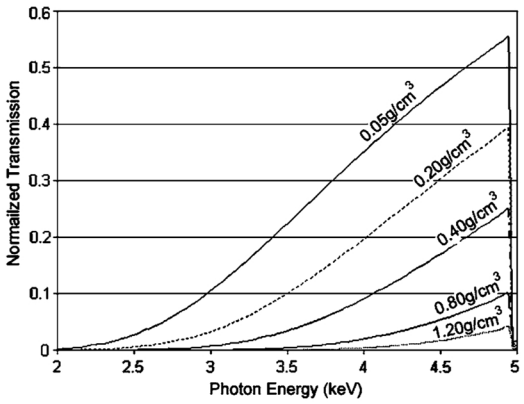


FIG. 13. Incident photon energy versus normalized transmission through 40 $\mu$m of W of varying density and 12.5 $\mu$m of solid density Ti. Bottom curve corresponds to one-sixteenth solid density W.

this is very likely to be happening it does not negate that there are very large, sharp density variations along the length of the wire-core. This claim is based on the simple fact that the core must transmit significant radiation in the 3–5 keV Ti window in the vicinity of these gaps in order for phase contrast effects to be observed. It can be assumed that late in the current pulse the density of the wire-core has dropped by at least a factor of 16 since its diameter has increased by about a factor of 4. In order to significantly change the transmission of 3–5 keV radiation for W at this density, the density must be decreased by an additional factor of at least 4, as shown in Fig. 13.

## IV. SUMMARY AND CONCLUSION

We have presented results of wire-array Z-pinch experiments with eight W wires in which an individual exploding wire in the array was imaged from two directions and at different times during the Z-pinch process. The timing of the X-pinch backlighter (XPBL) was varied with reasonable predictability by varying the XPBL mass per unit length. This radiography technique allowed the examination of W wire-cores as early as 49 ns and as late as 93 ns into a 100 ns, 1 MA current pulse.

Wire-cores seen in two images separated by an angle of 120° show that expansion is remarkably symmetric. This symmetry was observed throughout the time frame covered by the XPBL system. The high degree of symmetry implies that forces driving core-expansion are symmetric about the wire-core. The time-independence of core symmetry implies that images taken at different angles and different times of the same wire-core can be used as a two-frame time-gated diagnostic with sub-ns resolution. This has enabled the precise measurement of wire-core expansion rates. It was found that 12.5 $\mu$m W wires in a nonimploding 8-wire array expanded linearly with time at a rate of about 250 m/s. This rate was not significantly changed by a 30 ns increase in pulse risetime. Data from 16-wire imploding W arrays strongly suggests that core expansion eventually stagnates.

The final wire-core diameter reached in 16-wire arrays appears to be correlated with initial wire diameter. Furthermore, data from vastly different machines with different array configurations suggest that wire-core expansion is insensitive to pulse shape, array dimensions and wire-number. This insensitivity is further supported by Fig. 7 in Ref. 18 where W wire-cores in the inner and outer arrays of nested array have both expanded to ~20 $\mu$m from an initial diameter of 6 $\mu$m.

Coronal plasma was seen to reach detectable densities around 75 ns into the current pulse. Based on previous research,[28] a minimum ion density of about $5\times10^{18}/\mathrm{cm}^3$ can be inferred for this plasma. Using this density, an estimate for the minimal ablation velocity of 24 km/s is made. This velocity is in reasonable agreement with 2D MHD wire-core ablation plasma simulations in Ref. 29.

Ablation plasmas were seen to exhibit a characteristic axial wavelength of 0.25–0.3 mm. Ablation plasma structure was strongly correlated with the axial diameter modulation on the dense wire-cores. Furthermore, plasma appears to ablate preferentially from portions of the wire-core that have undergone the most expansion.

Micron scale gaps or breaks in wire-cores were seen after about 75 ns. This structure appears to be similar to the 5–20 $\mu$m structure reported in Refs. 15–18. These gaps tended to widen with time up to about 7 $\mu$m. The mechanism that leads to the formation of these gaps is unknown. The presence of gaps in a wire-core seemed to have little effect on radial core expansion, even in the immediate vicinity of gaps as large as 7 $\mu$m. This observation implies that forces driving core expansion from 50 to 100 ns must be external to the dense wire-core.

The remarkable level of symmetry in wire-core structure implies that the global magnetic field of the pinch plays no part in the formation of this structure. The 0.25–0.3 mm diameter modulation is strongly correlated with the axial density fluctuations seen in the coronal plasma surrounding the wire-core, suggesting the two mediums are strongly coupled. Combining these observations and inferences leads to the conclusion that core expansion is driven by radiative or thermal conduction heating from the surrounding coronal plasma, as suggested in Ref. 17. Based upon the assertion that this heating is symmetric it is assumed that only coronal plasma within 200 $\mu$m of the wire-core surface contributes to heating since the corona is highly asymmetric outside of this radius. This conjecture is quite similar to the theory outlined in Ref. 29 by Chittenden *et al.*

## ACKNOWLEDGMENTS

We wish to thank Dr. Sergey Lebedev of Imperial College for a critical reading of our manuscript.

This work was partially supported by DOE Grant No. DE-FG03-98ER54496, by Sandia National Laboratories Contract No. AO258, and by the Stewardship Sciences Academic Alliances program of the National Nuclear Security Administration under DOE Cooperative Agreement No. DE-FC03-02NA00057.

[1] R. B. Spielman, C. Deeney, G. A. Chandler, M. R. Douglas, D. L. Fehl, M. K. Matzen, D. H. McDaniel, T. J. Nash, J. L. Porter, T. W. L. Sanford, J. F. Seamen, W. A. Stygar, K. W. Struve, S. P. Breeze, J. S. McGurn, J. A. Torres, D. M. Zagar, T. L. Gilliland, D. O. Jobe, J. L. McKenney, R. C. Mock, M. Vargas and T. Wagoner, Phys. Plasmas **5**, 2105 (1998).
[2] M. K. Matzen, M. A. Sweeney, R. G. Adams, J. R. Asay, J. E. Bailey, G. R. Bennett, D. E. Bliss, D. D. Bloomquist, T. A. Brunner, R. B. Campbell, G. A. Chandler, C. A. Coverdale, M. E. Cuneo, J.-P. Davis, C. Deeney, M. P. Desjarlais, G. L. Donovan, C. J. Garasi, T. A. Haill, C. A. Hall, D. L. Hanson, M. J. Hurst, B. Jones, M. D. Knudson, R. J. Leeper, R. W. Lemke, M. G. Mazarakis, D. H. McDaiel, T. A. Mehlhorn, T. J. Nash, C. L. Olson, J. L. Porter, P. K. Rambo, S. E. Rosenthal, G. A. Rochau, L. E. Ruggles, C. L. Ruiz, T. W. L. Sanford, J. F. Seamen, D. B. Sinars, S. A. Slutz, I. C. Smith, K. W. Struve, W. A. Stygar, R. A. Vesey, E. A. Weinbrecht, D. F. Wenger, and E. P. Yu, Phys. Plasmas **12**, 055503 (2005).
[3] S. V. Lebedev, A. Ciardi, D. J. Ampleford, S. N. Bland, S. C. Bott, J. P. Chittenden, G. N. Hall, J. Rapley, C. A. Jennings, A. Frank, E. G. Blackman, and T. Lery, Mon. Not. R. Astron. Soc. **361**, 97 (2005).
[4] S. V. Lebedev, D. J. Ampleford, S. N. Bland, S. C. Bott, J. P. Chittenden, J. Goyer, C. Jennings, M. G. Haines, G. N. Hall, D. A. Hammer, J. B. A. Palmer, S. A. Pikuz, T. A. Shelkovenko, and T. Christoudias, Plasma Phys. Controlled Fusion **47**, 91 (2005).
[5] J. P. Chittenden, S. V. Lebedev, S. N. Bland, F. N. Beg, and M. G. Haines, Phys. Plasmas **8**, 2305 (2001).
[6] D. B. Sinars, Min Hu, K. M. Chandler, T. A. Shelkovenko, S. A. Pikuz, J. B. Greenly, D. A. Hammer, and B. R. Kusse, Phys. Plasmas **8**, 216 (2001).
[7] P. U. Duselis, J. A. Vaughan, and B. R. Kusse, Phys. Plasmas **11**, 4025 (2004).
[8] G. S. Sarkisov, K. W. Struve, and D. H. McDaniel, Phys. Plasmas **12**, 052702 (2005).
[9] S. V. Lebedev, F. N. Beg, S. N. Bland, J. P. Chittenden, A. E. Dangor, M. G. Haines, K. H. Kwek, S. A. Pikuz, and T. A. Shelkovenko, Phys. Plasmas **8**, 3734 (2001).
[10] D. D. Ryutov, M. S. Derzon, and M. K. Matzen, Rev. Mod. Phys. **72**, 167 (2000).
[11] S. V. Lebedev, R. Aliaga-Rossel, S. N. Bland, J. P. Chittenden, A. E. Dangor, M. G. Haines, and I. H. Mitchell, Phys. Plasmas **6**, 2016 (1999).
[12] D. B. Sinars, M. E. Cuneo, E. P. Yu, D. E. Bliss, T. J. Nash, J. L. Porter, C. Deeney, M. G. Mazarakis, G. S. Sarkisov, and D. F. Wenger, Phys. Rev. Lett. **93**, 145002 (2004).
[13] D. B. Sinars, M. E. Cuneo, E. P. Yu, S. V. Lebedev, K. R. Cochrane, B. Jones, J. J. MacFarlane, T. A. Melhorn, J. L. Porter, and D. F. Wenger, Phys. Plasmas **13**, 042704 (2006).
[14] I. H. Mitchell, J. M. Bayley, J. P. Chittenden, J. F. Worley, A. E. Dangor, and P. Choi, Rev. Sci. Instrum. **67**, 1533 (1996).
[15] V. V. Alexandrov, I. N. Frolov, M. V. Fedulov, E. V. Grabovsky, K. N. Mitrofanov, S. L. Nedoseev, G. M. Oleinik, I. Yu. Porofeev, A. A. Samokhin, P. V. Sasorov, V. P. Smirnov, G. S. Volkov, M. M. Zurin, and G. G. Zukakischvili, IEEE Trans. Plasma Sci. **30**, 559 (2002).
[16] G. S. Volkov, E. V. Grabovskii, M. V. Zurin, K. N. Mitrofanov, G. M. Oleinik, and I. Yu. Porofeev, Instrum. Exp. Tech. **47**, 376 (2004).
[17] E. V. Grabovskii, K. N. Mitrofanov, G. M. Oleinik, and I. Yu. Porofeev, Plasma Phys. Rep. **30**, 121 (2004).
[18] E. V. Grabovsky, K. N. Mitrofanov, S. L. Nedoseev, G. M. Oleinik, I. Yu. Porofeev, A. A. Samokhin, and I. N. Frolov, Contrib. Plasma Phys. **45**, 553 (2005).
[19] D. B. Sinars, G. R. Bennett, D. F. Wenger, M. E. Cuneo, D. L. Hanson, J. L. Porter, R. G. Adams, P. K. Rambo, D. C. Rovang, and I. C. Smith, Rev. Sci. Instrum. **75**, 3672 (2004).
[20] J. D. Douglass, J. B. Greenly, D. A. Hammer, and B. R. Kusse, "Capabilities of the reconfigured COBRA accelerator," in the *Proceedings of the 15th IEEE International Pulsed Power Conference*, Monterey, 2005 (to be published).
[21] D. H. Kalantar and D. A. Hammer, Rev. Sci. Instrum. **66**, 779 (1995).
[22] T. A. Shelkovenko, D. B. Sinars, S. A. Pikuz, and D. A. Hammer, Phys. Plasmas **8**, 1305 (2001).
[23] T. A. Shelkovenko, S. A. Pikuz, J. D. Douglass, R. D. McBride, J. B. Greenly, and D. A. Hammer, IEEE Trans. Plasma Sci. **34**, 2236 (2006).
[24] T. A. Shelkovenko, D. B. Sinars, S. A. Pikuz, K. M. Chandler, and D. A. Hammer. Rev. Sci. Instrum. **72**, 667 (2001).

[25]D. H. Kalantar and D. A. Hammer, Phys. Rev. Lett. **71**, 3806 (1993).
[26]B. M. Song, S. A. Pikuz, T. A. Shelkovenko, and D. A. Hammer, Appl. Opt. **44**, 2349 (2005).
[27]P. K. Rambo, I. C. Smith, J. L. Porter, M. J. Hurst, C. S. Speas, R. G. Adams, A. J. Garcia, E. Dawson, B. D. Thurston, C. Wakefield, J. F. Kellogg, M. J. Slattery, H. C. Ives, R. S. Broyles, J. A. Caird, A. C. Erlandson, J. E. Murray, W. C. Behrendt, N. D. Neilsen, and J. M. Narduzzi, Appl. Opt. **44**, 2421 (2005).
[28]S. A. Pikuz, T. A. Shelkovenko, A. R. Mingaleev, D. A. Hammer, and H. P. Neves. Phys. Plasmas **6**, 4272 (1999).
[29]J. P. Chittenden, S. V. Lebedev, B. V. Oliver, E. P. Yu, and M. E. Cuneo. Phys. Plasmas **11**, 1118 (2004).

APPENDIX E

**3-D MONOCHROMATIC RAY TRACING**

## E.1 Introduction

This appendix contains an example of a 3-D monochromatic ray tracing program. This program generates a simulated image of a wire-array. A sub-function generates a list of points that represent the outline of each wire in the array; the main function determines where (and if) each of these points will be mapped onto the detector plane, thus forming the simulated image. The main function is fairly general and allows one to manipulate source size and location, aperture diameter and array location. The user also sets array parameters like wire number, wire diameter and array diameter. For simplicity the wires are assumed to be completely opaque.

In order for a point to be mapped from the edge of a wire to the film plane it must satisfy spectral and geometric requirements. The first requirement is the existence of at least one line-of-sight from the test point to the crystal mirror that satisfies the Bragg condition (see Appendix B). The first geometric requirement is that any line(s)-of-sight that satisfy the Bragg condition must also intersect the source. If these two requirements are met then the reflected ray is calculated. The final geometric requirement is that the reflected ray pass within the limiting aperture. Finally, the point where each line-of-sight, that satisfies all three of these requirements, intersects the detector plane, is calculated. Generally, each test point in a realistic system results in tens to hundreds of points mapped to the detector plane, the extent to which these points are spread across the detector plane is a measure of how well the test point is focused.

## E.2 Main Function

```
function image_map
%   This function generates a simulated image for a point-projection based
%   monochromatic imaging system.

close('all');
theta_c = 5.818;    % Central angle of normal incidence, also the rotaion
                    % x'-y' plane realtive to x-y plane in degrees

two_d = 6.687;      % Crystal lattice spacing in angstroms
n=1;                % Order of reflectio nto use in Bragg calculation
R = 250;            % Radius of mirror curvature
```

```
A = 145;            % Distance from mirror center (0,R,0) to array axis
sp = [0 A-R 0];     % Center of source in array (primed) basis
sd = .5;            % Source diameter ?
lamda_center = 6.65255; % Wavelength of line radiation source in angstroms
d_lam = 0.5;     % Spectral width of line source in angstroms
dims = [48;12];     % Mirror dimensions in mm

% Film corners in film basis (array basis mirrored about y-axis)
film_olp = 100*[-.5,0,-.5;.5,0,-.5;.5,0,.5;-.5,0,.5;-.5,0,-.5];
resolution = .05;   % Mirror map resolution in mm
wire_num = 30;      % Number of wires in the array
array_diam = 8;     % Array diameter
array_height = 5;   % Array height
wire_radius = 0.01; % Wire radius in mm
array_phase = -2;   % Rotation of array about z' axis in degrees

%   Generate cell array of the points (in the array basis) along each wire
%   edge in the x'-z' plane.
dat = array_points(wire_num,array_diam,array_height,wire_radius,array_phase);

%   Transform the wire edge points (of the first wire) from the array
%   (primed) basis to the Rowland (unprimed) basis
ax = dat{1}(:,1)*cosd(theta_c) + (dat{1}(:,2)-A)*sind(theta_c);
ay = (dat{1}(:,2)-A)*cosd(theta_c) - dat{1}(:,1)*sind(theta_c) + R;
az = dat{1}(:,3);

%   Find the film position in the Rowland basis where the lens equation is
%   satisfied, 1/a +1/b = 2/R
fn = film_pos(A,R,theta_c);     % fn = [normal vector, center coordinates]

%   Separate center coordiantes from fn
fx = fn(2,:);

%   Isolate film normal vector
fn = fn(1,:);

%   Transform film corner coordinates from the film basis to the Rowland basis
film_ol = [film_olp(:,1)*cosd(theta_c)+fx(1),film_olp(:,1)*sind(theta_c)+fx(2),
film_olp(:,3)+fx(3)];

%   Find the normal vector and center coordinates of the limiting aperature
aper_n = aper_pos(R,theta_c);
aper_x = aper_n(2,:);
aper_n = aper_n(1,:);
```

```
% Set the aperature radius in mm
aper_rad = 2;

% Find the location of the source in the Rowland basis
s = [-(A-sp(2))*sind(theta_c),R-(A-sp(2))*cosd(theta_c),sp(3)];

% Generate color map
color_map = color_m;

% Linearly space colors by number of wires (unique color for each wire)
colori = round(linspace(128,254,size(dat,1)));

% Open imaging system figure
figure('name','System Configuration','numbertitle','off')

% Plot the outline of the first wire
plot3(ax,ay,az,'color',color_map(colori(1),:));
hold on

% Plot the remaining wires
for j = 2:size(dat,1)
    ax = dat{j}(:,1)*cosd(theta_c) + (dat{j}(:,2)-A)*sind(theta_c);
    ay = (dat{j}(:,2)-A)*cosd(theta_c) - dat{j}(:,1)*sind(theta_c) + R;
    az = dat{j}(:,3);
    plot3(ax,ay,az,'color',color_map(colori(j),:));
end

% Generate Rowland circle outline
rc = r_circle(R/2);

% Generate mirror outline points in Rowland basis
m_ol = mirror_ol(dims',R);

%   Plot the Rowland circle outline
plot3(rc(:,1),rc(:,2),rc(:,3),'-k')

%   Plot the mirror surface outline
plot3(m_ol(:,1),m_ol(:,2),m_ol(:,3),'-k')

%   Plot the film outline
plot3(film_ol(:,1),film_ol(:,2),film_ol(:,3),'-k')

%   Plot the source location
```

```
plot3(s(1),s(2),s(3),'xr')

%   Plot the aperature location
plot3(aper_x(1),aper_x(2),aper_x(3),'ok')
hold off
axis('image')
set(gca,'ytick',[]);
set(gca,'xtick',[]);
set(gca,'ztick',[]);

%%%%%%%%%%%%%%%%%%%%%%%%%%%%%%%%%%%%%%%%%%%%%%%%%%%%%%%%%%%%%%%%%%%%%%%%%%%%%%%
%   Start ray tracing through each point in the cell array 'dat'
%%%%%%%%%%%%%%%%%%%%%%%%%%%%%%%%%%%%%%%%%%%%%%%%%%%%%%%%%%%%%%%%%%%%%%%%%%%%%%%

%   Step through each wire
q = 0;  %   Initialize imaged wire counter
for w=1:size(dat,1)
    ap = dat{w};
    f = [];
    %   Step through each point of wire(w)
    for k=1:size(ap,1)
        ft=[];
        ar=[];
        %   Transform a' to a
        ax = ap(k,1)*cosd(theta_c) + (ap(k,2)-A)*sind(theta_c);
        ay = (ap(k,2)-A)*cosd(theta_c) - ap(k,1)*sind(theta_c) + R;
        az = ap(k,3);
        a = [ax ay az];

        %   Generate source outline projected through ap onto mirror
        %   surface
        s_ol = round_source(sd,ap(k,:),sp,theta_c,A,R);

        %   Find x and z limits of source mapping
        s_limits = [min(s_ol(:,1));max(s_ol(:,1));min(s_ol(:,3));
max(s_ol(:,3))];

        % Find approximate center and radius of source projection
        s_center = [mean(s_limits(1:2,1)),mean(s_limits(3:4,1))];
        s_rad = mean([(s_limits(2,1)-s_limits(1,1)),
s_limits(4,1)-s_limits(3,1)])/2;

        %   Build polar list of source projection area (approximate as
        %   circular)
```

```
        b = [0,0];
        np = round(s_rad/resolution);
        dr = s_rad/np;
        for j=1:np
            nt = round(2*3.14159*j*dr/resolution);
            dt = 2*3.14159/nt;
            temp = j*dr*[cos((0:nt)'*dt),sin((0:nt)'*dt)];
            b = [b;temp];
        end

        %   Trim source point list by mirror dimensions
        x = b(:,1);
        y = b(:,2);
        outliers = excludedata(x,y,'box',[-dims(1,1)/2, dims(1,1)/2,
-dims(2,1)/2 dims(2,1)/2]);
        b = [x(~outliers),y(~outliers)];

        %   Calculate Bragg wavlength at each point in b
        map = [b,lambda(b,ap(k,:),theta_c,A,R,two_d,n)];

        %   Exclude points that do not fall within spectral range
        x = map(:,1);
        z = map(:,2);
        lam = map(:,3);
        outliers = excludedata(x,lam,'range',(lamda_center+[-d_lam/2 d_lam/2]));
        bragg_p = [x(~outliers),z(~outliers),lam(~outliers)];
        if size(bragg_p,1)>=1
            bragg_p = [bragg_p(:,1),sqrt(R^2-bragg_p(:,1).^2-bragg_p(:,2).^2),
bragg_p(:,2:3)];

            %   Find the vector for the refleted ray from each point that
            %   satisfies the Bragg condition
            for j=1:size(bragg_p,1)
                ar(j,1:3) = reflected(a,bragg_p(j,1:3));
            end

            %   Find the points in the film plane that intersect ar
            ft = plane_intersect(ar,bragg_p(:,1:3),fn,fx);

            %   Find the points in the aperature plane that intersect ar
            aper_int = plane_intersect(ar,bragg_p(:,1:3),aper_n,aper_x);

            %   Find the distance from the aperature center that each ray
            %   intersects the aperature plane
```

```
            aper_dis = [aper_int(:,1)-aper_x(1),aper_int(:,2)-aper_x(2),
aper_int(:,3)-aper_x(3)];
            aper_dis = sqrt(dot(aper_dis,aper_dis,2));

            %   Exclude points that fall outside of the aperature
            x = ft(:,1);
            y = ft(:,2);
            z = ft(:,3);
            outliers = excludedata(x,aper_dis,'range',[0 aper_rad]);
            ft = [x(~outliers),y(~outliers),z(~outliers)];

            %   Average the list of points, record blurring (std(ft,0,1)),
            %   and intensity (size(ft,1))
            ft = [mean(ft,1),std(ft,0,1),size(ft,1)];

            %   Concatenate data to wire(w) master point list
            f = [f;ft];
        end
    end
    if size(f,1)~=0
        %   Transform points from wire(w) to the film basis
        temp = [film_trans(f(:,1:3),fx),film_trans(f(:,4:6),[0 0 0])];
        q=q+1;  %   Increment imaged wire counter

        %   Add film basis points for wire(w) to cell array
        fp(q,1) = {temp(:,:)};
    end
end

%   Generate color indexing for imaged wires
colori = round(linspace(128,254,size(fp,1)));

%   Plot imaged points of array in 'Image' figure
if size(fp,1)>0
    figure('name','Image','numbertitle','off')
    errorbar(fp{1}(:,1),fp{1}(:,3),fp{1}(:,4),fp{1}(:,6),'color',
color_map(colori(1),:))
    hold on
    for j=2:size(fp,1)
errorbar(fp{j}(:,1),fp{j}(:,3),fp{j}(:,4),fp{j}(:,6),'color',
color_map(colori(j),:))
    end
    hold off
end
```

```
axis('image')
```

## E.3 Subroutines

### E.3.1 array_points Function

```
function y = array_points(n,d,h,rw,phase)

%   n    -   Array wire number
%   d    -   Array diameter in mm
%   h    -   Array height in mm
%   rw   -   Array wire diameter in mm
%   phase - Rotation of wire array about its axis in degrees

hres = 1;       %   Resolution in the vertical (z) direction in mm

%   Find the (x',y') coordinates of the center of each wire in the array
angles = (0:(n-1))'*360/n+phase;
center = (d/2)*[cosd(angles),sind(angles)];

%   Build list of points along the edges of each wire in the x'-z' plane
for k=1:n
    % Initialize array for left edge of wire k
    temp = ones(round(h/hres)+1,3);
    temp(:,1) = center(k,1)*temp(:,1)-rw;       % find x' of left edge
    temp(:,2) = center(k,2)*temp(:,2);          % use y' from 'center'
    temp(:,3) = (0:round(h/hres))'*hres-h/2;    % Go from bottom to top

    % Initialize array
    temp2 = flipud(temp);           % go from top to bottom
    temp2(:,1) = temp2(:,1)+2*rw;   % Make right edge relative to left
    temp = [temp;temp2];            % concatenate left and right edges
    p(k,1) = {temp};                % add data to cell array of wire edges
end

%   Plot resulting points
%{
figure(1);
hold on
for k=1:n
```

```
    plot(p{k}(:,1),p{k}(:,3))
end
hold off
%}

%   Return cell array containg edges of array wires in the x'-z' plane
y = p;
```

### E.3.2 film_pos Function

```
function y = film_pos(A,R,theta)
%   This function determines the position of the film in the Rowland basis
%   where the lens quation is satisfied, i.e. the array is in focus.
%
%   A   -   distance from mirror to array axis
%   R   -   radius of curvature of mirror
%   theta - Central angle of normal incidence, also rotation of x'-y'
%           (array basis)plane relative to x-y (Rowland basis) plane.

%   Find distance from mirror to film
B = 1/(2/R-1/A);

%   Find film center (x,y,0) in Rowland basis
x = B*sind(theta);
y = R-B*cosd(theta);

%   Find normal of film surface
n = [-sind(theta) cosd(theta) 0];

%   Return film normal and center coordinates in Rowland basis
y = [n;[x,y,0]];
```

### E.3.3 aper_pos Function

```
function y = aper_pos(R,theta_c)
%   This function generates the normal vector and center coordinates to a
%   limiting aperature placed on the Rowland circle
%
%   R   -   Radius of curvature of mirror (2*Rowland radius)
%   theta_c - Angle from normal incidence that aperature is rotated in the
```

```
%             x-y plane about the point (0,R,0)

%   Calculate the x and y coordinates of the aperature in the Rowland basis
x = R*cosd(theta_c)*sind(theta_c);
y = R-R*cosd(theta_c)^2;

%   Calculate the normal vector of the aperature
n = [-sind(theta_c),cosd(theta_c),0];

%   Return the normal and center of the aperature to the calling function
y = [n;[x,y,0]];
```

### E.3.4 color_m Function

```
function y = color_m
%   This function emulates the 'jet' colormap found in Matlab

d_lam_gray = 128;
d_gray = round(d_lam_gray/4);
c_trap = [linspace(0,254,d_gray)';254*ones(d_gray-1,1);linspace(254,0,d_gray+1)'];
red = [c_trap(1:round(2.5*d_gray),1);c_trap(round(2.5*d_gray-1):-1:1,1)];
green = [c_trap(:,1);zeros(d_gray-1,1);c_trap(2:size(c_trap,1),1)];
blue = [c_trap(round(d_gray/2):size(c_trap,1),1);zeros(round(1.5*d_gray),1)];
blue = [blue;blue((size(blue,1)-1):-1:1,1)];
color_map(:,3) = blue;
diff = size(blue,1)-size(green,1);
start = round(diff/2);
color_map(((start+1)+(1:size(green,1))),2) = green(:,1);
diff = size(blue,1)-size(red,1);
start = round(diff/2);
color_map(((start+1)+(1:size(red,1))),1) = red(:,1);
color_map = color_map/254;

y = color_map;
```

### E.3.5 r_circle Function

```
function y = r_circle(R)
%   This function generates a list ofpoints in the Rowland surface that
%   will be used to plot the Rowland circle in the x-y plane
```

```
res = 0.1;
np = round(2*3.14159*R/res);
dt = 2*3.14159/np;
for j=1:np
    rc(j,1:2) = [R*cos(j*dt),(R*sin(j*dt)+R)];
end
rc(:,3) = zeros(np,1);
y = rc;
```

### E.3.6 mirror_ol Function

```
function y = mirror_ol(dim,R)
%   This function generates an outline of the rectangular mirror in the
%   Rowland basis
%
%   dim   -   mirror dimensions [width, height] in mm
%   R     -   mirror radius of curvature

%   Build liast of mirror corners starting from lower left and going
%   counter clockwise, returning to [0,0]
ol = [0,0;dim(1,1),0;dim;0,dim(1,2);0,0];

%   Shift outline origin from lower left to center of dimensions
ol(:,1) = ol(:,1)-dim(1,1)/2;
ol(:,2) = ol(:,2)-dim(1,2)/2;

%   Move y-column to z-column
ol(:,3) = ol(:,2);

%   Use R as the y-coordinate
ol(:,2) = R*ones(size(ol,1),1);

%   Return outline
y = ol;
```

### E.3.7 round_source Function

See Appendix F, F.2.1.

### E.3.8 lambda Function

See Appendix F, F.2.3.

### E.3.9 reflected Function

```
function y = reflected(a,m)
%   This function finds the reflection of the vector from point a to m
%   about the line from the origin to the point m in the plane formed by
%   points a, m, and the origin.

%   Find the distance from the origin to point m.
R = sqrt(m*m');

%   Build the first transformation tensor which is a pre rotation and
%   rotates the x-y plane such that m' will lie in the x'=0 plane
tran = [m(2)/R m(1)/R 0;-m(1)/R m(2)/R 0;0 0 1];

%   Transform a and m to a' and m'
ap = a*tran;
mp = m*tran;

%   Build the second tranformation tensor which is a pure rotation about
%   the x' axis and will transform m' so that m'' will lie on the y'' axis
tranp = [1 0 0;0 mp(2)/R -mp(3)/R;0 mp(3)/R mp(2)/R];

%   Tranform a' and m' to a'' and m''
app = ap*tranp;
mpp = mp*tranp;

%   Build the reflection tensor
reflect = [-1 0 0;0 1 0;0 0 -1];

%   Reflect a'' about the y'' axis in the plane formed by a'', m'' (which
%   lies on the y'' axis), and the origin, result is ar''
appr = app*reflect;

%   Transform ar'' to ar'
apr = (tranp*appr')';

%   Transform ar' to ar
```

```
ar = (tran*apr')';

%   Return reflected vector
y = ar;
```

### E.3.10 plane_intersect Function

```
function y = plane_intersect(ar,m,n,x)
%   This function finds the points on the plane defined by the coordinate,
%   x, and the normal vector, n, where it intersects the vectors, ar, which
%   also pass through the respective points, m.

n = [n(1)*ones(size(m,1),1),n(2)*ones(size(m,1),1),n(3)*ones(size(m,1),1)];
x = [x(1)*ones(size(m,1),1),x(2)*ones(size(m,1),1),x(3)*ones(size(m,1),1)];
t = dot((x-m),n,2)/dot((ar-m),n,2);
fp = m + t*(ar-m);
y = fp;
```

### E.3.11 film_trans Function

```
function y = film_trans(f,fx)
%   This function transforms the points in the list f from the Rowland
%   basis to the film basis.
%
%   f   -   list of points to be transformed
%   fx  -   location of film center on the Rowland basis

f = f-[fx(1)*ones(size(f,1),1),fx(2)*ones(size(f,1),1),fx(3)*ones(size(f,1),1)];
fpx = sign(f(:,1)).*sqrt(f(:,1).^2+f(:,2).^2);
fpy = zeros(size(f,1),1);
fpz = f(:,3);
fp = [fpx fpy fpz];
y = fp;
```

APPENDIX F

**MATLAB SCRIPTS**

## F.1 Abel Inversion Function

```
function y = abel_inv(dat)
%   This function performs a cylindrical Abel inversion on the input matrix
%   called 'dat'. This matrix should be a two column list where the first
%   column is radial position and the second column is the chordal integral
%   value (areal density for instance).

% Determine radial position step size
dy = dat(2,1)-dat(1,1);

% Compute the discrete radial derivative of chordal integral
dat_p = diff(dat(:,2))/dy;

% Build list of indices that fall between each index of dat_p
x = (1:size(dat_p,1))'+0.5;

% Interpolate derivative values so that the length of dat_p equals the
% length of dat.
dat_p = interp1(x,dat_p,(1:size(dat,1))','linear','extrap');
a = size(dat,1);

%   Calculate Abel integral values, note method to avoid singularity at r=y
for n=1:size(dat_p,1)
    abel(n,1) =
-dy/3.14159*trapz(dat_p(n:a,1)./((dat(n:a,1).^2-0.999*dat(n,1)^2).^(1/2)));
end

%   Return position list and Abel transform
y = [dat(1:a,1),abel];
```

## F.2 Crystal Mapping Function

```
function y=crystal_map(ap,sp,diam)
%   This function generates a mapping of the wavelengths that reflect from
%   the surface of a spherically bent crystal.
%
```

```
%   ap  -   object point of interest in object (primed) basis
%   sp  -   source location in object basis
%   diam -  diameter of source

theta_c = 4.37;         % Central angle of indcidence measured from mirror
                        % normal in degrees, also rotation of x'-y' plane
                        % relative to x-y plane

A = 160;                % Distance from mirror center (0,R,0) to object
                        % origin (0',0',0') in mm

R = 182;                % Mirror radius of curvature in mm
two_d = 19.96;          % 2d spacing of crystal lattice in angstroms
n=3;                    % Order of reflection to be used
lamda_center = 6.6343;  % Wavelength of incident radiation in angstroms
d_lam = 0.005;          % Spectral width of incident radiation in angstroms
dimensions = [50;20];   % Dimensions of rectangular mirror (width x height)
resolution = .1;        % Resolution of mirror surface map in mm

%   Generate projection of source outline through ap onto mirror surface
s_ol = round_source(diam,ap,sp,theta_c,A,R);

%   Shift source projection so that the lower left corner of the mirror
%   dimensions is at (0,0) and grid mapping has unit spacing
s_plot = [s_ol(:,1)+dimensions(1,1)/2,s_ol(:,3)+dimensions(2,1)/2]/resolution;

% Generate mirror grid coordinates
bx = (-dimensions(1,1)/2):resolution:dimensions(1,1)/2;
bx=bx';
by = (-dimensions(2,1)/2):resolution:dimensions(2,1)/2;
by=by';

%   Calculate the wavelength that satisfies the Bragg condition at each
%   point in the mirror grid
map=[];
for j=1:size(bx,1)
    b = [bx(j)*ones(size(by,1),1),by];
    map = [map,lambda(b,ap,theta_c,A,R,two_d,n)];
end

%   Generate a color map with maximum contrast over the range of
%   wavelengths in the crystal map
lam_max = max(max(map));
lam_min = min(min(map));
```

```
lam_range = lam_max-lam_min;
center_gray = round((lamda_center - lam_min)*254/lam_range);
d_lam_gray = round(d_lam*254/lam_range);
d_gray = round(d_lam_gray/4);
c_trap = [linspace(0,254,d_gray)';254*ones(d_gray-1,1);linspace(254,0,d_gray+1)'];
red = [c_trap(1:round(2.5*d_gray),1);c_trap(round(2.5*d_gray-1):-1:1,1)];
green = [c_trap(:,1);zeros(d_gray-1,1);c_trap(2:size(c_trap,1),1)];
blue = [c_trap(round(d_gray/2):size(c_trap,1),1);zeros(round(1.5*d_gray),1)];
blue = [blue;blue((size(blue,1)-1):-1:1,1)];

color_map(:,3) = blue;
diff = size(blue,1)-size(green,1);
start = round(diff/2);
color_map(((start+1)+(1:size(green,1))),2) = green(:,1);
diff = size(blue,1)-size(red,1);
start = round(diff/2);
color_map(((start+1)+(1:size(red,1))),1) = red(:,1);
color_map = [zeros(255+d_lam_gray,3);color_map;zeros(255+d_lam_gray,3)];
color_map = color_map/254;

if (center_gray+d_lam_gray)<1 || (center_gray-d_lam_gray)>255
    c_map = zeros(255,3);
else
    center_map = round(size(color_map,1)/2);
    start = center_map-center_gray+1;
    c_map = color_map((0:254)+start,:);
end
c_map(256,:)=[1 1 1];

gray_map = round((map - lam_min)*254/lam_range);
max(max(gray_map));
min(min(gray_map));

legend = round(linspace(0,254,size(gray_map,1)))';
for j=1:4
    legend = [legend,legend];
end

gap = 255*ones(size(gray_map,1),round(size(legend,2)/2));

disp = [gray_map,gap,legend];
figure('name','Crystal Map','numbertitle','off')
imagesc(disp,[0 255])
colormap(c_map)
```

```
axis('image')
line(s_plot(:,1),s_plot(:,2),'color','b');
ax1 = gca;
set(ax1,'xtick',1:(dimensions(1,1)/(resolution*10)):(dimensions(1,1)/resolution+1));
set(ax1,'xticklabel',-(dimensions(1,1)/2):(dimensions(1,1)/10):(dimensions(1,1)/2));
set(ax1,'ytick',1:(dimensions(2,1)/(resolution*4)):(dimensions(2,1)/resolution+1));
set(ax1,'yticklabel',(dimensions(2,1)/2):-(dimensions(2,1)/4):-(dimensions(2,1)/2));
set(ax1,'ticklength',[0 0]);
xlabel('Horizontal Mirror Position (mm)');
ylabel('Vertical Mirror Position (mm)');
ax2 = axes('yaxislocation','right','color','none','xtick',[],'ytick',
                    [0:round(size(disp,1)/10):round(size(disp,1)/10)*10]);
axis([0 size(disp,2) 0 size(disp,1)])
axis('image')
set(ax2,'yticklabel',linspace(lam_max,lam_min,11));
ylabel('Wavelength \AA','interpreter','latex','fontsize',10)
```

### F.2.1 Round Source Function

```
function y = round_source(diam,ap,sp,theta_c,A,R)
%   This function generates a list of coordinates that describe the outline
%   of a spherical source at the source loaction, sp (s'). This outline
%   lies in the x'-z' plane, defined by the first and third column of the
%   ap and sp vectors. The "source" function is then called to refer this
%   outline to the mirror surface in the Rowland basis (unprimed). The
%   source outline referred to the mirror surface in te unprimed basis is
%   then returned to the calling function. All distances should have the
%   same units unless otherwise noted.
%
%   diam    -   x-ray source diameter
%   ap      -   object point of interest in the primed (object) basis
%   sp      -   location of x-ray source in primed (object) basis
%   theta_c -   central angle or normal incidence from source to mirror,
%               also should be rotation of x'-y' plane relative to x-y
%   A       -   distance from mirror center to primed origin (object
%               center)
%   R       -   radius of curvature of mirror (Rowland cicle diameter)

% Spacing of outline points around circumference in mm
resolution = .1;

% Source radius in mm
```

```
radius = diam/2;

% Approximate angle between each point in outline
dtheta = resolution/diam;

% Number of points in outline
np = round(2*3.14159/dtheta);

for j = 1:np
    %   Find each x-coordinate of outline
    border(j,1) = radius*cos(j*dtheta);

    %   Find each z-coordinate of outline
    border(j,3) = radius*sin(j*dtheta);
end

% Use y-coordinate of sp as outline y-values
border(:,2) = sp(2)*ones(size(border,1),1);

% Copy first coordinate to last coordinate
border = [border;border(1,:)];

% Return projection of source outline through ap onto mirror surface
y = source(ap,border,theta_c,A,R);
```

### F.2.2 Source Function

```
function  y = source(ap,sp,theta_c,A,R)
%   This function projects the list of source points in the obect basis,
%   sp, through the object point of interest, ap, onto the mirror surface.
%   The function then returns the projected source outline in the
%   Rowland (unprimed) basis, to the calling function.
%
%   ap  -   object point of interest in object basis
%   sp  -   list of points (source outline) to be projected through ap onto
%           the mirror surface
%   theta_c     -   Rotation of x'-y' plane realtive to x-y plane
%   A   -   distance from center of mirror surface (0,R,0) to center of
%           object (0',0',0')
%   R   -   radius of curvature of mirror

% Transform a' to a, see Eqn. B.5-7 in Appendix B
```

```
ax = ap(1)*cosd(theta_c) + (ap(2)-A)*sind(theta_c);
ay = (ap(2)-A)*cosd(theta_c) - ap(1)*sind(theta_c) + R;
az = ap(3);

% Build list of "a" equal in length to sp (for convenience)
a = [ax*ones(size(sp,1),1), ay*ones(size(sp,1),1), az*ones(size(sp,1),1)];

% Transform s' coordinates to Rowland basis
sx = sp(:,1)*cosd(theta_c) + (sp(:,2)-A)*sind(theta_c);
sy = (sp(:,2)-A)*cosd(theta_c) - sp(:,1)*sind(theta_c) + R;
sz = sp(:,3);
s = [sx sy sz];

% Find vectors form source outline points through object point of interest
b = a-s;

% Find quantities necessary to calculate intersection points of b-vectors
% with mirror surface (see Eqn. B.18 in Appendix B)
b_dot_s = dot(b,s,2);
bsqr = dot(b,b,2);
ssqr = dot(s,s,2);

%   Find the points on mirror surface where b-vectors intersect. Keep the
%   largest real roots grater than zero (points that intersect Rowland
%   sphere on mirror side).
p=[];
for j=1:size(sp,1)
    t = roots([bsqr(j) 2*b_dot_s(j) ssqr(j)-R^2]);
    if imag(t(1,1))~=0
        t(1,1)=0;
    end
    if imag(t(2,1))~=0
        t(2,1)=0;
    end
    t = max(max(t));

    %   Verify that there is a real root greater than zero
    if t==0
        continue
    end

    %   Add valid intersect point to list p
    p = [p;s(j,:)+t*b(j,:)];
end
```

```
% Return projection of source outline through ap onto mirror surface.
y = p;
```

### F.2.3 Lambda Function

```
function  y = lambda(b,ap,theta_c,A,R,two_d,n)
%   This function calculates the wavelength that satisfies the Bragg
%   condition at each point in list b.
%
%   b   -   list of coordinates (bx,bz) in Rowland basis to find Bragg
%           condition wavelength
%   ap  -   object point of interest in object basis where radiation is
%           emitting from
%   theta_c -   rotation of x'-y' (object) plane relative to x-y (Rowland)
%               plane
%   A   -   distance from mirror center (0,R,0) to object origin (0',0',0')
%   R   -   radius of curvature of mirror
%   two_d - crystal lattice spacing in angstroms
%   n   -   order of reflection to be used in Bragg calculation

%   Transform a' to a
ax = ap(1)*cosd(theta_c) + (ap(2)-A)*sind(theta_c);
ay = (ap(2)-A)*cosd(theta_c) - ap(1)*sind(theta_c) + R;
az = ap(3);

%   Build list of object points having same length as b list
a = [ax*ones(size(b,1),1), ay*ones(size(b,1),1), az*ones(size(b,1),1)];

%   Calculate y-components of points in b in order for them to lie on the
%   mirror surface
by = R*sqrt(1-(b(:,1).^2+b(:,2).^2)/R^2);

%   Build 3-D list of mirror intersection points
b = [b(:,1) by b(:,2)];

%   Calculate the values needed to evaluate Eqn. B.15 in Appendix B
b_dot_a = dot(b,a,2);
mag_b_min_a = sqrt(dot((b-a),(b-a),2));

%   Return the column list of wavelengths
y = (two_d/(R*n))*(R^2-b_dot_a)./(mag_b_min_a);
```

APPENDIX G
**IMAGES**

## G.1 Introduction

This appendix contains the raw data from which the results in chapters 10 through 12 were derived. A chart is included for each experiment that contains the electrical signals that give the timing of each image relative to the start of generator current. Images from all experiments where the STAR diagnostic was fielded are shown (false colored) along with the wire-array parameters of each experiment. The timing and wire diameter of each backlighting X-pinch are also given in table G.1.

As mentioned in chapter 11, approximately half of these images were not suitable for quantitative analysis due to the presence of multiple images as a result of multiple exposures from re-pinching in the backlighting X-pinches. The spatial dislocations of multiple exposures (if any) for each image are given in table G.2. The dislocation distances in table G.2 are referred to the wire-array. Images that contained multiple exposures that were displaced radially by more than 8$\mu$m and/or axially by more than 80$\mu$m at the array (2$\mu$m and 20$\mu$m at the X-pinch), were rejected from quantitative analysis.

Table G.1: Backlighting X-pinch parameters. The timing of each backlighter is given in nanoseconds relative to the start of current, along with the diameter of Mo wire ($\mu$m) that each X-pinch was made from.

| Shot | $t_C$ | $t_O$ | $t_B$ | $t_R$ | $t_A$ | $\phi_C$ | $\phi_O$ | $\phi_B$ | $\phi_R$ | $\phi_A$ |
|---|---|---|---|---|---|---|---|---|---|---|
| 784 | 60 | 70 | 72 | 83 | | 10.2 | 12.7 | 17.5 | 20.3 | 22.9 |
| 785 | 92 | 134 | 108 | 158 | 147? | 12.7 | 22.9 | 17.5 | 25.4 | 20.3 |
| 786 | | | | | | 12.7 | 22.9 | 17.5 | 25.4 | 20.3 |
| 787 | 80 | 109 | 90 | 133 | 93? | 17.5 | 25.4 | 20.3 | 30 | 22.9 |
| 788 | 80 | 110 | 95 | 151 | | 17.5 | 25.4 | 20.3 | 30 | 22.9 |
| 789 | 74 | 111 | 94 | | | 17.5 | 25.4 | 20.3 | 30 | 22.9 |
| 790 | | | 89 | 145 | | 17.5 | 25.4 | 20.3 | 30 | 22.9 |
| 791 | 88 | 122 | 108 | 168 | | 17.5 | 25.4 | 20.3 | 30 | 22.9 |
| 792 | 88 | 144 | | | | 17.5 | 25.4 | 20.3 | 30 | 22.9 |
| 793 | 73 | 139 | 85 | 171 | 108 | 12.7 | 25.4 | 17.5 | 30 | 20.3 |
| 794 | 87 | 106 | 92 | 168 | 116 | 17.5 | 25.4 | 20.3 | 30 | 22.9 |
| 795 | 78 | 109 | 89 | | 104 | 17.5 | 25.4 | 20.3 | 30 | 22.9 |
| 796 | 77 | 115 | 90 | | | 17.5 | 25.4 | 20.3 | 30 | 22.9 |
| 797 | 87 | 110 | 93 | | 125 | 17.5 | 25.4 | 20.3 | 30 | 22.9 |
| 798 | 73 | 110 | 88 | | | 12.7 | 22.9 | 17.5 | 25.4 | 20.3 |
| 799 | 81 | 108 | 92 | 143 | 106 | 12.7 | 22.9 | 17.5 | 25.4 | 20.3 |
| 800 | 75 | 99 | 90 | | 99 | 12.7 | 22.9 | 17.5 | 25.4 | 20.3 |
| 801 | 85 | 119 | 96 | | | 12.7 | 22.9 | 17.5 | 25.4 | 20.3 |
| 802 | 69 | 89 | | 82 | 105 | 12.7 | 20.3 | 25.4 | 17.5 | 22.9 |
| 803 | 93 | | 103 | 74 | 150 | 17.5 | 25.4 | 20.3 | 12.7 | 22.9 |
| 804 | 146 | 101 | 124 | 92 | 117 | 30 | 20.3 | 25.4 | 17.5 | 22.9 |
| 805 | 175 | | | 94 | 120 | 30 | 20.3 | 25.4 | 17.5 | 22.9 |
| 806 | | | 140 | 98 | | 30 | 20.3 | 25.4 | 17.5 | 22.9 |
| 807 | 68 | 97 | | 138 | | 12.7 | 22.9 | 17.5 | 25.4 | 20.3 |
| 887 | | 112 | 79 | | 104 | | | | | |
| 888 | | 133 | 92 | | 111 | | | | | |
| 891 | | | 84 | | 127 | | | | | |
| 892 | | 107 | | | 150 | | | | | |

Table G.2: Maximum multiple image displacements in $\mu$m at the array.

| Shot | $C_{\delta x}$ | $C_{\delta y}$ | $O_{\delta x}$ | $O_{\delta y}$ | $B_{\delta x}$ | $B_{\delta y}$ | $R_{\delta x}$ | $R_{\delta y}$ | $A_{\delta x}$ | $A_{\delta y}$ |
|---|---|---|---|---|---|---|---|---|---|---|
| 785 | 12 | 121 | 19 | 46 | 0 | 47 | 10 | 35 | | |
| 786 | 8 | 91 | 14 | 241 | 137 | 92 | 81 | 21 | | |
| 787 | 3 | 53 | 6 | 40 | 2 | 13 | 28 | 160 | 0 | 21 |
| 791 | | | 8 | 38 | 0 | 39 | 16 | 112 | | |
| 792 | 1 | 70 | 9 | 81 | | | | | | |
| 793 | 10 | 167 | 2 | 12 | 83 | 6 | 34 | 163 | 147 | 4 |
| 794 | 10 | 185 | 0 | 43 | 4 | 40 | 13 | 44 | 21 | 169 |
| 795 | | | 10 | 114 | | | | | 4 | 111 |
| 797 | | | | | 0 | 62 | | | 2 | 148 |
| 798 | | | | | | | | | | |
| 799 | 0 | 81 | 16 | 101 | 10 | 59 | | | 1 | 53 |
| 800 | 7 | 72 | 0 | 27 | 12 | 43 | | | 0 | 26 |
| 801 | 11 | 140 | 3 | 180 | | | | | | |
| 802 | 4 | 35 | | | | | | | | |
| 803 | 3 | 46 | | | 9 | 118 | | | 30 | 130 |
| 804 | 0 | 48 | 4 | 98 | 3 | 55 | | | 4 | 24 |
| 806 | | | | | 2 | 36 | | | | |
| 807 | | | 76 | 349 | | | | | | |
| 887 | | | | | 26 | 170 | | | | |
| 888 | | | | | | | | | 27 | 2 |
| 891 | | | | | | | | | 120 | 9 |
| 892 | | | 323 | 6 | | | | | 2 | 170 |

Figure G.1: Shot 784 $R_0$ = 8mm $\phi_0$=10.2$\mu$m N=16

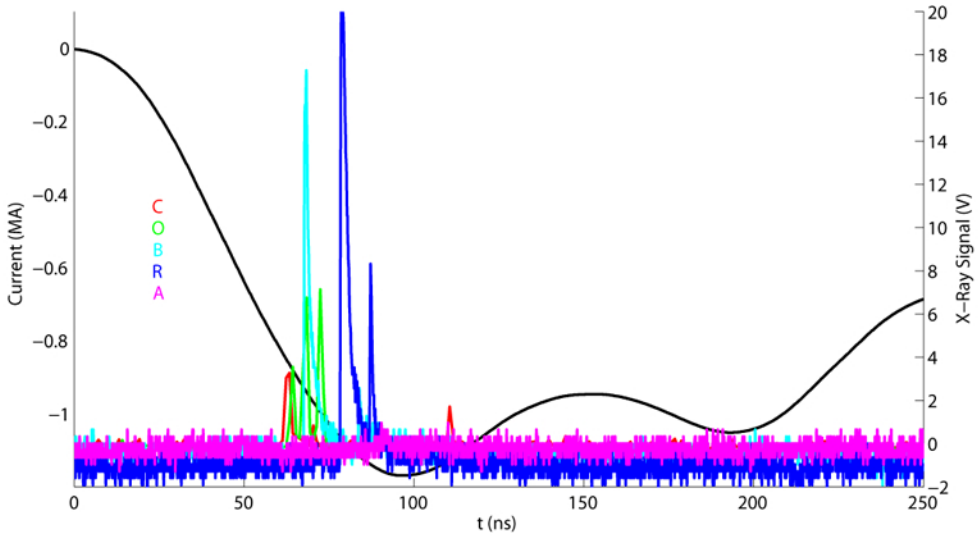


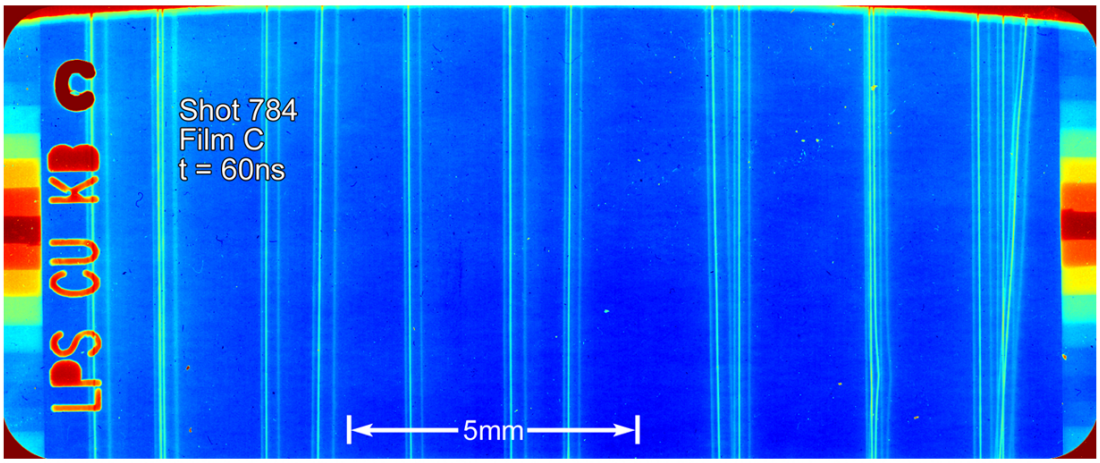


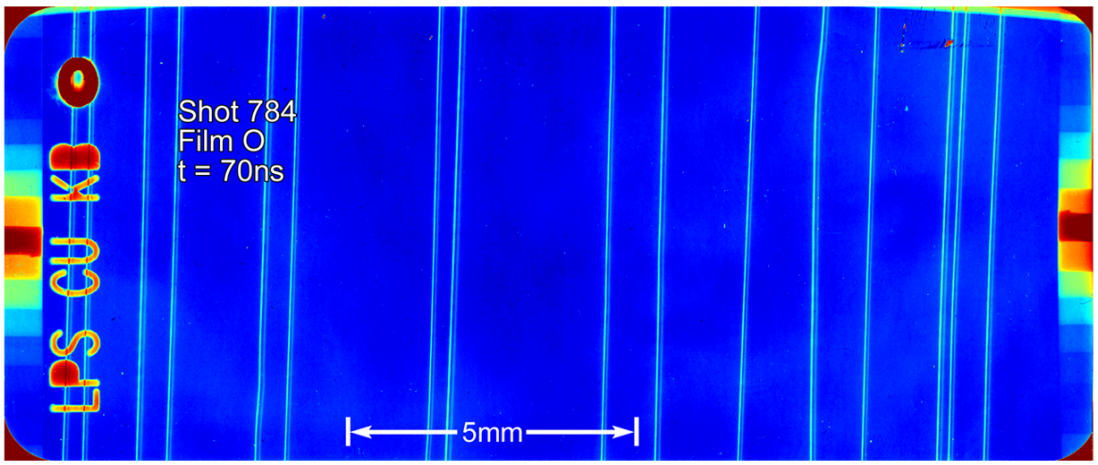

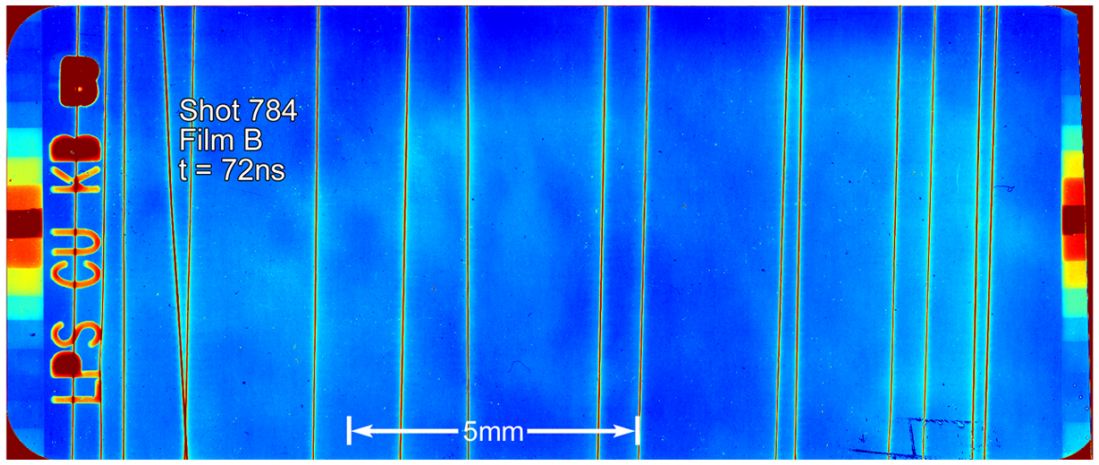
LPS CU KB B
Shot 784
Film B
t = 72ns
5mm

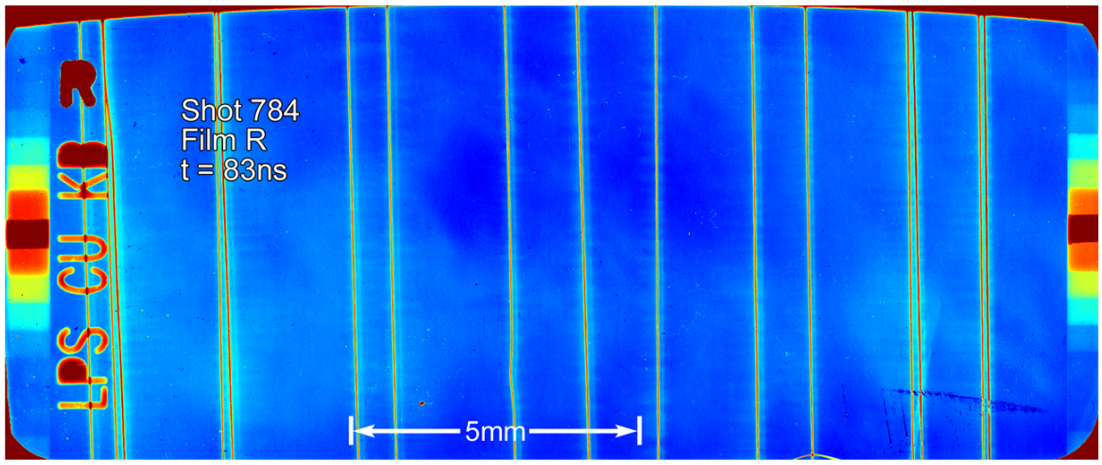
LPS CU KB R
Shot 784
Film R
t = 83ns
5mm

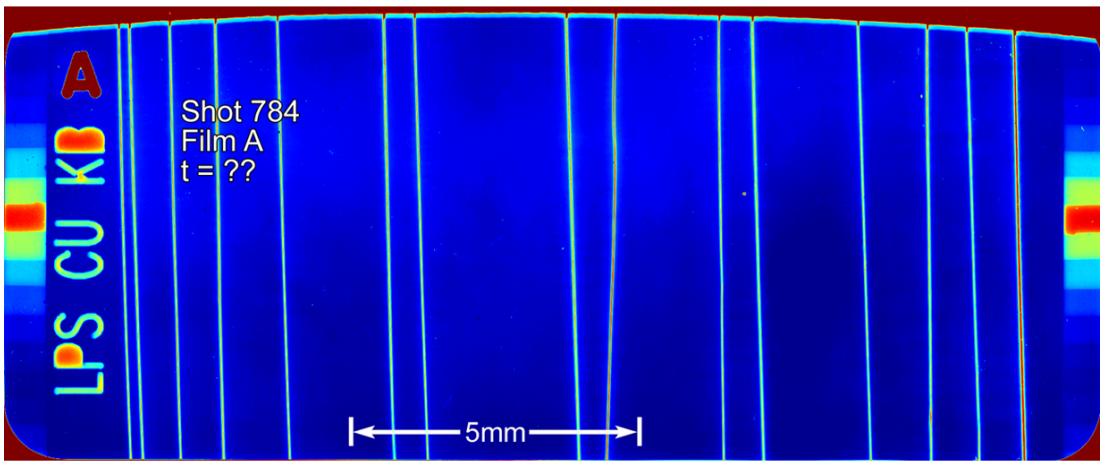
LPS CU KB A
Shot 784
Film A
t = ??
5mm

Figure G.2: Shot 785 $R_0$ = 6mm $\phi_0$=12.7$\mu$m N=10

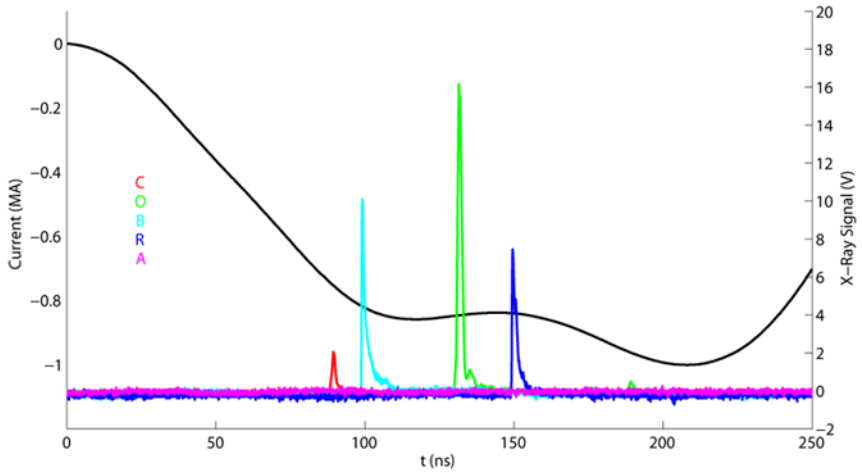


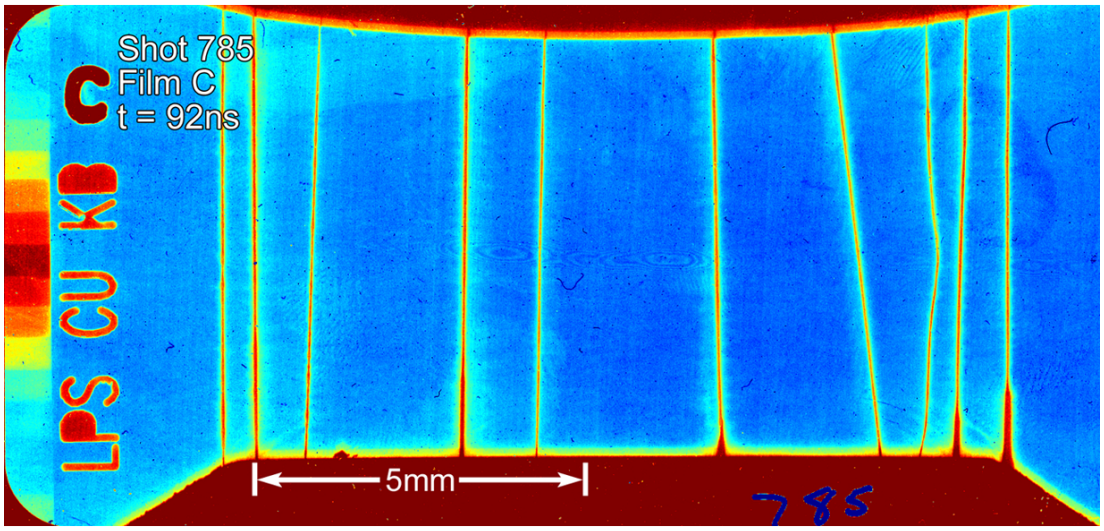


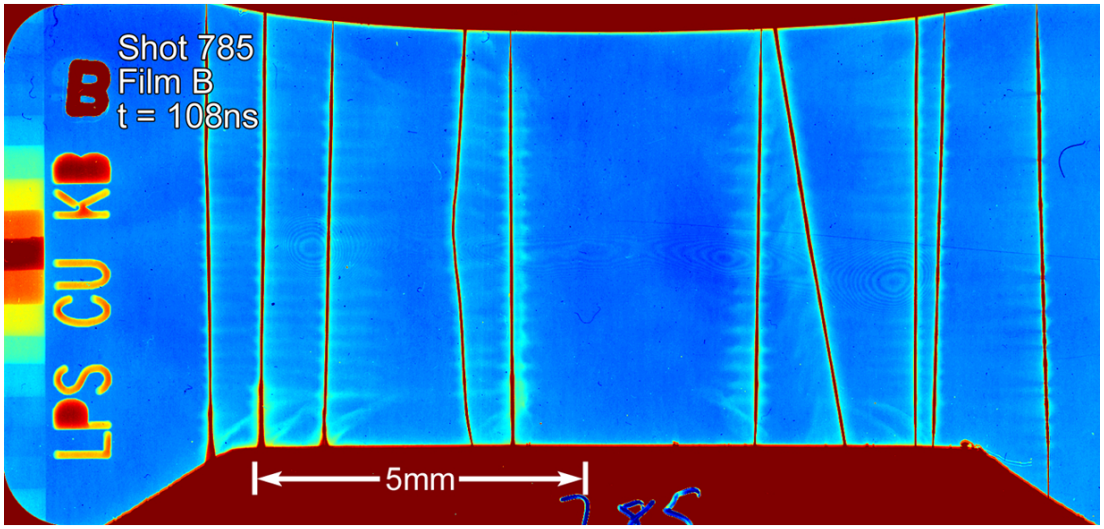

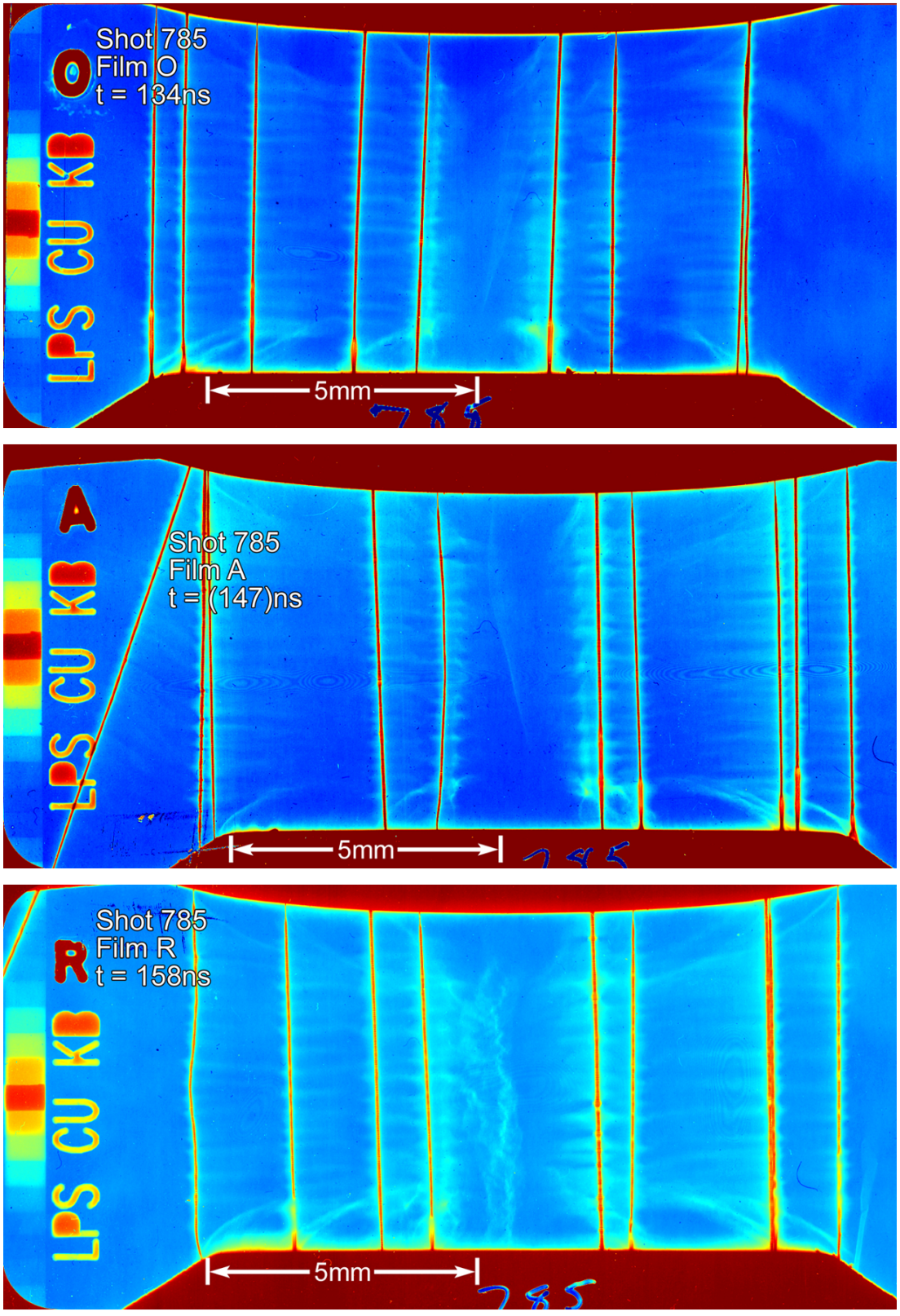
Shot 785
Film O
t = 134ns
O
LPS CU KB
5mm
785
Shot 785
Film A
t = (147)ns
A
LPS CU KB
5mm
785
Shot 785
Film R
t = 158ns
R
LPS CU KB
5mm
785

Figure G.3: Shot 786 $R_0$ = 6mm $\phi_0$=12.7$\mu$m N=10

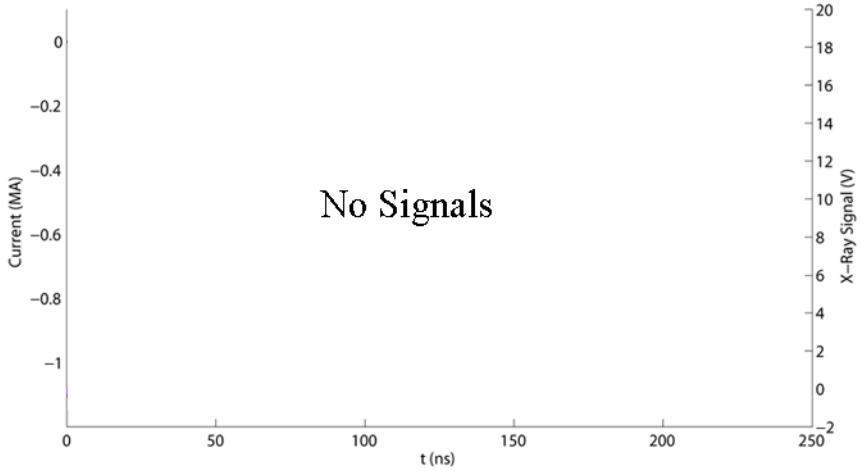


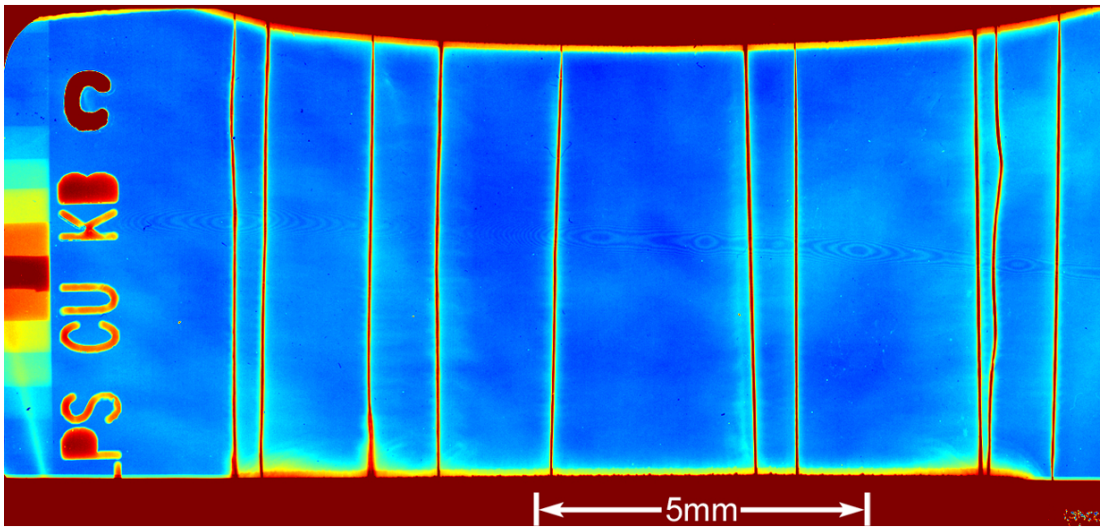


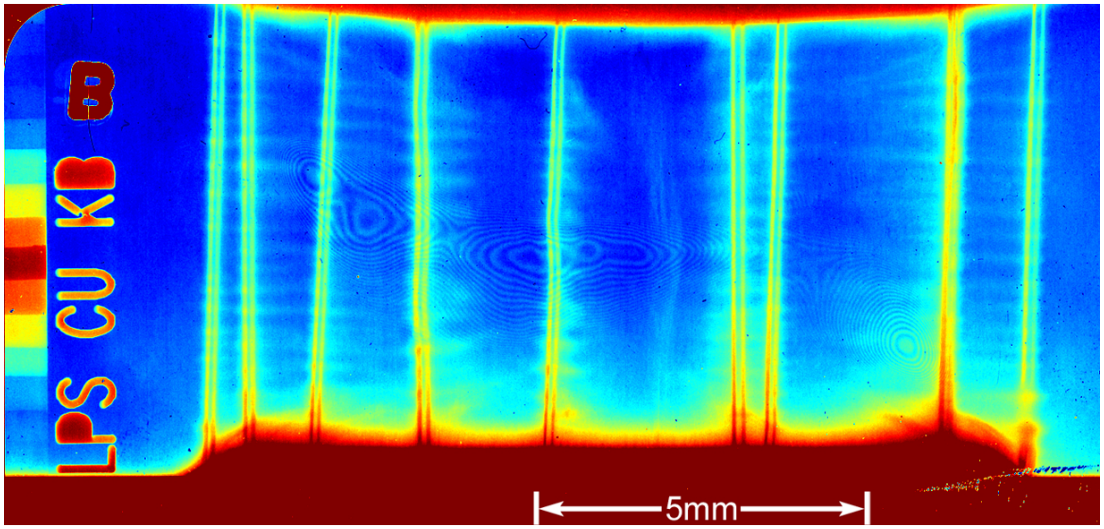

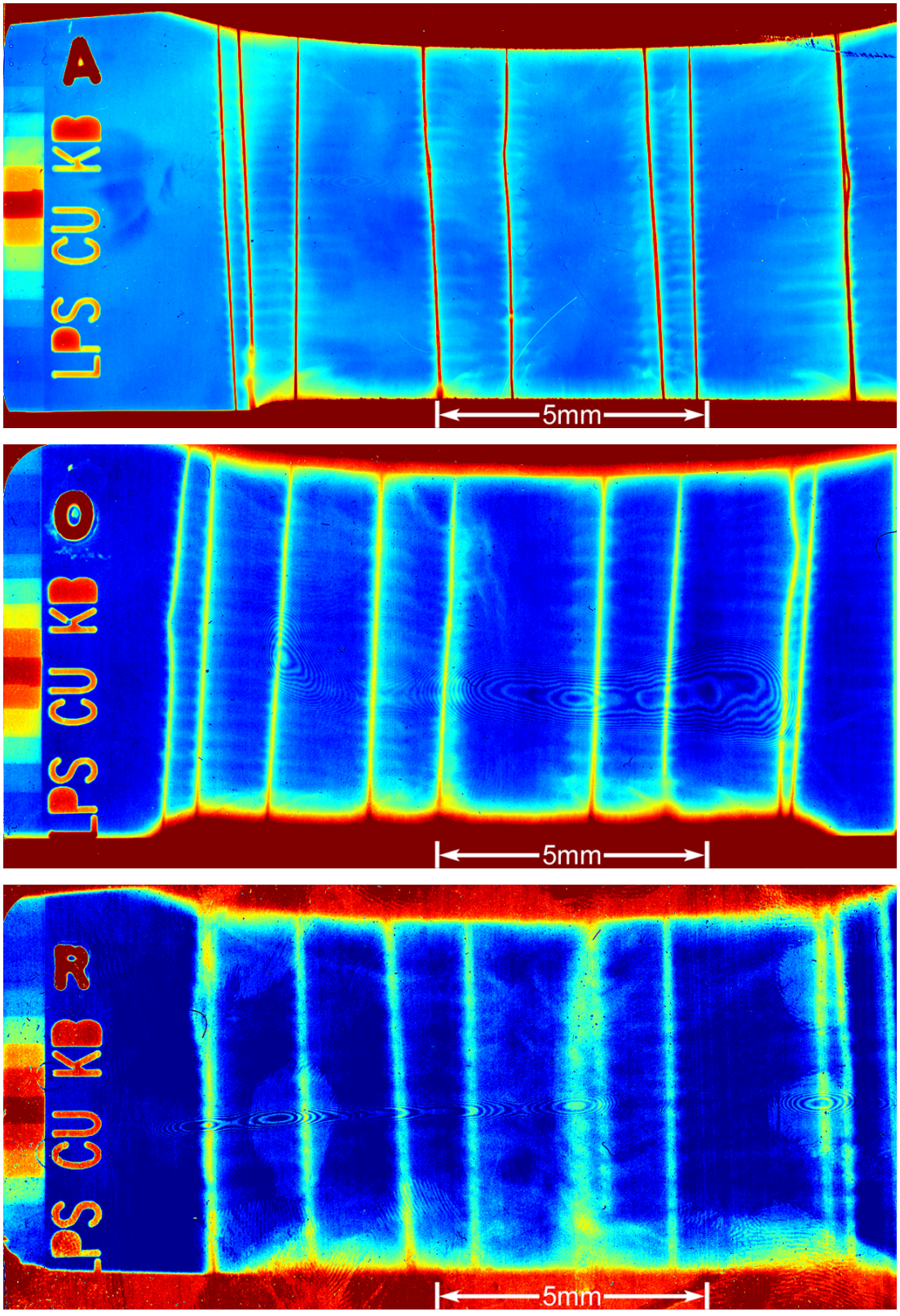
LPS CU KB A
5mm
LPS CU KB O
5mm
LPS CU KB R
5mm

Figure G.4: Shot 787 $R_0$ = 6mm $\phi_0$=12.7$\mu$m N=10

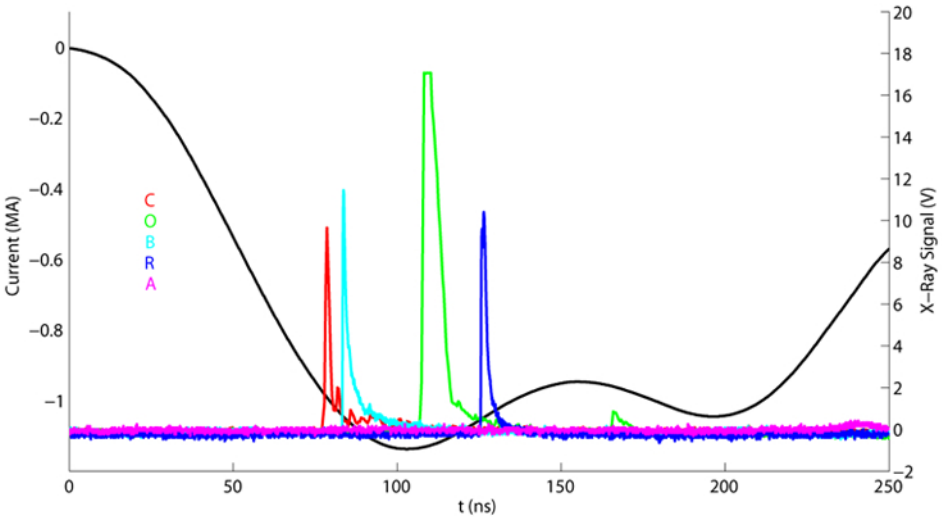


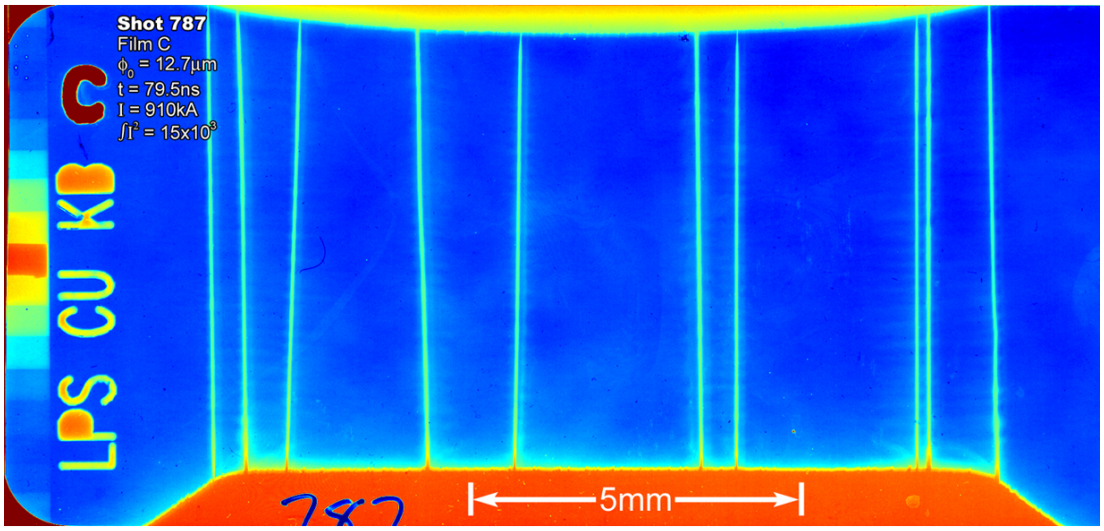


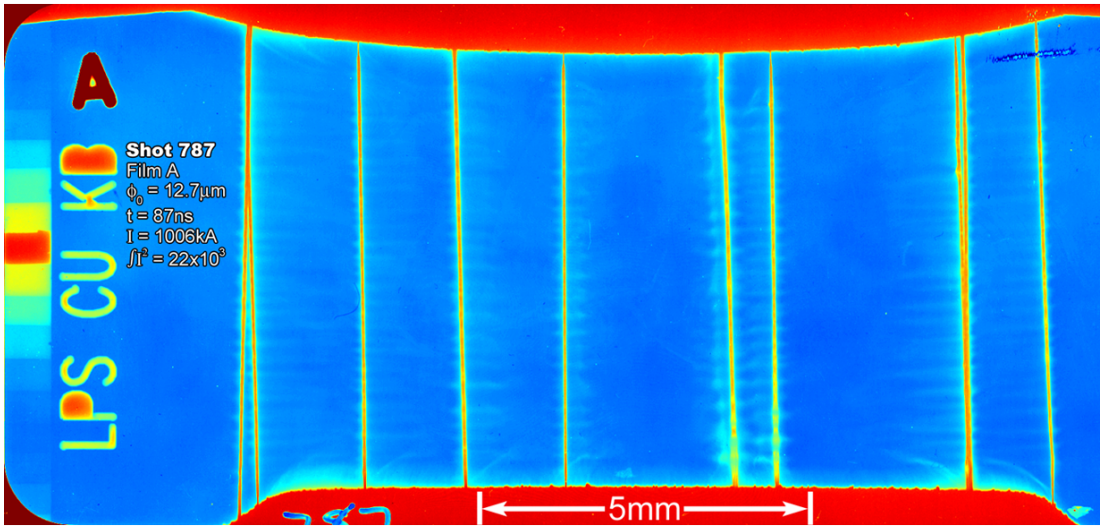

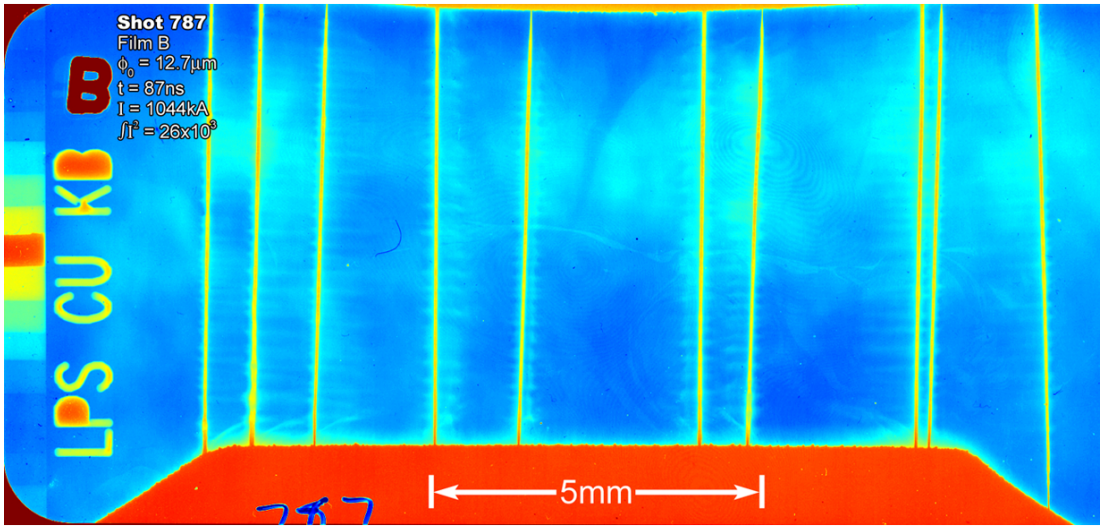
Shot 787
Film B
$\phi_0$ = 12.7µm
t = 87ns
I = 1044kA
$\int I^2$ = 26x10$^6$
B
LPS CU KB
787
5mm

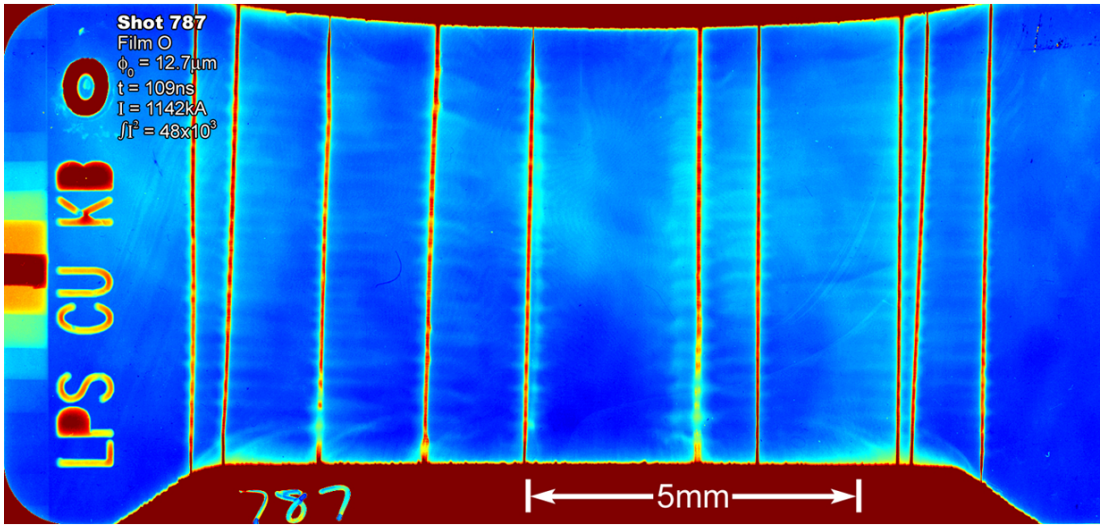
Shot 787
Film O
$\phi_0$ = 12.7µm
t = 109ns
I = 1142kA
$\int I^2$ = 48x10$^6$
O
LPS CU KB
787
5mm

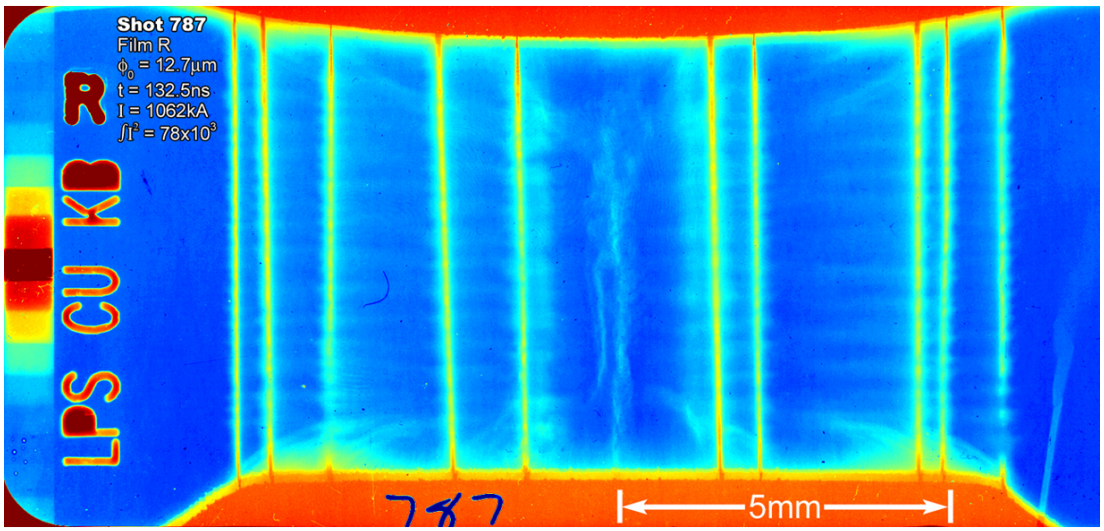
Shot 787
Film R
$\phi_0$ = 12.7µm
t = 132.5ns
I = 1062kA
$\int I^2$ = 78x10$^6$
R
LPS CU KB
787
5mm

Figure G.5: Shot 788 $R_0$ = 6mm $\phi_0$=10.2$\mu$m N=10

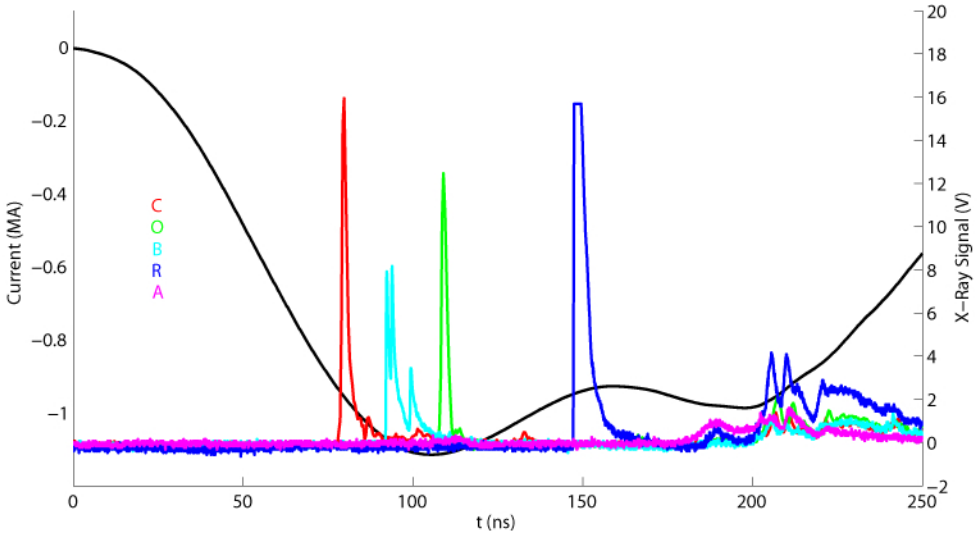


Figure G.6: Shot 789 $R_0$ = 6mm $\phi_0$=12.7$\mu$m N=10

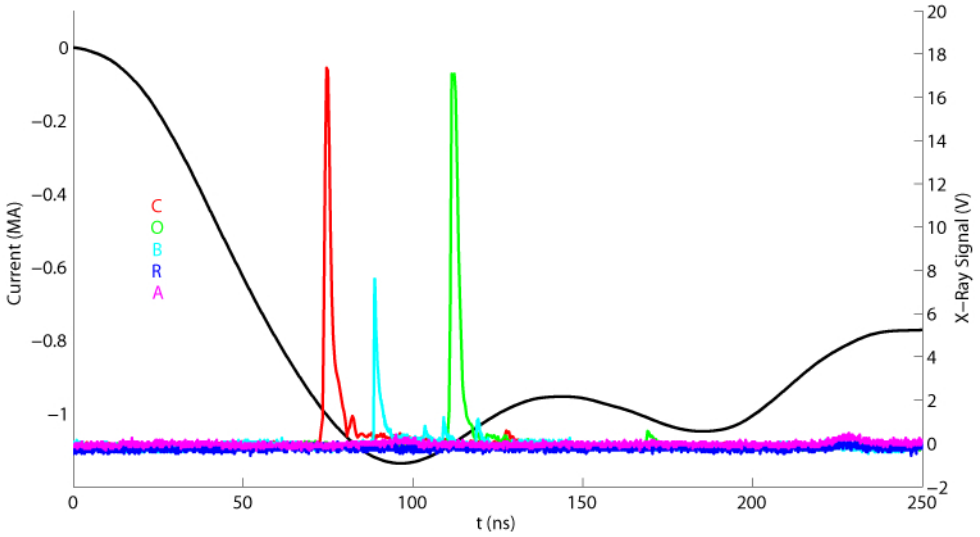

Figure G.7: Shot 790 $R_0$ = 6mm $\phi_0$=17$\mu$m N=10

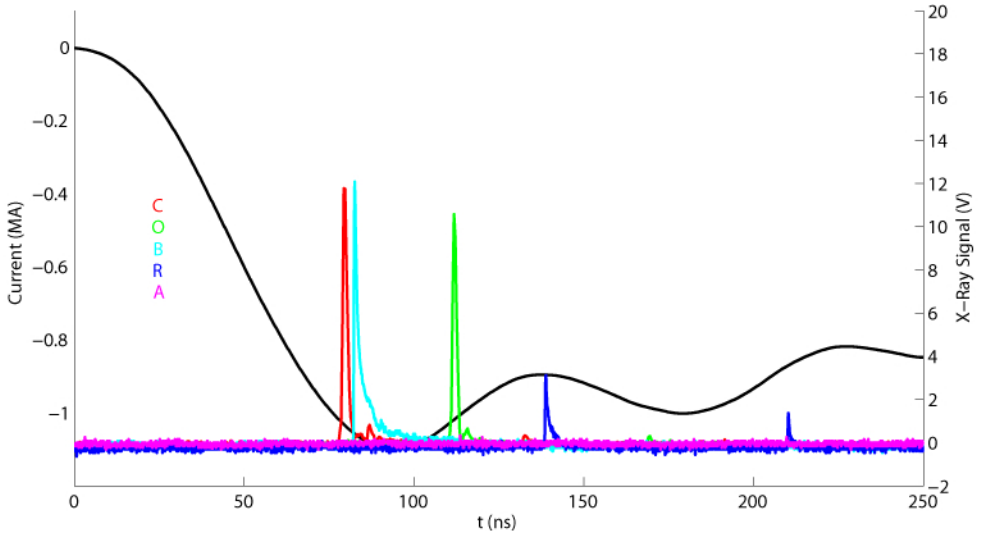

Figure G.8: Shot 791 $R_0$ = 6mm $\phi_0$=19.8$\mu$m N=10

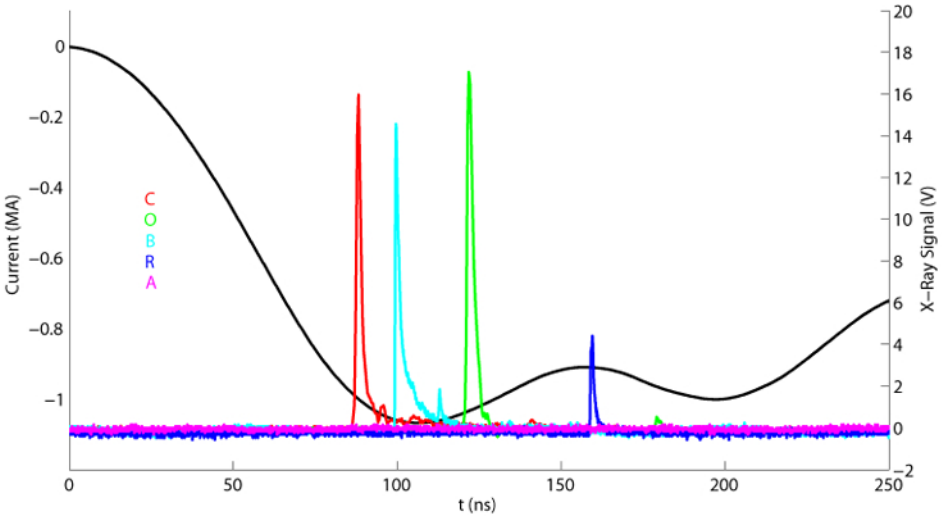


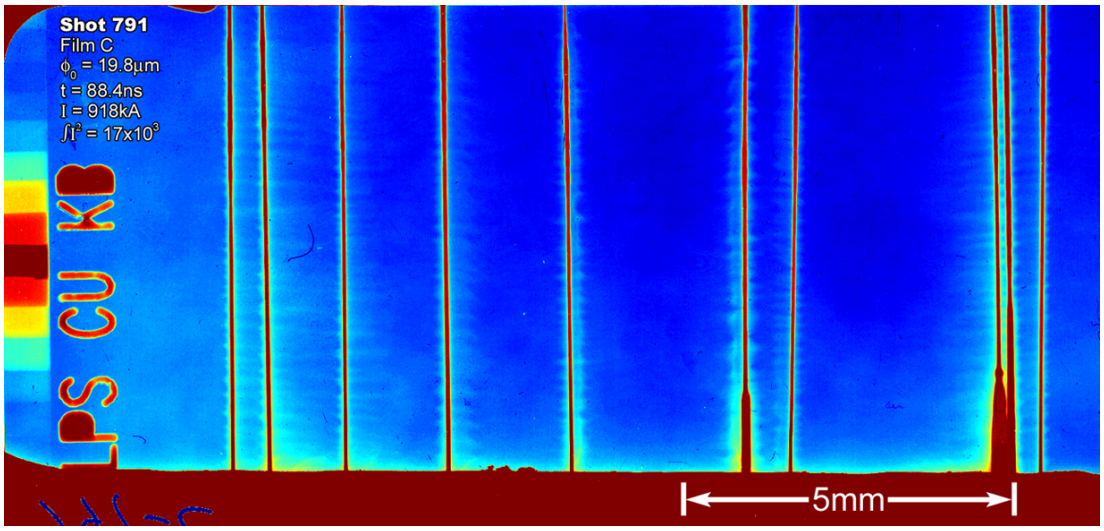


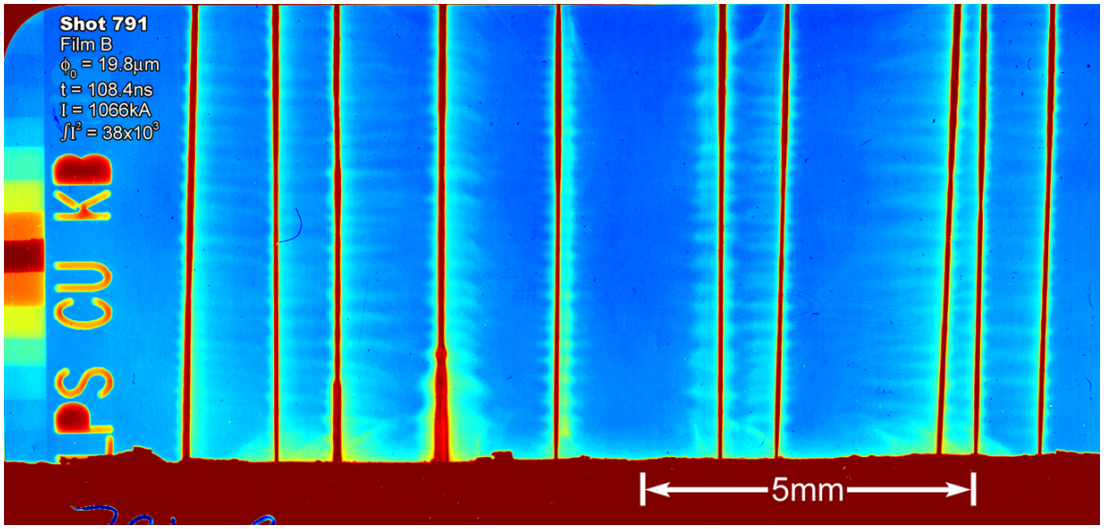

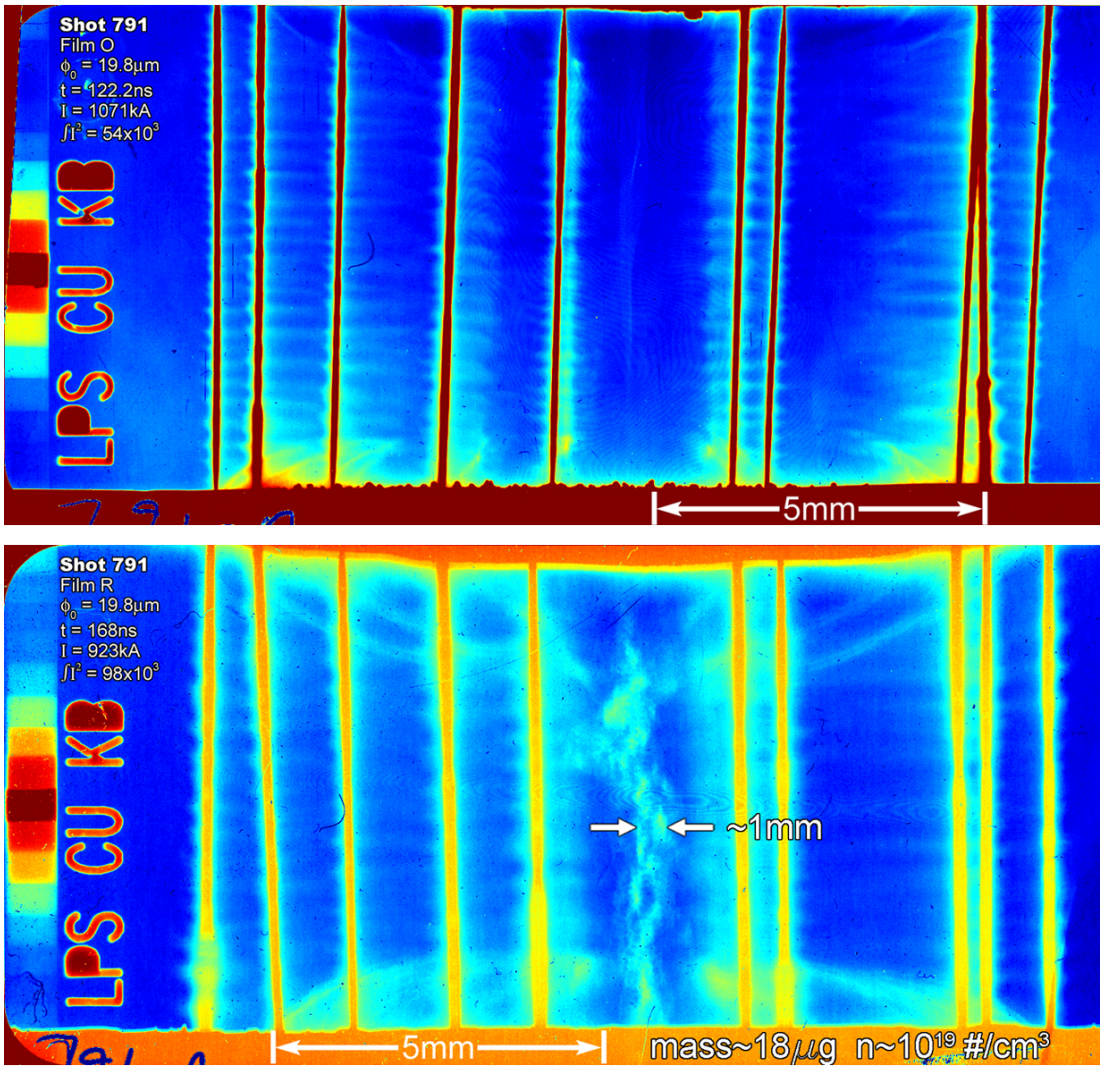
Shot 791
Film O
$\phi_0$ = 19.8μm
t = 122.2ns
I = 1071kA
$\int I^2$ = 54x10$^3$
LPS CU KB
5mm
Shot 791
Film R
$\phi_0$ = 19.8μm
t = 168ns
I = 923kA
$\int I^2$ = 98x10$^3$
LPS CU KB
~1mm
5mm
mass~18$\mu$g n~10$^{19}$ #/cm$^3$

Figure G.9: Shot 792 $R_0$ = 6mm $\phi_0$=25.4$\mu$m N=10

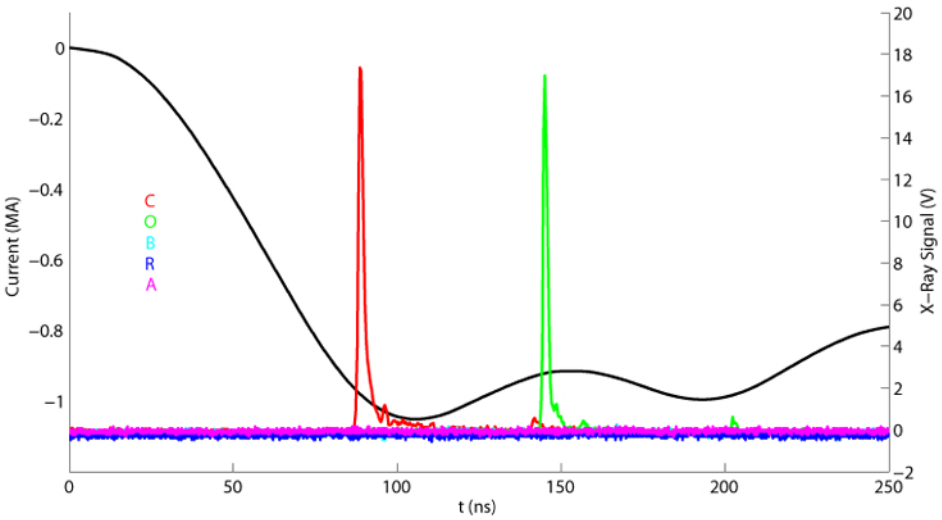


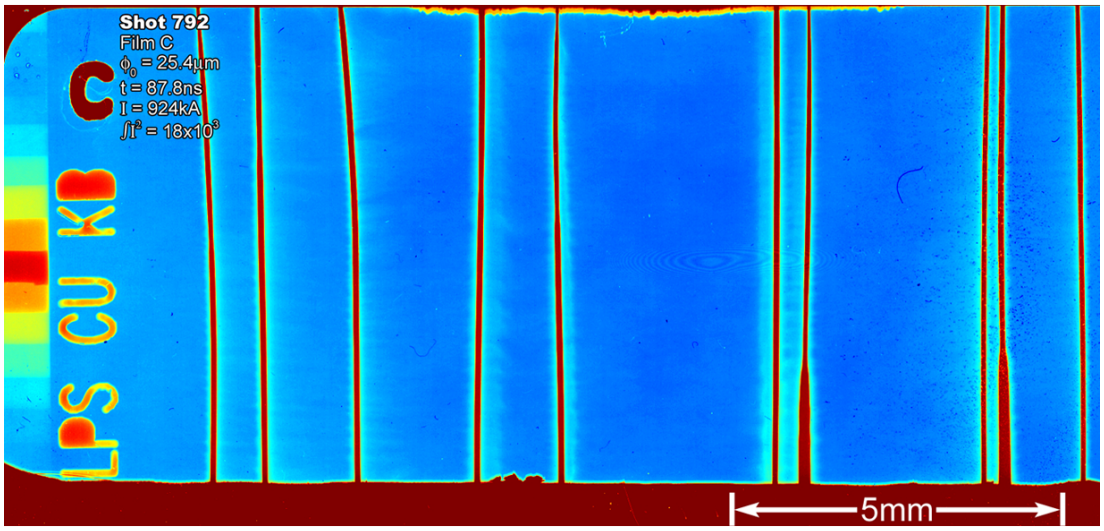


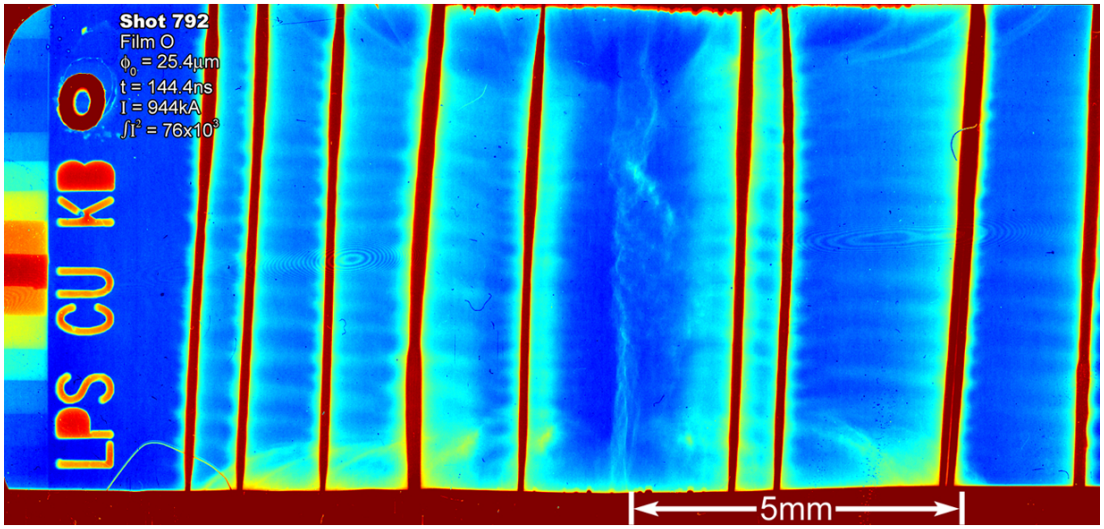

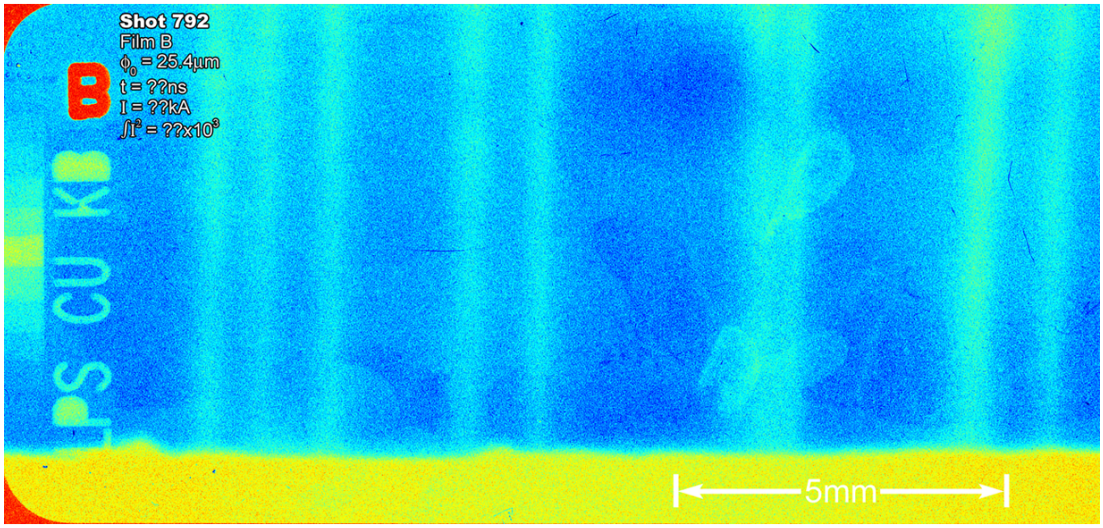
Shot 792
Film B
$\phi_0$ = 25.4μm
t = ??ns
I = ??kA
$\int I^2$ = ??x10$^6$
B
LPS CU KB
5mm

Figure G.10: Shot 793 $R_0$ = 6mm $\phi_0$=25.4$\mu$m N=10

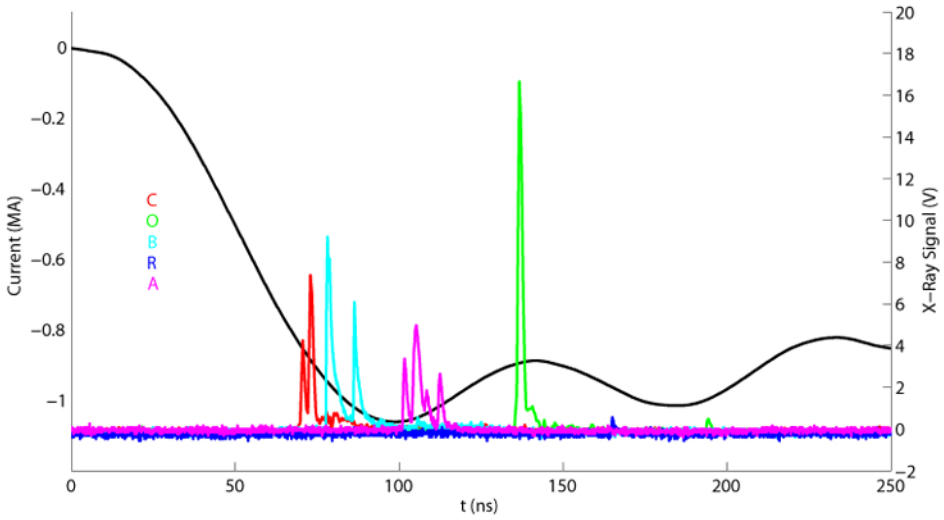


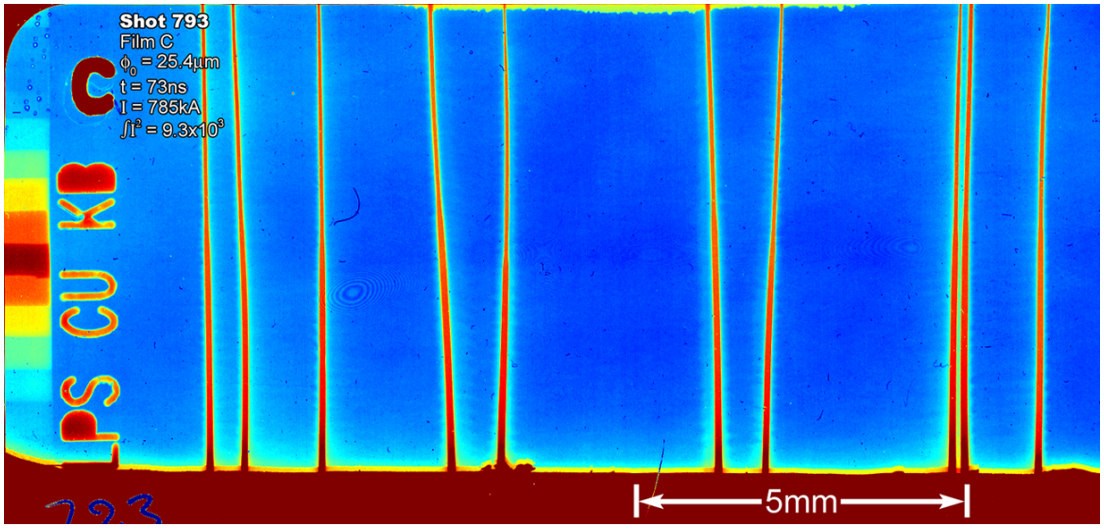


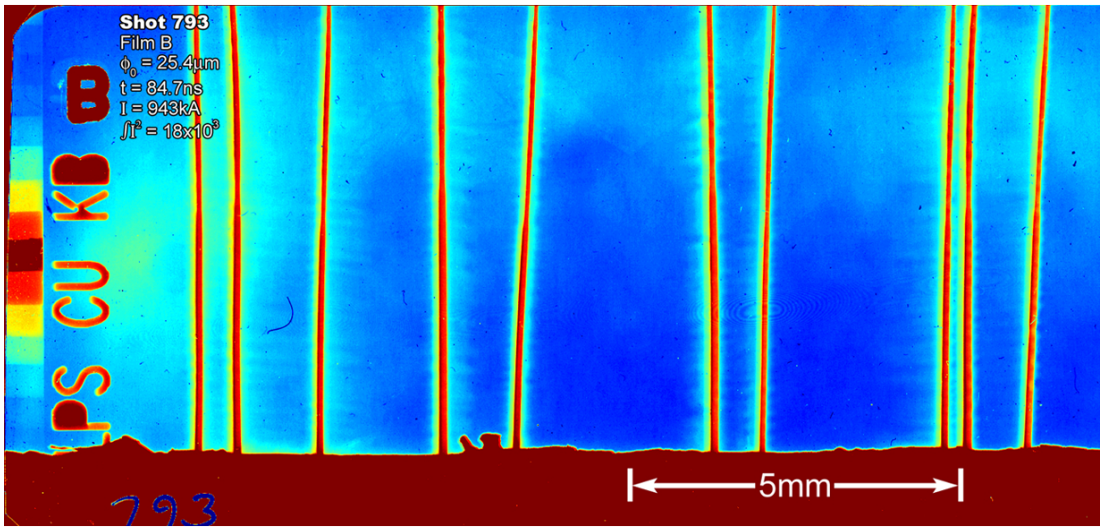

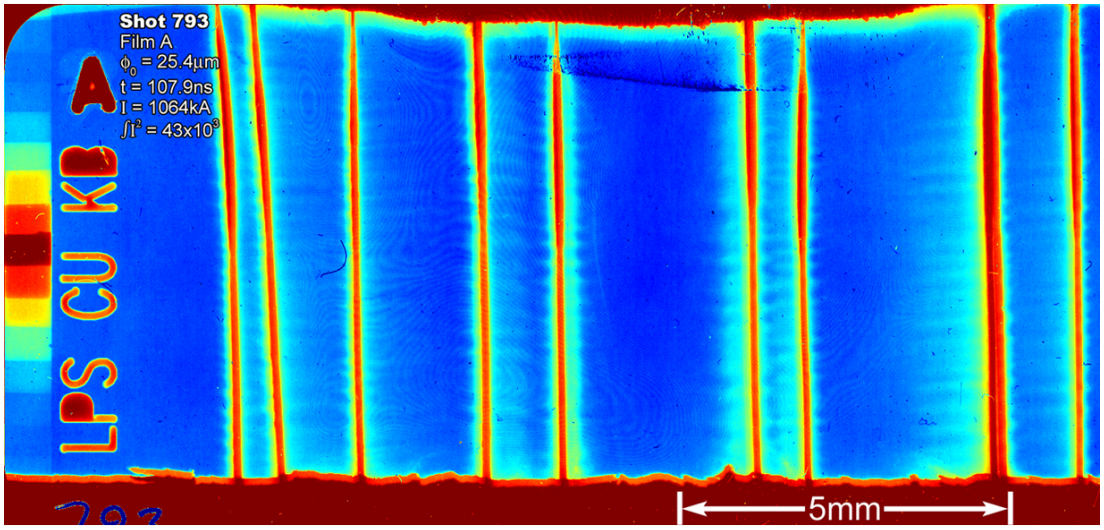
Shot 793
Film A
$\phi_0$ = 25.4μm
t = 107.9ns
I = 1064kA
$\int I^2$ = 43x10$^3$
A
LPS CU KB
5mm

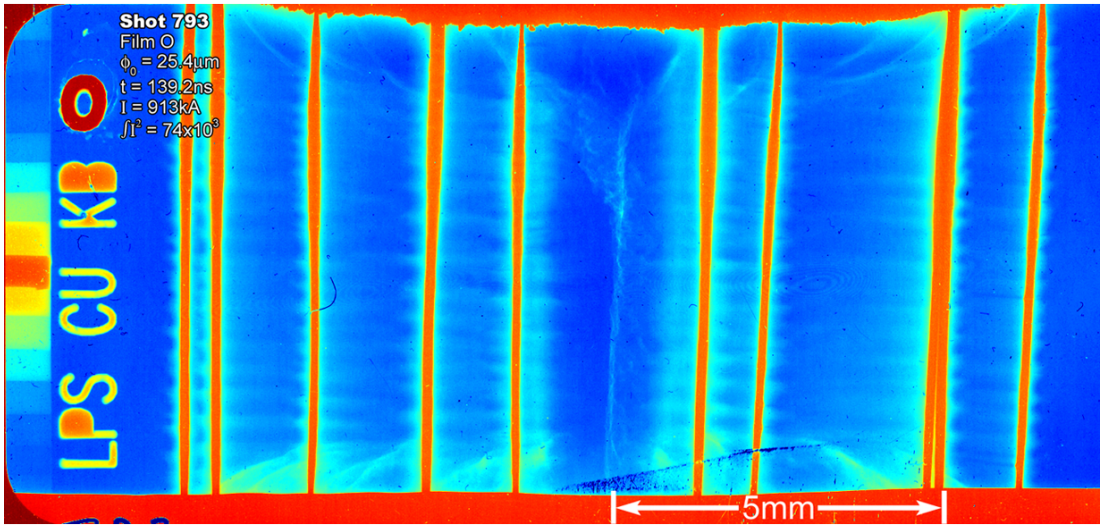
Shot 793
Film O
$\phi_0$ = 25.4μm
t = 139.2ns
I = 913kA
$\int I^2$ = 74x10$^3$
O
LPS CU KB
5mm

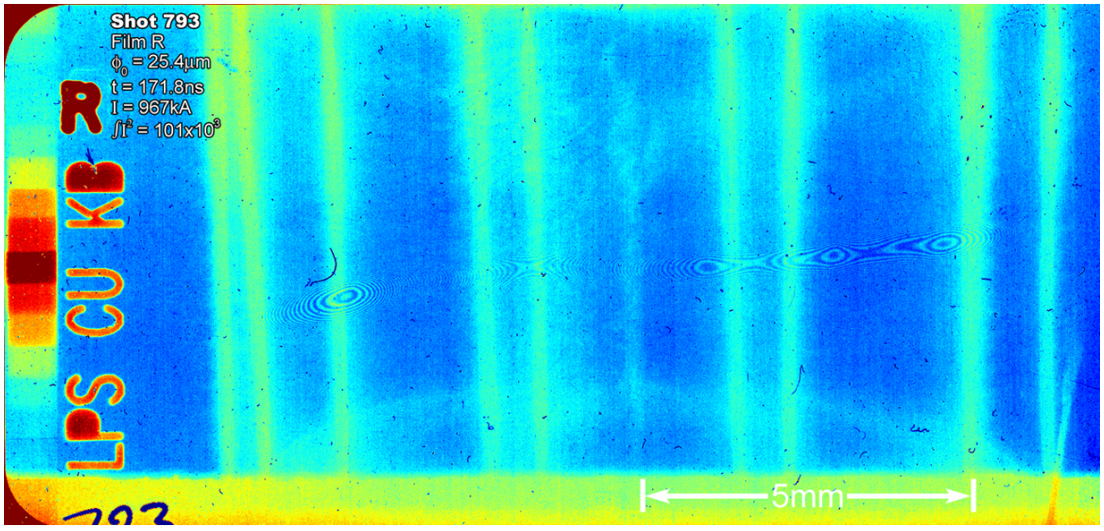
Shot 793
Film R
$\phi_0$ = 25.4μm
t = 171.8ns
I = 967kA
$\int I^2$ = 101x10$^3$
R
LPS CU KB
5mm

Figure G.11: Shot 794 $R_0$ = 6mm $\phi_0$=10.2$\mu$m N=10

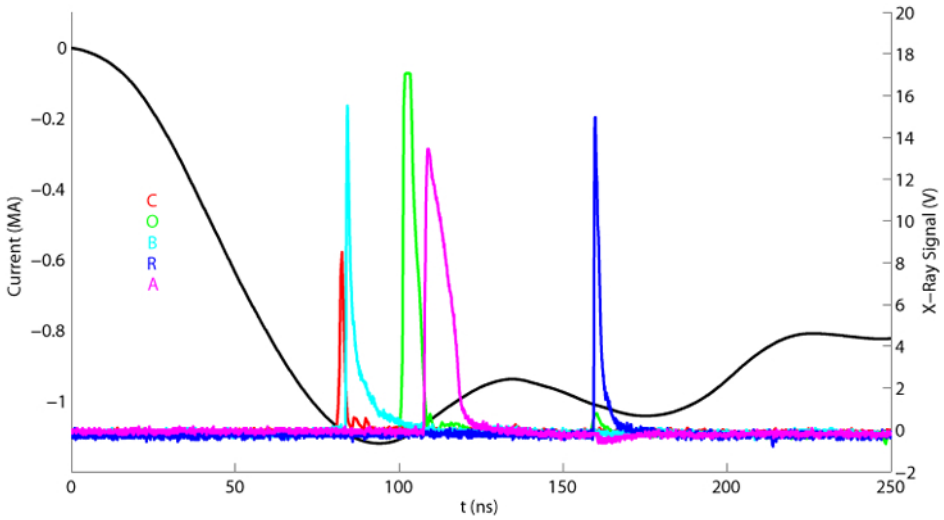


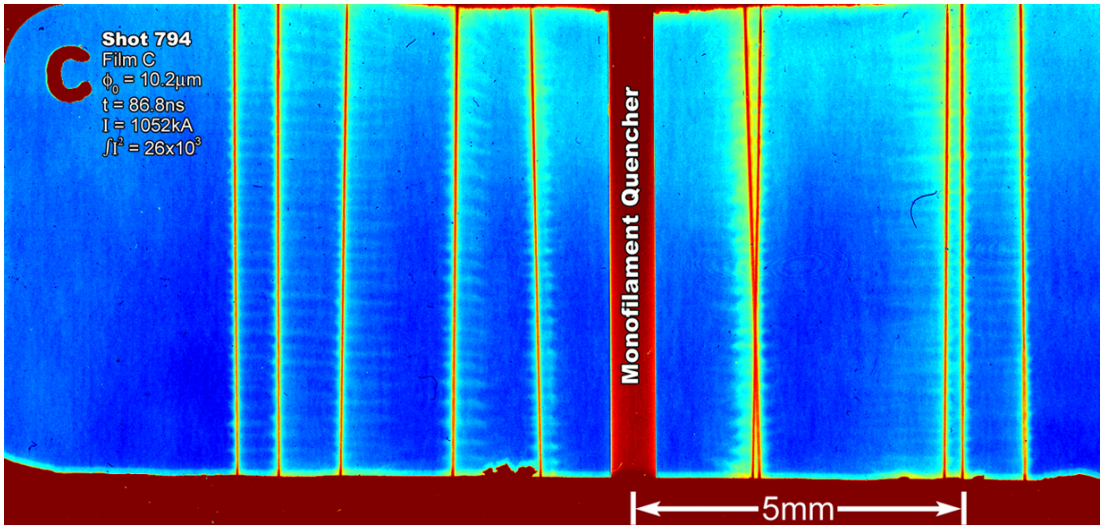


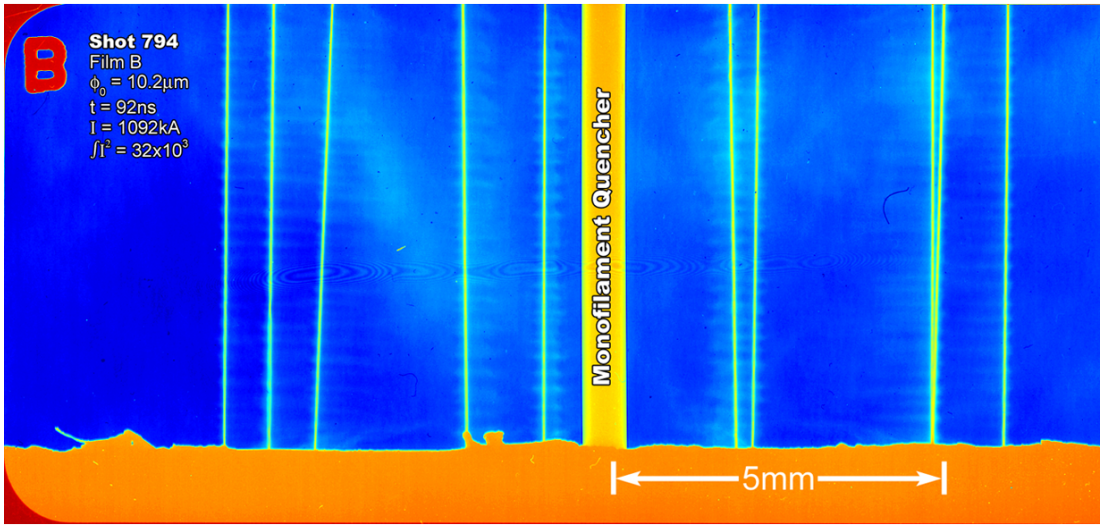

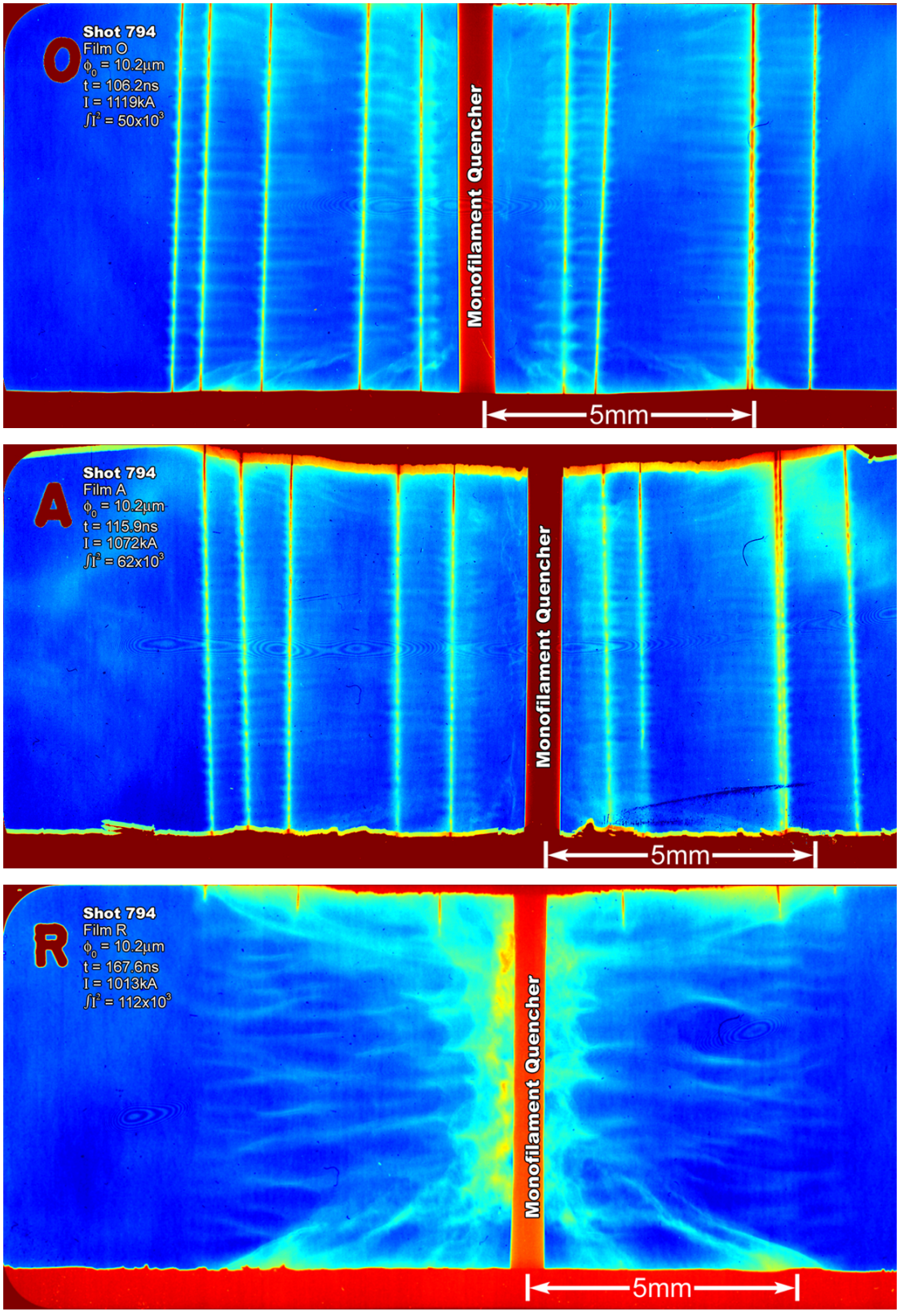
Shot 794
Film O
$\phi_0$ = 10.2µm
t = 106.2ns
I = 1119kA
$\int I^2$ = 50x10$^3$
Monofilament Quencher
5mm
Shot 794
Film A
$\phi_0$ = 10.2µm
t = 115.9ns
I = 1072kA
$\int I^2$ = 62x10$^3$
Monofilament Quencher
5mm
Shot 794
Film R
$\phi_0$ = 10.2µm
t = 167.6ns
I = 1013kA
$\int I^2$ = 112x10$^3$
Monofilament Quencher
5mm

Figure G.12: Shot 795 $R_0$ = 6mm $\phi_0$=7.4$\mu$m N=10

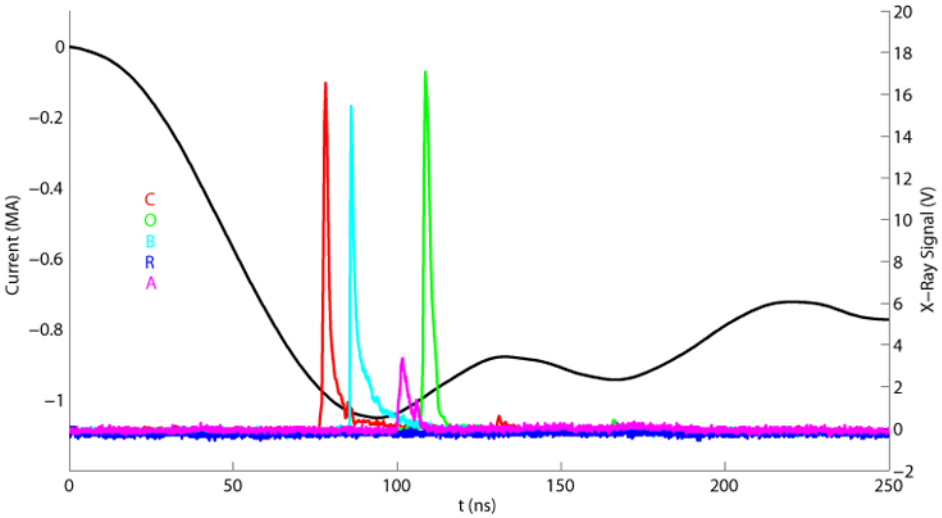


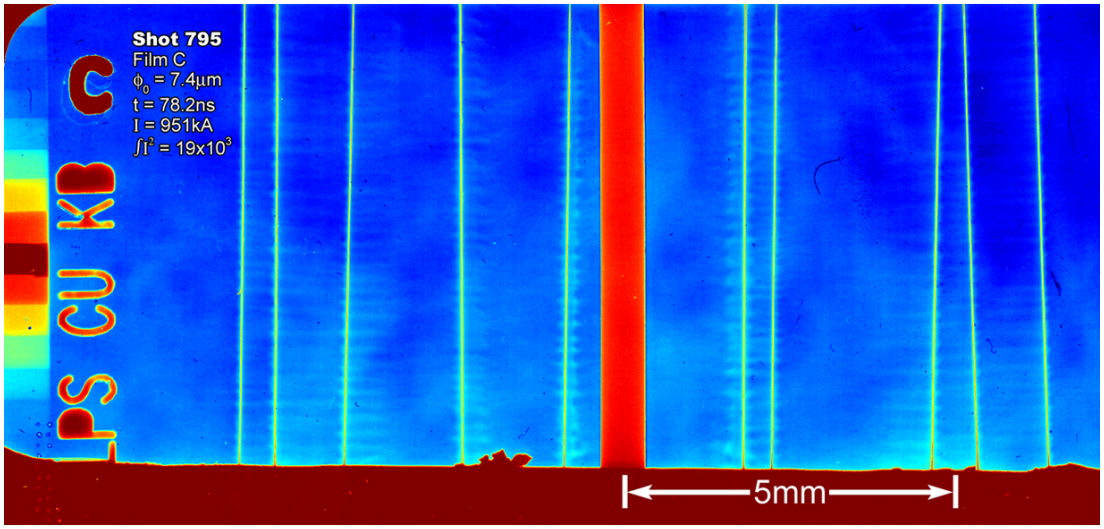


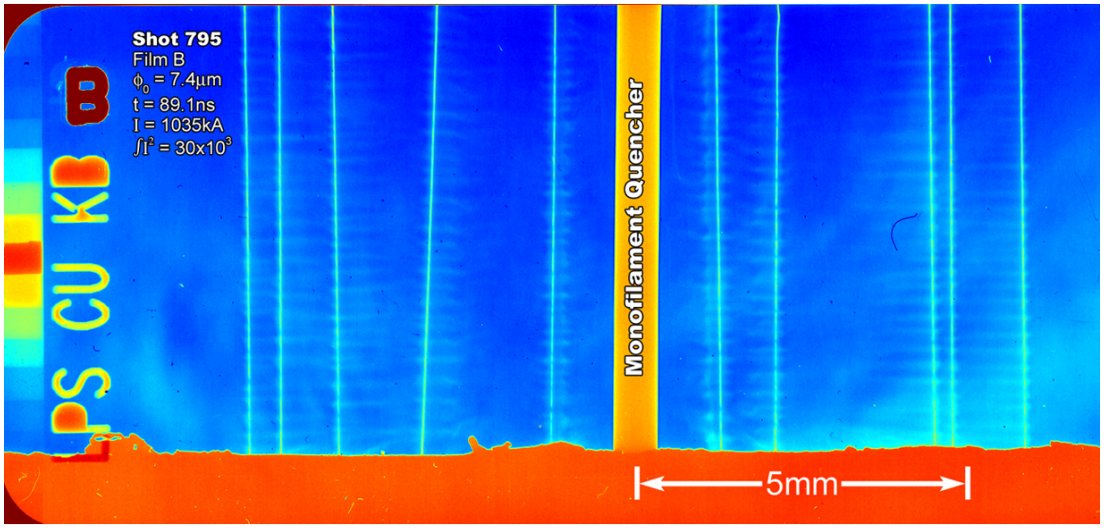

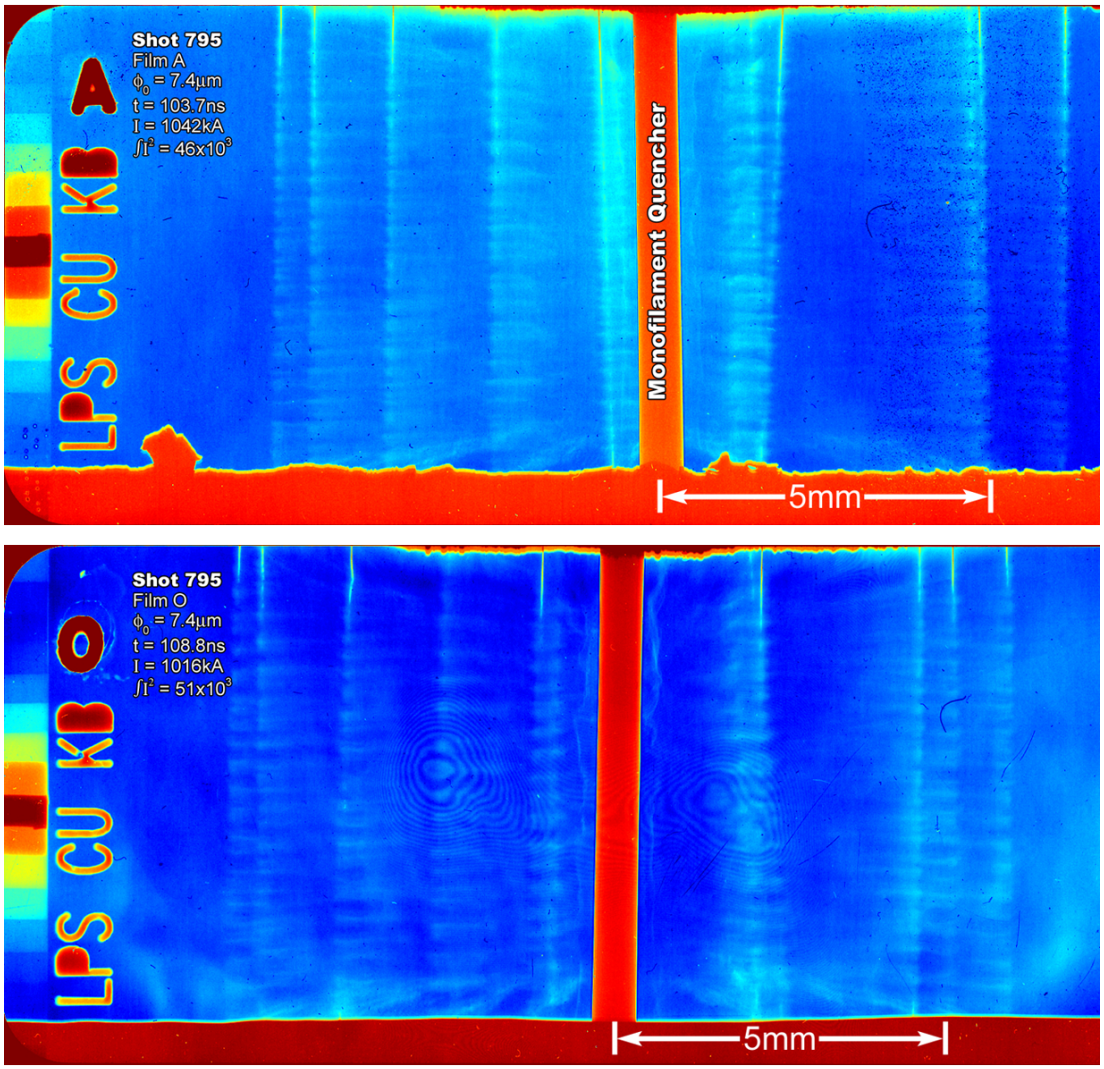
Shot 795
Film A
$\phi_0$ = 7.4μm
t = 103.7ns
I = 1042kA
$\int I^2$ = 46x10$^3$
LPS CU KB A
Monofilament Quencher
5mm
Shot 795
Film O
$\phi_0$ = 7.4μm
t = 108.8ns
I = 1016kA
$\int I^2$ = 51x10$^3$
LPS CU KB O
5mm

Figure G.13: Shot 796 $R_0$ = 6mm $\phi_0$=5.1$\mu$m N=10

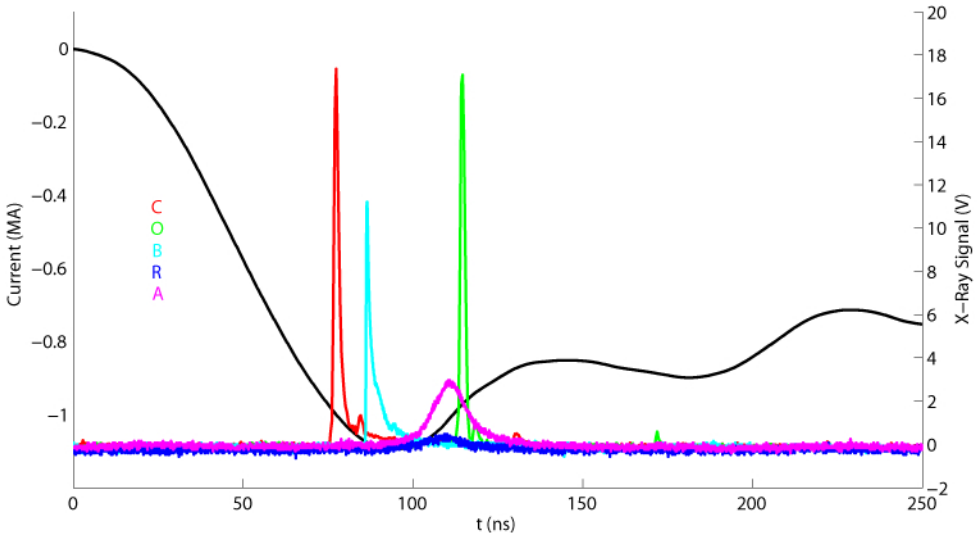

Figure G.14: Shot 797 $R_0$ = 6mm $\phi_0$=12.7$\mu$m N=10

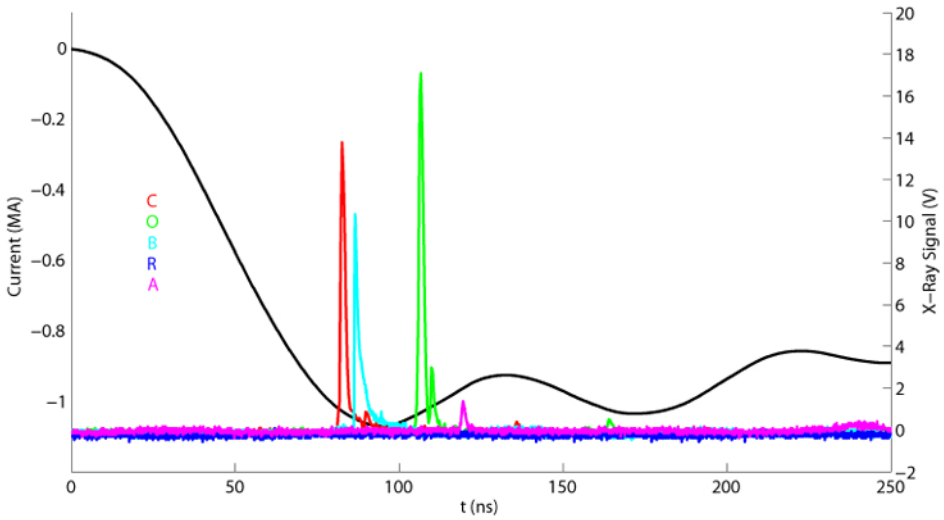


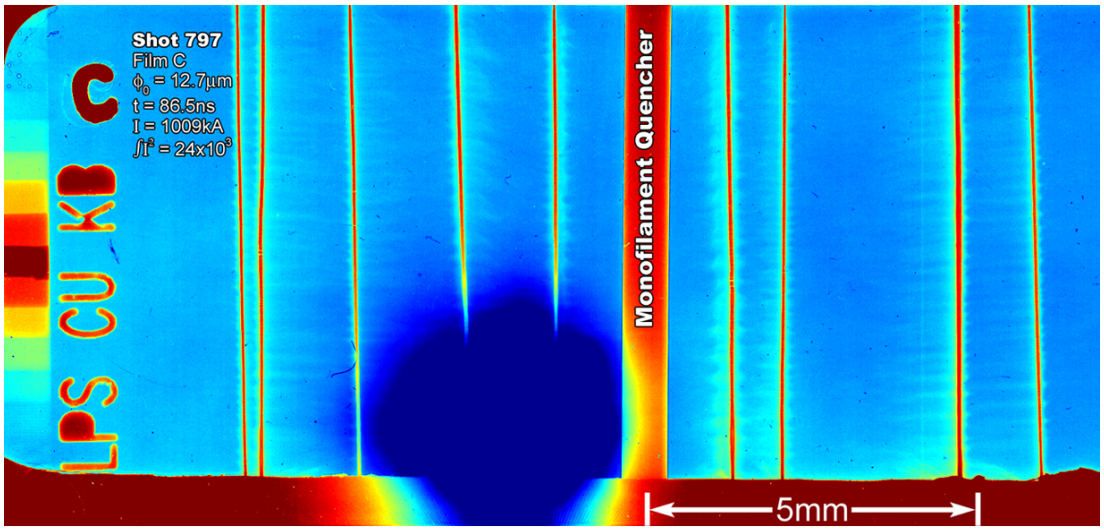


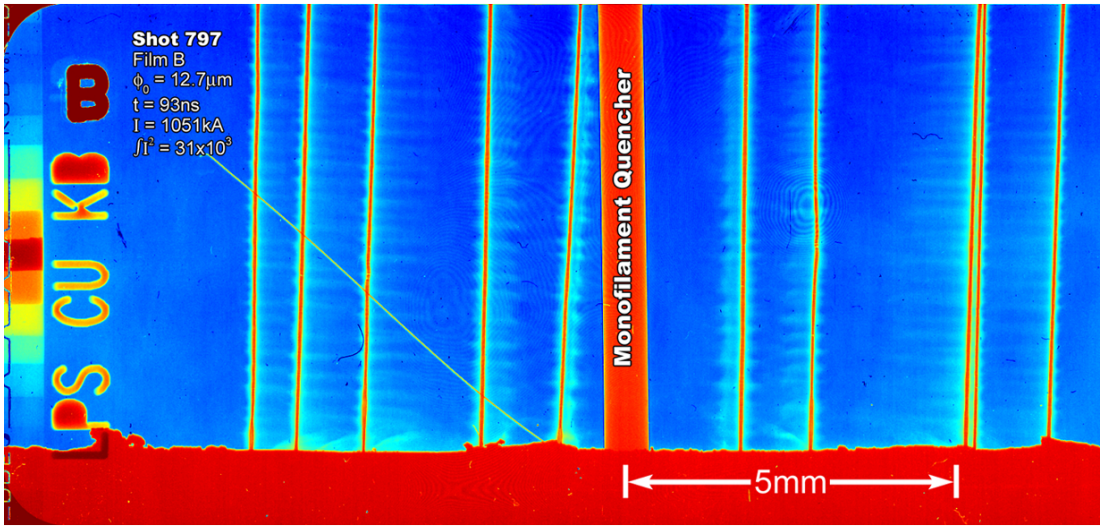

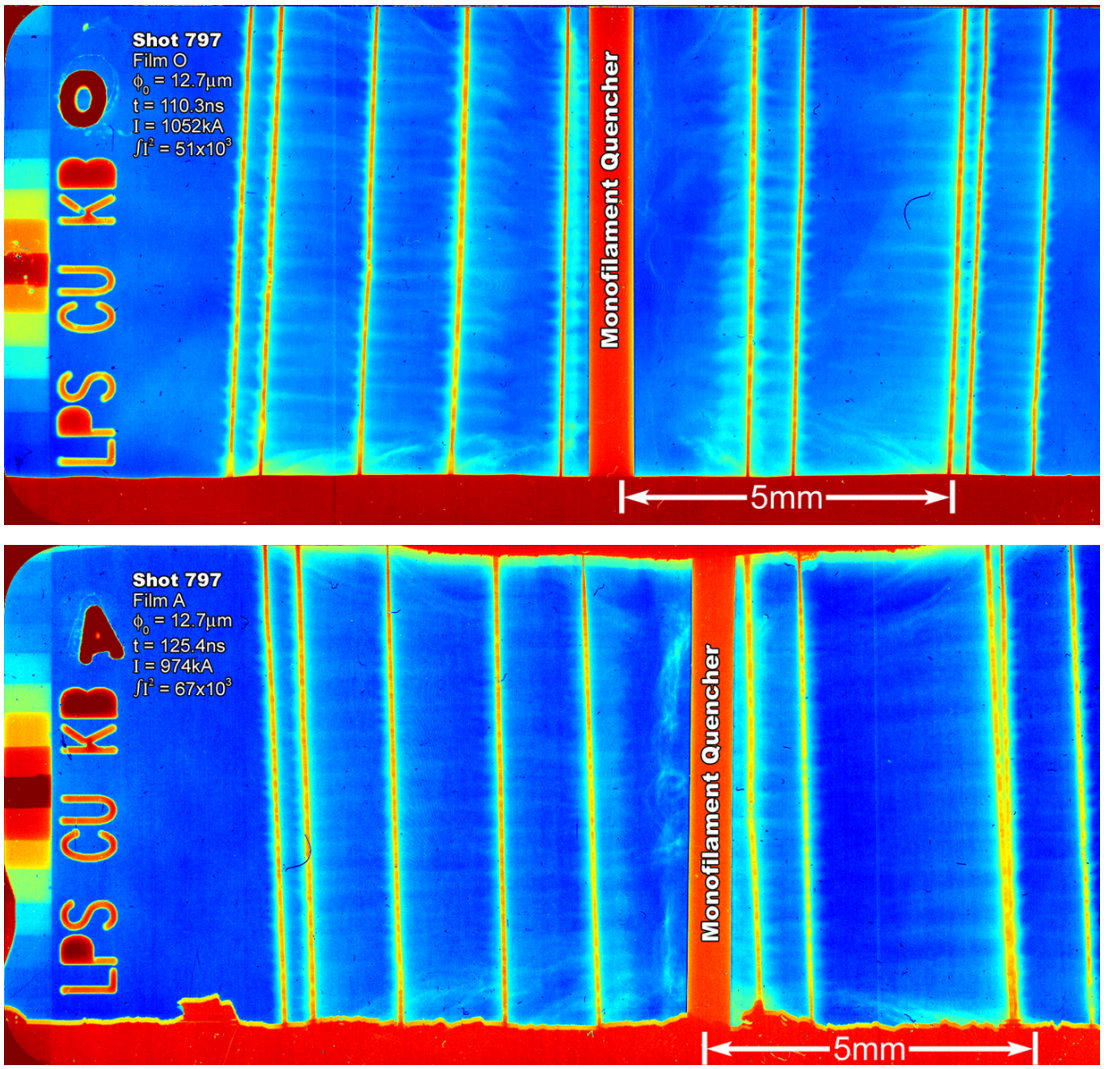
Shot 797
Film O
$\phi_0$ = 12.7µm
t = 110.3ns
I = 1052kA
$\int I^2$ = 51x10$^3$
LPS CU KB O
Monofilament Quencher
5mm
Shot 797
Film A
$\phi_0$ = 12.7µm
t = 125.4ns
I = 974kA
$\int I^2$ = 67x10$^3$
LPS CU KB A
Monofilament Quencher
5mm

Figure G.15: Shot 798 $R_0$ = 6mm $\phi_0$=10.2$\mu$m N=10

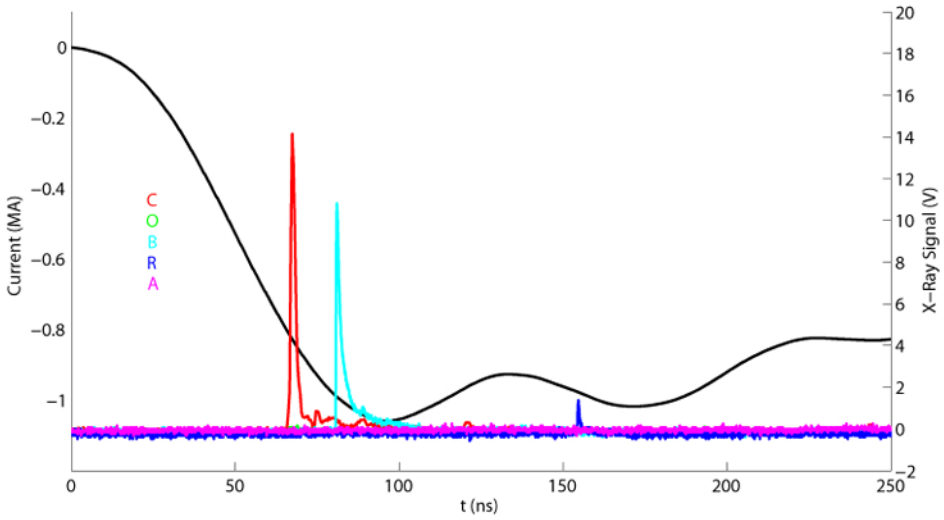


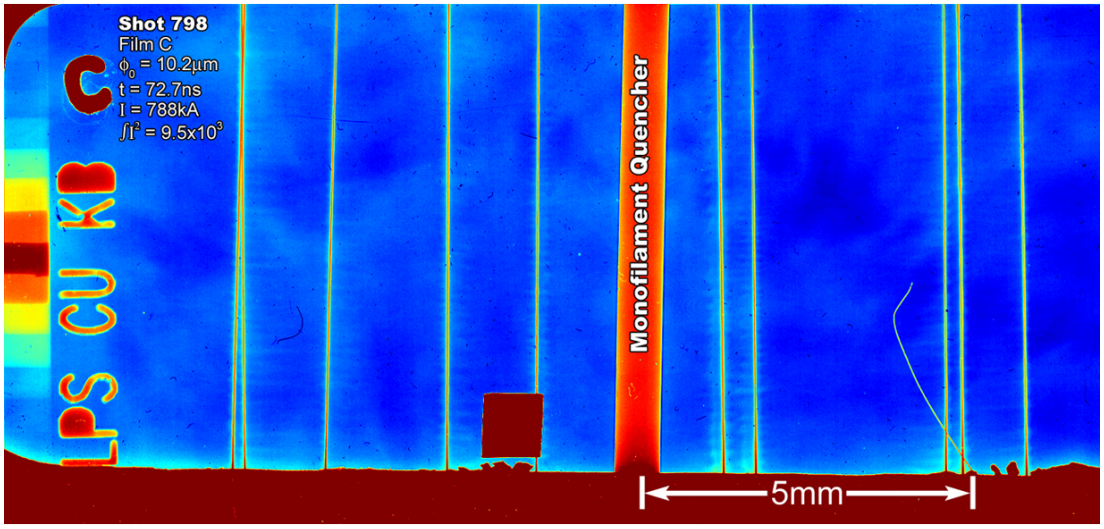


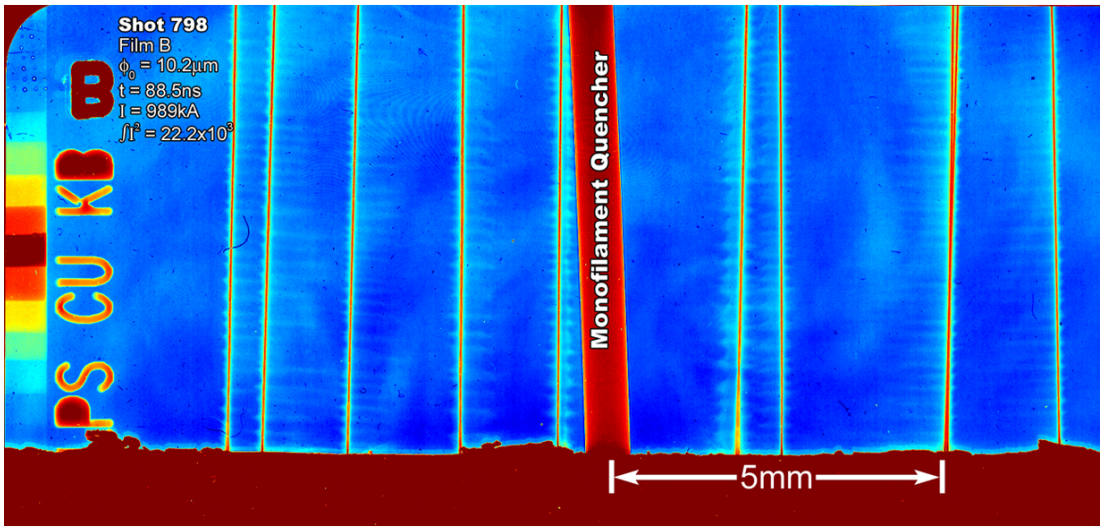

Figure G.16: Shot 799 $R_0$ = 4mm $\phi_0$=7.4$\mu$m N=10

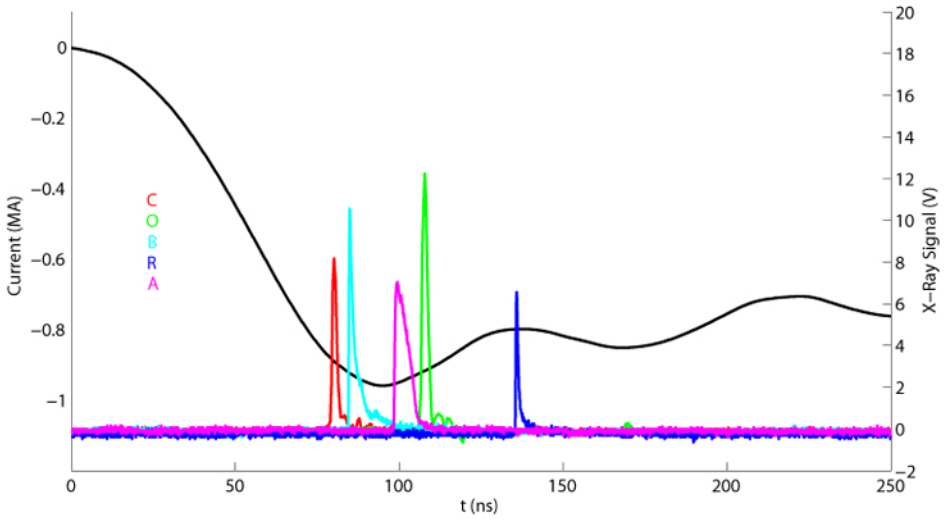


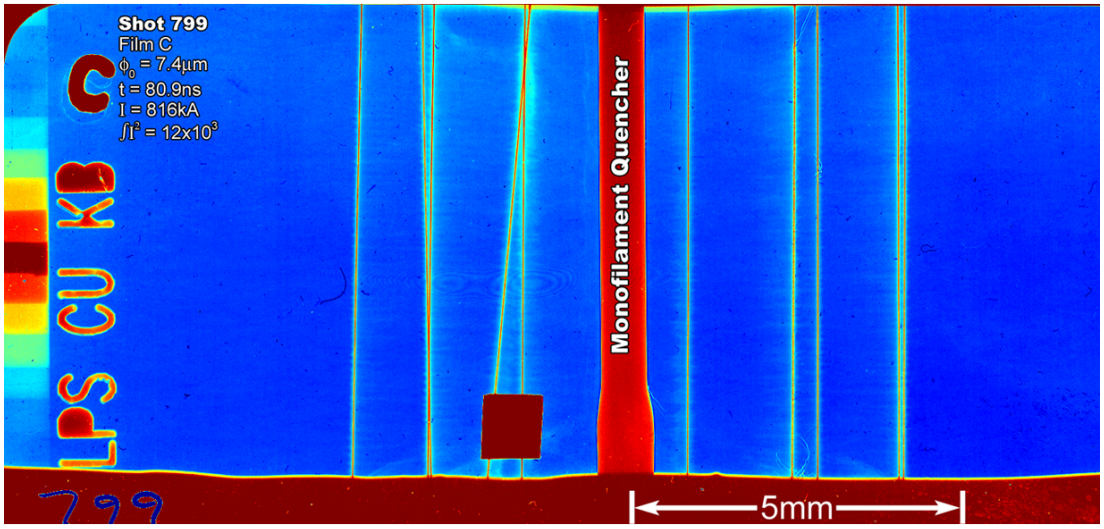


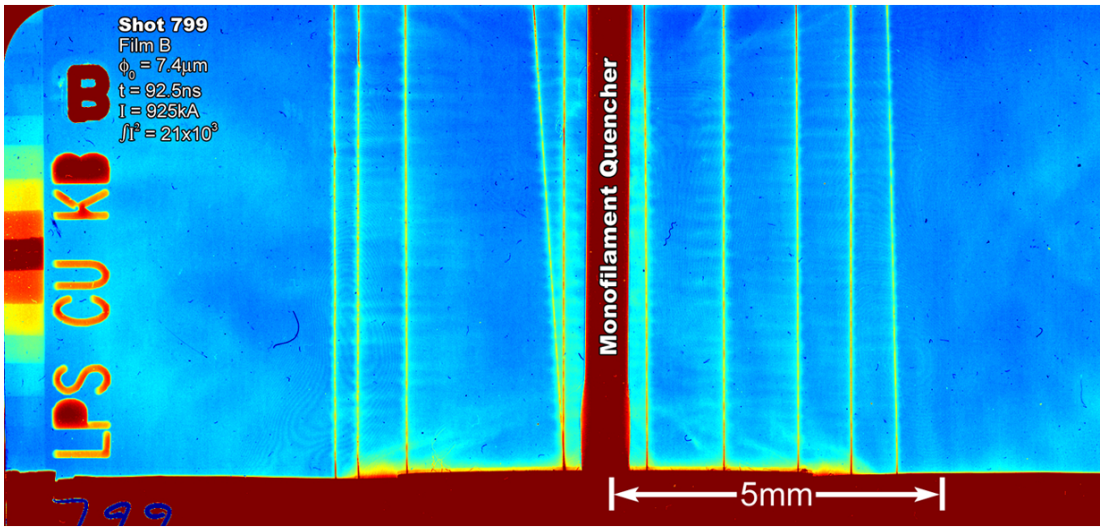

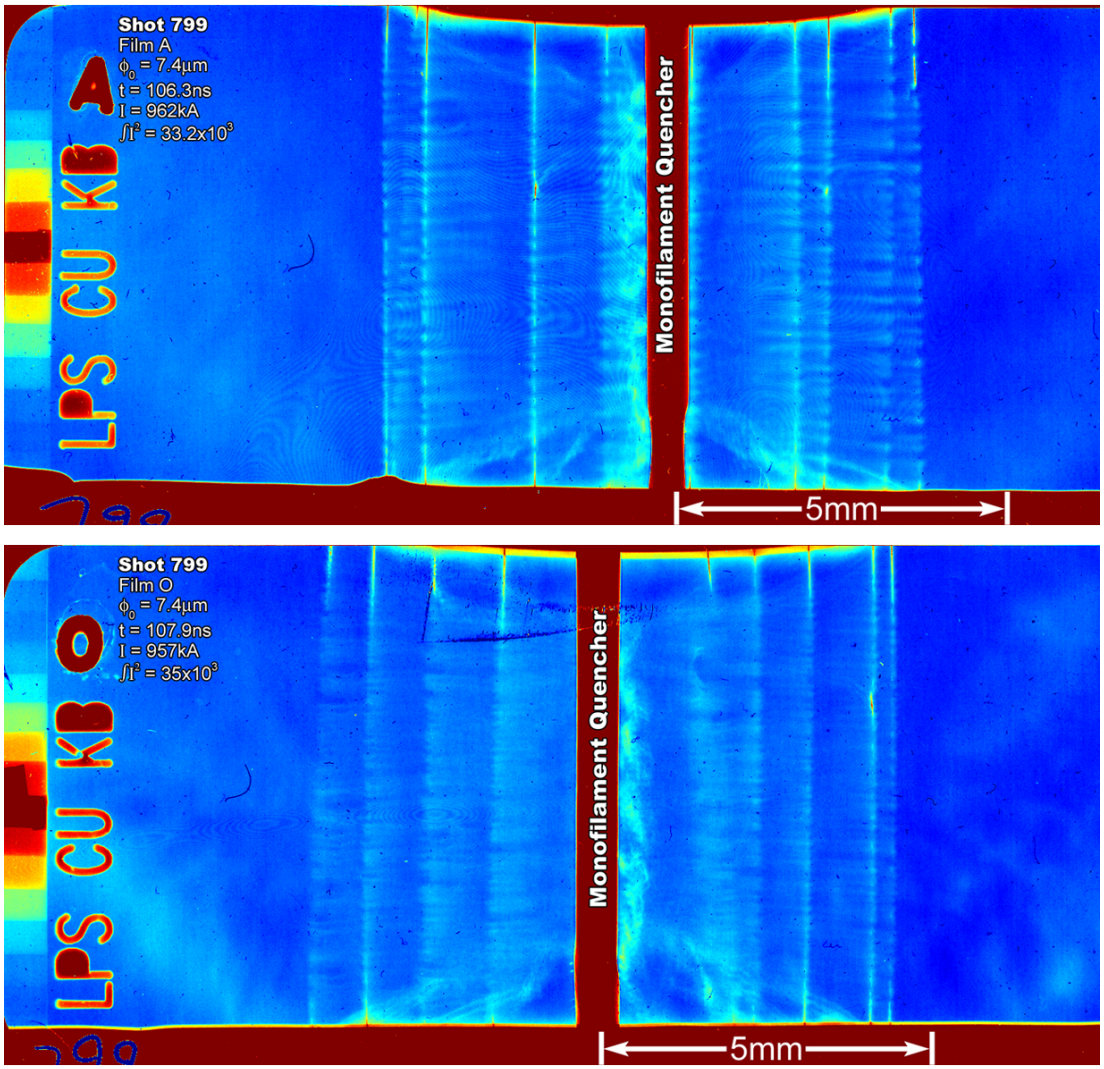
Shot 799
Film A
$\phi_0$ = 7.4μm
t = 106.3ns
I = 962kA
$\int I^2$ = 33.2x10$^3$
LPS CU KB A
Monofilament Quencher
5mm
Shot 799
Film O
$\phi_0$ = 7.4μm
t = 107.9ns
I = 957kA
$\int I^2$ = 35x10$^3$
LPS CU KB O
Monofilament Quencher
5mm

Figure G.17: Shot 800 $R_0$ = 4mm $\phi_0$=7.4$\mu$m N=10

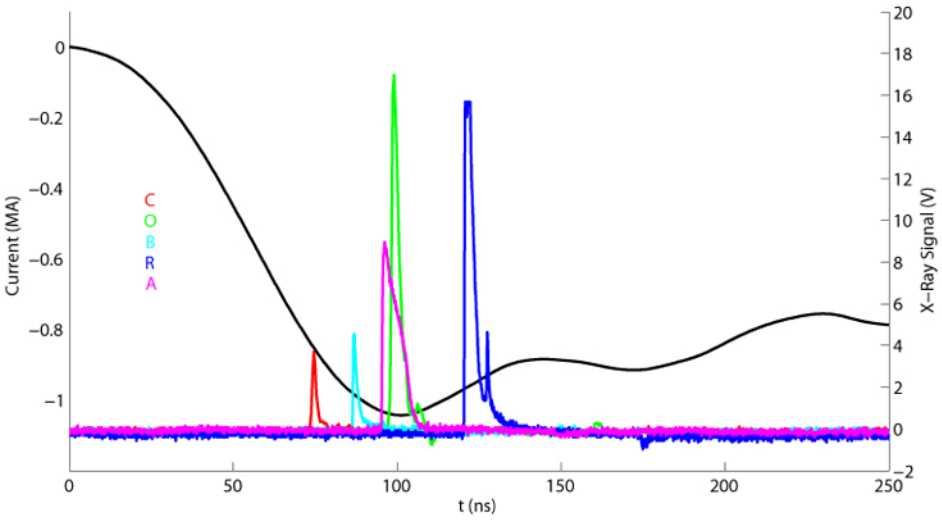


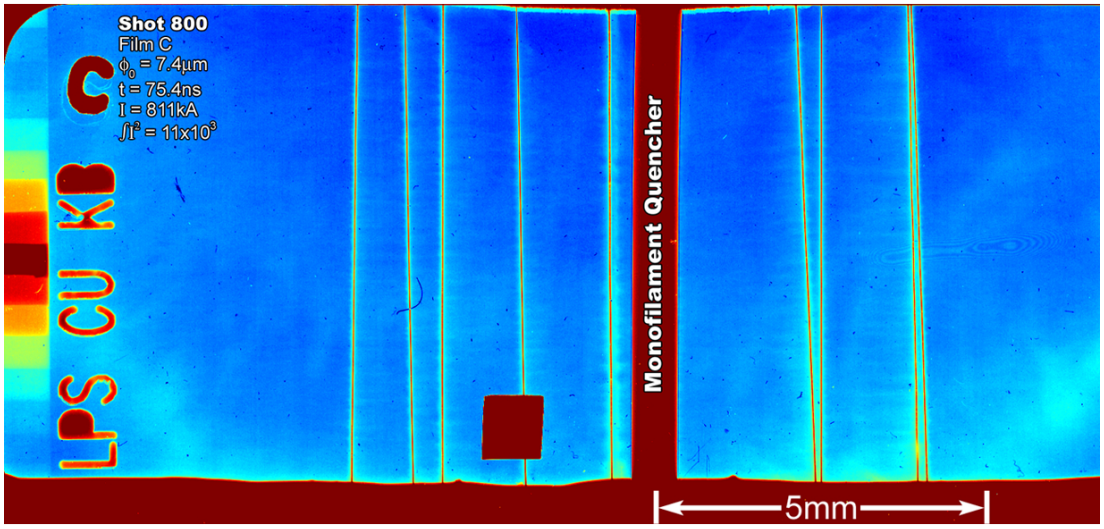


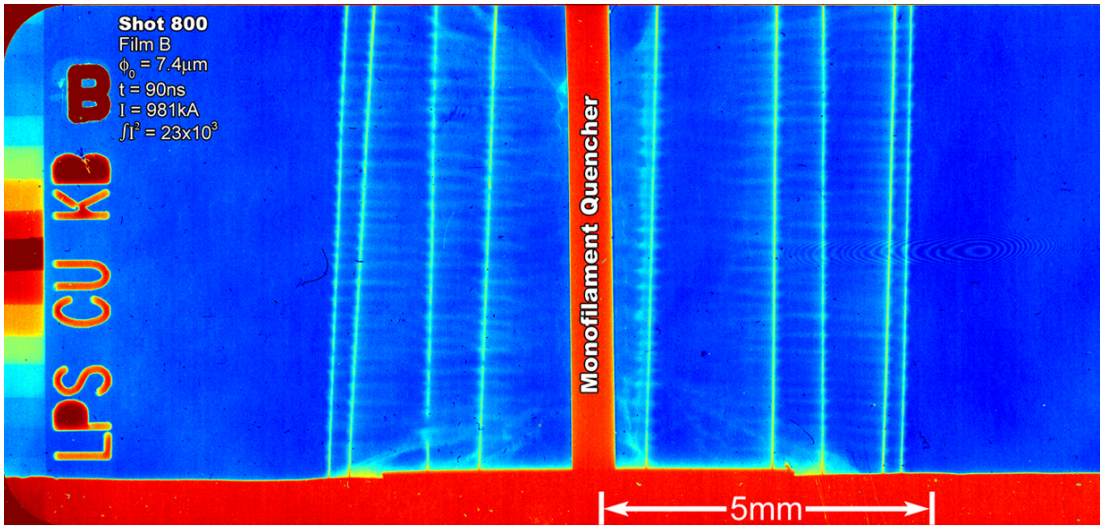

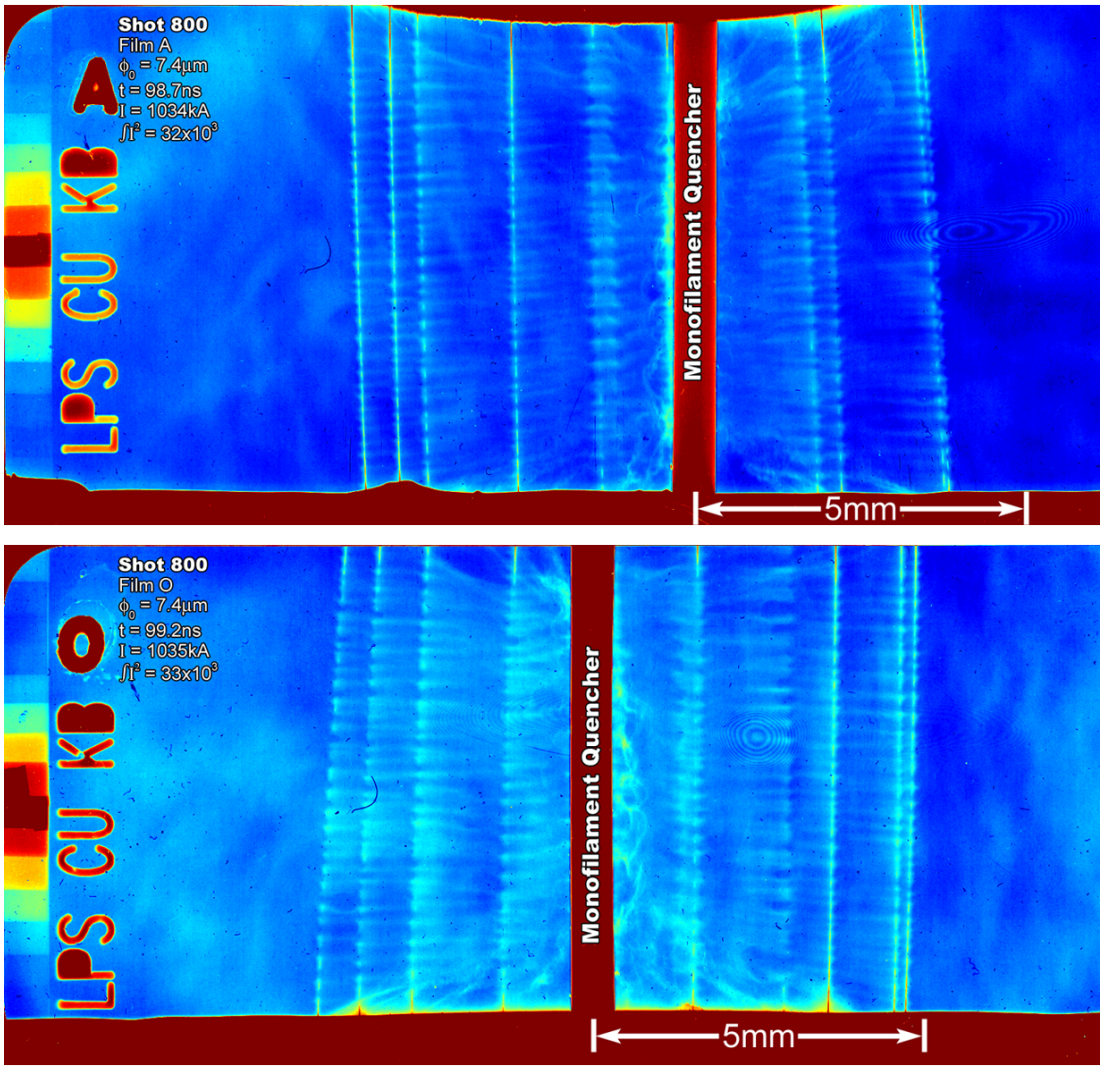
Shot 800
Film A
$\phi_0$ = 7.4μm
t = 98.7ns
I = 1034kA
$\int I^2$ = 32x10$^3$
LPS CU KB A
Monofilament Quencher
5mm
Shot 800
Film O
$\phi_0$ = 7.4μm
t = 99.2ns
I = 1035kA
$\int I^2$ = 33x10$^3$
LPS CU KB O
Monofilament Quencher
5mm

Figure G.18: Shot 801 $R_0$ = 4mm $\phi_0$=5.1$\mu$m N=10

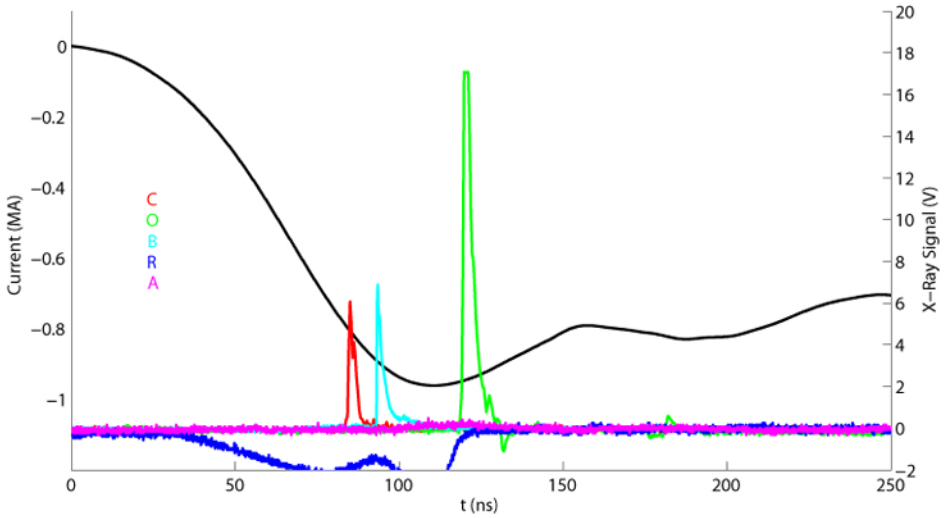


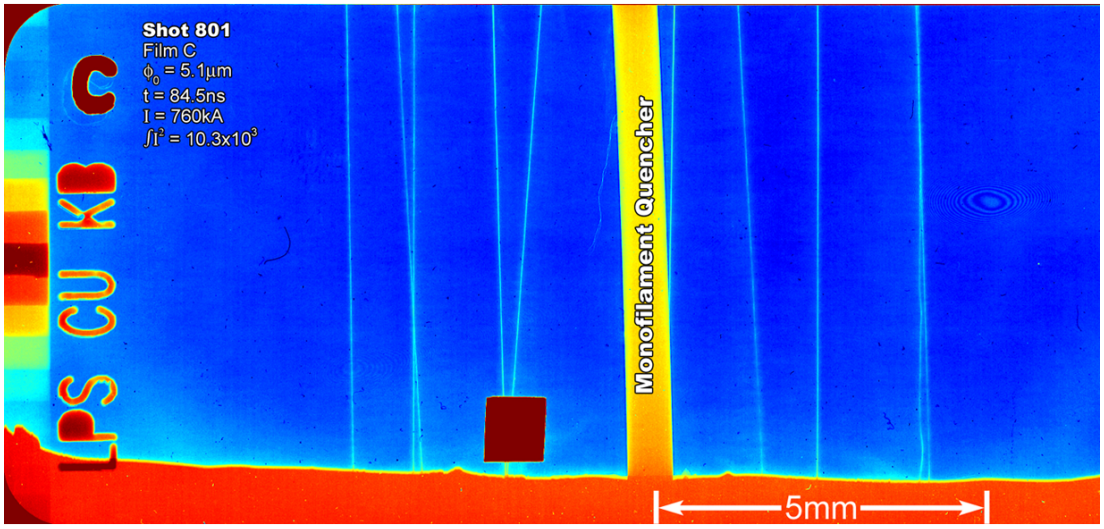


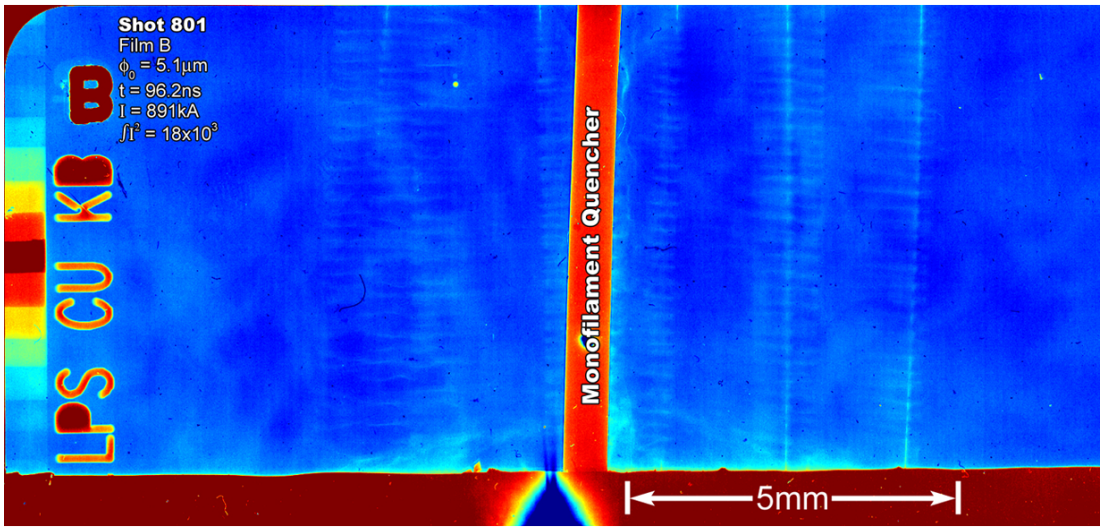

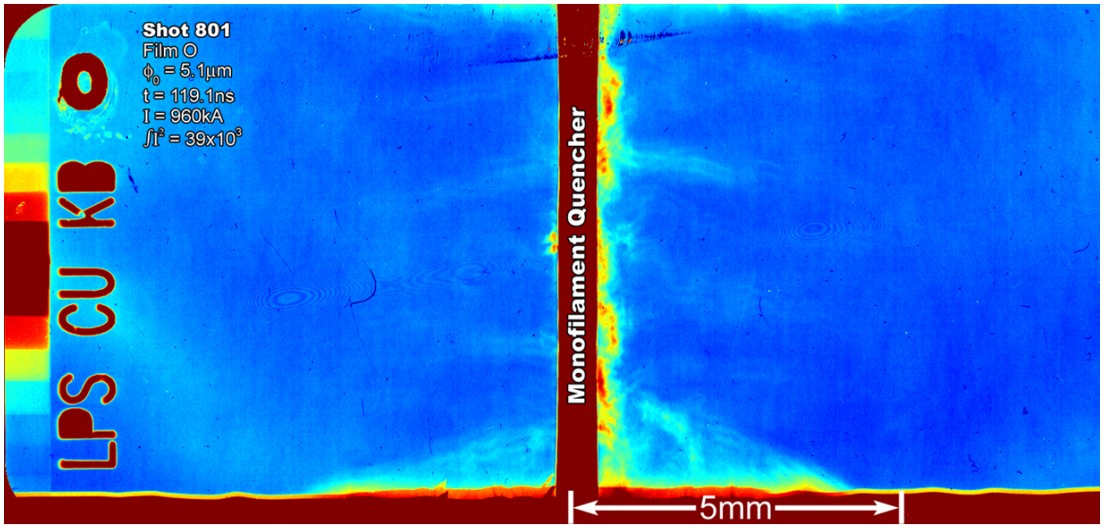
Shot 801
Film O
$\phi_0$ = 5.1µm
t = 119.1ns
I = 960kA
$\int I^2$ = 39x10$^3$
LPS CU KB
Monofilament Quencher
5mm

Figure G.19: Shot 802 $R_0$ = 4mm $\phi_0$=10.2$\mu$m N=10

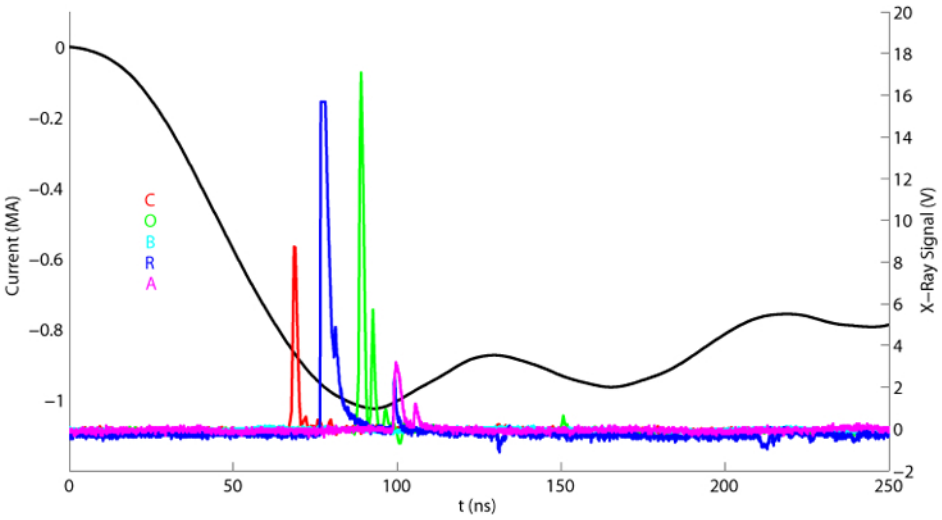


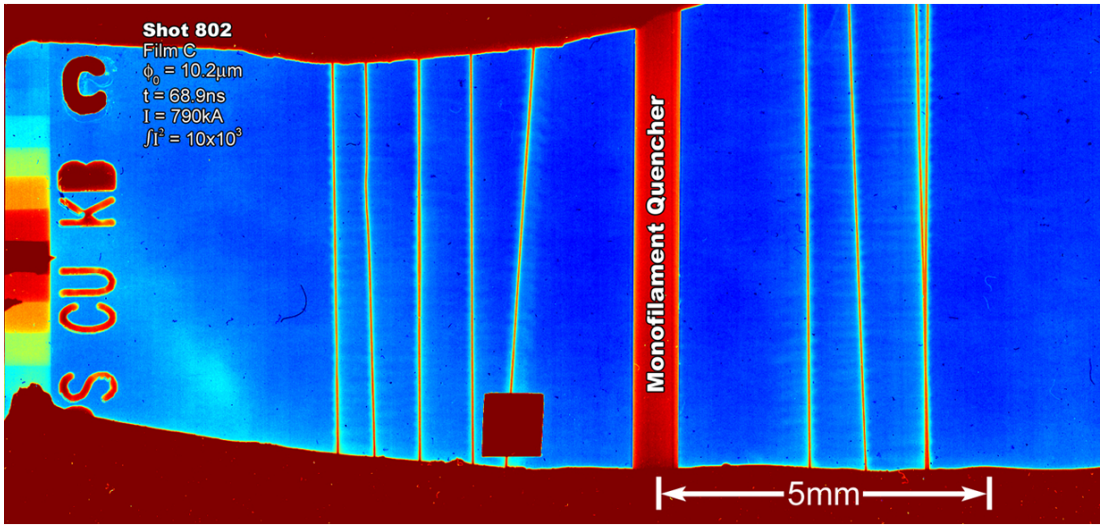


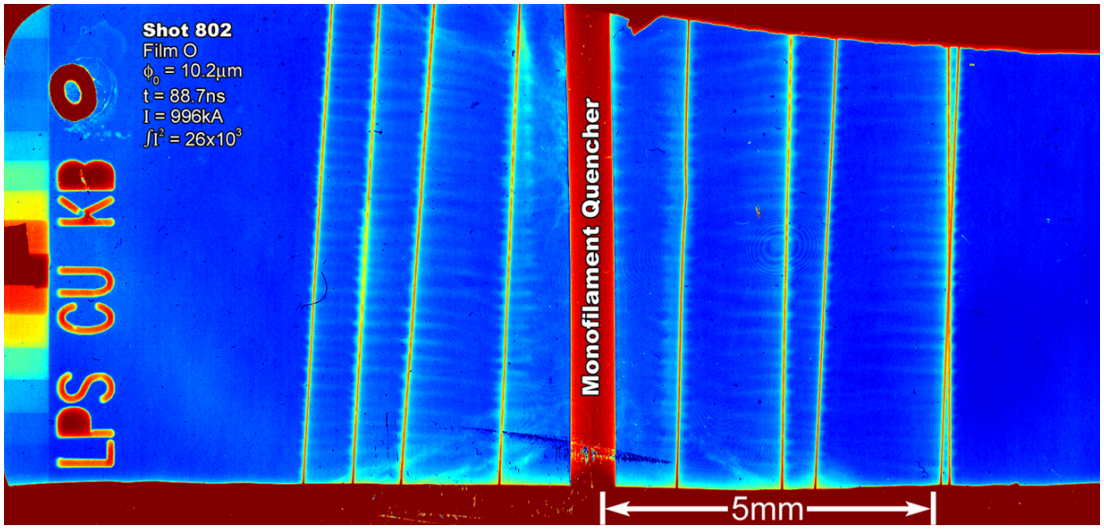

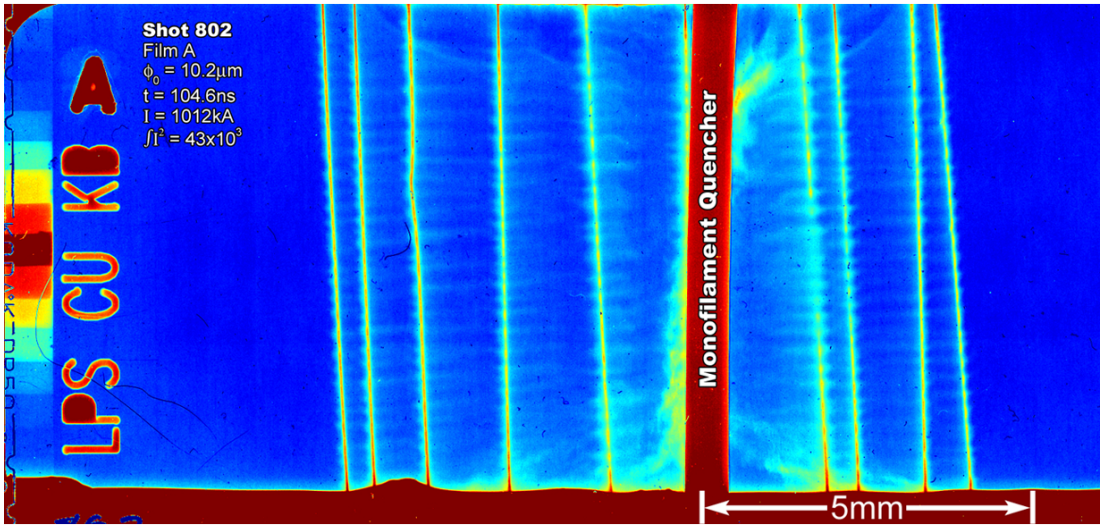
Shot 802
Film A
$\phi_0$ = 10.2µm
t = 104.6ns
I = 1012kA
$\int I^2$ = 43x10$^3$
LPS CU KB A
Monofilament Quencher
5mm

Figure G.20: Shot 803 $R_0$ = 4mm $\phi_0$=12.7$\mu$m N=10

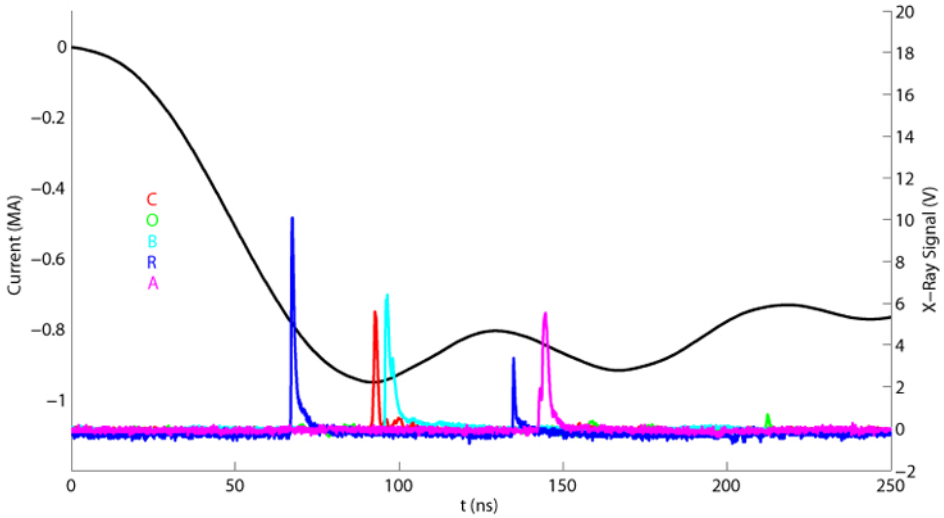


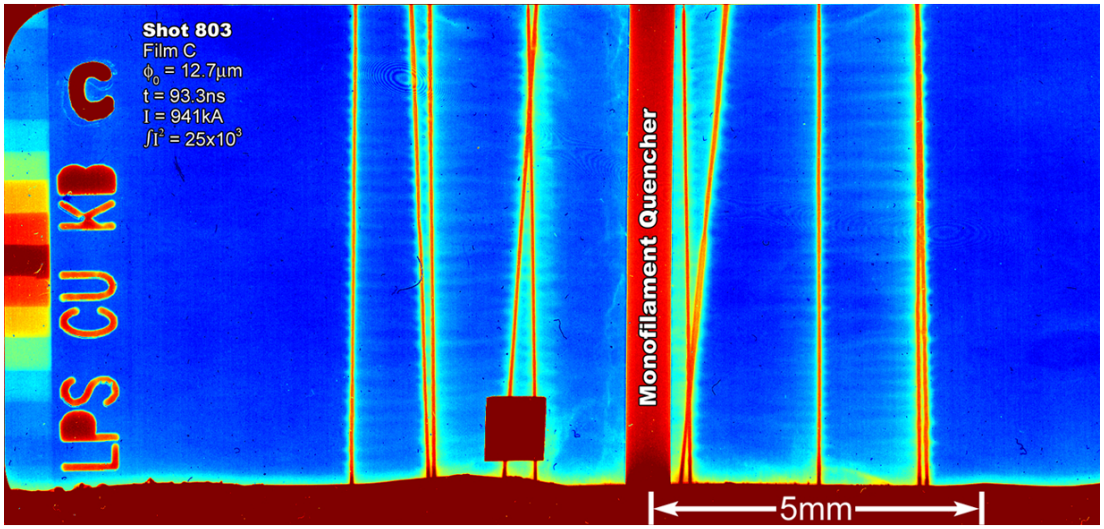


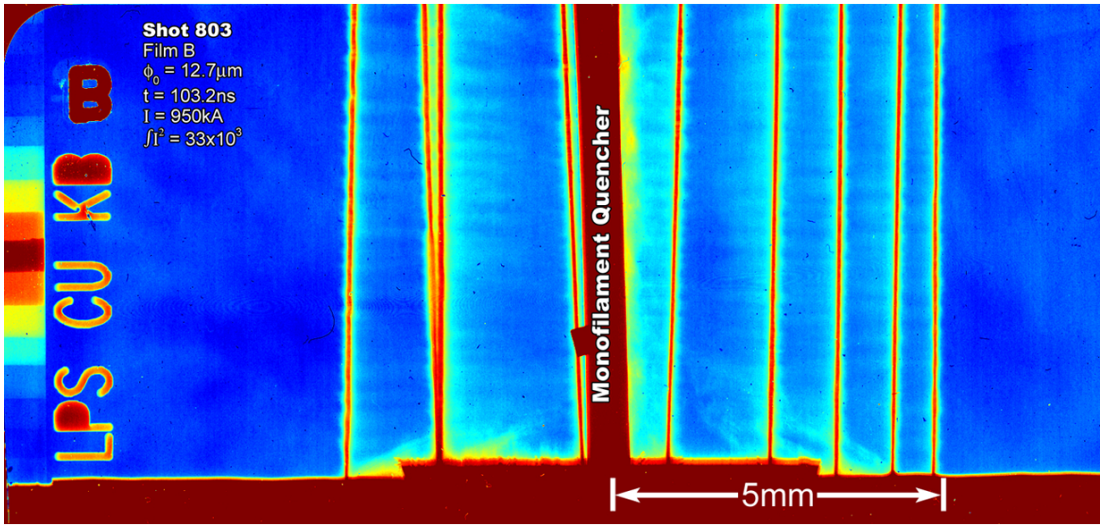

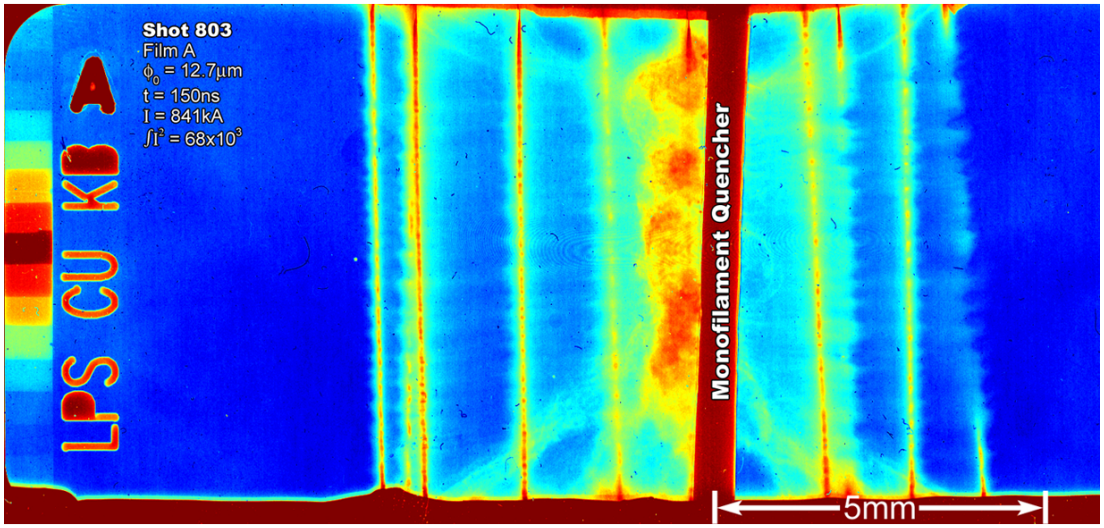
Shot 803
Film A
$\phi_0$ = 12.7µm
t = 150ns
I = 841kA
$\int I^2$ = 68x10$^3$
LPS CU KB A
Monofilament Quencher
5mm

Figure G.21: Shot 804 $R_0$ = 4mm $\phi_0$=17$\mu$m N=10

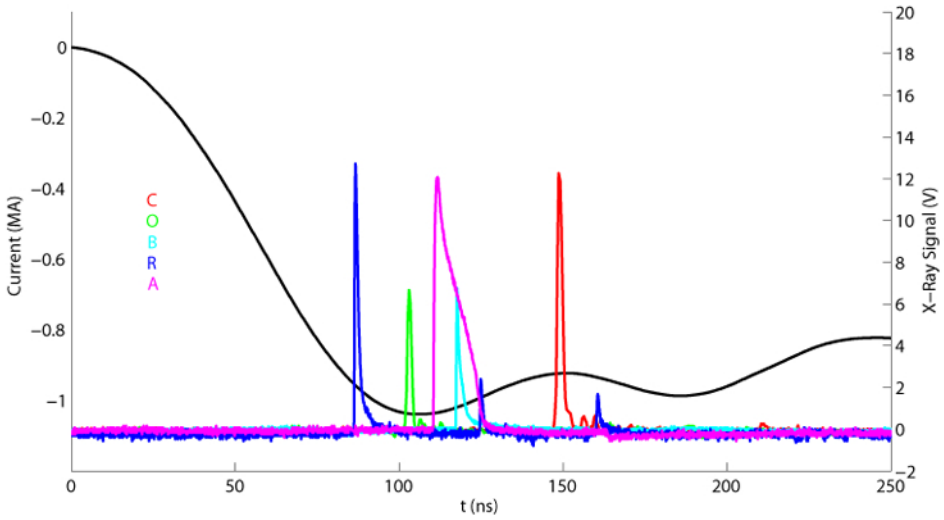


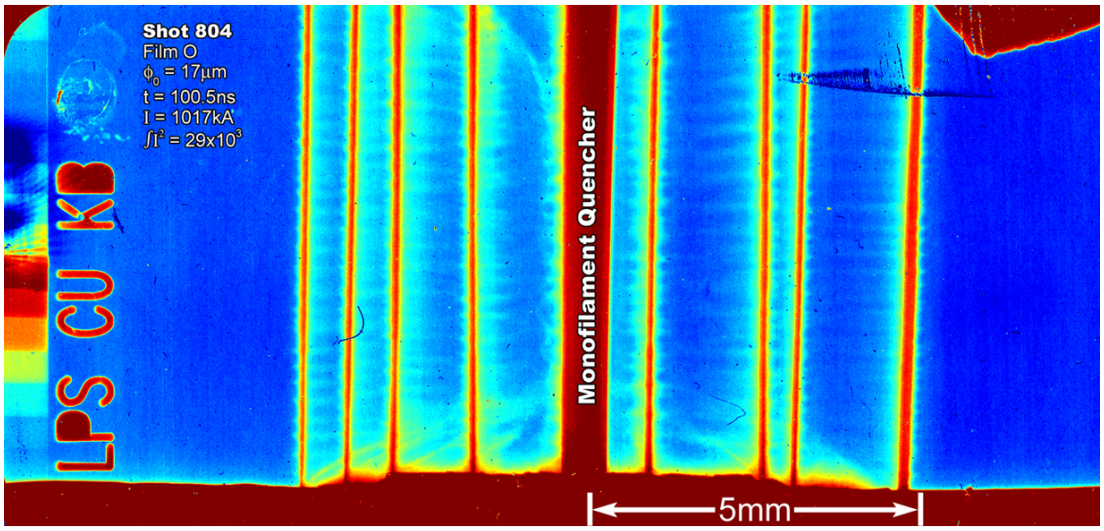


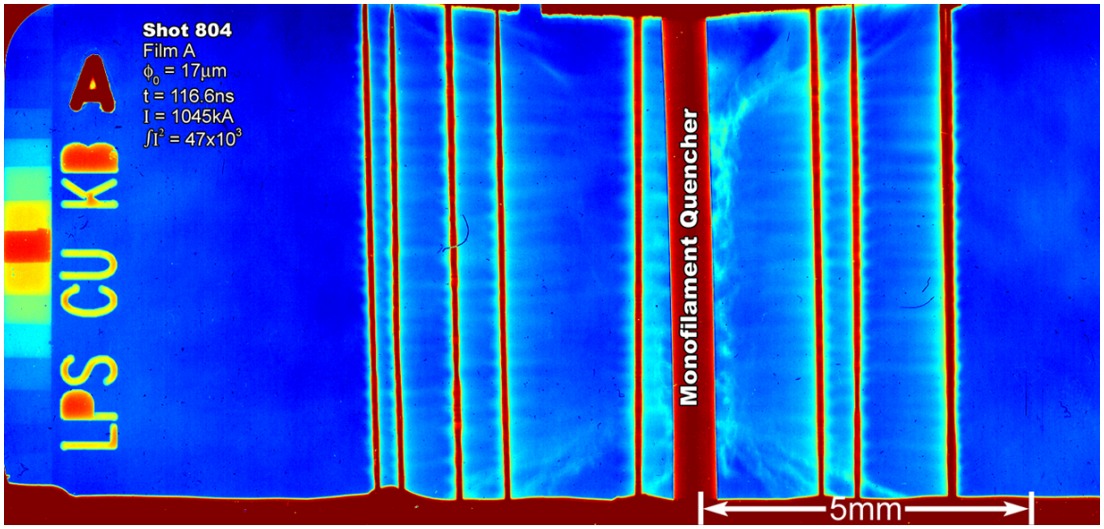

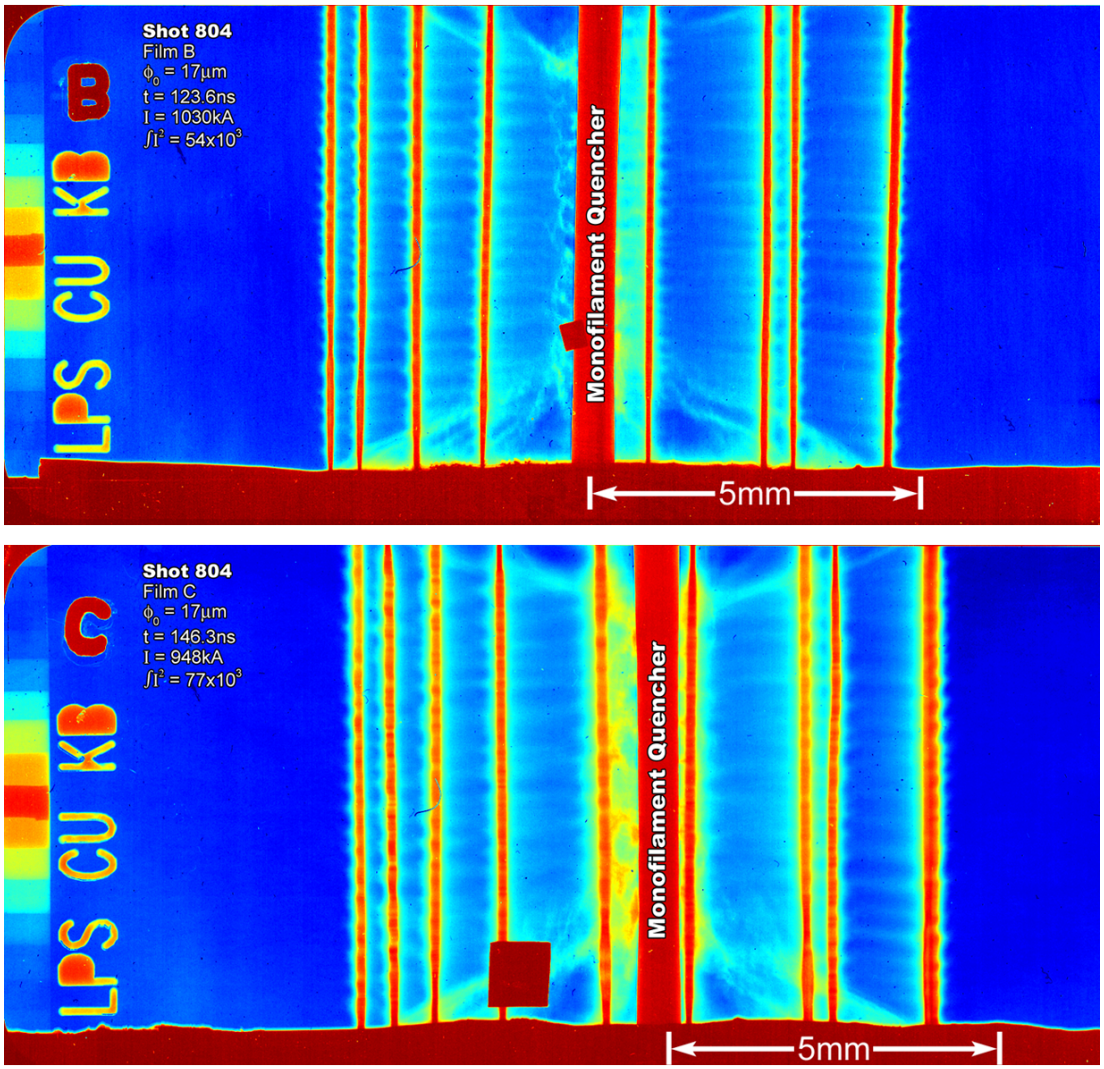
Shot 804
Film B
$\phi_0$ = 17μm
t = 123.6ns
I = 1030kA
$\int I^2$ = 54x10$^3$
LPS CU KB B
Monofilament Quencher
5mm
Shot 804
Film C
$\phi_0$ = 17μm
t = 146.3ns
I = 948kA
$\int I^2$ = 77x10$^3$
LPS CU KB C
Monofilament Quencher
5mm

Figure G.22: Shot 805 $R_0$ = 4mm $\phi_0$=19.8$\mu$m N=10

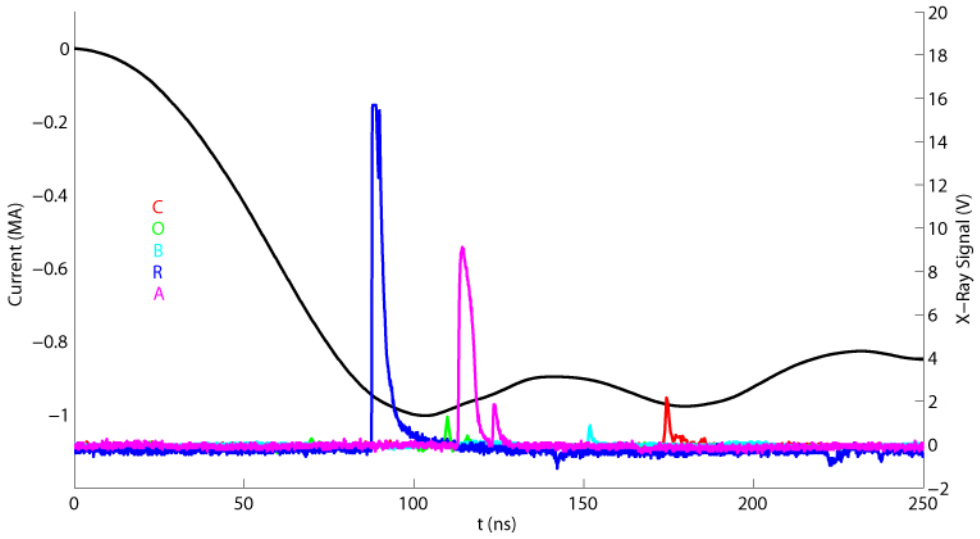

Figure G.23: Shot 806 $R_0$ = 4mm $\phi_0$=25.4$\mu$m N=10

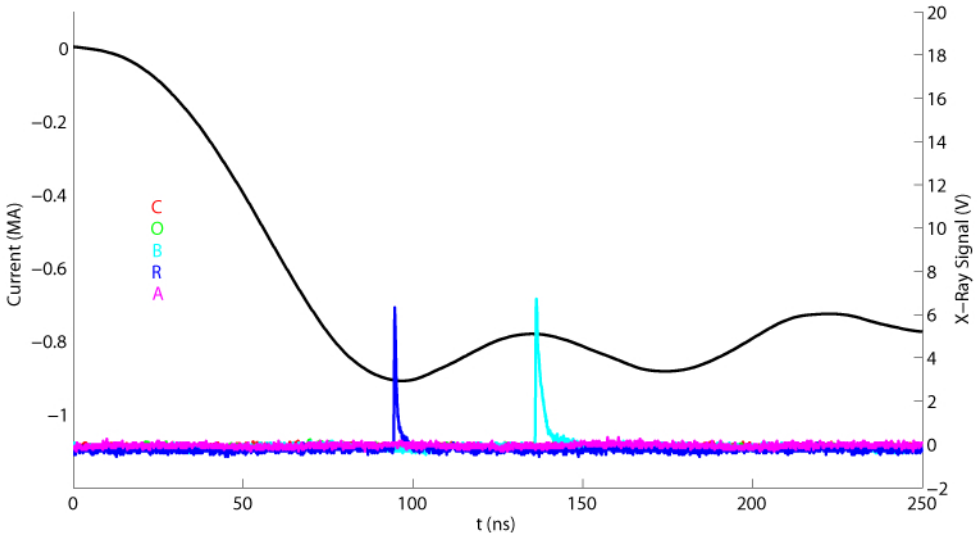


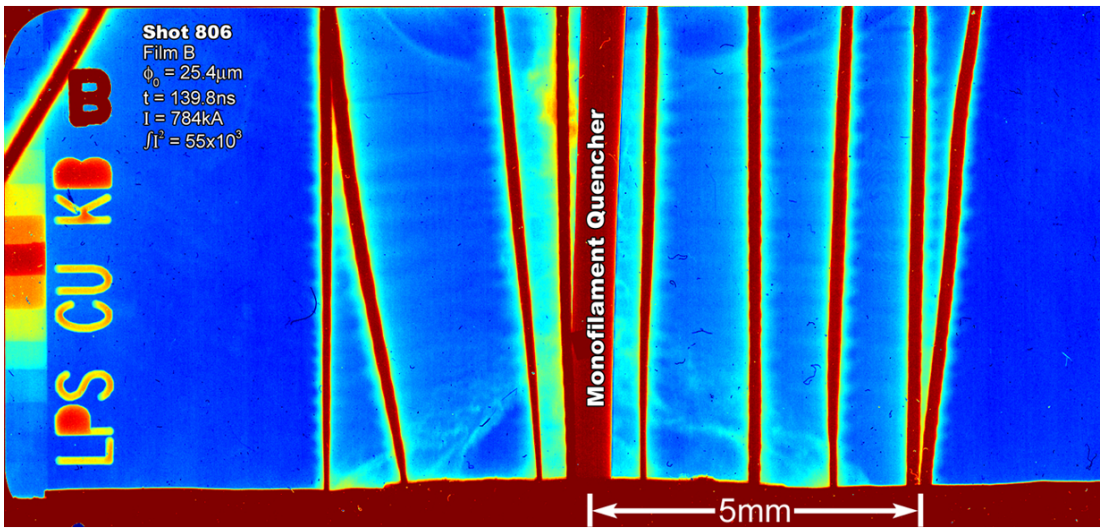

Figure G.24: Shot 807 $R_0$ = 4mm $\phi_0$=5.1$\mu$m N=10

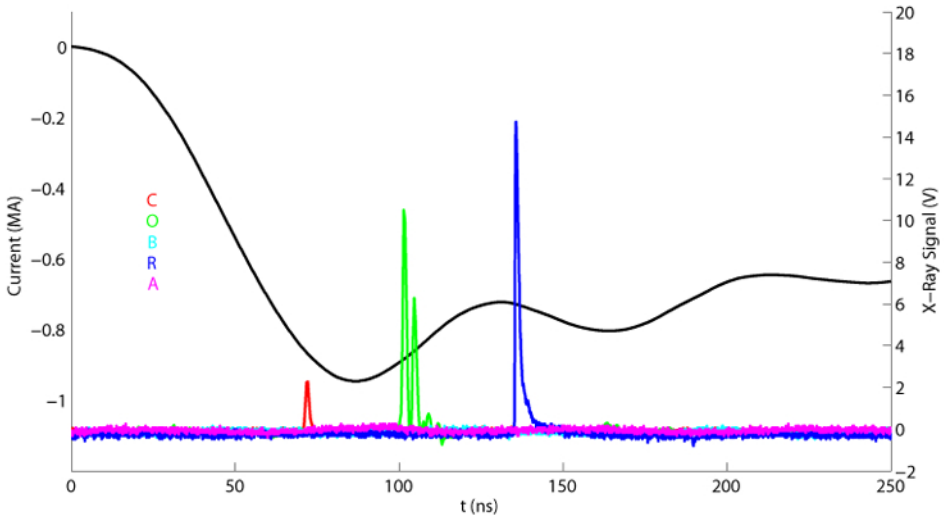


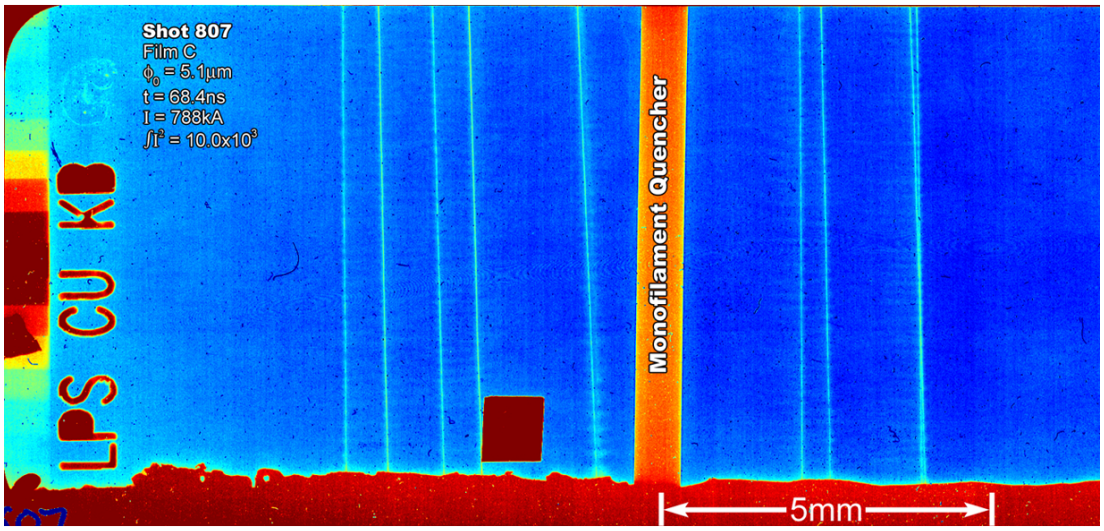


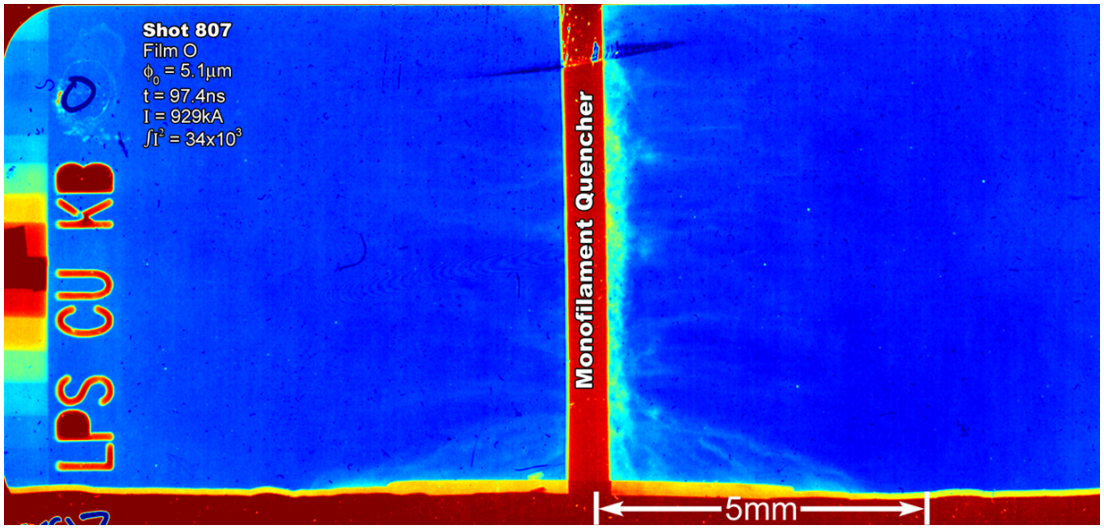

Figure G.25: Shot 887 $R_0$ = 8mm $\phi_0$=10.2$\mu$m N=16

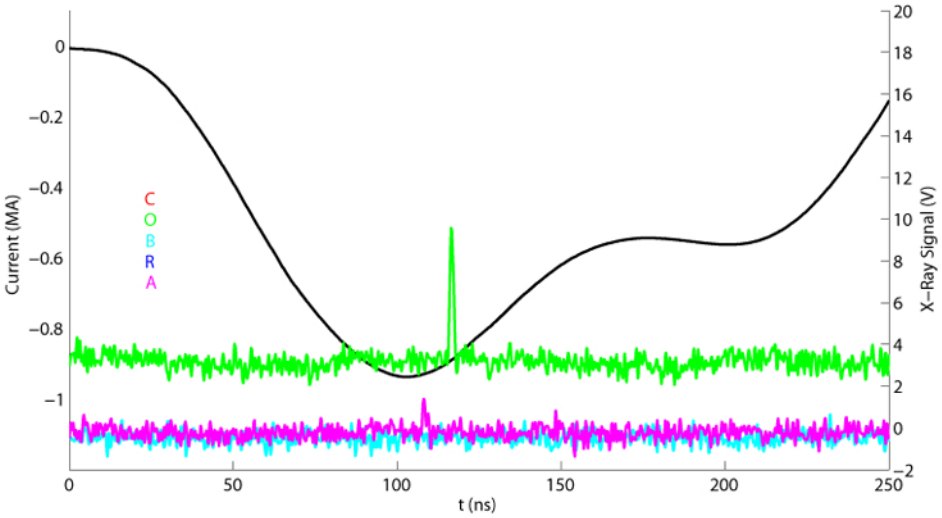


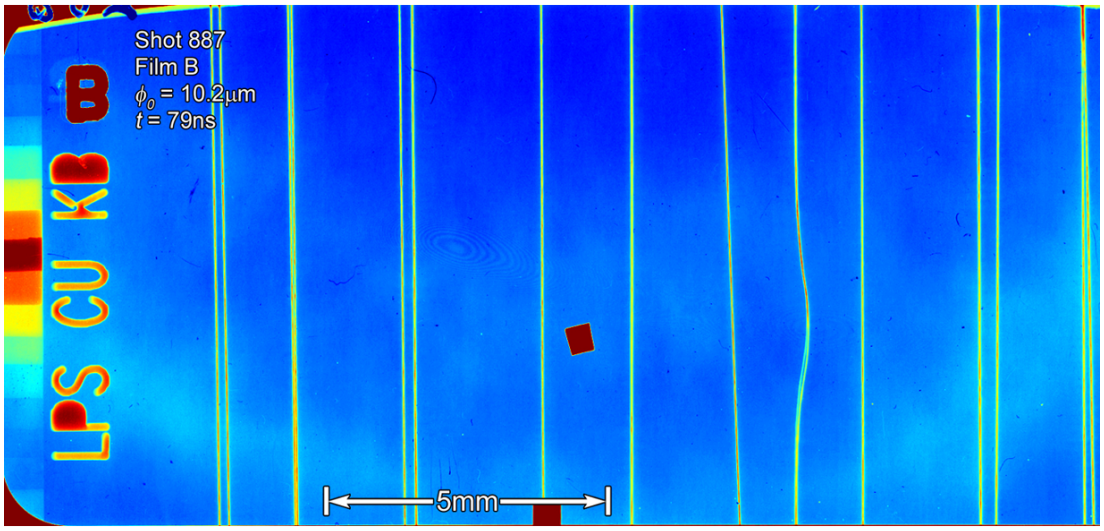


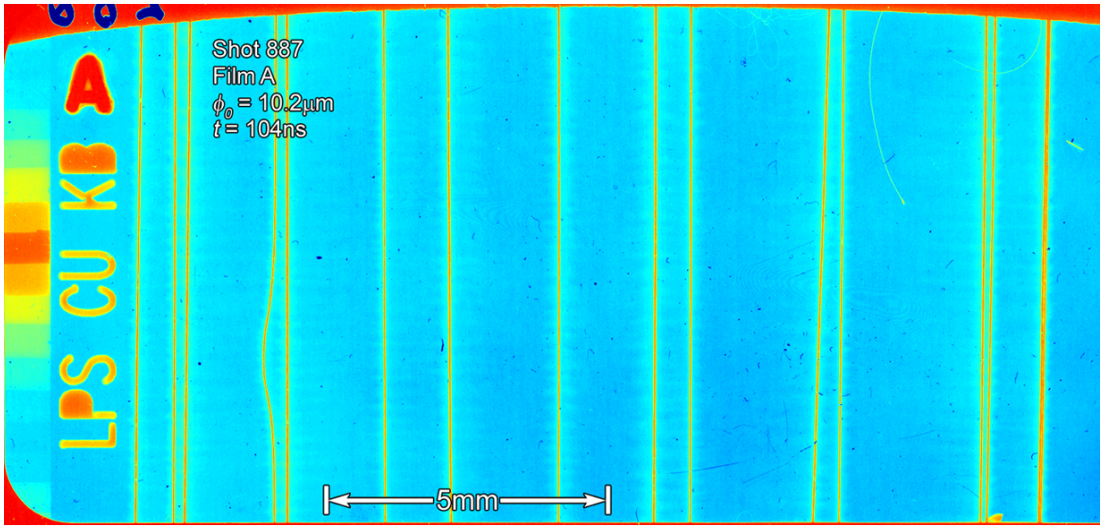

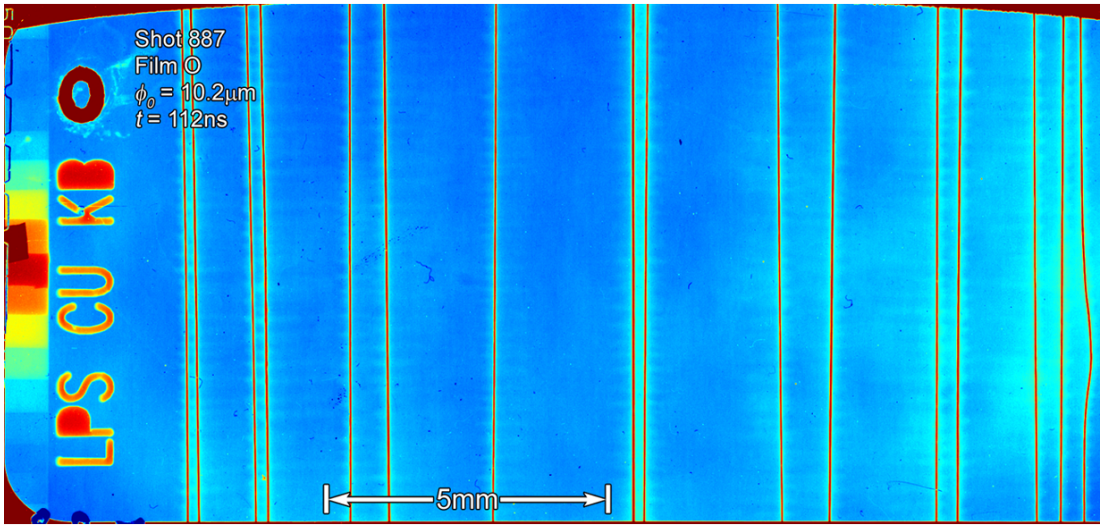
Shot 887
Film O
$\phi_o$ = 10.2μm
$t$ = 112ns
LPS CU KB O
5mm

Figure G.26: Shot 888 $R_0$ = 8mm $\phi_0$=10.2$\mu$m N=16

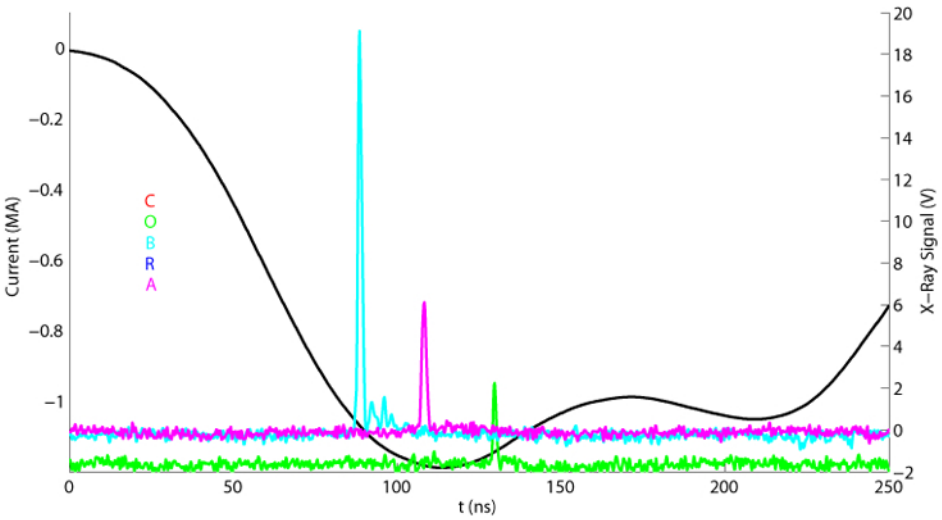


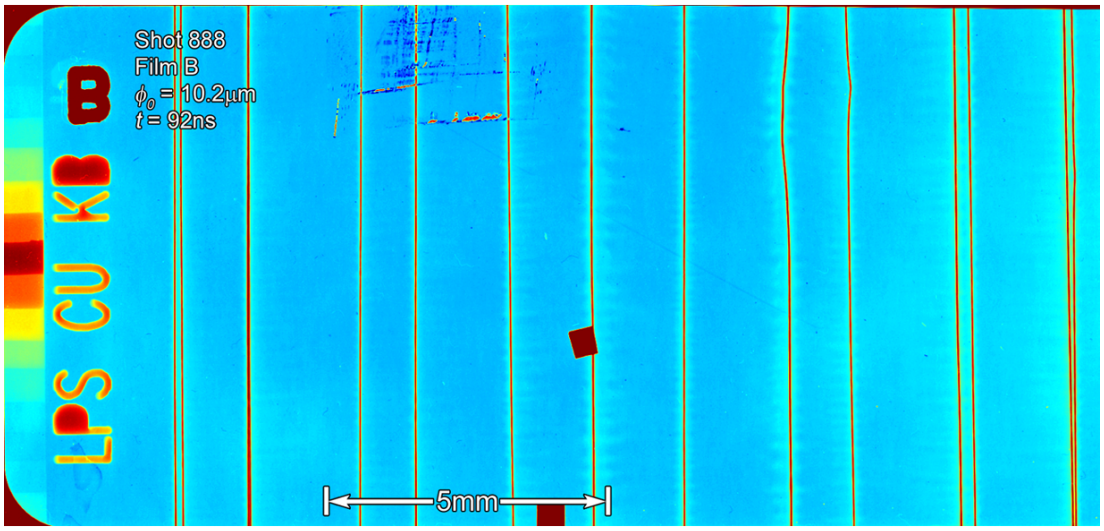


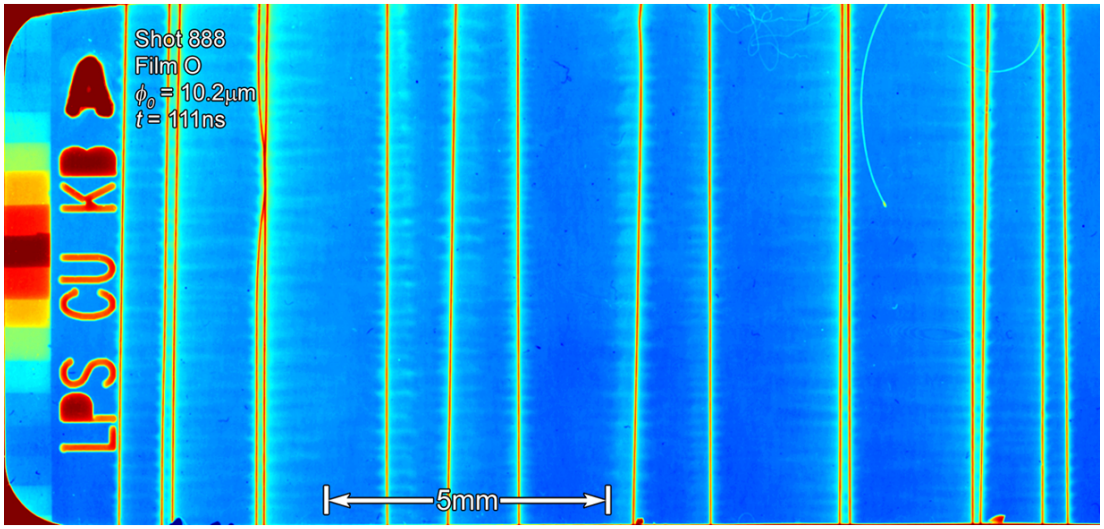

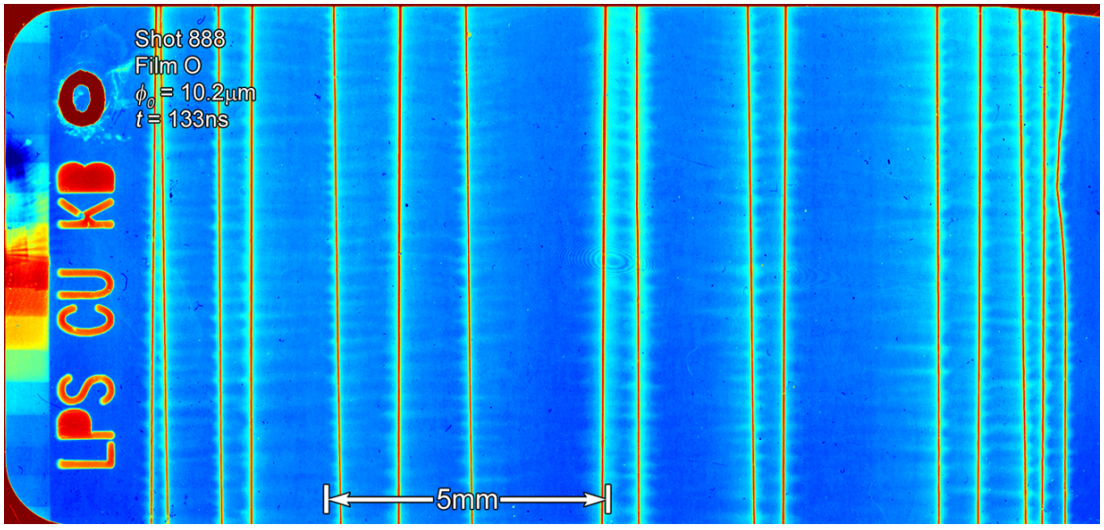
Shot 888
Film O
$\phi_o$ = 10.2μm
$t$ = 133ns
LPS CU KB O
5mm

Figure G.27: Shot 891 $R_0$ = 8mm $\phi_0$=10.2$\mu$m N=16

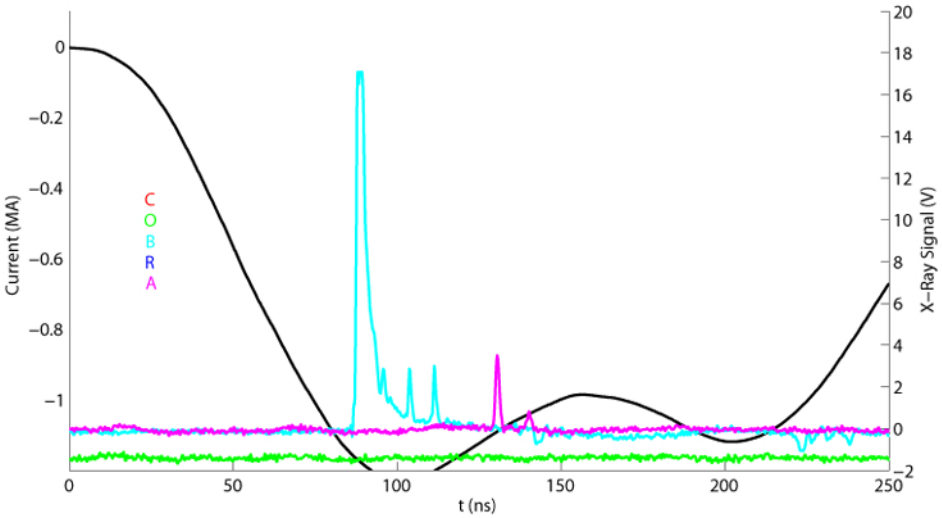


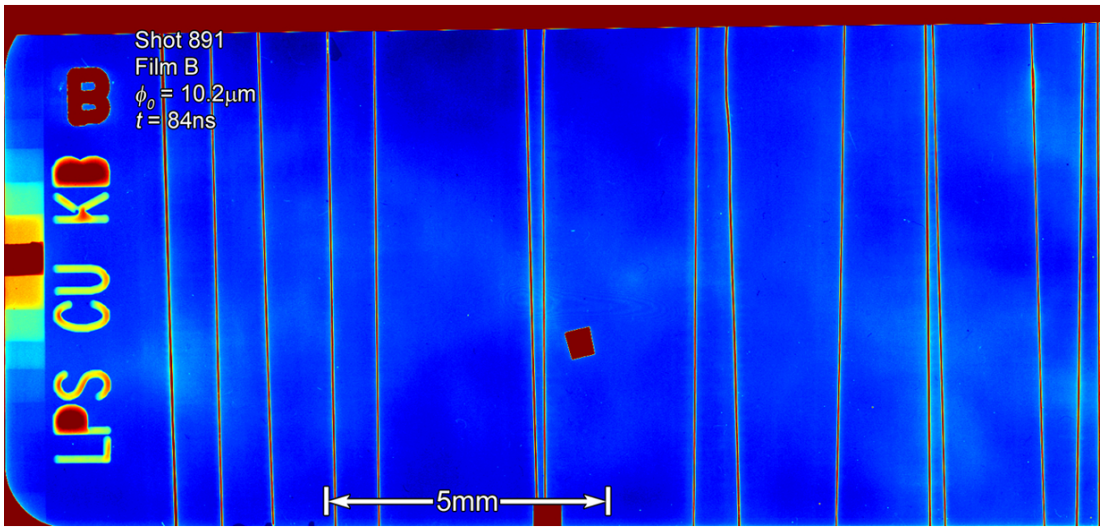


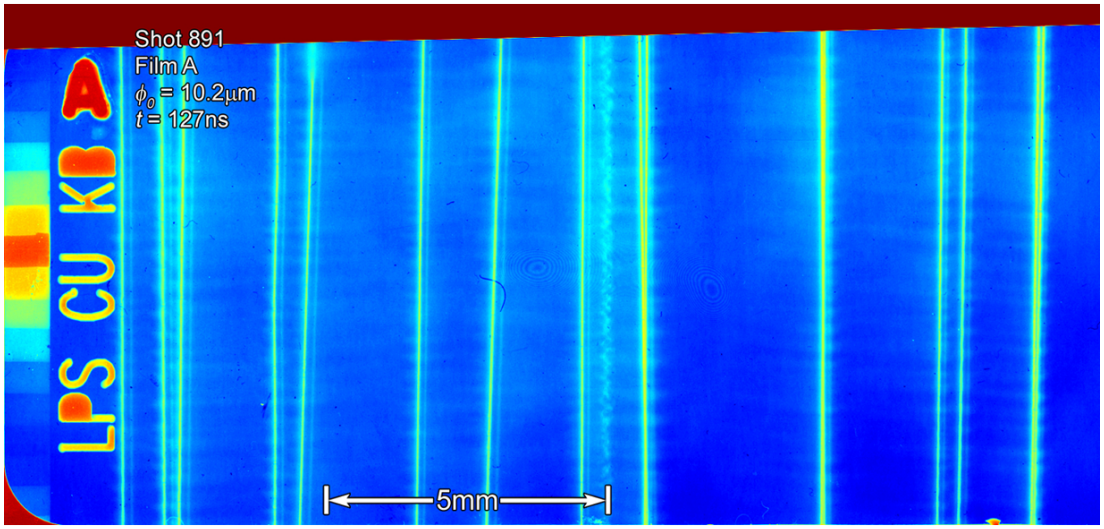

Figure G.28: Shot 892 $R_0$ = 8mm $\phi_0$=10.2$\mu$m N=16

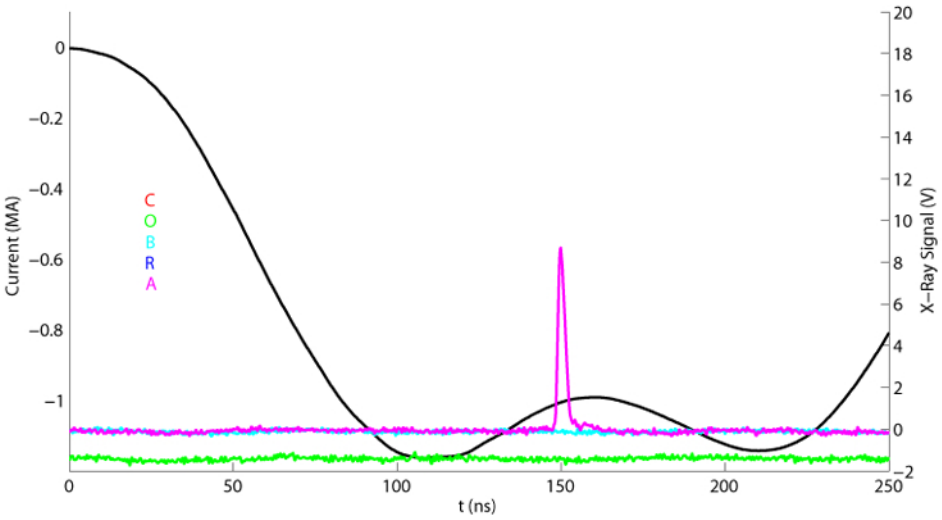


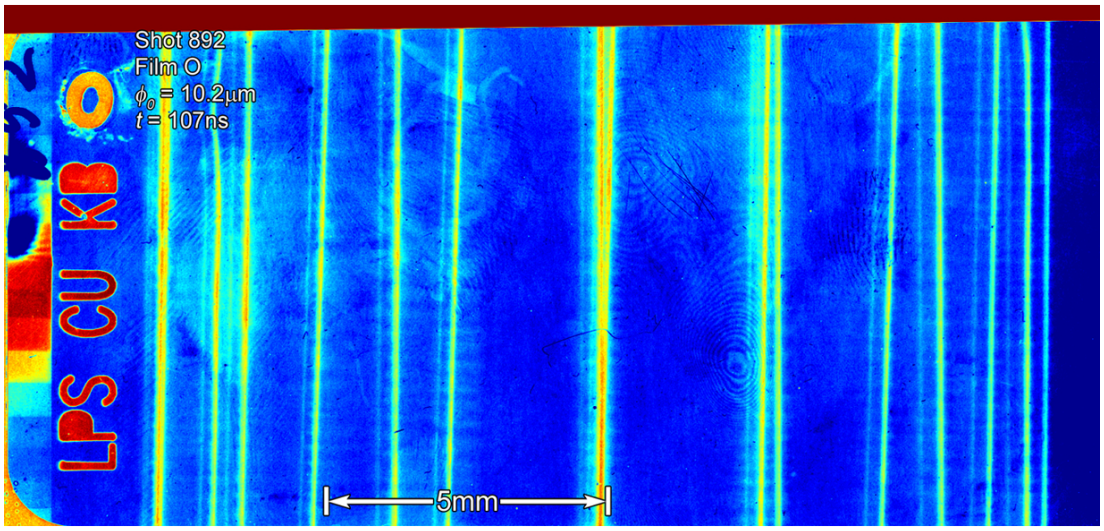


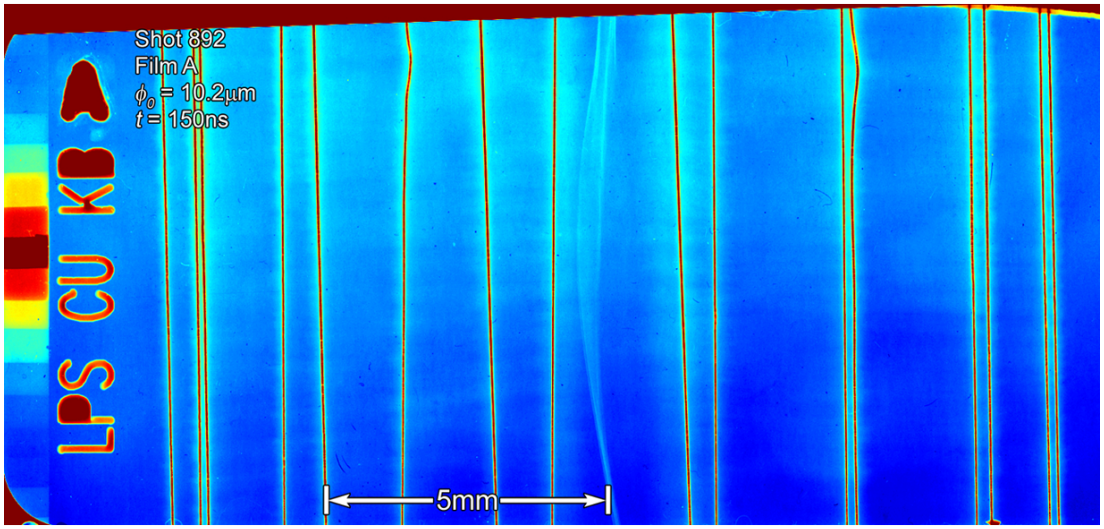

**BIBLIOGRAPHY**


[1] J. S Pearlman and J. C. Riordan. X-ray lithography using a pulsed plasma source. *Journal of Vacuum Science and Technology*, 19(4):1190–1193, 1981.

[2] B. Bernstein and I. Smith. Aurora, an electron accelerator. *IEEE Transactions on Nuclear Science*, NS-:294–300, 1973.

[3] R. A. Vesey, M. E. Cuneo, G. R. Bennett, J. L. Porter, R. G. Adams, R. A. Aragon, P. K. Rambo, L. E. Ruggles, W. W. Simpson, and I. C. Smith. Demonstration of radiation symmetry control for inertial confinement fusion in double $z$-pinch hohlraums. *Phys. Rev. Lett.*, 90(3):035005, Jan 2003.

[4] S. J. Stephanakis, L. S. Levine, D. Mosher, I. M. Vitkovitsky, and F. Young. Neutron production in exploding-wire discharges. *Phys. Rev. Lett.*, 29(9):568–569, Aug 1972.

[5] T. W. L. Sanford, G. O. Allshouse, B. M. Marder, T. J. Nash, R. C. Mock, R. B. Spielman, J. F. Seamen, J. S. McGurn, D. Jobe, T. L. Gilliland, M. Vargas, K. W. Struve, W. A. Stygar, M. R. Douglas, M. K. Matzen, J. H. Hammer, J. S. De Groot, J. L. Eddleman, D. L. Peterson, D. Mosher, K. G. Whitney, J. W. Thornhill, P. E. Pulsifer, J. P. Apruzese, and Y. Maron. Improved symmetry greatly increases x-ray power from wire-array $z$-pinches. *Phys. Rev. Lett.*, 77(25):5063–5066, Dec 1996.

[6] M. Friedman and I. M. Vitkovitsky. Implosion of an unneutralized drifting relativistic electron beam. *Applied Physics Letters*, 25(5):259–260, 1974.

[7] D. Mosher, S. J. Stephanakis, I. M. Vitkovitsky, C. M. Dozier, L. S. Levine, and D. J. Nagel. X radiation from high-energy-density exploded-wire discharges. *Applied Physics Letters*, 23(8):429–430, 1973.

[8] P. G. Burkhalter, C. M. Dozier, C. Stallings, and Robert D. Cowan. X-ray line emission and plasma conditions in exploded fe wires. *Journal of Applied Physics*, 49(3):1092–1098, 1978.

[9] G. B. Frazier. Owl ii pulsed-electron-beam generator. *Journal of Vacuum Science and Technology*, 12(6):1183–1187, 1975.

[10] S. A. Pikuz, T. A. Shelkovenko, D. B. Sinars, J. B. Greenly, Y. S. Dimant, and D. A. Hammer. Multiphase foamlike structure of exploding wire cores. *Phys. Rev. Lett.*, 83(21):4313–4316, Nov 1999.

[11] D. B. Sinars, Min Hu, K. M. Chandler, T. A. Shelkovenko, S. A. Pikuz, J. B. Greenly, D. A. Hammer, and B. R. Kusse. Experiments measuring the initial energy deposition, expansion rates and morphology of exploding wires with about 1 ka/wire. *Physics of Plasmas*, 8(1):216–230, 2001.

[12] G. S. Sarkisov, K. W. Struve, and D. H. McDaniel. Effect of deposited energy on the structure of an exploding tungsten wire core in a vacuum. *Physics of Plasmas*, 12(5):052702, 2005.

[13] William L. Baker, Miles C. Clark, James H. Degnan, Gerald F. Kiuttu, Charles R. McClenahan, and Robert E. Reinovsky. Electromagnetic-implosion generation of pulsed high-energy-density plasma. *Journal of Applied Physics*, 49(9):4694–4706, 1978.

[14] J. Shiloh, A. Fisher, and N. Rostoker. $z$ pinch of a gas jet. *Phys. Rev. Lett.*, 40(8):515–518, Feb 1978.

[15] James H. Degnan, Robert E. Reinovsky, David L. Honea, and Roger D. Bengtson. Electromagnetic implosions of cylindrical gas "shells". *Journal of Applied Physics*, 52(11):6550–6561, 1981.

[16] C. Stallings, K. Nielsen, and R. Schneider. Multiple-wire array load for high-power pulsed generators. *Applied Physics Letters*, 29(7):404–406, 1976.

[17] R. F. Benjamin, J. S. Pearlman, E. Y. Chu, and J. C. Riordan. Measurements of the dynamics of imploding wire arrays. *Applied Physics Letters*, 39(10):848–850, 1981.

[18] Peter J. Turchi and William L. Baker. Generation of high-energy plasmas by electromagnetic implosion. *Journal of Applied Physics*, 44(11):4936–4945, 1973.

[19] R. B. Spielman, D. L. Hanson, M. A. Palmer, M. K. Matzen, T. W. Hussey, and J. M. Peek. Efficient x-ray production from ultrafast gas-puff z pinches. *Journal of Applied Physics*, 57(3):830–833, 1985.

[20] M. Gersten, W. Clark, J. E. Rauch, G. M. Wilkinson, J. Katzenstein, R. D. Richardson, J. Davis, D. Duston, J. P. Apruzese, and R. Clark. Scaling of plasma temperature, density, size, and x-ray emission above 1 kev with array diameter and mass for aluminum imploding-wire plasmas. *Phys. Rev. A*, 33(1):477–484, Jan 1986.

[21] N. R. Pereira and J. Davis. X rays from z-pinches on relativistic electron-beam generators. *Journal of Applied Physics*, 64(3):R1–R27, 1988.

[22] C. Deeney, T. Nash, R. R. Prasad, L. Warren, K. G. Whitney, J. W. Thornhill, and M. C. Coulter. Role of the implosion kinetic energy in determining the kilovolt x-ray emission from aluminum-wire-array implosions. *Phys. Rev. A*, 44(10):6762–6775, Nov 1991.

[23] F. S. Felber and N. Rostoker. Kink and displacement instabilities in imploding wire arrays. *Physics of Fluids*, 24(6):1049–1055, 1981.

[24] D.D. Bloomquist, R.W. Stinnett, D.H. McDaniel, J.R. Lee, A.W. Sharpe, J.A. Halbleib, L.G. Schlitt, P.W. Spence, and P. Corcoran. Saturn, a large area x-ray simulation accelerator. In *Sandia National Laboratories Internal Publication*, pages 310 – 317, Arlington, VA, USA, 1987. Large Area X-Ray Simulation Accelerator;Magnetically Insulated Transmission Lines;Three-Ring Electron-Beam Diode;Saturn Accelerator;Marx Generators;.

[25] R. B. Spielman, C. Deeney, G. A. Chandler, M. R. Douglas, D. L. Fehl, M. K. Matzen, D. H. McDaniel, T. J. Nash, J. L. Porter, T. W. L. Sanford, J. F. Seamen, W. A. Stygar, K. W. Struve, S. P. Breeze, J. S. McGurn, J. A. Torres, D. M. Zagar, T. L. Gilliland, D. O. Jobe, J. L. McKenney, R. C. Mock, M. Vargas, T. Wagoner, and D. L. Peterson. Tungsten wire-array z-pinch experiments at 200 tw and 2 mj. *Physics of Plasmas*, 5(5):2105–2111, 1998.

[26] T W L Sanford, T J Nash, R E Olson, D E Bliss, R W Lemke, C L Olson, C L Ruiz, R C Mock, J E Bailey, G A Chandler, M E Cuneo, R J Leeper, M K Matzen, T A Mehlhorn, S A Slutz, W A Stygar, D L Peterson, R E Chrien, R G Watt, N F Roderick, G W Cooper, J P Apruzese, G S Sarkisov, J P Chittenden, and M G Haines. Progress in z-pinch driven dynamic-hohlraums for high-temperature radiation-flow and icf experiments at sandia national laboratories. *Plasma Physics and Controlled Fusion*, 46(12B):B423–B433, 2004.

[27] C. L. Ruiz, G. W. Cooper, S. A. Slutz, J. E. Bailey, G. A. Chandler, T. J. Nash, T. A. Mehlhorn, R. J. Leeper, D. Fehl, A. J. Nelson, J. Franklin, and L. Ziegler. Production of thermonuclear neutrons from deuterium-filled capsule implosions driven by z-pinch dynamic hohlraums. *Physical Review Letters*, 93(1):015001, 2004.

[28] Mary Ann Sweeney. History of z-pinch research in the u.s. *AIP Conference Proceedings*, 651(1):p9 –, 2002.

[29] M. Keith Matzen, M. A. Sweeney, R. G. Adams, J. R. Asay, J. E. Bailey, G. R. Bennett, D. E. Bliss, D. D. Bloomquist, T. A. Brunner, R. B. Campbell, G. A. Chandler, C. A. Coverdale, M. E. Cuneo, J.-P. Davis, C. Deeney, M. P. Desjarlais, G. L. Donovan, C. J. Garasi, T. A. Haill, C. A. Hall, D. L. Hanson, M. J. Hurst,

B. Jones, M. D. Knudson, R. J. Leeper, R. W. Lemke, M. G. Mazarakis, D. H. McDaniel, T. A. Mehlhorn, T. J. Nash, C. L. Olson, J. L. Porter, P. K. Rambo, S. E. Rosenthal, G. A. Rochau, L. E. Ruggles, C. L. Ruiz, T. W. L. Sanford, J. F. Seamen, D. B. Sinars, S. A. Slutz, I. C. Smith, K. W. Struve, W. A. Stygar, R. A. Vesey, E. A. Weinbrecht, D. F. Wenger, and E. P. Yu. Pulsed-power-driven high energy density physics and inertial confinement fusion research. *Physics of Plasmas*, 12(5):055503, 2005.

[30] M. E. Cuneo, E. M. Waisman, S. V. Lebedev, J. P. Chittenden, W. A. Stygar, G. A. Chandler, R. A. Vesey, E. P. Yu, T. J. Nash, D. E. Bliss, G. S. Sarkisov, T. C. Wagoner, G. R. Bennett, D. B. Sinars, J. L. Porter, W. W. Simpson, L. E. Ruggles, D. F. Wenger, C. J. Garasi, B. V. Oliver, R A. Aragon, W. E. Fowler, M. C. Hettrick, G. C. Idzorek, D. Johnson, K. Keller, S. E. Lazier, J. S. McGurn, T. A. Mehlhorn, T. Moore, D. S. Nielsen, J. Pyle, S. Speas, K. W. Struve, and J. A. Torres. Characteristics and scaling of tungsten-wire-array z-pinch implosion dynamics at 20 ma. *Physical Review E (Statistical, Nonlinear, and Soft Matter Physics)*, 71(4):046406, 2005.

[31] F. F. Chen. *Introduction to plasma physics and controlled fusion*. Plenum Press, 1984.

[32] Willard H. Bennett. Magnetically self-focussing streams. *Phys. Rev.*, 45(12):890–897, Jun 1934.

[33] Nino R. Pereira. A simple derivation of the peasebraginskii current. *Physics of Fluids B: Plasma Physics*, 2(3):p677 –, 1990.

[34] Willard H. Bennett. Self-focusing streams. *Phys. Rev.*, 98(6):1584–1593, Jun 1955.

[35] D. D. Ryutov, M. S. Derzon, and M. K. Matzen. The physics of fast $z$ pinches. *Rev. Mod. Phys.*, 72(1):167–223, Jan 2000.

[36] D.L. Smith, P. Ingwersen, L.F. Bennett, J.d. Boyes, D.E. Anderson, J.b. Greenly, and R.N. Sudan. Cobra accelerator for sandia icf diode research at cornell university. *Proceedings of the 1995 Particle Accelerator Conference*, 2:1204–1206, 1995.

[37] J.D. Douglass, J.B. Greenly, D.A. Hammer, B.R. Kusse, J.T. Blanchard, L.M. Maxson, R.D. Mcbride, S.C. Wilhelm, H. Glidden, S. Grasso, and H.D. Sanders. Capabilities of the reconfigured cobra accelerator. *Pulsed Power Conference, 2005 IEEE*, pages 273–276, 2005. Monterey, CA, USA.

[38] T. A. Shelkovenko, D. A. Chalenski, K. M. Chandler, J. D. Douglass, J. B. Greenly, D. A. Hammer, B. R. Kusse, R. D. McBride, and S. A. Pikuz. Diagnostics on the cobra pulsed power generator. *Review of Scientific Instruments*, 77(10):pN.PAG –, 2006.

[39] S. N. Bland, S. C. Bott, G. N. Hall, S. V. Lebedev, F. Suzuki, D. J. Ampleford, J. B. A. Palmer, S. A. Pikuz, and T. A. Shelkovenko. Diagnostics for studying the dynamics of wire array z pinches. *Review of Scientific Instruments*, 77(10):pN.PAG –, 2006.

[40] W. Clark, M. Wilkinson, J. Rauch, and J. LePage. X-ray measurements of imploding wire plasmas. *Journal of Applied Physics*, 53(3):1426–1429, 1982.

[41] W. Clark, M. Gersten, J. Katzenstein, J. Rauch, R. Richardson, and M. Wilkinson. Aluminum, calcium, and titanium imploding plasma experiments on the blackjack 5 pulse generator. *Journal of Applied Physics*, 53(6):4099–4104, 1982.

[42] S. V. Lebedev, I. H. Mitchell, R. Aliaga-Rossel, S. N. Bland, J. P. Chittenden, A. E. Dangor, and M. G. Haines. Azimuthal structure and global instability in the implosion phase of wire array *z*-pinch experiments. *Phys. Rev. Lett.*, 81(19):4152–4155, Nov 1998.

[43] S. V. Lebedev, F. N. Beg, S. N. Bland, J. P. Chittenden, A. E. Dangor, M. G. Haines, S. A. Pikuz, and T. A. Shelkovenko. Effect of core-corona plasma structure on seeding of instabilities in wire array *z* pinches. *Phys. Rev. Lett.*, 85(1):98, Jul 2000.

[44] S. V. Lebedev, F. N. Beg, S. N. Bland, J. P. Chittenden, A. E. Dangor, M. G. Haines, K. H. Kwek, S. A. Pikuz, and T. A. Shelkovenko. Effect of discrete wires on the implosion dynamics of wire array z pinches. *Physics of Plasmas*, 8(8):3734–3747, 2001.

[45] B. Song. *High-Resolution Radiography Using the X-Pinch X-Ray Source*. PhD thesis, Cornell University, 2004.

[46] J. D. Douglass, S. A. Pikuz, T. A. Shelkovenko, D. A. Hammer, S. N. Bland, S. C. Bott, and R. D. McBride. Structure of the dense cores and ablation plasmas in the initiation phase of tungsten wire-array z pinches. *Physics of Plasmas*, 14(1):012704, 2007.

[47] D. B. Sinars, S. A. Pikuz, T. A. Shelkovenko, K. M. Chandler, and D. A. Hammer. Temporal parameters of the x-pinch x-ray source. *Review of Scientific Instruments*, 72(7):2948–2956, 2001.

[48] S. A. Pikuz, T. A. Shelkovenko, A. R. Mingaleev, D. A. Hammer, and H. P. Neves. Density measurements in exploding wire-initiated plasmas using tungsten wires. *Physics of Plasmas*, 6(11):4272–4283, 1999.

[49] Ian H. Hutchinson. *Principles of Plasma Diagnostics*. Cambridge University Press, 2 edition, 2002.

[50] V.V. Alexandrov, I.N. Frolov, M.V. Fedulov, E.V. Grabovsky, K.N. Mitrofanov, S.L. Nedoseev, G.M. Oleinik, I.Yu. Porofeev, A.A. Samokhin, P.V. Sasorov, V.P. Smirnov, G.S. Volkov, M.M. Zurin, and G.G. Zukakischvili. Prolonged plasma production at current-driven implosion of wire arrays on angara-5-1 facility. *IEEE Transactions on Plasma Science*, 30(2):559–566, 2002.

[51] D. B. Sinars, M. E. Cuneo, E. P. Yu, D. E. Bliss, T. J. Nash, J. L. Porter, C. Deeney, M. G. Mazarakis, G. S. Sarkisov, and D. F. Wenger. Mass-profile and instability-growth measurements for 300-wire z-pinch implosions driven by 14–18 ma. *Physical Review Letters*, 93(14):145002, 2004.

[52] E. V. Grabovskii;, K. N. Mitrofanov, G. M. Oleinik, and I. Yu. Porofeev. X-ray backlighting of the periphery of an imploding multiwire array in the angara-5-1 facility. *Plasma Physics Reports*, 30(2):p121 – 127, 20040201.

[53] Peter U. Duselis, Jeffrey A. Vaughan, and Bruce R. Kusse. Factors affecting energy deposition and expansion in single wire low current experiments. *Physics of Plasmas*, 11(8):4025–4031, 2004.

[54] J. P. Chittenden and C. A. Jennings. The development of instabilities in wire array z-pinches. *Physical Review Letters*, page Submitted for publication, 2008.

[55] D. B. Sinars, G. R. Bennett, D. F. Wenger, M. E. Cuneo, D. L. Hanson, J. L. Porter, R. G. Adams, P. K. Rambo, D. C. Rovang, and I. C. Smith. Monochromatic x-ray imaging experiments on the sandia national laboratories z facility (invited). *Review of Scientific Instruments*, 75(10):3672–3677, 2004.

[56] S. A. Pikuz, T. A. Shelkovenko, V. M. Romanova, D. A. Hammer, A. Ya. Faenov, V. A. Dyakin, and T. A. Pikuz. High-luminosity monochromatic x-ray backlighting using an incoherent plasma source to study extremely dense plasmas (invited). In *Proceedings of the eleventh topical conference on high temperature plasma diagnostics*, volume 68, pages 740–744. AIP, 1997.